



HAL
open science

Representing the present and future release of carbon to rivers in permafrost regions using an earth system model

Simon Bowring

► To cite this version:

Simon Bowring. Representing the present and future release of carbon to rivers in permafrost regions using an earth system model. *Climatology*. Université Paris-Saclay, 2019. English. NNT : 2019SACLV034 . tel-02297093v1

HAL Id: tel-02297093

<https://theses.hal.science/tel-02297093v1>

Submitted on 25 Sep 2019 (v1), last revised 27 Sep 2019 (v2)

HAL is a multi-disciplinary open access archive for the deposit and dissemination of scientific research documents, whether they are published or not. The documents may come from teaching and research institutions in France or abroad, or from public or private research centers.

L'archive ouverte pluridisciplinaire **HAL**, est destinée au dépôt et à la diffusion de documents scientifiques de niveau recherche, publiés ou non, émanant des établissements d'enseignement et de recherche français ou étrangers, des laboratoires publics ou privés.

Representing the Present and Future Release of Carbon to Rivers in Permafrost Regions using an Earth System Model

Thèse de doctorat de l'Université Paris-Saclay
préparée à l'Université de Versailles Saint-Quentin-en-Yvelines

École doctorale N°129: Sciences de l'environnement d'Ile-de-France
Spécialité de doctorat: Météorologie, océanographie, physique de
l'environnement

Thèse présentée et soutenue à LSCE, le 23 Mai, 2019

Mr. Simon P. K. Bowring

Composition du Jury :

M. Philippe BOUSQUET Professeur, UVSQ	Président
M. Peter RAYMOND Professeur, Yale University (Etats-Unis)	Rapporteur
Mme. Jorien VONK Associate Professeur, VUA (Amsterdam)	Rapporteur
M. Lars TRANVIK Professeur, Uppsala University (Suède)	Examineur
M. Samuel ABIVEN Associate Professeur, UZH (Zurich)	Examineur
M. Philippe CIAIS Professeur, LSCE	Directeur de thèse
M. Bertrand GUENET Chargé de recherche, LSCE	Co-Directeur de thèse
M. Ronny LAUERWALD Chercheur contractuel, ULB (Bruxelles)	Co-Directeur de thèse

Titre : Représenter le rejet présent et futur de carbone dans les rivières dans les régions de pergélisol à l'aide d'un modèle de surface

Mots clés : pergélisol, rivières, carbone organique dissout (COD), alcalinité, changement climatique, couche active

Résumé : Pendant la majeure partie du Pléistocène, les régions de la Terre recouvertes de pergélisol ont été des puits nets de carbone (C) d'origine végétale et transférée au sol. L'accumulation de ce C organique dans les sols de la région de pergélisol circumpolaire nord a conduit à des stocks qui contiennent actuellement une masse C supérieure à celle qui existe dans l'atmosphère par un facteur de plus de deux. Dans le même temps, les rivières du pergélisol arctique rejettent environ 11% du flux d'eau fluvial global dans les océans, et ce dans un océan (l'Arctique) correspondant à 1% du volume d'eau total des océans mais d'une très grande surface ce qui le rend relativement sensible aux afflux de matières dérivées des surfaces terrestres. Ce flux fluvial provient de précipitations sous forme de pluie ou de neige qui, lors du contact initial avec la surface, ont le potentiel immédiat d'interagir avec le C de l'une des deux manières suivantes: d'une part, l'eau qui coule sur des roches carbonatées ou silicatées provoquera une réaction dont le réactif nécessite l'absorption de CO₂ atmosphérique, qui est ensuite transporté dans l'eau des rivières. Ce C inorganique issu de l'interaction de l'eau, de l'atmosphère et de la lithosphère représente donc un vecteur de stockage ou de «puits» du C. D'autre part, l'eau qui interagit avec la matière organique présente dans les arbres, la litière ou le sol peut transporter le C qu'elle contient et le transférer par les eaux de surface et souterraines dans les rivières. Ce carbone peut ensuite être métabolisée vers l'atmosphère ou exportée dans la mer. Des améliorations récentes dans la compréhension de la dynamique du C terrestre indiquent que ce transfert hydrologique de matière organique représente le devenir dominant du carbone organique, après prise en compte de la respiration des plantes et du sol. Dans le contexte du réchauffement climatique d'origine anthropique amplifié de l'Arctique, l'exposition thermique imposée au stock de pergélisol de C, associé à d'une augmentation des précipitations futures, laisse présager des

changements importants dans le cycle du carbone organique et inorganique induit par les flux latéraux. Cependant, la totalité des processus impliqués rend difficile la prévision de ce changement. Partant de ce constat, cette thèse s'appuie sur les avancées antérieures en matière de modélisation du système terrestre pour inclure la production et le transport latéral de carbone organique dissout (COD), de CO₂ dérivé de la respiration et d'alcalinité dérivée au sein d'un modèle global de surface terrestre développé précédemment pour résoudre spécifiquement les processus des régions boréales. A l'aide de données issues des plus récent produits sur le sol, l'eau, la végétation et la climatologie pour forcer les conditions aux limites du modèle, nous sommes en mesure de reproduire les processus et les flux de transport latéraux existants ainsi que faire des projections futures. Dans cette thèse, nous montrons que les exportations d'alcalinité panarctique et l'absorption du CO₂ qui l'accompagne augmentent avec le réchauffement, que les flux de COD diminuent en grande partie à cause des circuits d'écoulement d'eau plus profonds dans le sol et des changements qui en résultent dans les interactions carbone-eau. Enfin, nous observons que la libération de COD dans l'Arctique n'est pas linéairement liée à la température. Par conséquent, la future libération de COD dans l'Arctique peut augmenter ou diminuer avec la température en fonction des modifications de l'état thermique et des trajectoires hydrologiques dans les sols profonds. L'effet net de ces flux sur les océans est de réduire l'acidification future de l'eau de mer d'origine terrestre. À l'inverse, nos simulations montrent que l'absorption de CO₂ due à l'altération chimique est supérieure à son évaporation de l'eau des rivières, ce qui signifie que, lorsque l'altération est prise en compte, le cycle du carbone dans les eaux intérieures passe d'une source nette de C à un puits net. En outre, ce puits augmente au 21^{ème} siècle, amortissant partiellement la perte de carbone du sol lors du dégel du pergélisol.



Title : Representing the Present and Future Release of Carbon to Rivers in Permafrost Regions using an Earth System Model

Keywords : permafrost, rivers, DOC, alkalinity, climate change, active layer

Abstract: For much of the Pleistocene, regions of the Earth underlain by permafrost have been net accumulators of terrestrially-fixed plant carbon (C), known as organic C, to the extent that in the present day the soils of the northern circumpolar permafrost region alone contain a C mass outweighing that which exists in the modern atmosphere by a factor of over two. At the same time, the rivers of the Arctic permafrost region discharge about 11% of the global volumetric river water flux into oceans, doing so into an ocean (the Arctic) with 1% of global ocean water volume and a very high surface area: volume ratio, making it comparatively sensitive to influxes of terrestrially derived matter. This river flux is sourced from precipitation as either rain or snow, which, upon initial contact with the landscape has the immediate potential to interact with C in one of two ways: Water running over carbonate or silicate-bearing rocks will cause a reaction whose reactant requires the uptake of atmospheric CO₂, which is subsequently transported in river water. This ‘inorganic’ C derived from interaction of water, atmosphere and lithosphere thus represents a C storage or ‘sink’ vector. In addition, water interacting with organic matter in tree canopies, litter or soil can dissolve C contained therein, and transfer it via surface and subsurface water flows into rivers, whereupon it may either be metabolised to the atmosphere or exported to the sea. Recent improvements in understanding of terrestrial C dynamics indicate that this hydrologic transfer of organic matter represents the dominant fate of organic carbon, after plant and soil respiration are accounted for. In the context of amplified Arctic anthropogenic warming, the thermal exposure imposed on the permafrost C stock with expectations of enhanced future precipitation point toward substantial shifts in the lateral flux-mediated organic and inorganic C cycle. However, the complex totality of the processes involved make prediction of this shift

difficult. Addressing this gap in instrumental power and theoretical understanding, this collection of studies builds upon previous advances in earth system modelling to include the production and lateral transport of dissolved organic C (DOC), respiration-derived CO₂, and rock-weathering derived alkalinity in a global land surface model previously developed to specifically resolve permafrost-region processes. By subjecting the resulting model to state of the art soil, water, vegetation and climatology datasets, we are able to reproduce existing lateral transport processes and fluxes, and project them into the future. In what follows, we show that while Pan-Arctic alkalinity exports and attendant CO₂ uptake increase over the 20th and 21st Centuries under warming, DOC fluxes decline largely as a result of deeper soil water flow-paths and the resulting changes in carbon-water interactions. Rather than displaying a clear continuous (linear or non-linear) temperature sensitivity, future Arctic DOC release can increase or decrease with temperature depending on changes in the thermal state and hydrologic flow paths in the deep soil. The net marine effect of these fluxes is to decrease future terrestrially derived seawater acidification. Conversely, our simulations show that CO₂ uptake from chemical weathering exceeds its evasion from river water, meaning that when weathering is considered, the inland water carbon cycle shifts from being a net C-source to a sink. Further, this sink increases into the 21st C, partially buffering soil C loss from permafrost thaw.





1 Acknowledgements

2
3 This was unforeseen. But a PhD thesis on the global numerical modeling of the
4 permafrost, for somebody from a sub-tropical island who started off professionally in
5 writing, was never all that likely. The succession of leaps, many thousands small and
6 some very large over the past three and a half years, have been intellectual, emotional,
7 organisational and –largely less positively –physical, and would have come to little
8 without many people, some of whom I hope have the opportunity, as it were, to be
9 reading these words now. I have gone from somebody who knew next to nothing of the
10 permafrost, of coding, or the importance of the process by which huge masses of the sky
11 are transferred by raindrops over the entire vast stretch of the global land mass into the
12 oceans, to somebody who knows a little bit more. I have met great scientists, colleagues
13 and individuals, and travelled to many places during this time to do so, briefly even
14 acquainting myself with the Lena River in Eastern Siberia. The process itself has been
15 painful, frustrating, stressful, sometimes rewarding, but its outcome has, I hope,
16 somewhat fulfilled its purpose of adding understanding and context to our
17 interpretation of what is happening and what could happen to our planet and the beings
18 that inhabit it, now and onward.

19
20 For now, I would like to first raise a glass to my supervisors: Bertrand for his kindness,
21 Philippe for his patience and huge depth of field. A glass more pungent I raise to Ronny
22 for his brilliance, help and humour, and without whom I would likely have abandoned
23 this attempt. Special thanks to Albert, for being there to deal with my code, to Pierre R.
24 and Pierre F. for having and giving belief, and to Jorien, Pete, Samuel and Lars for
25 agreeing to be on the committee tasked with reviewing this document. To my
26 collaborators in life and co-conspirators in laughter and friendship, you know who you
27 are. But here I'll shout out some names. Nefeli, Martin, Isa, Yannis, Ana, Ardalan, Lea,
28 Bob, Rashel, Patrick, Costa, Stefano, Joao, Edo, Imie, Gautham, Taco, Joris, Christos,
29 Giorgos, Niki, Dimi, Omer, Heike, Vale, Tsoef, Fekas, Ola, Timo, Braschi, Ryan, Olivia,
30 Yucca, Crystal, Sim, Matthi, Iain, Alex: Thank you for collectively carrying in you the
31 same flashing, giving, nonchalant and hilarious magic infused of life itself; I'd have been
32 defeated many times in many ways without it. To my parents for their timeless,
33 unconditional support and embodiment of the spirit of questioning, and to my brother
34 for his curiosity and bravery, for always providing a different. And to Monse for being
35 my light, and driving everything which makes everything worth everything.

49	Chapter 1: Introduction	4
50	Chapter 2	12
51	ORCHIDEE MICT LEAK, a global model for the production, transport and	
52	transformation of dissolved organic carbon from Arctic permafrost regions :	
53	model description and simulation protocol	12
54	Summary	12
55	Chapitre 2 ORCHIDEE MICT LEAK, un modèle global pour la production, le transport et	
56	la transformation du carbone organique dissous des régions de pergélisol de	
57	l'Arctique: description du modèle et protocole de simulation	14
58	Introduction	16
59	1.1 A giant, reactive, fast-draining funnel: A permafrost basin overview	18
60	2 Methods	21
61	2.1 Model Description	21
62	2.11 Soil layer processes: turbation adsorption	31
63	Soil Carbon Spinup and Simulation Protocol	33
64	Conclusion	34
65	Chapter 3	36
66	ORCHIDEE MICT-LEAK (r5459), a global model for the production, transport and	
67	transformation of dissolved organic carbon from Arctic permafrost regions, Part	
68	2: Model evaluation over the Lena River basin	36
69	Summary	36
70	Chapitre 3 ORCHIDEE MICT-LEAK (r5459), modèle mondial de production, de transport	
71	et de transformation du carbone organique dissous issu des régions de pergélisol de	
72	l'Arctique, partie 2: évaluation du modèle sur le bassin de la Lena.	38
73	1 Introduction	40
74	2 Simulation Rationale	40
75	3 Simulation Setup	41
76	4 Results and Discussion	42
77	Chapter 4	78
78	Arctic lateral carbon fluxes decline with future warming	78
79	Summary	78
80	Chapitre 4 Les flux de carbone latéraux dans l'Arctique diminuent avec le	
81	réchauffement futur.	80
82	Introduction	82
83	Results	83
84	21st Century changes and annualised outflow	84
85	More carbon-less DOC	86
86	DOC climate sensitivity	89
87	Chapter 5	92
88	CO₂ Uptake By Weathering Increasingly Exceeds CO₂ Evasion From Rivers As	
89	Permafrost Thaws	92
90	Summary	92
91	Chapitre 5 L'absorption de CO₂ par altération des roches dépasse de plus en plus le	
92	relargage de CO₂ des rivières à mesure que le pergélisol dégèle	94
93	1 Introduction	96
94	2 Materials and Methods	100

95	3 Data and Simulation	106
96	4 Results.....	107
97	5 Conclusions.....	116
98	Chapter 6:.....	118
99	Perspective and Outlook	118
100	General Summary	118
101	The Data Gap	118
102	The modelling gap.....	120
103	Appendices	123
104	Appendix 1.....	123
105	Appendix to Chapter 2:	123
106	ORCHIDEE MICT-LEAK (r5459), a global model for the production, transport and	
107	transformation of dissolved organic carbon from Arctic permafrost regions, Part 2:	
108	Model evaluation over the Lena River basin.....	123
109	Appendix 2.....	129
110	Appendix to Chapter 4:.....	129
111	Arctic lateral carbon fluxes decline with warming.....	129
112	Appendix 3.....	148
113	Appendix to Chapter 5:.....	148
114	References	150
115		
116		
117		
118		
119		
120		
121		
122		
123		
124		
125		
126		
127		
128		
129		
130		
131		
132		
133		
134		
135		
136		
137		
138		
139		
140		

Chapter 1: Introduction

141
142
143
144
145
146
147
148
149
150
151
152
153
154
155
156
157
158
159
160
161
162
163
164
165
166
167
168
169
170
171
172
173
174
175
176
177
178
179
180
181
182
183
184
185
186
187
188

The Earth's carbon cycle, fundamentally driven at source by volcanic activity, and at sink by the chemical weathering of carbonate-based rocks, is substantially mediated by the existence of life on this planet, in that uptake of carbon dioxide (CO₂) by photosynthetic organisms leads to substantial solid-state storage of CO₂ on the land or sea surface as biomass, causing a buffering or lag-time for the cycling of this element between lithosphere and atmosphere. The terrestrial storage rate of carbon depends on both its uptake rate by photosynthetic organisms, a function of the hospitability of living conditions on the Earth's surface, which is related to temperature and precipitation, and its turnover or release rate by plant and microbial/animal respiration –also a function of climatic conditions. In turn, by altering the concentration of atmospheric CO₂ and its subsequent impact on solar radiative forcing, carbon uptake and storage/release by living organisms themselves modulate climate and hence the conditions of their own existence(Kump, L.R., Kasting, J.F., Crane, 2010).

Soil carbon accumulation occurs when vegetation growth and litter production exceed the capacity of fauna and microfauna to consume them, leading to a net increase in organic matter stocks on the land surface. In the tropics, soil carbon accumulation rates tend to be low, reflecting the efficiency of carbon removal from the land surface due to the relative lack of temperature and moisture limitation on decomposition and mobilisation of photosynthetically-fixed carbon (e.g. ref. (Stuart Chapin et al., 2012)). In the high latitudes, sub-zero mean annual air temperatures can lead to a situation in which organic matter in the subsoil can remain permanently frozen throughout the year, despite seasonal aboveground temperatures far exceeding freezing point. When combined with substantial net primary production and plant litter inputs in boreal forests, sub-zero belowground temperatures result in low rates of soil carbon decomposition and turnover. Additionally, the activity of soil-burrowing organisms and the vertical churning of soil due to repeated freeze-thaw cycles, results in the downward-migration of soil surface matter to depth, where it can remain thermally shielded from decomposition for millennia.

As a result, over multi-millennial timescales this incremental soil accumulation results in the formation of massive organic carbon stocks, collectively known as 'permafrost soil carbon', which can be subdivided into more recent stocks of <10Ky, older >10Ky soils, and 'yedoma' soils, which consist of organic matter 'fixed' during the Pleistocene era (10My-10Ky) that are characterised by both high soil carbon concentrations and volumetric ice content. The soil column produced by this accumulation can reach depths of well over 30m, and are thought to contain 1330–1580 Petagrams (PgC, =10¹⁵grams or 'billion tonnes') of soil organic carbon (SOC) (Hugelius et al., 2013, 2014; Tarnocai et al., 2009), or the equivalent of ~25 cumulative yrs. of global terrestrial net plant growth or net primary production (NPP) at present day rates (~59PgC yr⁻¹)(Regnier et al., 2013).

As planetary warming proceeds with increases in atmospheric CO₂ and other greenhouse gas concentrations in the modern era, temperatures in the Arctic increase disproportionately relative to the global average –a process known as 'Arctic amplification'(Serreze and Barry, 2011). As a result, thermal shielding of permafrost-

189 region soil has recently diminished, and is expected to do so substantially in the coming
190 centuries. This will both slow the rate of (modern) humic SOC accumulation, and
191 increase the rate at which (older/ancient) stabilised soil carbon is mobilised from its
192 dormant, frozen state (Schädel et al., 2014; Schuur et al., 2009, 2015; Zimov et al., 2006).
193 This extent of this 'awakening' is the subject of a timely focussing of recent scientific
194 research, given the potential perturbations that such a large thermally-vulnerable SOC
195 stock can have on the global carbon cycle.

196

197 At the same time, there has been increasing recognition of the role of terrestrial
198 freshwaters in modulating the contemporary carbon cycle. In this regard, the linkage of
199 atmosphere and land with the ocean, with lakes rivers as the spatial conduit between
200 them, has long been understood on geological timescales, and refers to the inorganic
201 atmospheric carbon removal associated with chemical weathering of silicate and
202 carbonate rocks by rainwater. However, the role of inland waters in the contemporary,
203 short-term carbon cycle has only recently been appreciated (Aufdenkampe et al., 2011),
204 and refers to its mediation of the organic carbon component associated with plant
205 matter. Whereas the freshwater transfer of inorganic carbon is relatively 'passive',
206 organic carbon can be rapidly transformed to CO₂ in its transit over the land
207 surface (Raymond et al., 2013; Venkiteswaran et al., 2014), and the freshwater conduit is
208 in this case relatively 'reactive', and has for this reason been dubbed 'the Active
209 Pipe' (Cole et al., 2007).

210

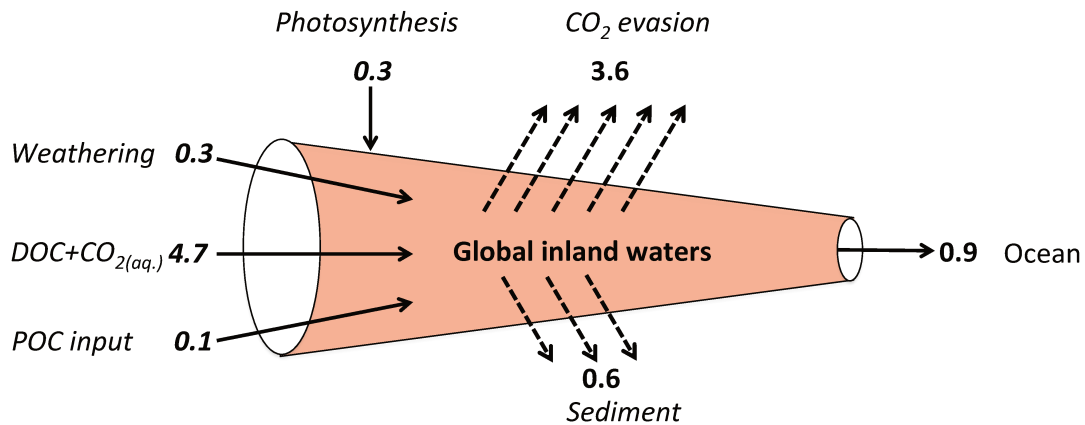
211 Thus lateral flows of carbon have 2 major pathways: organic and inorganic, largely
212 reflecting biogenic and lithogenic processes respectively. However, both pathways feed
213 off the same source: atmospheric CO₂. The organic pathway is comprised of dissolved
214 (DOC) and particulate carbon (POC), where the former is derived from the uptake of
215 hydrolysed plant matter to water fluxes in a process known as 'leaching', and the latter
216 either an erosive flux involving the direct removal of plant and soil matter from the land
217 surface, or derived from the in-stream fixation of atmospheric CO₂ by freshwater algae.
218 In addition to weathered material, the inorganic, or dissolved inorganic carbon (DIC)
219 flux includes dissolved carbon dioxide fluxes (CO_{2(aq.)}) and ions, both originating from
220 microbial consumption of photosynthetically-fixed carbon. CO_{2(aq.)} can be exported with
221 water fluxes either directly from the soil, or produced in situ, as matter that entered the
222 water column along the organic carbon pathway is respired by river-borne heterotrophs
223 and retained in a dissolved state. Depending (positively) on temperatures, water-
224 atmosphere CO₂ disequilibrium and water turbulence, CO_{2(aq.)} can either be exported to
225 the ocean or outgassed to the atmosphere. Outgassing, in turn, can take either the form
226 of CO₂ or methane (CH₄), depending on prevalence of available oxygen for the
227 decomposition of matter. Thus terrestrial carbon mobilised to inland waters are
228 largely restricted to one of three fates: export to the ocean, outgassing to the
229 atmosphere or settling and sedimentary storage prior to arrival at the coast.

230

231 While the first global quantification of the total lateral export of carbon from the land
232 surface was produced in 1981 (Schlesinger and Melack, 1981) and estimated at 0.37 PgC
233 yr⁻¹, surging research in this area has produced almost back-to-back increases in this
234 value (Bastviken et al., 2011; Battin et al., 2009; Borges et al., 2015; Cole et al., 2007;
235 Holgerson and Raymond, 2016; Regnier et al., 2013; Sawakuchi et al., 2017; Tranvik et
236 al., 2009). Today, against a backdrop 7.3 PgC yr⁻¹ of net ecosystem production

237 (NEP=Gross primary production -total ecosystem respiration) the total carbon
 238 throughput of global inland waters is now estimated at 5.4 PgC yr⁻¹ (including
 239 weathering (0.3PgC), POC input (0.1 PgC) and in-stream photosynthesis (0.3 PgC)), of
 240 which 3.9 PgC is outgassed, 0.6 PgC is stored in sediments, and 0.9 PgC reaches the
 241 ocean(Drake et al., 2017) (Fig. 1). Thus, lateral export constitutes the dominant fate of
 242 photosynthetically-fixed terrestrial carbon after autotrophic and soil heterotrophic
 243 respiration are accounted for.
 244

Global Land Ocean Aquatic Continuum Budget

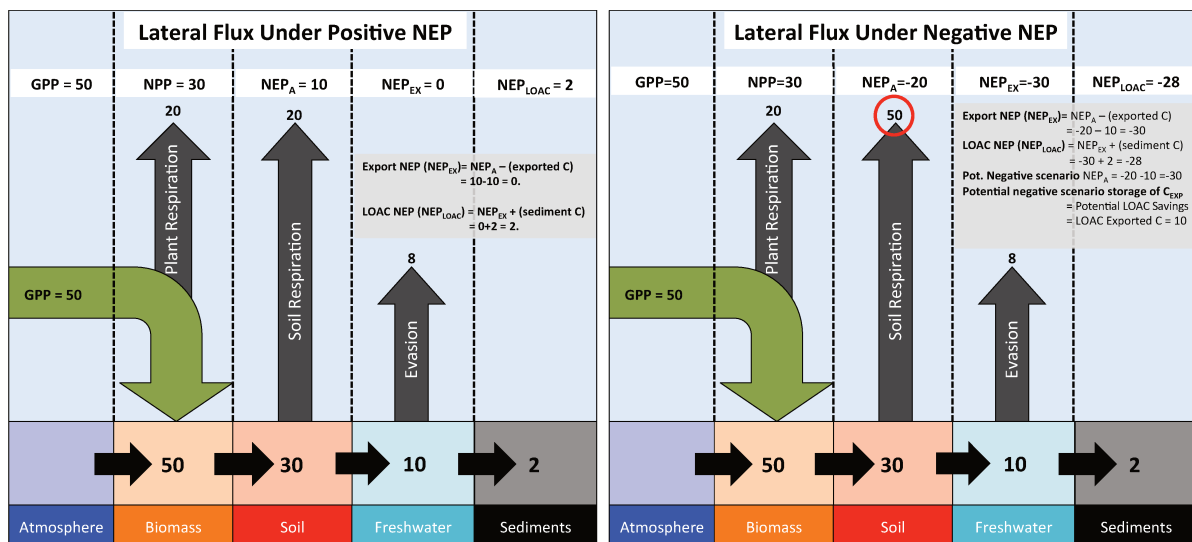


245 **Figure 1:** ‘Pipe’ schematic illustrating the global LOAC budget in a format first employed by Cole et al.
 246 (2007) and adapted to include different sources and sinks of carbon as well as updated values for these
 247 fluxes (PgC yr⁻¹) per the review paper by Drake et al. (2017). Photosynthesis refers to in-stream
 248 (‘autochthonous’) carbon uptake by river-borne algae.
 249

250
 251
 252 In the Arctic, a warming environment is expected to increase flows across the LOAC,
 253 owing to biotic and physical responses to increases in temperature and atmospheric
 254 CO₂ concentrations, respectively(Drake et al., 2018; Tank et al., 2012a, 2016). Changes
 255 in the flux of organic and inorganic carbon from terrestrial sources to the ocean may
 256 likewise have potentially pronounced effects on Arctic marine biogeochemistry, with
 257 attendant impacts on regional and global carbon budgets (Feely et al., 2004; Semiletov et
 258 al., 2016, 2007; Shakhova et al., 2015; Tesi et al., 2014). These arteries of Arctic riverine
 259 carbon are dominated by the six largest river basins north of 45°N: the Ob, Yenisey,
 260 Lena, Kolyma, Yukon and Mackenzie, together accounting for ~65% of aggregate water
 261 discharge, and drain 67% of the region by area(McClelland et al., 2012). These are
 262 followed by eight smaller watersheds, which export a further 15% of aggregate
 263 discharge. At present, the total outflow of terrestrially-derived carbon to the Arctic
 264 Ocean shelf is thought to total 45-54 teragrams of carbon (TgC, =10¹²g) yr⁻¹. Rivers
 265 supply it with an estimated 34 TgC dissolved organic carbon (DOC) per year(Holmes et
 266 al., 2012), and deposit 5.8 TgC yr⁻¹ particulate organic carbon (POC) on the seabed, these
 267 being sourced from those rivers draining low and high elevation headwaters,
 268 respectively(McClelland et al., 2016).
 269

270 The importance of permafrost thaw in the context of lateral carbon fluxes is traced by
 271 the following considerations for the high latitude land surface. 1) Do increases in carbon

272 uptake from primary production due to warming in permafrost areas outweigh
 273 increases in carbon loss due to destabilization of permafrost soil stocks, or vice versa?
 274 (In other words is net ecosystem production positive or negative?) 2) Will lateral carbon
 275 fluxes increase with increases in temperature and precipitation? The combined answer
 276 to these questions will drive the rate of change of the carbon system in permafrost
 277 regions. For example, if NEP is positive, then lateral transfer of organic carbon
 278 represents a potential atmospheric loss, via evasion, of carbon that may be otherwise
 279 not metabolized on the land surface itself. In the existing global positive-NEP case, this
 280 means that organic carbon that might otherwise have been become part of the soil
 281 carbon stock or be respired in the soil is instead exported, a large portion of which is
 282 subsequently 'lost' to the atmosphere (Fig. 1). In the hypothetical case that permafrost
 283 region NEP is negative in the future, an increase in DOC flux might actually reduce the
 284 total stock of carbon available that would otherwise be respired in the soil. In this
 285 scenario, an increase of lateral organic carbon fluxes would constitute a 'second chance'
 286 for that exported carbon to avoid transformation to gaseous form (if it is not evaded en-
 287 route). $\text{CO}_{2(\text{aq})}$ can return to solid-state carbon after export to the river by in-stream
 288 algal photosynthetic fixation, while enhanced alkalinity fluxes imply strengthened
 289 atmospheric CO_2 uptake by weathering reactions. Thus in this scenario, a strengthened
 290 lateral flux system in a weakened or negative NEP system could be a stabilizing force for
 291 carbon stocks (Fig. 2).



292
 293 **Figure 2:** Figure illustrating fluxes between ecosystem scale carbon storage components for **(left)**
 294 positive and **(right)** negative NEP cases, to demonstrate how 2 systems with the same fluxes between
 295 storage components (lower segment in the images) can be considered to have differing interpretations of
 296 the LOAC lateral flux, depending on whether the system is net heterotrophic (negative NEP) or
 297 autotrophic (positive NEP). For simplicity, the diagram assumes no in-stream primary production or
 298 biomass accumulation in plants themselves (all NPP goes to soil and litter). NEP_A refers to NEP before
 299 carbon export to the inland water network, NEP_{EX} refers to NEP after terrestrial export has occurred,
 300 while NEP_{LOAC} refers to NEP after accounting for sedimentary storage (or photosynthetic uptake). See
 301 inset box for explanation. On the right hand side, the notion of 'potential LOAC savings' is explored in the
 302 case of negative NEP, in which we assume that, because of the optimized conditions for heterotrophic
 303 respiration potentially all the river export flux could be respired in the soil if it was not exported, and
 304 second, that all the exported C can hypothetically be re-stored on the land through sedimentation. In this
 305 situation, we can say that LOAC export potentially stabilizes C that would otherwise be respired.

306
 307 **Permafrost in depth**

308

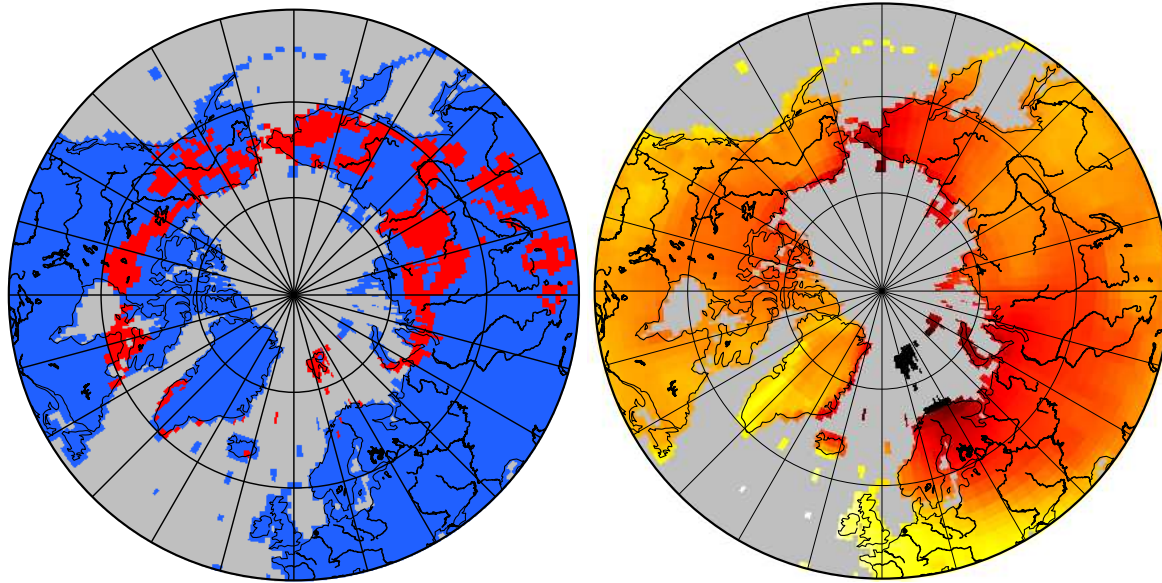
309 Characteristic Arctic river processes are largely driven by two latitude-specific controls.
310 First, many key phenomena are determined by phase changes of water, be they in the
311 atmosphere, on the soil surface, in the soil, or in the river network itself. Second, the
312 presence of permafrost –its cap on vertical water flow-paths in the soil, and thermally-
313 determined accommodation/release of the ~1300PgC of SOC underlying it –act as a
314 fulcrum for landscape-scale biogeochemical dynamics. The combination of these
315 permafrost-region characteristics gives rise to the following dynamics. Rapid melting of
316 snow and soil or river ice in Arctic spring (May-June) following ~6 months of continuous
317 accumulation drives massive water runoff rates almost entirely restricted to overland
318 flow by the permafrost barrier. This causes intensely seasonal river discharge, with
319 annual peaks often two orders of magnitude above baseflow rates(Ye et al., 2003).
320 Vigorous water flux rates mean that particulate carbon and nutrients are rapidly eroded
321 from elevated headwater catchments, as observed in the N. American Arctic with high
322 POC:DOC ratios(McClelland et al., 2016). In lower-lying areas, litter and moss material
323 at the soil surface are intensely leached, with mobilization and transformation of this
324 subsequently dissolved matter via inland waters. DOC concentrations tend to be similar
325 to those in the tropics(Holmes et al., 2012; McClelland et al., 2012) particularly in the
326 flatter Eurasian rivers (lower POC:DOC ratio). In some areas, high DOC concentrations
327 are the result of snowmelt-induced soil water saturation, which favours the
328 establishment of moss and sedge-based peat ecosystems characterized by
329 correspondingly high SOC concentrations that are mobilized upon thaw.

330

331 In mid-summer, runoff and river discharge rates decline, while the depth to which the
332 soil is unfrozen (referred to as the ‘active layer’) increases. These are thus periods
333 during which soil respiration rates are highest, and where leached DOC may be of
334 greatest age of origin. Once mobilized to headwaters, it appears that this often-ancient,
335 low molecular weight SOC matter can be preferentially and rapidly metabolized by
336 microbes in headwater streams, to the extent that respiration of ancient plant matter
337 may dominate aggregate summer CO₂ evasion in Arctic rivers(Denfeld et al., 2013; Feng
338 et al., 2013; Vonk et al., 2013; Vonk and Gustafsson, 2013). As Arctic warming proceeds,
339 it has been suggested that volumes of freshwater and total energy flux in runoff and
340 river discharge will increase with rising precipitation and permafrost thaw(Lammers et
341 al., 2007). In addition, guided by rising temperatures, thermal and physical exposure of
342 SOC (see Fig. 3), along with increases in plant growth and litter inputs to the soil, are
343 thought to increase the total pool of carbon available to DOC leaching and
344 transport(Frey and Smith, 2005; Laudon et al., 2012).

21stC Newly Thawed Areas (ALT_{max}< 3m)

Δ 2m Air Temperature (°C)



345
346
347
348
349
350

Figure 3: Simulated increases in (left) areas transitioning from continuous to discontinuous permafrost; (right) mean annual 2m air temperatures; over the 21st Century (2090-2099 against a 1996-2005 baseline), under the ‘intermediate-high warming’ scenario (RCP 6.0), generated by the simulation output from our model. Major rivers are outlined in black.

351 In addition, high latitude weathering processes are subject to substantial modulation by
352 phenomena such as cryoturbation, glacial action and mineral exposure due to cracking
353 under freeze/thaw cycles. Beyond the focus on the organic carbon cycle, this can further
354 affect the carbon balance of these areas in their impacts on chemical weathering, in
355 which rainwater dissolution of atmospheric CO₂ is ‘fixed’ as to bicarbonate (HCO₃⁻)
356 upon weathering of carbonate rocks by its conversion to HCO₃⁻; which reduces its
357 chemical susceptibility to atmospheric release. Likewise, the vertical percolation of
358 water through the soil column allows for the fixation of biogenic CO₂ residing in soil
359 pore space as HCO₃⁻(Beaulieu et al., 2012; Gaillardet et al., 1999; Stets et al., 2017; Tank
360 et al., 2012a, 2016, 2018). The riverine flux of weathering products has been shown to
361 have increased markedly over high latitude regions in the last decades(Drake et al.,
362 2018; Tank et al., 2016), driven by temperature, precipitation, thaw-related increaess in
363 mineral surface area, agricultural liming, mining and acid rain(Kaushal et al., 2018;
364 Maher and Chamberlain, 2014; Raymond and Hamilton, 2018; White and Blum, 1995),
365 and can be expected to increase with time, with the potential to partially offset CO₂
366 emissions from permafrost thaw(Drake et al., 2018).

367
368 Permafrost regions are subject to further processes of potential destabilization:
369

370 Under thaw conditions, microbial activity increases and can generate its own heat,
371 which incubation experiments have shown may be sufficient to significantly warm the
372 soil further(Hollesen et al., 2015). ‘Thermokarst’, or the melting of massive soil ice
373 inclusions can lead to the physical collapse of the soil column and sudden exposure of
374 ancient soil carbon to the surface(Abbott et al., 2015; Kanevskiy et al., 2011; Tanski et

375 al., 2017). An extreme version collapse/erosion process occurs in coastal areas,
376 exacerbated by water and wind activity there(Fritz et al., 2017; Tanski et al., 2017; Vonk
377 et al., 2012). Arctic region fire events are on the rise and likely to increase with
378 temperature and severity over time(Ponomarev et al., 2016). The initial burning of
379 biomass is accompanied by active layer deepening, 'priming' of deeper soil horizons(De
380 Baets et al., 2016), and a significant loading of pyrogenic DOC in Arctic watersheds, up to
381 half of which is rapidly metabolized(Myers-Pigg et al., 2015).

382
383 The riverine flux of weathering products has been shown to have increased markedly
384 over high latitude regions in the last decades(Drake et al., 2018; Tank et al., 2016),
385 driven by temperature, precipitation, thaw-related increaess in mineral surface area,
386 agricultural liming, mining and acid rain(Kaushal et al., 2018; Maher and Chamberlain,
387 2014; Raymond and Hamilton, 2018; White and Blum, 1995), and can be expected to
388 increase with time, with the potential to partially offset CO₂ emissions from permafrost
389 thaw(Drake et al., 2018).

390
391 Cumulatively, the above processes imply that with warming of Arctic watersheds we
392 might expect a potentially sizeable aquatic mobilization and microbial metabolism
393 (Xue et al., 2016) of dissolved and eroded organic matter, deeper hydrological flow
394 paths, increased thermokarst formation, an increase in total mass, heat and alkalinity
395 transfer to the river network and, ultimately, the Arctic Ocean and atmosphere. As a
396 result of this transfer, both terrestrially-exported and older shelf carbon in the Arctic
397 Ocean face considerable disruption(McGuire et al., 2009; Schuur et al., 2015) from the
398 combined effects of increased freshwater, heat, sediment, nutrient and
399 organic/inorganic carbon flows from rapidly warming Arctic river watersheds, as well
400 as those from melting sea ice, warmer marine water temperatures and geothermal heat
401 sources(Janout et al., 2016; Shakhova et al., 2015).

402
403 On the other hand, suggestions of an inevitable increase in Arctic terrestrial DOC
404 throughput may ignore the potential co-variation of increasing water inputs with a
405 deeper active layer, which would promote deeper water flowpaths and a
406 correspondingly different leaching substrate regime (SOC) from that which normally
407 prevails in permafrost systems. This could entail lower leaching rates or concentrations,
408 diminishing the lateral transport of dissolved carbon. Likewise, it assumes that warming
409 won't increase carbon respiration in greater proportion than DOC mobilization (also
410 reducing DOC lateral fluxes), which has yet to be established.

411
412 Indeed, theoretical understanding of permafrost region terrestrial systems has been
413 hampered by a dearth of empirical data over permafrost-representative spatio-temporal
414 scales. This is particularly true when attempting to resolve lateral carbon dynamics in
415 these systems, due to the practical difficulties in taking both spot and continuous
416 measurement in some of the coldest, most dynamic and extreme river discharge regimes
417 in the world. It is into this context of great uncertainty over a spectrum of hypothetical
418 outcomes that this thesis assumes its relevance. The spatial, temporal and process
419 scales that projecting the warming-response of the permafrost region and its lateral
420 carbon transfer involves are not at present amenable to resolution by anything other
421 than process based modeling approaches that can incorporate these processes, scales
422 and dimensions to the extent that they are currently perceived to be well-understood.

423
424
425
426
427
428
429
430
431
432
433
434
435
436
437
438
439
440
441
442
443
444
445
446
447
448
449
450
451
452
453
454
455
456
457
458
459
460
461
462
463
464
465
466
467
468
469
470

In what follows, we first trace the development of a spatially-explicit, high temporal resolution model that to our knowledge, is unique in its combination of state-of-the-art theory and representation of both permafrost and lateral flux systems in a global land surface model equipped for coupling with a earth system model. The resulting simulation product, given the name ORCHIDEE MICT-LEAK, simulates the production, transport and transformation of soil and litter carbon to DOC and CO₂ in permafrost regions, and is described in detail in **Chapter 1**. This model is subjected to an in-depth evaluation over a wide range of biogeochemical processes and data for its ability to accurately simulate the processes represented over a single, relatively well-studied basin –the Lena –in **Chapter 2**. Chapters 1 and 2 have been written and submitted to the journal Geoscientific Model Development (in review). Having concluded that the model is able to reasonably represent the relevant dynamics for permafrost systems, **Chapter 3** employs state-of-the-art climate projections to 2100 under a given climate warming scenario (RCP 6.0) to examine the lateral-transfer response of the Pan-Arctic to future warming, and finds that contrary to most literature-based expectations, lateral carbon fluxes decline over the 21st Century. The causes of this are explored and explained therein. This manuscript is being prepared for submission to Nature. In **Chapter 4**, we describe and evaluate a simple model developed as an additional module for ORCHIDEE-MICT LEAK, which is able to simulate at a daily timestep chemical weathering/alkalinity production rates and their fluvial transport to the ocean. To our knowledge this is the first such module in a global climate model resolved for both high spatial (integrating both surface and subsurface flows) and temporal (daily/monthly versus yearly) resolution. We then project the response of Pan-Arctic weathering and riverine alkalinity fluxes to climate warming, assessing the implied change in atmospheric carbon uptake that results. This paper is being prepared for submission to the journal Environmental Science and Technology.

471
472 **Chapter 2**

473 **ORCHIDEE MICT LEAK, a global model for the production, transport**
474 **and transformation of dissolved organic carbon from Arctic permafrost**
475 **regions : model description and simulation protocol¹**
476
477
478

479 **Summary**
480

481 High latitude permafrost soils contain very large stores of frozen, often ancient and
482 relatively labile carbon up to depths of over 30m. Surface warming caused by
483 contemporary anthropogenic climate change can be reasonably expected to destabilize
484 these stores via microbial or hydrological mobilization following spring/summer thaw,
485 as the permafrost line migrates pole-ward over time. However, few Earth System
486 models adequately represent the unique permafrost soil biogeochemistry and its
487 respective processes; this significantly contributes to uncertainty in estimating their
488 responses, and that of the planet at large, to warming. The potential feedbacks owing to
489 such a response are of particular acuity and concern. Likewise, the riverine component
490 of what is known as the ‘boundless carbon cycle’ is seldom recognized in Earth System
491 modeling. Hydrological mobilization of organic material from the Arctic land surface to
492 the river network results either in sedimentary settling or atmospheric ‘evasion’ within
493 rivers or their geographic end-points, the marine realm. These processes are widely
494 expected to increase in strength and with amplified Arctic climate warming. Thus,
495 representing this spectrum of phenomena, their interaction, and the response of these to
496 changes in environmental drivers (heat, water, their timing, and atmospheric CO₂) are
497 necessary components for the projection of the Arctic’s future carbon cycle changes.
498

499 Here, the production, transport and atmospheric release of dissolved organic carbon
500 (DOC) from high-latitude permafrost soils into inland waters and the ocean is explicitly
501 represented for the first time in the land surface component (ORCHIDEE) of a CMIP6
502 global climate model (IPSL). The model, ORCHIDEE MICT-LEAK, mechanistically
503 represents: (1) Vegetation and soil physical processes for high latitude snow, ice and soil
504 phenomena, including snow thermal buffering of the soil surface, mediation of soil
505 temperature by organic carbon concentration, bio- and cryo-turbation of particulate
506 and dissolved soil carbon to depth via vertical diffusion over a discretely subdivided soil
507 column and the interaction of these processes with a large-scale soil-carbon stock,
508 representing permafrost soil carbon. (2) The cycling of DOC and CO₂, including
509 atmospheric evasion, along the terrestrial-aquatic continuum from soils through the
510 river network to the coast, at 0.5° to 2° resolution. This dissolved carbon cycling
511 includes the processes of floodplain inundation and flooded mobilisation of dissolved
512 litter and soil organic matter to the river network, soil-type modulation of soil column
513 DOC filtration and decomposition, ‘priming’ of organic matter decomposition by more
514 reactive carbon, and atmospheric and canopy DOC inputs to the soil. By including these
515 mechanisms in a process-based manner, we hope to capture some of the more

¹ Submitted to *Geoscientific Model Development*, in review.

516 important landscape-scale emergent phenomena that arise from the interaction of
517 permafrost environments with organic matter and the hydrological realm. This paper,
518 the first in a two-part study, presents the rationale for including these processes in a
519 high latitude specific land surface model, then describes the model with a focus on novel
520 process implementations, followed by a summary of the model configuration and
521 simulation protocol.

522

523 The results of the model evaluation simulations, conducted for the Lena River basin, are
524 evaluated against observational data in Chapter 2 of this thesis.

525

526

527

528

529

530

531

532

533

534

535

536

537

538

539

540

541

542

543

544

545

546

547

548

549

550

551

552

553

554

555

556

557

558

559

560

561

562

Chapitre 2

ORCHIDEE MICT LEAK, un modèle global pour la production, le transport et la transformation du carbone organique dissous des régions de pergélisol de l'Arctique: description du modèle et protocole de simulation

Résumé

Les pergélisols à haute latitude contiennent de très vastes réserves de carbone gelé, souvent ancien et relativement labile, jusqu'à une profondeur de plus de 30 m. On peut raisonnablement s'attendre à ce que le réchauffement de la surface provoqué par les changements climatiques anthropiques contemporains déstabilise ces réserves via une mobilisation microbienne ou hydrologique après le dégel du printemps / été, à mesure que la ligne de pergélisol migre vers le nord. Cependant, peu de modèles du système Terre représentent de manière adéquate la biogéochimie unique des pergélisol et ses processus respectifs; cela contribue de manière significative à l'incertitude dans l'estimation de leurs réponses, et de celle de la planète dans son ensemble, au réchauffement. Les réactions potentielles résultant d'une telle réponse sont d'une acuité et d'une préoccupation particulières. De même, la composante fluviale de ce que l'on appelle le «cycle du carbone sans bornes» est rarement reconnue dans la modélisation du système Terre. La mobilisation hydrologique de matières organiques de la surface des terres arctiques vers le réseau fluvial entraîne soit un tassement sédimentaire, soit une «évasion» atmosphérique dans les cours d'eau, ou leur limite géographique, le domaine marin. On s'attend généralement à ce que ces processus deviennent plus puissants et entraînent un réchauffement accru du climat arctique. Ainsi, représenter ce spectre de phénomènes, leurs interactions et leur réponse aux changements de facteurs environnementaux (chaleur, eau, leur synchronisation et le CO₂ atmosphérique) sont des éléments nécessaires à la projection des futurs changements du cycle du carbone dans l'Arctique.

Ici, la production, le transport et les rejets atmosphériques de carbone organique dissous (COD) provenant des sols de pergélisol à haute latitude dans les eaux intérieures et l'océan sont explicitement représentés pour la première fois dans la composante de surface terrestre (ORCHIDEE) d'un modèle climatique mondial CMIP6 (IPSL). Le modèle, ORCHIDEE MICT-LEAK, représente mécaniquement: (1) Les processus physiques de la végétation et du sol pour les phénomènes de neige, de glace et de sol sous les hautes latitudes, y compris la compensation thermique de la neige par la surface, la médiation de la température du sol par la concentration de carbone organique, la bio et la cryo-turbation du carbone du sol dissous et dissous jusqu'à sa profondeur par diffusion verticale sur une colonne de sol discrètement divisée et interaction de ces processus avec un stock de carbone sol à grande échelle, représentant le carbone du sol pergélisol. (2) Le cycle du COD et du CO₂, y compris l'évasion atmosphérique, le long du continuum aquatique terrestre des sols à travers le réseau fluvial jusqu'à la côte, à une résolution de 0,5 ° à 2 °. Ce cycle du carbone dissous comprend les processus d'inondation des plaines inondables et de mobilisation COD du sol et de la litère vers le réseau hydrographique, la modulation du type de sol de la filtration et de la décomposition de la colonne de sol DOC, la "préparation" de la décomposition de la matière

610 organique par du carbone plus réactif, et COD atmosphériques et de la canopée entrant dans le
611 sol. En incluant ces mécanismes d'une manière basée sur les processus, nous espérons
612 capturer certains des phénomènes d'émergence les plus importants à l'échelle du paysage qui
613 résultent de l'interaction des environnements de pergélisol avec la matière organique et le
614 domaine hydrologique. Cet article, le premier d'une étude en deux parties, présente les raisons
615 d'inclure ces processus dans un modèle de surface terrestre spécifique de latitude élevée, puis
616 décrit le modèle en mettant l'accent sur les nouvelles implémentations de processus, suivi d'un
617 résumé de la configuration du modèle et de la simulation. protocole.

618

619 Les résultats des simulations, effectuées pour le bassin de la rivière Lena, sont évalués par
620 rapport aux données d'observation présentées au chapitre 2 de cette thèse.

621

622

623

624

625

626

627

628

629

630

631

632

633

634

635

636

637

638

639

640

641

642

643

644

645

646

647

648

649

650

651

652

653

654

655

656

657

658 **Introduction**

659
660 High-latitude permafrost soils contain large stores of frozen, often ancient and relatively
661 reactive carbon up to depths of over 30m. Soil warming caused by contemporary
662 anthropogenic climate change can be expected to destabilize these stores (Schuur et al.,
663 2015) via microbial or hydrological mobilization following spring/summer thaw and
664 riverine discharge (Vonk et al., 2015a) as the permafrost line migrates poleward over
665 time. The high latitude soil carbon reservoir may amount to ~1330–1580 PgC (Hugelius
666 et al., 2013, 2014; Tarnocai et al., 2009) –over double that stored in the contemporary
667 atmosphere, while the yearly lateral flux of carbon from soils to running waters may
668 amount to ~40% of net ecosystem carbon exchange (McGuire et al., 2009), the majority
669 as dissolved organic carbon (DOC).

670
671 The fact that, to our knowledge, no existing land surface models are able to adequately
672 simultaneously represent this unique high latitude permafrost soil environment, the
673 transformation of soil organic carbon (SOC) to its eroded particulate and DOC forms and
674 their subsequent lateral transport, as well as the response of all these to warming,
675 entails significant additional uncertainty in projecting global-scale biogeochemical
676 responses to human-induced environmental change.

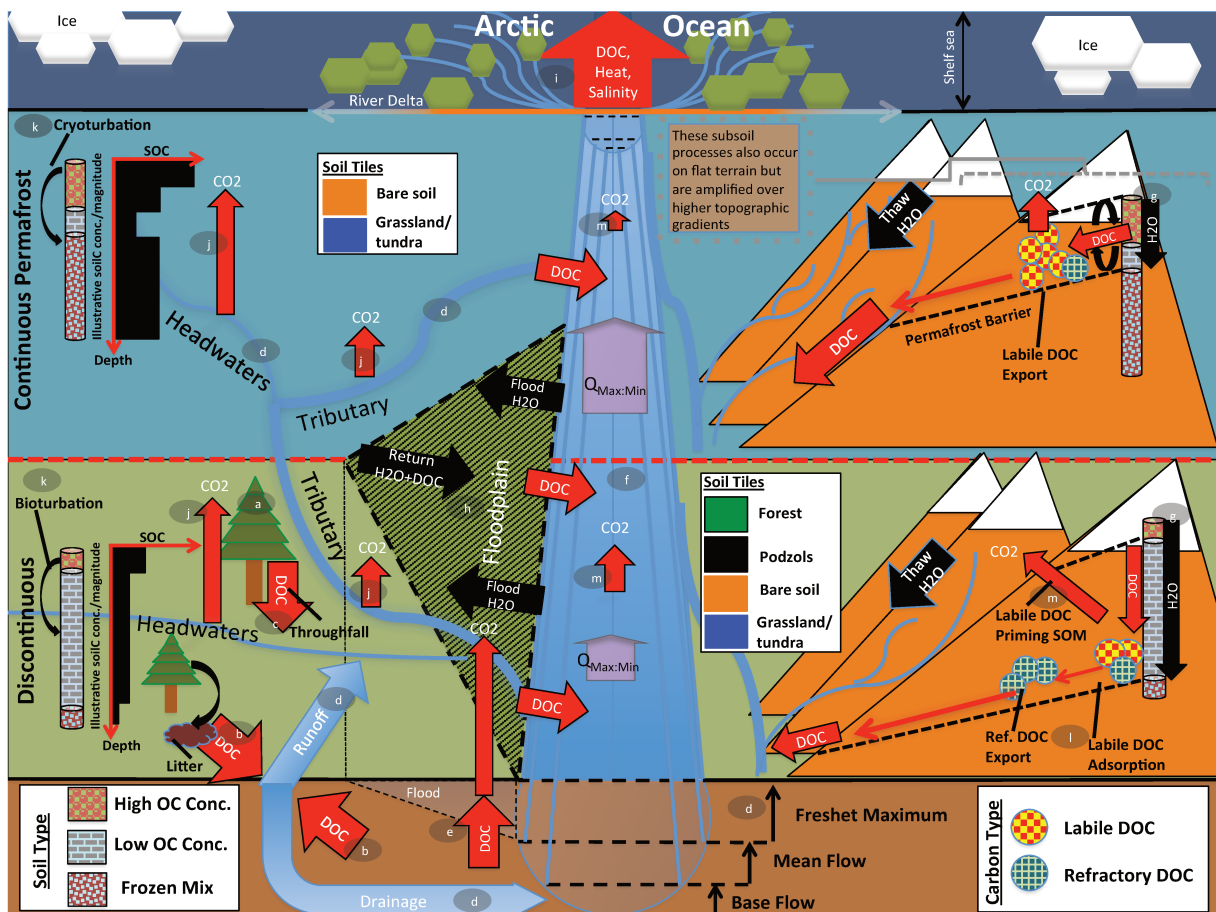
677
678 Fundamental to these efforts is the ability to predict the medium under which carbon
679 transformation will occur: in the soil, streams, rivers or sea, and under what
680 metabolising conditions –since these will determine the process mix that will ultimately
681 enable either terrestrial redeposition and retention, ocean transfer, or atmospheric
682 release of permafrost-derived organic carbon. In the permafrost context, this implies
683 being able to accurately represent (i) the source, reactivity and transformation of
684 released organic matter, and; (ii) the dynamic response of hydrological processes to
685 warming, since water phase determines carbon, heat, and soil moisture availability for
686 metabolism and lateral transport.

687
688 To this end, we take a specific version of the terrestrial component of the IPSL global
689 Earth System model (ESM) ORCHIDEE (Organising Carbon and Hydrology In Dynamic
690 Ecosystems), one that is specifically coded for, calibrated with and evaluated on high
691 latitude phenomena and permafrost processes, called ORCHIDEE-MICT (Guimberteau et
692 al., 2018). This code is then adapted to include DOC production in the soil (ORCHIDEE-
693 SOM, (Camino-Serrano et al., 2018)), ‘priming’ of SOC (ORCHIDEE-PRIM,(Guenet et al.,
694 2016, 2018)) and the riverine transport of DOC and CO₂, including in-stream
695 transformations, carbon and water exchanges with wetland soils and gaseous exchange
696 between river surfaces and the atmosphere (ORCHILEAK, (Lauerwald et al., 2017)).

697
698 The resulting model, dubbed ORCHIDEE MICT-LEAK, hereafter referred to as MICT-L for
699 brevity, is therefore able to represent: (a) Permafrost soil and snow physics,
700 thermodynamics to a depth of 38m and dynamic soil hydrology to a depth of 2m; (b)
701 Improved representation of biotic stress response to cold, heat and moisture in high
702 latitudes; (c) Explicit representation of the active layer and frozen-soil hydrologic
703 barriers; buildup of soil carbon stocks via primary production and vertical translocation
704 (turbation) of SOC and DOC; (d) DOC leaching from tree canopies, atmospheric
705 deposition, litter and soil organic matter, its adsorption/desorption to/from soil

706 particles, its transport and transformation to dissolved CO₂ (CO₂^(aq.)) and atmospheric
 707 release, as well as the production and hydrological transport of plant root-zone derived
 708 dissolved CO₂; (e) Improved representation of C cycling on floodplains; (f) Priming of
 709 organic matter in the soil column and subsequent decomposition dynamics. In
 710 combination, these model properties allow us to explore the possibility of reproducing
 711 important emergent phenomena observed in recent empirical studies (Fig. 1) arising
 712 from the interaction of a broad combination of different processes and factors.

714 To our knowledge very few attempts have been made at the global scale of modelling
 715 DOC production and lateral transfer from the permafrost region that explicitly accounts
 716 for such a broad range of high latitude-specific processes, which in turn allows us to
 717 match and evaluate simulation outputs with specific observed processes, enhancing our
 718 ability to interpret the output from these models and improve our understanding of the
 719 processes represented. The only other attempt at doing so is a Pan-Arctic modelling
 720 study by Kicklighter et al. (2013)(Kicklighter et al., 2013), which is based on a relatively
 721 simplified scheme for soil, water and biology. The following segment briefly overviews
 722 the dynamics, emergent properties and their overall significance across scales, of
 723 permafrost region river basins.
 724



725
 726
 727 **Figure 1:** Cartoon diagram illustrating the landscape-scale emergent phenomena observed in high-latitude river systems that are captured by the processes represented in this model. Here, the terrestrial area is shown, in vertically-ascending order, as subsoil, discontinuous permafrost, continuous permafrost and the maritime boundary. Representative soil types, their distributions and carbon concentrations are shown for the two permafrost zones, as well as the different dynamics occurring on 'flat' (left) and 'sloping'

732 land (right) arising from their permafrost designation. Carbon exports from one subsystem to another are
733 shown in red. The relative strength of the same processes occurring in each permafrost band are indicated
734 by relative arrow size. Note that the high CO₂ evasion in headwaters versus tributaries versus mainstem
735 is shown here. Proposed and modelled mechanisms of soil carbon priming, adsorption and rapid
736 metabolisation are shown. The arrows $Q_{\text{Max:Min}}$ refer to the ratio of maximum to minimum discharge at a
737 given point in the river, the ratio indicating hydrologic volatility, whose magnitude is influenced by
738 permafrost coverage. Soil tiles, a model construct used for modulating soil permeability and
739 implicit/explicit decomposition, are shown to indicate the potential differences in these dynamics for the
740 relevant permafrost zones. Note that the marine shelf sea system, as shown in the uppermost rectangle, is
741 not simulated in this model, although our outputs can be coupled for that purpose. Letter markings mark
742 processes of carbon flux in permafrost regions and implicitly or explicitly included in the model, and can
743 be referred to in subsections of the Methods text. These refer to: (a) Biomass generation; (b) DOC
744 generation and leaching; (c) Throughfall and its DOC; (d) Hydrological mobilisation of soil DOC; (e) Soil
745 flooding; (f) Landscape routing of water and carbon; (g) Infiltration and topography; (h) Floodplain
746 representation; (i) Oceanic outflow; (j) Dissolved carbon export and riverine atmospheric evasion; (k)
747 Turbation; (l) Adsorption; (m) Priming.

748
749

750 **1.1 A giant, reactive, fast-draining funnel: A permafrost basin overview**

751

752 Permafrost has a profound impact on Arctic river hydrology. In permafrost regions, a
753 permanently frozen soil layer acts as a ‘cap’ on ground water flow (see ‘permafrost
754 barrier’, right hand side of Fig. 1). This implies that: (i) Near-surface runoff becomes by
755 far the dominant flowpath draining permafrost watersheds (Ye et al., 2009), as shown
756 in Fig. 1d; (ii) The seasonal amplitude of river discharge, expressed by the ratio of
757 maximum to minimum discharge ($Q_{\text{max:min}}$ in Fig. 1), over continuous versus
758 discontinuous permafrost catchments is higher as a result of the permafrost barrier;
759 (iii) This concentration of water volume near the surface causes intense leaching of DOC
760 from litter and relevant unfrozen soil layers (Fig. 1g, 1d, and e.g. refs. (Drake et al., 2015;
761 Spencer et al., 2015; Vonk et al., 2013)); (iv) Permafrost SOC stocks beneath the active
762 layer are physically and thermally shielded from aquatic mobilization and
763 metabolization, respectively (Fig. 1g).

764

765 Rapid melting of snow and soil or river ice during spring freshet (May-June) drives
766 intensely seasonal discharge, with peaks often two orders of magnitude (Van Vliet et al.,
767 2012, 2013) above baseflow rates (Fig. 1d). These events are the cause of four, largely
768 synchronous processes: (i) Biogenic matter is rapidly transported from elevated
769 headwater catchments (Fig. 1, right hand side) (McClelland et al., 2016); (ii) Plant
770 material at the soil surface is intensely leached, with subsequent mobilization and
771 transformation of this dissolved matter via inland waters (Fig. 1d,b,j); During spring
772 freshet, riverine DOC concentrations increase and bulk annual marine DOC exports are
773 dominated by the terrestrial DOC flux to the rivers that occurs at this time (Holmes et al.,
774 2012). Indeed, DOC concentrations during the thawing season tend to be greater than
775 or equal to those in the Amazon particularly in the flatter Eurasian rivers (Holmes et al.,
776 2012; McClelland et al., 2012), and DOC concentrations are affected at watershed scale
777 by parent material and ground ice content (O’Donnell et al., 2016).

778

779 (iii) Sudden inundation of the floodplain regions in spring and early summer (Fig. 1h),
780 (Smith and Pavelsky, 2008), further spurs lateral flux of both particulate and dissolved
781 matter in the process and its re-deposition (Zubrzycki et al., 2013) or atmospheric

782 evasion (Fig. 1j,m); (iv) Snowmelt-induced soil water saturation, favoring the growth of
783 moss and sedge-based ecosystems (e.g. refs.(Selvam et al., 2017; Tarnocai et al., 2009;
784 Yu, 2011)) and the retention of their organic matter (OM),.i.e., peat formation, not
785 shown in Fig. 1 as this isn't represented in this model version, but is generated in a
786 separate branch of ORCHIDEE (Qiu et al., 2018)).

787

788 Mid-summer river low-flow and a deeper active layer allow for the hydrological
789 intrusion and leaching of older soil horizons (e.g. the top part of Pleistocene-era Yedoma
790 soils), and their subsequent dissolved transport(Wickland et al., 2018). These
791 sometimes-ancient low molecular weight carbon compounds appear to be preferentially
792 and rapidly metabolized by microbes in headwater streams (Fig. 1j), which may
793 constitute a significant fraction of aggregate summer CO₂ evasion in Arctic
794 rivers(Denfeld et al., 2013; Vonk et al., 2013) This is likely due to the existence of a
795 significant labile component of frozen carbon(Drake et al., 2015; Vonk et al., 2015 ;
796 Woods et al., 2011) .

797

798 CO₂ evasion rates from Arctic inland waters (Fig. 1j,e,m) are estimated to be in the
799 region of 40-84 TgC yr⁻¹ (McGuire et al., 2009), to be compared with estimates of Pan
800 Arctic DOC discharge from rivers of 25-36 TgC yr⁻¹. The influx of terrestrial carbon to
801 the shelf zone is thought to total 45-54 TgC yr⁻¹ (Holmes et al., 2012; Raymond et al.,
802 2007). Rivers supply the Arctic Ocean (AO) an estimated 34 Tg DOC-C yr⁻¹ (Holmes et al.,
803 2012), while depositing 5.8 Tg yr⁻¹ of particulate carbon, these being sourced from those
804 rivers draining low and high elevation headwaters, respectively (McClelland et al.,
805 2016). These dynamics are all subject to considerable amplification by changes in
806 temperature and hydrology(Frey and McClelland, 2009; Tank et al., 2018).

807

808 Average annual discharge in the Eurasian Arctic rivers has increased by at least 7%
809 between 1936-1999 (Peterson et al., 2002), driven by increasing temperatures and
810 runoff (Berezovskaya et al., 2005), and the subsequent interplay of increasing annual
811 precipitation, decreasing snow depth and snow water equivalent (SWE) mass (Kunkel et
812 al., 2016; Mudryk et al., 2015), and greater evapotranspiration (Zhang et al., 2009).
813 Although net discharge trend rates over N. America were negative over the period 1964-
814 2003, since 2003 they have been positive on average (Dery et al., 2016). These dynamic
815 and largely increasing hydrologic flux trends point towards temperature and
816 precipitation -driven changes in the soil column, in which increased soil water/snow
817 thaw and microbial activity (Graham et al., 2012; MacKelprang et al., 2011; Schuur et al.,
818 2009) converge to raise soil leaching and DOC export rates to the river basin and
819 beyond. Further, microbial activity generates its own heat, which incubation
820 experiments have shown may be sufficient to significantly warm the soil further
821 (Hollesen et al., 2015), in a positive feedback.

822

823 Arctic region fire events are also on the rise and likely to increase with temperature and
824 severity over time (Ponomarev et al., 2016). The initial burning of biomass is
825 accompanied by active layer deepening, priming of deeper soil horizons (De Baets et al.,
826 2016), and a significant loading of pyrogenic DOC in Arctic watersheds, up to half of
827 which is rapidly metabolized (Myers-Pigg et al., 2015).

828

829 In these contexts, the implications of (polar-amplified) warmer temperatures leading to
830 active layer deepening towards the future (transition from Continuous to Discontinuous
831 Permafrost, as shown in the upper/lower segments of Fig. 1) are clear and unique:
832 potentially sizeable aquatic mobilization and microbial metabolization (Xue, 2017) of
833 dissolved and eroded OM, deeper hydrological flow paths, an increase in total carbon
834 and water mass and heat transfer to the aquatic network and, ultimately, the Arctic
835 Ocean and atmosphere (Fig. 1i).

836

837 The advantage of having a terrestrial model that can be coupled to a marine component
838 of an overarching global climate model (GCM) is in this case the representation of a
839 consistent transboundary scheme, such that output from one model is integrated as
840 input to another. This is particularly important given the context in which these
841 terrestrial outflows occur :

842

843 Because of its small size, a uniquely large and shallow continental shelf, the global
844 climatological significance of its seasonal sea ice (Rhein et al., 2013) and its rapid decline
845 (Findlay et al., 2015a), the AO has been described as a giant estuary (McClelland et al.,
846 2012), acting as a funnel for the transport, processing and sedimentation of terrestrial
847 OM. Because of its small surface area and shallow seas (Jakobsson, 2002), the AO holds
848 relatively little volume and is consequently sensitive to inputs of freshwater, heat,
849 alkalinity and nutrients that flush out from terrestrial sources, particularly at discharge
850 peak.

851

852 High suspended particle loads in river water as they approach the mouth (Heim et al.,
853 2014) cause lower light availability and water albedo and hence higher temperatures
854 (Bauch et al., 2013; Janout et al., 2016), which can affect the near-shore sea ice extent,
855 particularly in spring (Steele and Ermold, 2015). Volumes of riverine freshwater and
856 total energy flux (Lammers et al., 2007) are expected to increase with warmer
857 temperatures, along with an earlier discharge peak (Van Vliet et al., 2012, 2013). In
858 doing so, freshwaters may in the future trigger earlier onset of ice retreat (Stroeve et al.,
859 2014; Whitefield et al., 2015) via a freshwater albedo, ice melt, seawater albedo, ice
860 melt, feedback, amplified by intermediary state variables such as water vapor and
861 cloudiness (Serreze and Barry, 2011).

862

863 Both terrestrially-exported and older shelf carbon in the AO face considerable
864 disruption (McGuire et al., 2009; Schuur et al., 2015) from the combined effects of
865 increased freshwater, heat, sediment, nutrient and organic carbon flows from rapidly
866 warming Arctic river watersheds, as well as those from melting sea ice, warmer marine
867 water temperatures and geothermal heat sources (Janout et al., 2016; Shakhova et al.,
868 2015). Because ORCHIDEE is a sub-component of the overarching IPSL ESM, there is
869 scope for coupling riverine outputs of water, DOC, CO_{2(aq)} and heat from the terrestrial
870 model as input for the IPSL marine components (Fig. 1i). Nonetheless, these are not the
871 objectives of the present paper, whose aim is rather to validate the simulated variable
872 output produced by the model described in detail below against observations and
873 empirical knowledge for the Lena basin, but are included here descriptively to scope the
874 plausible future applications of ORCHIDEE MICT-LEAK, given our present empirical
875 understanding of their potential significance.

876

877 The Methods section summarises the model structure and associated rationale for each
878 of the model sub-branches or routines relevant to this study, and follows with the setup
879 and rationale for the simulations carried out as validation exercises.

880

881 **2 Methods**

882

883 This section overviews the processes represented in the model being described in this
884 manuscript, which is referred to as ORCHIDEE MICT-LEAK, hereafter referred to MICT-L
885 for brevity. MICT-L is at its heart a merge of two distinct models : the high-latitude land
886 surface component of the IPSL Earth System Model ORCHIDEE MICT, and the DOC-
887 production and transport branch of ORCHIDEE's default or 'trunk' version (Krinner et
888 al., 2005), ORCHILEAK. The original merger of these two code sets was between
889 ORCHILEAK and ORCHIDEE-MICT, which are described in ref.(Camino-Serrano et al.,
890 2018; Lauerwald et al., 2017) and ref(Guimberteau et al., 2018) respectively.

891

892 However, numerous bug fixes and process additions post-dating these publications have
893 been included in this code. Furthermore, novel processes included in neither of these
894 two core models are added to MICT-L in response to phenomena reported in recent
895 empirical publications, such as the diffusion of DOC (novel in ORCHIDEE-MICT) through
896 the soil column to represent its turbation and preferential stabilisation at depth in the
897 soil, in a process not necessarily the same as its adsorption –also represented here.

898

899 In terms of code architecture, the resulting model is substantially different from either
900 of its parents, owing to the fact that the two models were developed on the basis of
901 ORCHIDEE trunk revisions 2728 and 3976 for ORCHILEAK and MICT respectively, which
902 have a temporal model development distance of over 2 years, and subsequently evolved
903 in their own directions. These foundational differences, which mostly affect the
904 formulation of soil, carbon and hydrology schemes, mean that different aspects of each
905 are necessarily forced into the subsequent code. Where these differences were
906 considered scientific or code improvements, they were included in the resulting scheme.

907

908 Where these differences were so large as to prove a burden in excess of the scope of this
909 first model version, such as the inclusion of the soil carbon spinup module, they were
910 omitted from this first revision of MICT-L. The direction of the merge –which model was
911 the base which incorporated code from the other –was from ORCHILEAK into MICT,
912 given that the latter contains the bulk of the fundamental (high latitude) processes
913 necessary for this merge. Despite architectural novelties introduced, MICT-L carries
914 with it a marriage of much the same schemes detailed exhaustively in Guimberteau et al.
915 (2018)(Guimberteau et al., 2018) and Lauerwald et al. (2017)(Lauerwald et al., 2017).
916 As such, the following model description details only new elements of the model, those
917 that are critical to the production and transport of DOC from permafrost regions, and
918 parameterisations specific to this study (Fig. 2).

919

920 **2.1 Model Description**

921

922 MICT-L is based largely on ORCHIDEE-MICT, into which the DOC production, transport
923 and transformation processes developed by Lauerwald et al. and tested insofar only for
924 the Amazon, have been transplanted, allowing for these same processes to be generated

925 in high latitude regions with permafrost soils and a river flow regime dominated by
926 snow melt. The description that ensues roughly follows the order of the carbon and
927 water flow chain depicted in Fig. 2b. At the heart of the scheme is the vegetative
928 production of carbon, which occurs along a spectrum of 13 plant functional types (PFTs)
929 that differ from one another in terms of plant physiological and phenological uptake and
930 release parameters (Krinner et al., 2005). Together, these determine grid-scale net
931 primary production. In the northern high latitudes, the boreal trees (PFTs 7-9) and C3
932 grasses (PFT 10) dominate landscape biomass and primary production. Thus, in
933 descending order yearly primary production over the Lena basin is roughly broken
934 down between C3 grasses (48%), boreal needleleaf summergreen trees (27%), boreal
935 needleleaf evergreen trees (12%), boreal broadleaf summergreen trees (8%) and
936 temperate broad-leaved evergreen trees (6%). Naturally these basin aggregates are
937 heterogeneously distributed along latitude and temperature contours, with
938 grasses/tundra dominating at the high latitudes and (e.g.) temperate broadleaf trees
939 existing only at the southern edges of the basin.

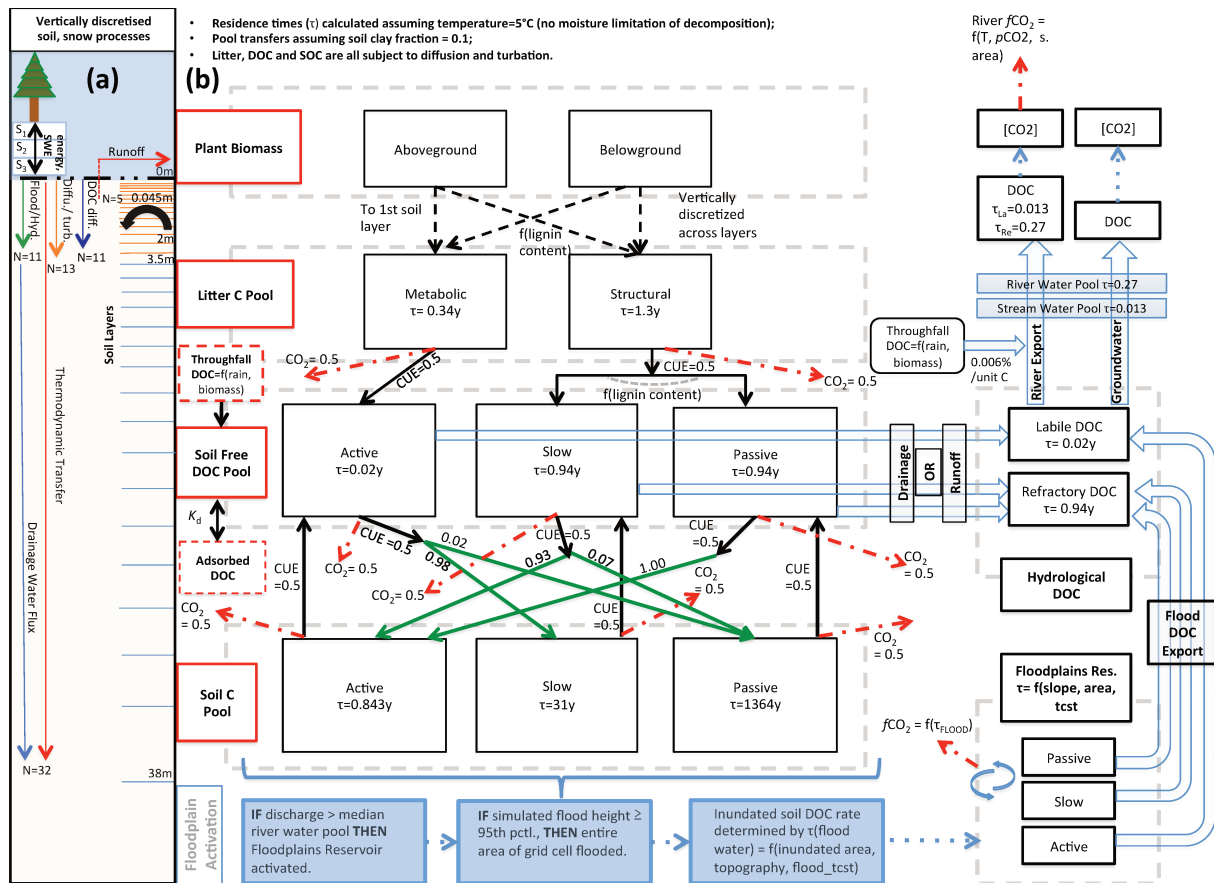
940

941 **2.2 Biomass generation (Fig. 1a)**

942

943 Biomass generation, consisting of foliage, roots, above and below -ground sap and heart
944 wood, carbon reserves and fruit pools in the model, results in the transfer of these
945 carbon stores to two downstream litter pools, the structural and metabolic litter (Figure
946 2b). This distinction, defined by lignin concentration of each biomass pool (Krinner et
947 al., 2005), separates the relatively reactive litter fraction such as leafy matter from its
948 less-reactive, recalcitrant counterpart (woody, 'structural' material), with the
949 consequence that the turnover time of the latter is roughly four-fold that of the former.
950 These two litterpools are further subdivided into above and below -ground pools, with
951 the latter explicitly discretised over the first two metres of the soil column, a feature first
952 introduced to the ORCHIDEE model by Camino-Serrano et al. (2014, 2018)(Camino-
953 Serrano et al., 2014, 2018). This marks a significant departure from the original litter
954 formulation in ORCHIDEE-MICT, in which the vertical distribution of litter influx to the
955 soil carbon pool follows a prescribed root profile for each PFT. This change now allows
956 for the production of DOC from litter explicitly at a given soil depth in permafrost soils.

957



958
 959 **Figure 2** :Carbon and water flux map for core DOC elements in model structure relating to DOC transport
 960 and transformation. **(a)** Summary of the differing extent of vertical discretisation of soil and snow for
 961 different processes calculated in the model. Discretisation occurs along 32 layers whose thickness
 962 increases geometrically from 0-38m. N refers to the number of layers, SWE=snow water equivalent, S_n =
 963 Snow layer n. Orange layers indicate the depth to which diffusive carbon (turbation) fluxes occur. **(b)**
 964 Conceptual map of the production, transfer and transformation of carbon in its vertical and lateral (i.e.,
 965 hydrological) flux as calculated in the model. Red boxes indicate meta-reservoirs of carbon, black boxes
 966 the actual pools as they exist in the model. Black arrows indicate carbon fluxes between pools, dashed red
 967 arrows give carbon loss as CO₂, green arrows highlight the fractional distribution of DOC to SOC (no
 968 carbon loss incurred in this transfer), a feature of this model. For a given temperature (5°C) and soil clay
 969 fraction, the fractional fluxes between pools are given for each flux, while residence times for each pool (
 970 τ) are in each box. The association of carbon dynamics with the hydrological module are shown by the
 971 blue arrows. Blue dashed boxes illustrate the statistical sequence which activates the boolean floodplains
 972 module. Note that for readability, the generation and lateral flux of dissolved CO₂ is omitted from this
 973 diagram, but is described at length in the Methods section.

974
 975
 976 **2.3 DOC generation and leaching (Fig. 1b)**

977
 978 The vast majority of DOC produced by the model is generated initially from the litter
 979 pools via decomposition, such that half of all of the decomposed litter is returned to the
 980 atmosphere as CO₂, as defined by the microbial carbon use efficiency (CUE) –the fraction
 981 of carbon assimilated versus respired by microbes post-consumption –here set at 0.5
 982 following Manzoni et al. (2012)(Manzoni et al., 2012). The non-respired half of the litter
 983 feeds into ‘Active’, ‘Slow’ and ‘Passive’ free DOC pools, which correspond to DOC
 984 reactivity classes in the soil column. Metabolic litter contributes exclusively to the

985 Active DOC pool, while Structural litter feeds into the other two, the distribution
986 between them dependent on the lignin content of the Structural litter. The reactive SOC
987 pools then derive directly from this DOC reservoir, in that fractions of each DOC pool,
988 defined again by the CUE, are directly transferred to three different SOC pools, while the
989 remainder adds to the heterotrophic soil respiration. Depending on clay content and
990 bulk density of the soil, a fraction of DOC is adsorbed to the mineral soil and does not
991 take part in these reactions until it is gradually desorbed when concentrations of free
992 DOC decrease in the soil column. This scheme is explained in detail in Camino-Serrano
993 (2018)(Camino-Serrano et al., 2018). The value of the fractional redistributions
994 between free DOC and SOC after adsorption are shown in Fig. 2b.

995
996 The approximate ratio of relative residence times for the three SOC
997 (Active :Slow :Passive) is (1 :37:1618) at a soil temperature of 5°C, or 0.843 years, 31
998 yrs. and 1364 yrs. for the three pools respectively (Fig. 2b). The residence times of the
999 active DOC pool is ~7 days (0.02 yrs.), while the slow and passive DOC pools both have a
1000 residence time of ~343 days (0.94 yrs.) at that same temperature. Upon microbial
1001 degradation in the model, SOC of each pool reverts either to DOC or to CO₂, the ratio
1002 between these determined again by the CUE which is set in this study at 0.5 for all donor
1003 pools, in keeping with the parameter configuration in Lauerwald et al.,
1004 (2017)(Lauerwald et al., 2017) from Manzoni et al. (2012)(Manzoni et al., 2012). This
1005 step in the chain of flows effectively represents leaching of SOC to DOC. Note that the
1006 reversion of SOC to DOC occurs only along Active-Active, Slow-Slow and Passive-Passive
1007 lines in Fig. 2b, while the conversion of DOC to SOC is distributed differently so as to
1008 build up a reasonable distribution of soil carbon stock reactivities. Note also that the
1009 microbial CUE is invoked twice in the chain of carbon breakdown, meaning that the
1010 'effective' CUE of the SOC-litter system is approximately 0.25.

1011 1012 **2.4 Throughfall and its DOC (Fig. 1c)**

1013
1014 In MICT-L, DOC generation also occurs in the form of wet and dry atmospheric
1015 deposition and canopy exudation, collectively attributed to the throughfall, i.e. the
1016 amount of precipitation reaching the ground. Wet atmospheric deposition originates
1017 from organic compounds dispersed in atmospheric moisture which become deposited
1018 within rainfall, and are assumed here to maintain a constant concentration. This
1019 concentration we take from the average of reported rainfall DOC concentrations in the
1020 empirical literature measured at sites >55°N (Bergkvist and Folkeson, 1992; Clarke et
1021 al., 2007; Fröberg et al., 2006; Lindroos et al., 2011; Rosenqvist et al., 2010; Starr et al.,
1022 2003; Wu et al., 2010), whose value is 3 mgC L⁻¹ of rainfall. Dry DOC deposition occurs
1023 through aerosol-bound organic compounds, here assumed to fall on the canopy ; canopy
1024 exudation refers to plant sugars exuded from the leaf surface (e.g. honey dew) or from
1025 their extraction by heterotrophs such as aphids. These two are lumped together in our
1026 estimates of canopy DOC generation (gDOC per g leaf carbon), which is calibrated as
1027 follows.

1028
1029 We take the average total observation-based throughfall DOC flux rate per m² of forest
1030 from the aforementioned literature bundle (15.7 gC m⁻² yr⁻¹) and subtract from it the
1031 wet deposition component (product of rainfall over our simulation area and the rain
1032 DOC content). The remainder is then the canopy DOC, which we scale to the average leaf

1033 biomass simulated in a 107-year calibration run over the Lena river basin, to obtain a
1034 constant, non-conservative canopy DOC production rate of $9.2 \cdot 10^{-4}$ g DOC-C per gram
1035 leaf biomass per day (Eq. 1), except for the crop PFTs for which this value equals 0. Note
1036 that this production of DOC should be C initially fixed by photosynthesis, but it is here
1037 represented as an additional carbon flux. The dry deposition of DOC through the canopy
1038 is given by:
1039

$$(1) \quad TF_{\text{DRY}} = M_{\text{LEAF}} * 9.2 * 10^{-4} \frac{dt}{day}$$

1040
1041 Where TF_{DRY} is dry deposition of DOC from the canopy and M_{LEAF} is leaf biomass. This
1042 accumulates in the canopy and can be flushed out with the throughfall and percolates
1043 into the soil surface or adds to the DOC stock of surface waters. The wet and canopy
1044 deposition which hits the soil is then assumed to be split evenly between the labile and
1045 refractory DOC pools (following ref.(Aitkenhead-Peterson et al., 2003)).
1046

1047

1048 **2.5 Hydrological mobilisation of soil DOC** (Fig. 1d)

1049

1050 All DOC pools, leached from the decomposition of either litter and SOC or being
1051 throughfall inputs, reside at this point in discrete layers within the soil column, but are
1052 now also available for vertical advection and diffusion, as well as lateral export from the
1053 soil column as a carbon tracer, via soil drainage and runoff.
1054

1055

1056 Export of DOC from the soil to rivers occurs through surface runoff, soil-bottom
1057 drainage, or flooding events (see sections 'soil flooding' and 'floodplain representation').
1058 Runoff is activated when the maximum water infiltration rate of the specific soil has
1059 been exceeded, meaning that water arrives at the soil surface faster than it can enter,
1060 forcing it to be transported laterally across the surface. DOC is drawn up into this
1061 runoff water flux from the first 5 layers of the soil column, which correspond to a
1062 cumulative source depth of 4.5cm.

1063

1064 Drainage of DOC occurs first as its advection between the discrete soil layers, and its
1065 subsequent export from the 11th layer, which represents the bottom of the first 2m of
1066 the soil column, from which export is calculated as a proportion of the DOC
1067 concentration at this layer. Below this, soil moisture and DOC concentrations are no
1068 longer explicitly calculated, except in the case that they are cryoturbated below this, up
1069 to a depth of 3m. DOC drainage is proportional to but not a constant multiplier of the
1070 water drainage rate for two reasons. First, in the process of drainage DOC is able to
1071 percolate from one layer to another, through the entirety of the soil column, meaning
1072 that vertical transport is not solely determined by 11th layer concentrations, given that
1073 DOC can be continuously leached and transported over the whole soil column. Secondly,
1074 in order to account for preferential flow paths in the soil created by the subsoil actions
1075 of flora and fauna, and for the existence of non-homogenous soil textures at depth that
1076 act as aquitards, DOC infiltration must account for the fact that area-aggregated soils
1077 drain more slowly, increasing the residence time of DOC in the soil. Thus a reduction
factor which reduces the vertical advection of DOC in soil solution by 80% compared to

1078 the advection is applied to represent a slow down in DOC percolation through the soil
1079 and increase its residence time there.

1080
1081 In MICT-L, as in ORCHILEAK, a ‘poor soils’ module reads off from a map giving fractional
1082 coverage of land underlain by Podzols and Arenosols at the 0.5° grid-scale, as derived
1083 from the Harmonized World Soil Database (Nachtergaele, 2010). Due to their low pH
1084 and nutrient levels, areas identified by this soil-type criterion experience soil organic
1085 matter decomposition rates half that of other soils (Lauerwald et al. (2017)(Lauerwald
1086 et al., 2017), derived from Bardy et al. (2011); Vitousek & Sanford (1986); Vitousek &
1087 Hobbie (2000)(Bardy et al., 2011; Vitousek and Hobbie, 2000; Vitousek and Sanford,
1088 1986)). To account for the very low DOC-filtering capacity of these coarse-grained, base-
1089 and clay-poor soils (DeLuca & Boisvenue (2012)(DeLuca and Boisvenue, 2012), Fig. 2b),
1090 no reduction factor in DOC advection rate relative to that of water in the soil column is
1091 applied when DOC is generated within these “poor soils”.

1092
1093 By regulating both decomposition and soil moisture flux, the “poor soil” criterion
1094 effectively serves a similar if not equal function to a soil ‘tile’ for DOC infiltration in the
1095 soil column (inset box of Fig. 1), because soil tiles (forest, grassland/tundra/cropland
1096 and bare soil) are determinants of soil hydrology which affects moisture-limited
1097 decomposition. Here however, the ‘poor soil’ criteria is applied uniformly across the
1098 three soil tiles of each grid cell. This modulation in MICT-L is of significance for the
1099 Arctic region, given that large fractions of the discontinuous permafrost region are
1100 underlain by Podzols, particularly in Eurasia. For the Arctic as a whole, Podzols cover
1101 ~15% of total surface area (DeLuca and Boisvenue, 2012). Further, in modelled frozen
1102 soils, a sharp decline in hydraulic conductivity is imposed by the physical barrier of ice,
1103 which retards the flow of water to depth in the soil, imposing a cap on drainage and thus
1104 potentially increasing runoff of water laterally, across the soil surface (Gouttevin et al.,
1105 2012). In doing so, frozen soil layers overlain by liquid soil moisture will experience
1106 enhanced residence times of water in the carbon-rich upper soil layers, potentially
1107 enriching their DOC load.

1108
1109 Thus, for all the soil layers in the first 2m, DOC stocks are controlled by production from
1110 litter and SOC decay, their advection, diffusion, and consumption by DOC mineralization,
1111 as well as buffering by adsorption and desorption processes.

1112 1113 **2.6 Routing Scheme:**

1114
1115 The routing scheme in ORCHIDEE, first described in detail in Ngo-Duc et al. (2007)(Ngo-
1116 Duc et al., 2007) and presented after some version iterations in Guimberteau et al.
1117 (2012)(Guimberteau et al., 2012), is the module which when activated, represents the
1118 transport of water collected by the runoff and drainage simulated by the model along the
1119 prescribed river network in a given watershed. In doing so, its purpose is to coarsely
1120 represent the hydrologic coupling between precipitation inputs to the model and
1121 subsequent terrestrial runoff and drainage (or evaporation) calculated by it on the one
1122 hand, and the eventual discharge of freshwater to the marine domain, on the other. In
1123 other words, the routing scheme simulates the transport of water by rivers and streams,
1124 by connecting rainfall and continental river discharge with the land surface.

1125

1126 To do so, the routing scheme first inputs a map of global watersheds at the 0.5 degree
1127 scale (Oki et al., 1999; Vorosmarty et al., 2000) which gives watershed and sub-basin
1128 boundaries and the direction of water-flow based on topography to the model. The
1129 water flows themselves are comprised of three distinct linear reservoirs within each sub-basin
1130 ('slow', 'fast', 'stream'). Each water reservoir is represented at the subgrid scale (here: 4
1131 subgrid units per grid cell), and updated with the lateral in- and outflows at a daily time-step.
1132 The 'slow' water reservoir aggregates the soil drainage, i.e. the vertical outflow from the 11th
1133 layer (2 m depth) of the soil column, effectively representing the 'shallow groundwater'
1134 storage. The 'fast' water reservoir aggregates surface runoff simulated in the model,
1135 effectively representing overland hydrologic flow. The 'slow' and 'fast' water reservoirs feed a
1136 delayed outflow to the 'stream' reservoir' of the adjacent subgrid-unit in the downstream
1137 direction.

1138
1139 The water residence time in each reservoir depends on the nature of the reservoir (increasing
1140 residence time in the order : stream < fast < slow reservoir). More generally, residence time
1141 decreases with the steepness of topography, given by the product of a local topographic
1142 index and a constant with decreasing values for the 'slow', 'fast' and 'stream' reservoirs.
1143 The topographic index is the ratio of the grid-cell length to the square root of the mean
1144 slope, to reproduce the effect of geomorphological factors in Manning's equation
1145 (Ducharne et al., 2003; Guimberteau et al., 2012; Manning, 1891) and determines the
1146 time that water and DOC remain in soils prior to entering the river network. In this way
1147 the runoff and drainage are exported from sub-unit to sub-unit and from grid-cell to grid-cell.

1148
1149

1150 **2.7 Grid-scale water and carbon routing** (Fig. 1f, 1g)

1151
1152
1153 Water-borne, terrestrially-derived DOC and dissolved CO₂ in the soil solution are
1154 exported over the land surface using the same routing scheme. When exported from
1155 soil or litter, DOC remains differentiated in the numerical simulations according to its
1156 initial reactivity within the soil (Active, Slow, Passive). However, because the terrestrial
1157 Slow and Passive DOC pools (Camino-Serrano et al., 2018) are given the same residence
1158 time, these two pools are merged when exported (Lauerwald et al., 2017): Active DOC
1159 flows into a Labile DOC hydrological export pool, while the Slow and Passive DOC pools
1160 flow into a Refractory DOC hydrological pool (Fig. 2b). The water residence times in each
1161 reservoir of each subgrid-unit determine the decomposition of DOC into CO₂ within water
1162 reservoirs, before non-decomposed DOC is passed on to the next reservoir downstream.

1163
1164 The river routing calculations, which occur at a daily timestep, are then aggregated to
1165 one-day for the lateral transfer of water, CO_{2(aq)} and DOC from upstream grid to
1166 downstream grid according to the river network. Note that carbonate chemistry in
1167 rivers and total alkalinity routing are not calculated here.

1168
1169 In this framework, the 'fast' and 'slow' residence times of the water pools in the routing
1170 scheme determine the time that water and DOC remains in overland and groundwater
1171 flow before entering the river network. Note that while we do not explicitly simulate
1172 headwater streams as they exist in a geographically determinant way in the real world,
1173 we do simulate what happens to the water before it flows into a river large enough to be

1174 represented in the routing scheme by the water pool called 'stream'. The 'fast' reservoir,
1175 which is indicative of the pool of runoff water that is destined for entering the 'stream'
1176 water reservoir, is implicitly representative of headwater streams non resolved by the
1177 model routing as an explicit stream pool at a given spatial resolution, as it fills the spatial
1178 and temporal niche between runoff and the river stem. The dynamics of headwater
1179 hydrological and DOC dynamics (Section 2.10) are of potentially great significance with
1180 respect to carbon processing, as headwater catchments have been shown to be
1181 'hotspots' of carbon metabolism and outgassing in Arctic rivers, despite their
1182 relatively small areal fraction (Denfeld et al., 2013; Drake et al., 2015; Mann et al., 2015;
1183 Venkiteswaran et al., 2014; Vonk et al., 2013, 2015a, 2015c). Thus, in what follows in
1184 this study, we refer to what in the code are called the 'fast' and 'stream' pools, which
1185 represent the small streams and large stream or river pools, respectively, using 'stream'
1186 and 'river' to denote these from hereon in.

1187
1188 Furthermore, the differentiated representation of water pools as well as mean grid cell
1189 slope, combined with the dynamic active layer simulated for continuous versus
1190 discontinuous permafrost, is important for reproducing the phenomena observed by
1191 Kutscher et al. (2017)(Kutscher et al., 2017) and Zhang et al. (2017)(Zhang et al., 2017)
1192 for sloping land as shown on the right hand side of Fig. 1. In discontinuous permafrost
1193 and permafrost free regions, these phenomena encompass landscape processes (sub-
1194 grid in the model), through which water flow is able to re-infiltrate the soil column and
1195 so leach more refractory DOC deeper in the soil column, leading to a more refractory
1196 signal in the drainage waters. In contrast, in continuous permafrost region, the shallow
1197 active layer will inhibit the downward re-infiltration flux of water and encourage
1198 leaching at the more organic-rich and labile surface soil layer, resulting in a more labile
1199 DOC signal from the drainage in these areas (Fig. 1). These re-infiltration processes are
1200 thought to be accentuated in areas with higher topographic relief (Jasechko et al., 2016),
1201 which is why they are represented on sloping areas in Fig. 1.

1202 1203 **2.8 Representation of floodplain hydrology and their DOC budget (Fig. 1e,1h)**

1204
1205 The third terrestrial DOC export pathway in MICT-L is through flooding of floodplains, a
1206 transient period that occurs when stream water is forced by high discharge rates over
1207 the river 'banks' and flows onto a flat floodplain area of the grid cell that the river
1208 crosses, thus inundating the soil. Such a floodplain area is represented as a fraction of a
1209 grid-cell with the maximum extent of inundation, termed the 'potential flooded area'
1210 being predefined from a forcing file (Tootchi et al., 2019). Here, the DOC pools that are
1211 already being produced in these inundated areas from litter and SOC decomposition in
1212 the first 5 layers of the soil column are directly absorbed by the overlying flood waters.
1213 These flood waters may then either process the DOC directly, via oxidation to CO₂,
1214 (Sections 2.10, 2.11) or return them to the river network, as floodwaters recede to the
1215 river main stem, at which point they join the runoff and drainage export flows from
1216 upstream.

1217
1218 MICT-L includes the floodplain hydrology part of the routing scheme (D'Orgeval et al.,
1219 2008; Guimberteau et al., 2012), as well as additions and improvements described in
1220 Lauerwald et al. (2017). The spatial areas that are available for potential flooding are
1221 pre-defined by an input map originally based on the map of Prigent et al. (2007)(Prigent

1222 et al., 2007). However, for this study, we used an alternative map of the “regularly
1223 flooded areas” derived from the method described in Tootchi et al., (2018), which in this
1224 study uses an improved input potential flooding area forcing file specific to the Lena
1225 basin, that combines three high-resolution surface water and inundation datasets
1226 derived from satellite imagery: GIEMS-D15 (Fluet-Chouinard et al., 2015), which results
1227 from the downscaling of the map of Prigent et al. (2007)(Prigent et al., 2007) at 15-arc-
1228 sec (ca 500 m at Equator); ESA-CCI land cover (at 300 m ~ 10 arc-sec); and JRC surface
1229 water at 1 arc-sec (Pekel et al., 2016). The ‘fusion’ approach followed by this forcing
1230 dataset stems from the assumption that the potential flooding areas identified by the
1231 different datasets are all valid despite their uncertainties, although none of them is
1232 exhaustive. The resulting map was constructed globally at the 15 arc-sec resolution and
1233 care was taken to exclude large permanent lakes from the potential flooding area based
1234 on the HydroLAKES database (Messenger et al., 2016). In the Lena river basin, the basin
1235 against which we evaluate ORCHIDEE MICT-LEAK in Part 2 of this study, this new
1236 potential floodplains file gives a maximum floodable area of 12.1% ($2.4 \times 10^5 \text{ km}^2$) of the
1237 $2.5 \times 10^6 \text{ km}^2$ basin, substantially higher than previous estimates of 4.2%(Prigent et al.,
1238 2007).

1239
1240 With this improved forcing, river discharge becomes available to flood a specific pre-
1241 defined floodplain grid fraction, creating a temporary floodplains hydrologic reservoir,
1242 whose magnitude is defined by the excess of discharge at that point over a threshold
1243 value, given by the median simulated water storage of water in each grid cell over a 30
1244 year period. The maximum extent of within-grid flooding is given by another threshold,
1245 the calculated height of flood waters beyond which it is assumed that the entire grid is
1246 inundated. This height, which used to be fixed at 2 m, is now determined by the 90th
1247 percentile of all flood water height levels calculated per grid cell from total water
1248 storage of that grid cell over a reference simulation period for the Lena basin, using the
1249 same methodology introduced by Lauerwald et al. (2017). The residence time of water
1250 on the floodplains (τ_{flood}) is a determinant of its resulting DOC concentration, since
1251 during this period it appropriates all DOC produced by the top 5 layers of the soil
1252 column.

1253 **2.9 Oceanic outflow (Fig. 1i)**

1254
1255
1256 Routing of water and DOC through the river network ultimately lead to their export
1257 from the terrestrial system at the river mouth (Fig. 1), which for high latitude rivers are
1258 almost entirely sub-deltas of the greater ‘estuary’, described by McClelland et al. (2012),
1259 draining into the Arctic Ocean. Otherwise, the only other loss pathway for carbon
1260 export once in the river network is through its decomposition to CO_2 and subsequent
1261 escape to the atmosphere from the river surface. DOC decomposition is ascribed a
1262 constant fraction for the labile and refractory DOC pools of 0.3 d^{-1} and 0.01 d^{-1} at 25°C ,
1263 respectively, these modulated by a water-temperature dependent Arrhenius rate term.
1264 Because the concentration of dissolved CO_2 (referred to as $\text{CO}_{2(\text{aq})}$) in river water is
1265 derived not only from in-stream decomposition of DOC, but also from $\text{CO}_{2(\text{aq})}$ inputs
1266 from the decomposition of litter, SOC and DOC both in upland soils and in inundated
1267 soils, the model also represents the lateral transport of $\text{CO}_{2(\text{aq})}$ from soils through the
1268 river network. Note that autochthonous primary production and derivative carbon

1269 transformations are ignored here, as they are considered relatively minor contributors
1270 in the Arctic lateral flux system (Cauwet and Sidorov, 1996; Sorokin and Sorokin, 1996).

1271

1272 **2.10 Dissolved CO₂ export and river evasion** (Fig. 1j)

1273

1274 Soil CO_{2(aq.)} exports are simulated by first assuming a constant concentration of CO_{2(aq.)}
1275 with surface runoff and drainage water fluxes, of 20 and 2 mgC L⁻¹, corresponding to a
1276 pCO₂ of 50000 μ atm and 5000 μ atm at 25°C in the soil column, respectively. These
1277 quantities are then scaled with total (root, microbial, litter) soil respiration by a scaling
1278 factor first employed in Lauerwald et al. (2019, *in review*). In the high latitudes soil
1279 respiration is dominantly controlled by microbial decomposition, and for the Lena basin
1280 initial model tests suggest that its proportional contribution to total respiration is
1281 roughly 90%, versus 10% from root respiration. Thus CO_{2(aq.)} enters and circulates the
1282 rivers via the same routing scheme as that for DOC and river water. The lateral transfers
1283 of carbon are aggregated from the 30 minute time steps at which they are calculated,
1284 with a 48 timestep period, so that they occur within the model as a daily flux. The
1285 calculation of the river network pCO₂ can then be made from CO_{2(aq.)} and its equilibrium
1286 with the atmosphere, which is a function of its solubility (K_{CO2}) with respect to the
1287 temperature of the water surface T_{WATER} (Eq.2).

1288

$$(2) \quad pCO_{2POOL} = \frac{[CO_{2(aq)}]}{12.011 * K_{CO_2}}$$

1289

1290 Where the pCO₂ of a given (e.g. 'stream', 'fast', 'slow' and floodplain) water pool
1291 (pCO_{2POOL}) is given by [CO_{2(aq)}] the dissolved CO₂ concentration in that pool, and K_{CO2}.
1292 Water temperature (T_{WATER}, (°C)) isn't simulated by the model, but is derived here from
1293 the average daily surface temperature (T_{GROUND}, (°C)) in the model (Eq. 3), a set up used
1294 by Lauerwald et al. (2017) and retained here. Note that while dissolved CO₂ enters from
1295 the terrestrial reservoir from organic matter decomposition, it is also generated *in situ*
1296 within the river network as DOC is respired microbially.

1297

1298 With our water temperature estimate, both K_{CO2} and the Schmidt number (Sc) from
1299 Wanninkhof (1992)(Wanninkhof, 1992) can be calculated, allowing for simulation of
1300 actual gas exchange velocities from standard conditions. The CO₂ that evades is then
1301 subtracted from the [CO₂] stocks of each of the different hydrologic reservoirs –river,
1302 flood and stream.

1303

$$(3) \quad T_{WATER} = 6.13^{\circ}C + (0.8 * T_{GROUND})$$

1304

$$(4) \quad Sc = ((1911 - 118.11) * T_{WATER}) + (3.453 * T_{WATER}^2) - (0.0413 * T_{WATER}^3)$$

1305

1306 CO₂ evasion is therefore assumed to originate from the interplay of CO₂ solubility,
1307 relative gradient in partial pressures of CO₂ between air and water, and gas exchange
1308 kinetics. Evasion as a flux from river and floodplain water surfaces is calculated at a
1309 daily timestep, however in order to satisfy the sensitivity of the relative gradient of
1310 partial pressures of CO₂ in the water column and atmosphere to both CO₂ inputs and
1311 evasion, the pCO₂ of water is calculated at a more refined 6 minute timestep. The daily

1312 lateral flux of CO₂ inputs to the water column are thus equally broken up into 240 (6
 1313 min.) segments per day and distributed to the pCO₂ calculation. Other relevant carbon
 1314 processing pathways, such as the photochemical breakdown of riverine OC, are not
 1315 explicitly included here, despite the suggestion by some studies that the photochemical
 1316 pathway dominate DOC processing in Arctic streams(Cory et al., 2014). Rather, these
 1317 processes are bundled into the aggregate decomposition rates used in the model, which
 1318 thus include both microbial and photochemical oxidation. This is largely because it is
 1319 unclear how different factors contribute to breaking down DOC in a dynamic
 1320 environment and also the extent to which our DOC decomposition and CO₂ calculations
 1321 implicitly include both pathways –e.g. to what extent the equations and concepts used in
 1322 their calculation confound bacterial with photochemical causation, since both microbial
 1323 activity and incident UV light are a function of temperature and total incident light.

1324

1325 **2.11 Soil layer processes: turbation adsorption**

1326

1327 The soil carbon module is discretised into a 32-layer scheme totalling 38m depth, which
 1328 it shares with the soil thermodynamics to calculate temperature through the entire
 1329 column. An aboveground snow module (Wang et al., 2013) is discretised into 3 layers of
 1330 differing thickness, heat conductance and density, which collectively act as a
 1331 thermodynamically-insulating intermediary between soil and atmosphere (Fig. 2a).
 1332 Inputs to the three soil carbon pools are resolved only for the top 2m of the soil, where
 1333 litter and DOC are exchanged with SOC in decomposition and adsorption/desorption
 1334 processes. Decomposition of SOC pools, calculated in each soil layer, is dependent on
 1335 soil temperature, moisture and texture (Koven et al., 2009; Zhu et al., 2016), while
 1336 vertical transfer of SOC is enabled by representation of cryoturbation (downward
 1337 movement of matter due to repeated freeze-thaw) in permafrost regions, and
 1338 bioturbation (by soil organisms) in non-permafrost regions in terms of a diffusive flux.

1339

1340 Cryoturbation, given a diffusive mixing rate (Diff) of 0.001 m² yr⁻¹ (Koven et al., 2009), is
 1341 possible to 3 m depth (diffusive rate declines linearly to zero from active layer bottom to
 1342 3 m), and extends the soil column carbon concentration depth in permafrost regions
 1343 from 2 m. Bioturbation is possible to 2 m depth, with a mixing rate of 0.0001 m² yr⁻¹
 1344 (Koven et al., 2013b) declining to zero at 2 m (Eq. 5). In MICT-L, these vertical
 1345 exchanges in the soil column are improved on. Now, we explicitly include the
 1346 cryoturbation and bioturbation of both belowground litter and DOC. These were not
 1347 possible in ORCHIDEE-MICT because, for the former, the belowground litter distribution
 1348 was not explicitly discretised or vertically dynamic, and for the latter because DOC was
 1349 not produced in prior versions. Diffusion is given by :

1350

$$((5)) \quad \frac{\delta DOC_i(z)}{\delta t} = IN_{DOC_i}(z) - k_i(z) * \Phi * DOC_i(z) + Diff \frac{\delta DOC_i^2(z)}{\delta z^2}$$

1351

1352 Where DOC_i is the DOC in pool i at depth z, (gC m⁻³) IN_{DOC_i} the inflow of carbon to that
 1353 pool (gCm⁻³d⁻¹), k_i the decomposition rate of that pool (d⁻¹), Φ the temperature
 1354 dependent rate modifier for DOC decomposition and Diff the diffusion coefficient (m² yr⁻¹).
 1355 The vertical diffusion of DOC in non-permafrost soils represented here (that is, the
 1356 non-cryoturbated component) appears to be consistent with recent studies reporting an
 1357 increased retention of DOC in the deepening active layer of organic soils (Zhang et al.,

1358 2017). This vertical translocation of organic carbon, whether in solid/liquid phase
1359 appears to be an important component of the high rates of SOC buildup observed at
1360 depth in deep permafrost soils.

1361 1362 **2.11 Priming** (Fig. 1m)

1363
1364 MICT-L also incorporates a scheme for the ‘priming’ of organic matter decomposition, a
1365 process in which the relative stability of SOC is impacted by the intrusion of or contact
1366 with SOC of greater reactivity, resulting in enhanced rates of decomposition. This was
1367 first introduced by Guenet et al. (2016)(Guenet et al., 2016) and updated in Guenet et al.
1368 (2018)(Guimberteau et al., 2018). This process has shown itself to be of potentially
1369 large significance for SOC stocks and their respiration in high latitude regions, in
1370 empirical in situ and soil incubation studies (De Baets et al., 2016; Walz et al., 2017; Wild
1371 et al., 2014, 2016; Zhang et al., 2017), as well as modelling exercises (Guenet et al.,
1372 2018). Here, priming of a given soil pool is represented through the decomposition of
1373 soil carbon (dSOC/dt) by the following equation :

1374

$$(6) \quad \frac{dSOC}{dt} = IN_{SOC} - k * (1 - e^{-c*FOC}) * SOC * \theta * \phi * \gamma$$

1375

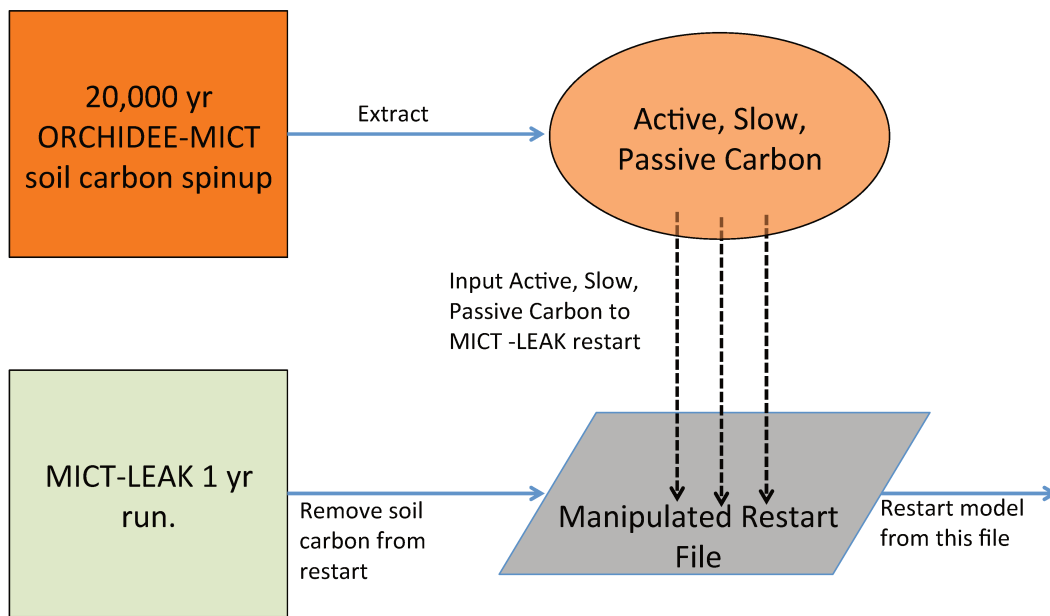
1376 Where IN_{SOC} is the carbon input to that pool, k is the SOC decomposition rate, FOC is a
1377 stock of matter interacting with this SOC pool to produce priming, c is a parameter
1378 controlling this interaction, SOC is the SOC reservoir, and θ , Φ and γ the moisture,
1379 temperature and texture functions that modulate decomposition in the code. The
1380 variable FOC (‘fresh organic carbon’) is an umbrella term used for specifying all of the
1381 carbon pools which together constitute that carbon which is considered potential
1382 priming donor material –ie. more labile – to a given receptor carbon pool. Thus, for the
1383 slow soil carbon pool FOC incorporates the active soil carbon pool plus the above and
1384 below ground structural and metabolic litter pools, because these pools are donors to
1385 the slow pool, and considered to accelerate its turnover through priming. Importantly,
1386 previous studies with priming in ORCHIDEE employed this scheme on a version which
1387 resolves neither the vertical discretisation of the soil column nor the explicit vertical
1388 diffusion processes presented here. This is potentially significant, since the vertical
1389 diffusion of relatively reactive matter may strongly impact (accelerate) the
1390 decomposition of low reactivity matter in the deeper non-frozen horizons of high
1391 latitude soils, while the explicit discretisation of the soil column is a significant
1392 improvement in terms of the accuracy of process-representation within the column
1393 itself.

1394

1395 Other carbon-relevant schemes included in MICT-L are: A prognostic fire routine
1396 (SPITFIRE), calibrated for the trunk version of ORCHIDEE (Yue et al., 2016) is available
1397 in our code but not activated in the simulations conducted here. As a result, we do not
1398 simulate the ~13% of Arctic riverine DOC attributed to biomass burning by Myers-Pigg
1399 et al. (2015)(Myers-Pigg et al., 2015), or the ~8% of DOC discharge to the Arctic Ocean
1400 from the same source (Stubbins et al., 2017). Likewise, a crop harvest module
1401 consistent with that in ORCHIDEE-MICT exists in MICT-L but remains deactivated for
1402 our simulations.

1403

1404 A module introduced in the last version of ORCHIDEE-MICT (Guimberteau et al., 2018),
 1405 in which the soil thermal transfer and porosity and moisture are strongly affected by
 1406 SOC concentration, is deactivated here, because it is inconsistent with the new DOC
 1407 scheme. Specifically, while carbon is conserved in both MICT and MICT-L soil schemes,
 1408 MICT-L introduces a new reservoir into which part of the total organic carbon in the soil
 1409 –the DOC –must now go. This then lowers the SOC concentration being read by this
 1410 thermix module, causing significant model artefact in soil thermodynamics and
 1411 hydrology in early exploratory simulations. Ensuring compatibility of this routine with
 1412 the DOC scheme will be a focal point of future developments in MICT-L. Other processes
 1413 being developed for ORCHIDEE-MICT, including a high latitude peat formation (Qiu et
 1414 al., 2018), methane production and microbial heat generating processes that are being
 1415 optimised and calibrated, are further pending additions to this particular branch of the
 1416 ORCHIDEE-MICT series.
 1417



1418
 1419 **Figure 3:** Flow diagram illustrating the step-wise stages required to implement the model's soil carbon
 1420 stock prior to conducting transient, historical simulations.
 1421

1422 **Soil Carbon Spinup and Simulation Protocol**

1423
 1424 The soil carbon spinup component of ORCHIDEE, which is available to both its trunk and
 1425 MICT branches, was omitted from this first version of MICT-L, owing to the code burden
 1426 required for ensuring compability with the soil carbon scheme in MICT-L. However,
 1427 because we are simulating high latitude permafrost regions, having a realistic soil
 1428 carbon pool at the outset of the simulations is necessary if we are to untangle the
 1429 dynamics of SOC and DOC with a changing environment. Because the soil carbon spinup
 1430 in ORCHIDEE-MICT is normally run over more than 10,000 years (Guimberteau et al.,
 1431 2108), and because running MICT-L for this simulation period in its normal, non-spinup
 1432 simulation mode would impose an unreasonable burden on computing resources, here
 1433 we directly force the soil carbon output from a MICT spinup directly into the restart file
 1434 of a MICT-L simulation.
 1435

1436 A 20,000 year spinup loop over 1961-1990 (these years chosen to mimic coarsely
 1437 warmer mid-Holocene climate) -forced by GSWP-3 climatology, whose configuration
 1438 derives directly from that used in Guimberteau et al. (2018), was thus used to replace
 1439 the three soil carbon pool values from a 1-year MICT-L simulation to set their initial
 1440 values. A conversion of this soil carbon from volumetric to areal units was applied,
 1441 owing to different read/write standards in ORCHILEAK versus ORCHIDEE-MICT. This
 1442 artificially imposed, MICT-derived SOC stock would then have to be exposed to MICT-L
 1443 code, whose large differences in soil carbon module architecture as compared to MICT,
 1444 would drive a search for new equilibrium soil carbon stocks.

1446 Due to the long residence times of the passive SOC pool, reaching full equilibrium for it
 1447 requires a simulation length on the order of 20,000y –again an overburden. As we are
 1448 interested primarily in DOC in this study, which derives mostly from the Active and Slow
 1449 SOC pools, the model was run until these two pools reached a quasi-steady state
 1450 equilibria (Part 2 Supplement, Fig. S1). This was done by looping over the same 30 year
 1451 cycle (1901-1930) of climate forcing data from GSWP-3 during the pre-industrial period
 1452 (Table 1) and the first year (1901) of a prescribed vegetation map (ESA CCI Land Cover
 1453 Map(Bontemps et al., 2013)) –to ensure equilibrium of DOC, dissolved CO₂ and Active
 1454 and Slow SOC pools is driven not just by a single set of environmental factors in one year
 1455 –for a total of 400 years. The parameter configuration adhered as close as possible to
 1456 that used in the original ORCHIDEE-MICT spinup simulations, to avoid excessive
 1457 equilibrium drift from the original SOC state (Fig. 3).

1459 **Table 1:** Data type, name and sources of data files used to drive the model in the study
 1460 simulations.

Data Type	Name	Source
Vegetation Map	ESA CCI Land Cover Map	Bontemps et al., 2013
Topographic Index	STN-30p	Vörösmarty et al., 2000
Stream flow direction	STN-30p	Vörösmarty et al., 2000
River surface area		Lauerwald et al., 2015
Soil texture class		Reynolds et al. 1999
Climatology	GSWP3 v0, 1 degree	http://hydro.iis.u-tokyo.ac.jp/GSWP3/
Potential floodplains	Multi-source global wetland maps	Tootchi et al., 2018
Poor soils	Harmonized World Soil Database map	Nachtergaele et al., 2010
Spinup Soil Carbon Stock	20ky ORCHIDEE-MICT soil carbon spinup	Based on config. in Guimberteau et al. (2018)

1462

1463

1464 Conclusion

1465

1466 This first part of a two-part study has described a new branch of the high latitude
 1467 version of ORCHIDEE-MICT land surface model, in which the production, transport and
 1468 transformation of DOC and dissolved CO₂ in soils and along the inland water network of
 1469 explicitly-represented northern permafrost regions has been implemented for the first
 1470 time. Novel processes with respect to ORCHIDEE-MICT include the discretisation of
 1471 litter inputs to the soil column, the production of DOC and CO_{2(aq)} from organic matter
 1472 and decomposition, respectively, transport of DOC into the river routing network and its

1473 potential mineralisation to CO_{2(aq.)} in the water column, as well as subsequent evasion
1474 from the water surface to the atmosphere. In addition, an improved floodplains
1475 representation has been implemented which allows for the hydrologic cycling of DOC
1476 and CO₂ in these inundated areas. In addition to descriptions of these processes, this
1477 paper outlines the protocols and configuration adopted for simulations using this new
1478 model that will be used for its evaluation over the Lena river basin in the second part of
1479 this study.

1480
1481
1482
1483
1484
1485
1486
1487
1488
1489
1490
1491
1492
1493
1494
1495
1496
1497
1498
1499
1500
1501
1502
1503
1504
1505
1506
1507
1508
1509
1510
1511
1512
1513
1514
1515
1516
1517
1518
1519
1520

Chapter 3

ORCHIDEE MICT-LEAK (r5459), a global model for the production, transport and transformation of dissolved organic carbon from Arctic permafrost regions, Part 2: Model evaluation over the Lena River basin².

Summary

In this second part of a two-part study, we perform simulations of the carbon and water budget of the Lena catchment with the land surface model ORCHIDEE MICT-LEAK, enabled to simulate dissolved organic carbon (DOC) production in soils and its transport and fate in high latitudes inland waters. A soil carbon stock representative of permafrost soils carbon concentrations and quantities is equilibrated with the new carbon and DOC modules described in Chapter 1 and the model allowed to run over the 20th Century under state-of-the-art climate forcing data suite. The model results are evaluated in their ability to reproduce the fluxes of DOC and carbon dioxide (CO₂) along the soil-inland water continuum, and the exchange of CO₂ with the atmosphere, including the evasion outgassing of CO₂ from inland waters. We present simulation results over years 1901-2007, and show that the model is able to broadly reproduce observed state variables and their emergent properties across a range of interacting physical and biogeochemical processes, including:

1) Net primary production (NPP), respiration and riverine hydrologic amplitude, seasonality and inter-annual variation; 2) DOC concentrations, bulk annual flow and their volumetric attribution at the sub-catchment level; 3) High headwater versus downstream CO₂ evasion, an emergent phenomenon consistent with observations over a spectrum of high latitude observational studies. (4) These quantities obey emergent relationships with environmental variables like air temperature and topographic slope that have been described in the literature. This gives us confidence in reporting the following additional findings: (5) Of the ~34TgC yr⁻¹ left over as input to terrestrial and aquatic systems after NPP is diminished by heterotrophic respiration, 7 TgC yr⁻¹ is leached and transported into the aquatic system. Of this, over half (3.6 TgC yr⁻¹) is evaded from the inland water surface back into the atmosphere and the remainder (3.4 TgC yr⁻¹) flushed out into the Arctic Ocean, proportions in keeping with other, empirically derived studies. (6) DOC exported from the floodplains is dominantly sourced from recent, more 'labile' terrestrial production, in contrast to DOC leached from the rest of the watershed with runoff and drainage, which is mostly sourced from recalcitrant soil and litter. (7) All else equal, both historical climate change (a spring/summer warming of 1.8°C over the catchment) and rising atmospheric CO₂ (+85.6ppm) are diagnosed from factorial simulations to contribute similar, significant increases in DOC transport via primary production, although this similarity may not hold in the future.

² Submitted to *Geoscientific Model Development*, in review.

1566 The ability of ORCHIDEE MICT-LEAK to reasonably reproduce individual DOC-specific
1567 phenomena, and their interaction and response to seasonal and interannual changes in
1568 environmental drivers, and the emergent phenomena that arise as a result,
1569 demonstrate that this model is a potentially powerful new tool for diagnosing and
1570 reproducing past, present and potentially future states of the Arctic carbon cycle.
1571 Furthermore, our results appear to suggest that, if the historical response of the Lena
1572 basin to environmental drivers is generalisable to its future response, and if the Lena
1573 basin can be used to generalise permafrost basins as a whole, DOC cycling in the Arctic
1574 may increase under enhanced warming and primary production. Further, if DOC
1575 temperature responses follow the pathway witnessed for parts of western Siberia, this
1576 likely increase may occur in a highly non-linear fashion. In Chapter 3, these questions
1577 are addressed by simulating the past and future of the Pan-Arctic region, driven by
1578 climate input data representative of a future intermediate-warming scenario.

1579
1580
1581
1582
1583
1584
1585
1586
1587
1588
1589
1590
1591
1592
1593
1594
1595
1596
1597
1598
1599
1600
1601
1602
1603
1604
1605
1606
1607
1608
1609
1610
1611
1612
1613

Chapitre 3

ORCHIDEE MICT-LEAK (r5459), modèle mondial de production, de transport et de transformation du carbone organique dissous issu des régions de pergélisol de l'Arctique, partie 2: évaluation du modèle sur le bassin de la Lena.

Résumé

Dans cette deuxième partie d'une étude en deux parties, nous effectuons des simulations avec le modèle de surface terrestre ORCHIDEE MICT-LEAK décrit dans le chapitre 1 dans le but de reproduire le bilan carbone et eau du bassin versant de Lena, en particulier la production de carbone organique dissous (COD) dans les sols et son transport dans les eaux intérieures des hautes latitudes au cours du XXe siècle avec une suite de données de forçage climatique ultramoderne. Les capacités du modèle à reproduire les flux de COD et de dioxyde de carbone (CO₂) le long du continuum sol-eaux intérieures et l'échange de CO₂ avec l'atmosphère, y compris l'évacuation dégagée de CO₂ des eaux intérieures sont évaluées. Nous présentons les résultats de la simulation sur les années 1901-2007 et montrons que le modèle est capable de reproduire à grande échelle les variables d'état observées et leurs propriétés émergentes dans une gamme de processus physiques et biogéochimiques en interaction, notamment:

1) Production primaire nette (PPN), la respiration et l'amplitude hydrologique des rivières (saisonnalité et variation interannuelle); 2) les concentrations de COD, le débit annuel global et leur attribution volumétrique au niveau du sous-captage; 3) Évasion du CO₂ en amont et en aval, un phénomène émergent cohérent avec les observations sur un spectre d'études observationnelles à haute latitude. Ces quantités obéissent à des relations émergentes avec des variables environnementales telles que la température de l'air et la pente topographique décrites dans la littérature. Nous estimons grâce au modèle que sur les ~ 34 TgC an⁻¹ restants comme intrants dans les systèmes terrestres et aquatiques et après soustraction de la respiration par la respiration hétérotrophe, 7 TgC an⁻¹ sont lessivés et transportés dans le milieu aquatique. Sur ce total, plus de la moitié (3,6 TgC an⁻¹) est évacuée de la surface des eaux intérieures vers l'atmosphère et le reste (3,4 TgC an⁻¹) est évacué dans l'océan Arctique. Ces proportions sont conformes à celles estimées par d'autres études empiriques. Le COD exporté des plaines d'inondations provient principalement de la production terrestre récente, plus «labile», contrairement au COD lessivé du reste du bassin versant avec ruissellement et drainage, principalement à partir de sol et de litière récalcitrants. Toutes choses étant égales par ailleurs, les effets directs des changements climatiques historiques (réchauffement printemps / été de 1,8 ° C sur le bassin versant) et de la hausse des émissions de CO₂ dans l'atmosphère (+ 85,6 ppm) ont été diagnostiquées à l'aide de simulations factorielles comme contribuant à des augmentations similaires et significatives du transport de C production, bien que cette similitude puisse ne pas être vraie à l'avenir.

La capacité d'ORCHIDEE MICT-LEAK à reproduire de manière raisonnable des phénomènes individuels spécifiques au COD, leurs interactions et leurs réponses aux changements saisonniers et interannuels des facteurs environnementaux, ainsi que les phénomènes émergents qui en résultent, démontrent que ce modèle constitue un nouvel outil

1662 potentiellement puissant pour diagnostiquer et reproduire les états passés, présents et
1663 potentiellement futurs du cycle du carbone arctique. De plus, nos résultats semblent suggérer
1664 que, si la réponse historique du bassin de Lena aux facteurs environnementaux est
1665 généralisable pour sa réponse future, et si le bassin de Lena peut être utilisé pour généraliser
1666 l'ensemble des bassins de pergélisol, le cycle de COD dans l'Arctique pourrait s'accélérer à
1667 cause du réchauffement accru et d'une augmentation de la production primaire. En outre, si les
1668 réponses de température du COD suivent le chemin observé dans certaines parties de la
1669 Sibérie occidentale, cette augmentation risque de se produire de manière très non linéaire.
1670 Dans le chapitre 3, ces questions sont traitées en simulant le passé et l'avenir de la région
1671 panarctique, à l'aide de données climatologiques représentatives d'un futur scénario de
1672 réchauffement intermédiaire.

1673
1674
1675
1676
1677
1678
1679
1680
1681
1682
1683
1684
1685
1686
1687
1688
1689
1690
1691
1692
1693
1694
1695
1696
1697
1698
1699
1700
1701
1702
1703
1704
1705
1706
1707
1708
1709

1710
1711
1712
1713
1714
1715
1716
1717
1718
1719
1720
1721
1722
1723
1724
1725
1726
1727
1728
1729
1730
1731
1732
1733
1734
1735
1736
1737
1738
1739
1740
1741
1742
1743
1744
1745
1746
1747
1748
1749
1750
1751
1752
1753
1754
1755
1756
1757

1 Introduction

A new branch of the high latitude-specific land surface component of the IPSL Earth System model, ORCHIDEE MICT-LEAK (r5459), was enabled to simulate new model processes of soil dissolved organic carbon (DOC) and CO₂ production, and their advective/diffusive vertical transport within a discretized soil column as well as their transport and transformation within the inland water network, in addition to improved representation of hydrological and carbon processes in floodplains. These additions, processes first coded in the model ORCHILEAK (Lauerwald et al., 2017) and implemented within the high latitude base model ORCHIDEE-MICT v8.4.1 (Guimberteau et al., 2018), were described in detail in Part 1 of this study. This second part of our study deals with the validation and application of our model. We validate simulation outputs against observation for present-day and run transient simulations over the historical period (1901-2007) using the Lena River basin as test case. The simulation setup and rationale for choice of simulation basin are outlined below.

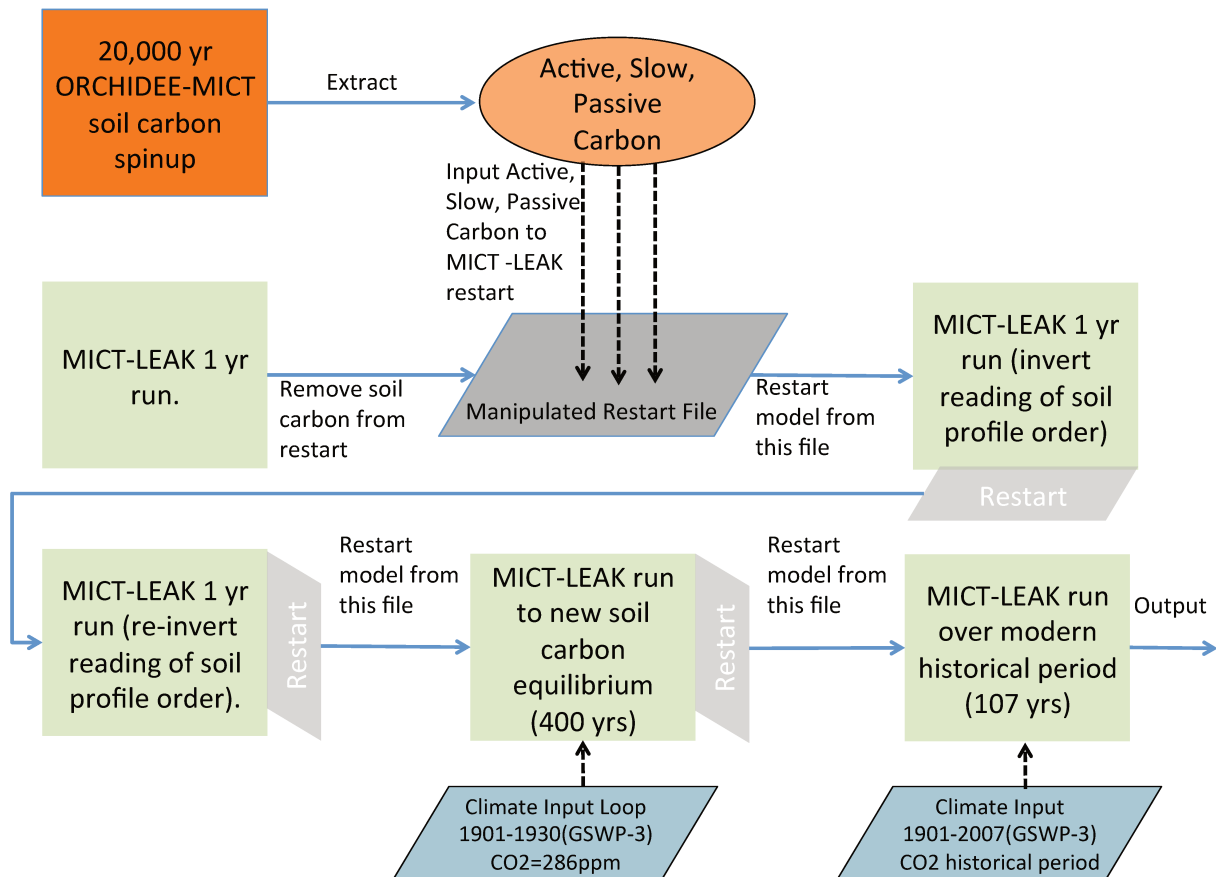
2 Simulation Rationale

The Lena river basin, which is bounded by the region 52-72°N; 102-142°E, was chosen as the basin for model evaluation because it is the largest DOC discharge contribution amongst the Arctic rivers, according to some estimates (Raymond et al., 2007; Holmes et al., 2012), with its 2.5 million km² area (befitting our coarse-grid resolution) discharging almost 20% of the summed discharge of the largest six Arctic rivers, its large areal coverage by Podzols (DeLuca and Boisvenue, 2012), and the dominance of DOC versus particulate organic carbon (POC) with 3-6Tg DOC-C yr⁻¹ vs. 0.03-0.04 Tg POC-C yr⁻¹ (Semiletov et al., 2011) in the total OC discharge load –factors all broadly representative of the Eurasian Arctic rivers. Compared to other Eurasian rivers, the Lena is relatively well studied, which provides data across the range of soil, hydrologic, geochemical and ecological domains over space and time, that enable us to perform adequate model evaluation.

Climatological forcing is input from the Global Soil Wetness Project Phase 3 (GSWP3) v.0 data at a 1 degree 3-hourly resolution covering the period 1901 to 2007 (Supplement, Table S1), which is then interpolated to a 30 minute timestep to comply with the timestep of the model's surface water and energy balance calculation period. This dataset was chosen for its suitability as input for reproducing the amplitude and seasonality of Northern Hemisphere high latitude riverine discharge in ORCHIDEE-MICT, as compared to other datasets (Guimberteau et al., 2018). An improved floodplains area input file for the Lena basin (Tootchi et al., 2019) was used to drive the simulation of floodplain dynamics (Supplement, Table S1).

Simulations were run over the Lena river basin (Fig. 3a) at a 1 degree resolution (Fig. 1) for the historical period between 1901 and 2007 to evaluate the simulated output of relevant carbon fluxes and hydrologic variables against their observed values, as well as those of emergent phenomena arising from their interplay (Fig. 1), at both the grid and basin scale. We evaluate at the basin scale because the isolation of a single geographic unit allows for a more refined analysis of simulated variables than doing the same over

1758 the global Pan-Arctic, much of which remains poorly accounted for in empirical
 1759 databases and literature.
 1760



1761
 1762 **Figure 1:** Flow diagram illustrating the step-wise stages required to set up the model, up to and including
 1763 the historical period. The two stages that refer to the inverted reading of restart soil profile order point to
 1764 the fact that the restart inputs from ORCHIDEE-MICT are read by our model in inverse order, so that one
 1765 year must be run in which an activated flag reads it properly, before the reading of soil profile restarts is
 1766 re-inverted for all subsequent years.
 1767

1769 3 Simulation Setup

1770
 1771 As detailed in Part 1 (Section 3.1), the soil carbon stock used by our model was
 1772 reconstituted from the soil carbon spinup of an ORCHIDEE-MICT run from Guimberteau
 1773 et al. (2018)(Guimberteau et al., 2018) and run to quasi-steady state equilibrium for the
 1774 Active and Slow carbon pools (Supplement, Fig. S1) under the new soil carbon scheme
 1775 used in the model configuration of the present study (Fig. 1). After some adjustment
 1776 runs to account for different data read/write norms between ORCHIDEE-MICT and this
 1777 model version, the model was then run in transient mode under historical climate, land
 1778 cover and atmospheric CO₂ concentrations. A summary of the step-wise procedure for
 1779 simulation setup described above is detailed graphically in Fig. 1. The model was forced
 1780 with and run over the climate, CO₂ and vegetation input forcing data for the period
 1781 spanning 1901-2007 (Supplement, Table S1).
 1782
 1783

1784 **Table 1:** Summary describing of the factorial simulations undertaken to examine the relative drivers of
 1785 lateral fluxes in our model.
 1786

Simulation Name	Abbreviation	Historical Input Data	Input* Held Constant
Control	CTRL	Climate, CO ₂ , Vegetation	None
Constant Climate	CLIM	CO ₂ , Vegetation	Climate
Constant CO ₂	CO ₂	Climate, Vegetation	CO ₂ (Pre-industrial)

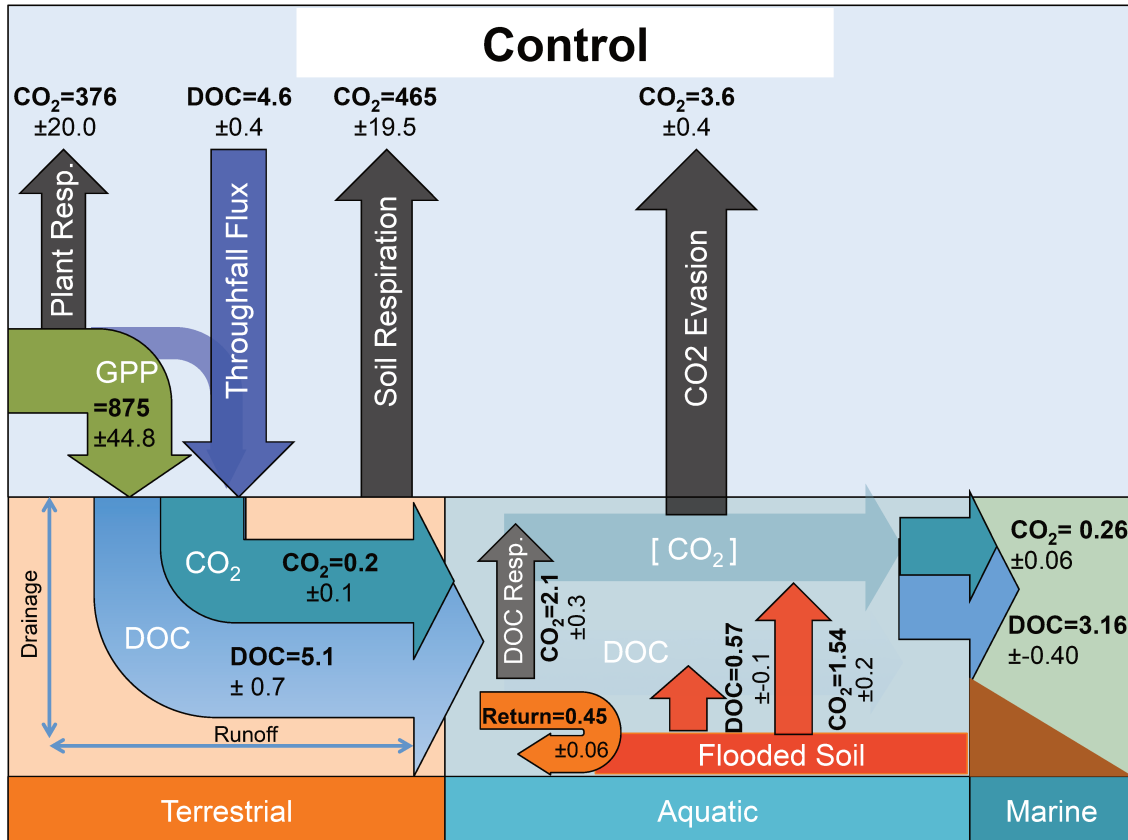
*Historically-variable input

1787
 1788
 1789 In order to derive an understanding of the environmental drivers of carbon cycling in
 1790 the Lena watershed and analyze the model sensitivity to the corresponding forcing
 1791 data, alternative simulations were run with constant climate and CO₂ conditions (Table
 1792 1, and Supplement Table S1). Thus a factorial simulation was devised, consisting of 2
 1793 factors and 3 simulations whose inputs were otherwise identical but for the investigated
 1794 factor (Table 1).
 1795
 1796

1797 **4 Results and Discussion**

1798
 1799 We refer to different simulations performed in this study according to the sensitivity
 1800 factors to which they are subjected. The 'Control' (CTRL) simulation is that for which
 1801 transient climate and atmospheric CO₂ forcings are used. CLIM and CO₂ are those
 1802 simulations for which climate variability and atmospheric CO₂ were held constant at
 1803 their pre-industrial levels, respectively (Table 1). The following evaluation sections
 1804 compare observations solely against the CTRL. The subsequent section will evaluate this
 1805 comparison against the factorial simulations described above.
 1806

1807 The overall carbon budgets and their fluxes as generated by each of the simulations are
 1808 shown in Figs. 2 and 11 and discussed in detail at the end of the evaluation. Below, we
 1809 examine that budget's component parts, in the following sequential order: In section 4.1
 1810 we briefly look through the overall carbon budget of the entire basin, discussing
 1811 component fluxes of the budget, their values and what they mean. Section 4.2 evaluates
 1812 DOC discharge, followed by DOC concentrations in export (4.3), dissolved CO₂ transport
 1813 in rivers and its evasion from the river surface (4.4), emergent phenomena with respect
 1814 to CO₂ evasion compared to river size (4.5.1) and DOC concentrations and slope (4.5.2),
 1815 followed by DOC reactivity pools (4.6) and NPP and soil respiration (4.7). Wherever
 1816 possible, model output are compared with available in situ observations, while
 1817 emergent relationships between fluxes or concentrations and environmental controls
 1818 found in observations are also drawn from the model output, to provide a 'process
 1819 oriented' evaluation of the model. In Section 4.8 we discuss the overall drivers of the
 1820 fluxes simulated by our model with respect to the two CLIM and CO₂ factorial
 1821 simulations and the implications of these for the future.
 1822

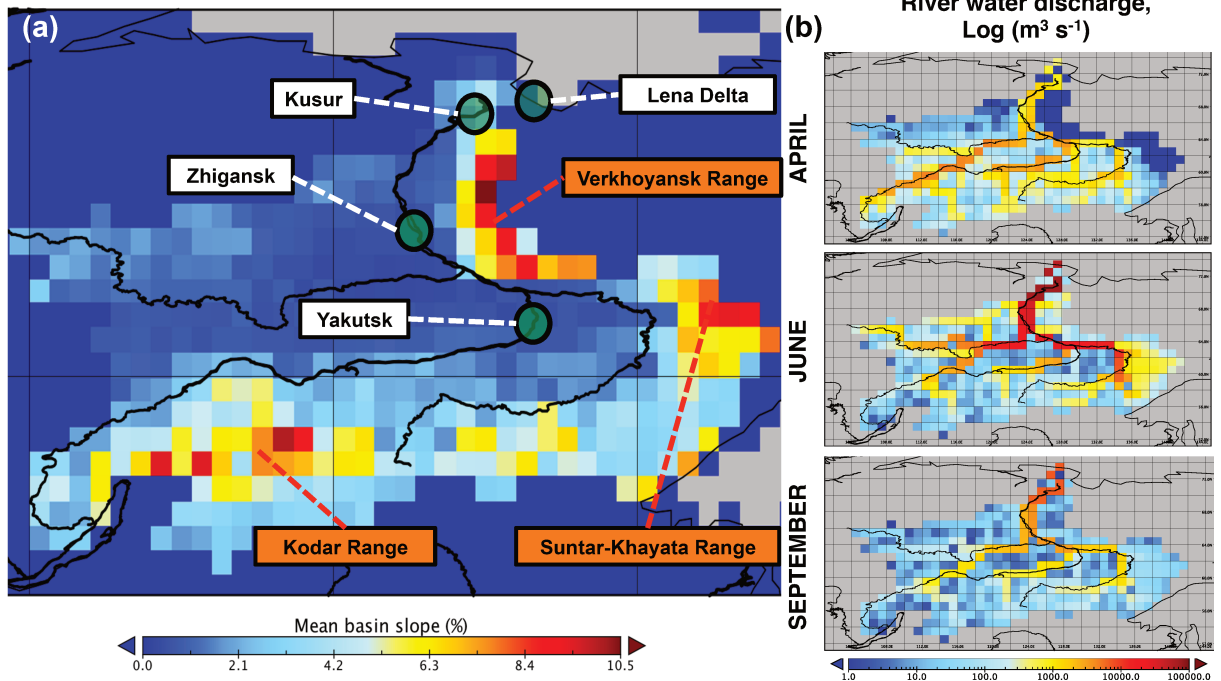


1823
1824
1825
1826
1827
1828
1829
1830
1831
1832
1833
1834
1835
1836
1837
1838
1839
1840
1841
1842
1843

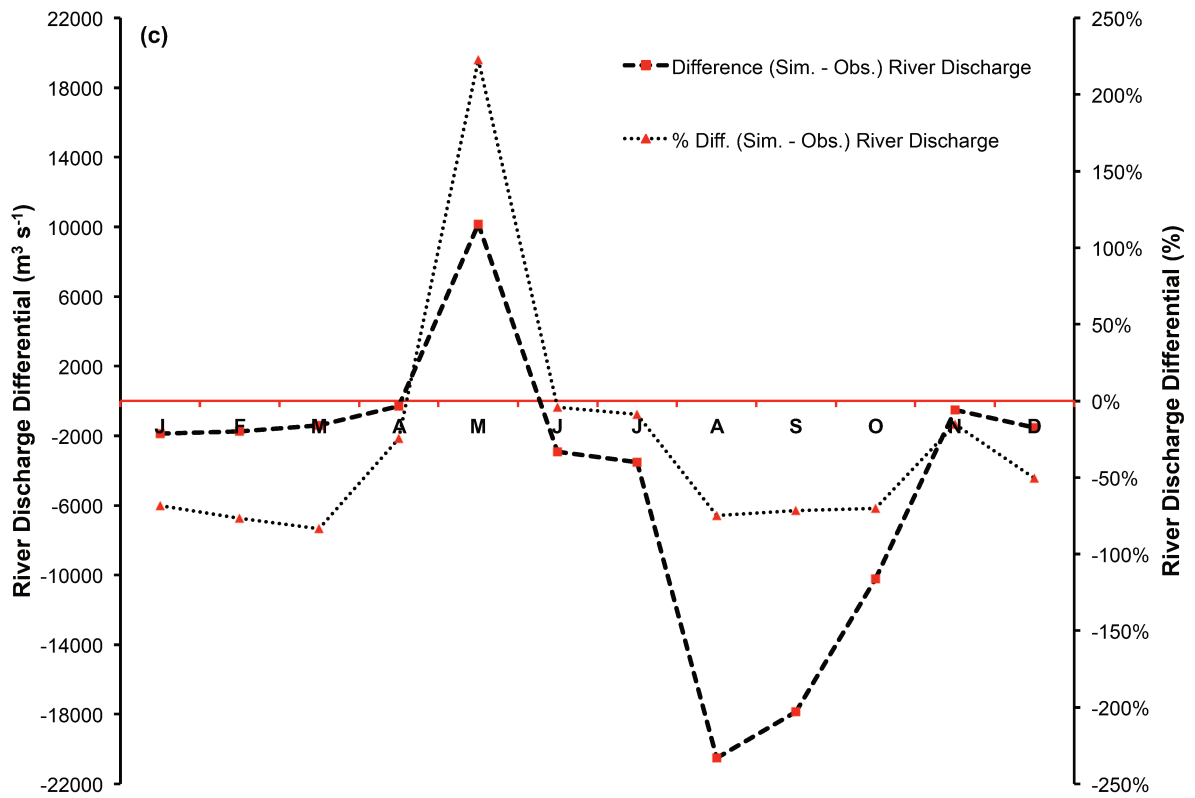
Figure 2: Schematic diagrams detailing the major yearly carbon flux outputs (TgC yr⁻¹) from the Control simulation averaged over the period 1998-2007 as they are transformed and transported across the land-aquatic continuum.

4.1 Carbon Budget: Simulated yearly fluxes

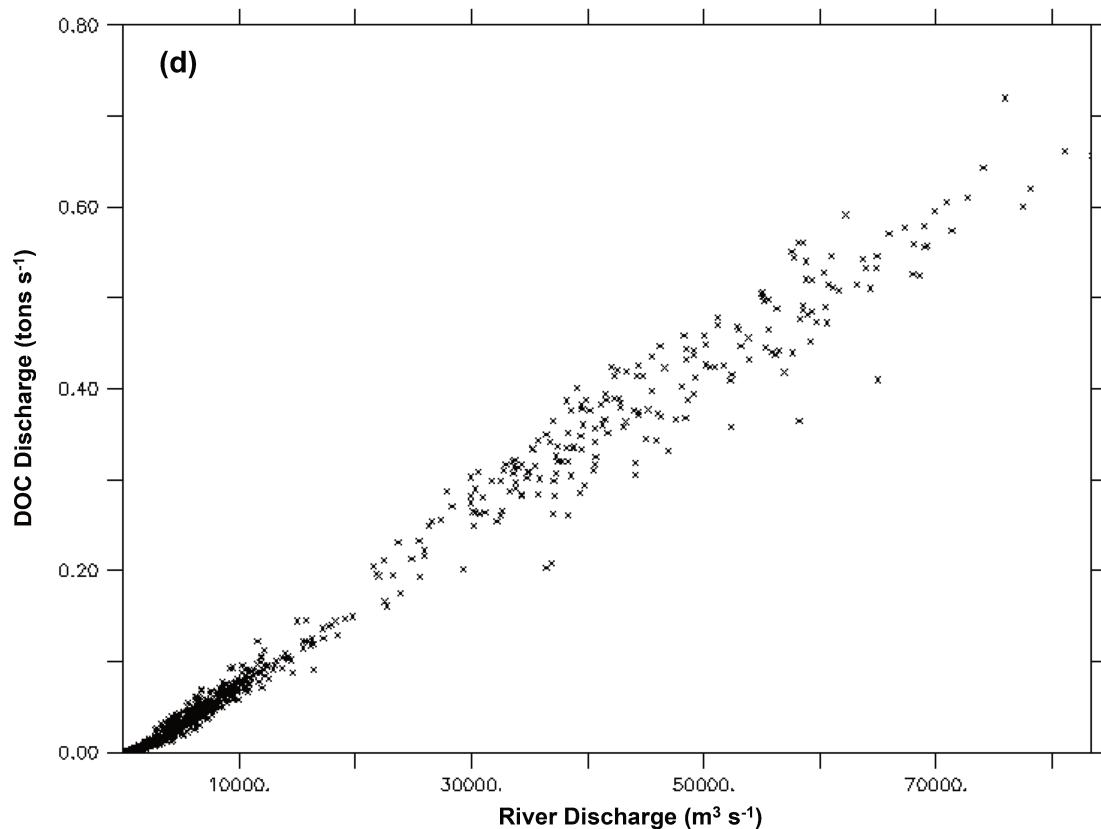
Fig. 2 summarises the components of the carbon cycle across the Lena basin, averaged over the decade 1998-2007. All units are in TgC yr⁻¹ and the errors are derived from average yearly standard deviations for each of these fluxes. Modelled carbon inputs to terrestrial ecosystems are dominated by photosynthetic input (GPP). GPP assimilates (875 TgC yr⁻¹) are either used as metabolic substrate by plants and lost as CO₂ by plant respiration processes (376 TgC yr⁻¹) or soil respiration processes (465 TgC yr⁻¹), leaving behind annual terrestrial carbon storage in living biomass and soil, known as net biome productivity (NBP, a sink of atmospheric CO₂ of 34 TgC yr⁻¹). Further carbon inputs are delivered to the terrestrial surface via a combination of atmospheric deposition, rainwater dissolved carbon, and the leaching of canopy carbon compounds, all of which summing up to a flux transported to the soil surface (4.6 TgC yr⁻¹) by throughfall (see Part 1, Section 2.5).



1844
1845
1846



1847
1848



1849
 1850 **Figure 3:** Map of the Lena (a) with the scale bar showing the mean grid cell topographic slope from the
 1851 simulation, and the black line the satellite-derived overlay of the river main stem and sub-basins.
 1852 Mountain ranges of the Lena basin are shown in orange. Green circles denote the outflow gridcell (Kusur)
 1853 from which our simulation outflow data are derived, as well as the Zhigansk site, from which out
 1854 evaluation against data from Raymond et al. (2007) are assessed. The regional capital (Yakutsk) is also
 1855 included for geographic reference. (b) Maps of river water discharge ($\log(\text{m}^3 \text{s}^{-1})$) in April, June and
 1856 September, averaged over 1998-2007. (c) The mean monthly river discharge differential between
 1857 observed discharge for the Lena (Ye et al., 2009) and simulated discharge averaged over 1998-2007, in
 1858 absolute ($\text{m}^3 \text{s}^{-1}$) and percentage terms. (d) Regression of simulated monthly DOC discharge versus
 1859 simulated river discharge at the river mouth (Kusur) over the entire simulation period (1901-2007).

1860
 1861
 1862 In the soil, DOC is produced by the decomposition of litter and soil organic carbon (SOC)
 1863 pools (see Part 1, Section 2.4 and Fig. 2) and can be ad- or de- sorbed to solid particles
 1864 (see Part 1, Section 2.11), while there is a continuous exchange of DOC with (solid) soil
 1865 organic carbon. The interplay between decomposition and sorption leads to DOC
 1866 concentration changes in the soil solution. DOC in the soil solution as well as a fraction of
 1867 dissolved CO_2 produced in the root zone from root and microbial respiration is exported
 1868 to rivers along the model's two hydrological export vectors, surface runoff and deep
 1869 drainage (Part 1, Section 2.6). For the Lena basin simulations, these fluxes of C exported
 1870 from soils amount to 5.1 and 0.2 TgC yr^{-1} , for DOC and CO_2 respectively. Three water
 1871 pools, representing streams, rivers and groundwater and each containing dissolved CO_2
 1872 and well as DOC of different reactivity, are routed through the landscape and between
 1873 grid cells following the river network in the catchment (Part 1, Section 2.7). In addition,
 1874 seasonally flooded soils located in low, flat grid cells next to the river network (see Part
 1875 1, Section 2.8) export DOC (0.57 TgC yr^{-1}) and CO_2 (1.54 TgC yr^{-1}) to the river network
 1876 when their inundation occurs. Part of this leached inundated material is reinfiltated

1877 back into the soil from the water column during floodplain recession ('Return' flux, 0.45
1878 TgC yr⁻¹). During its transport through inland waters, DOC can be decomposed into CO₂
1879 (2.1 TgC yr⁻¹) and a fraction of river CO₂ produced from DOC and transferred from soil
1880 escapes to the atmosphere (3.6TgC yr⁻¹) through gas exchange kinetics (Part 1, Section
1881 2.10). This flux is termed 'CO₂ evasion' in Fig. 2 of this study. Carbon that 'survives' the
1882 inland water reactor is exported to the coastal ocean in the form of DOC (3.16 TgC yr⁻¹)
1883 and CO₂ (0.26 TgC yr⁻¹). These fluxes and their interpretation within the context of the
1884 Land-Ocean-Aquatic Continuum (LOAC) are returned to in Section 4.8 of this study.
1885

1886 **4.2 Discharge and DOC flux to the ocean**

1887

1888 Simulated river water discharge captures the key feature of Arctic river discharge – that
1889 of a massive increase in flow to ~80,000 m³s⁻¹ in April-June caused by melting snow and
1890 ice, otherwise known as ice-out or spring freshet, but underestimates observed river
1891 discharge in August to October by around 70% which is in the range of ~15,000-28,000
1892 m³s⁻¹ (Figs. 3c, 4b). Given that DOC fluxes are almost directly proportional to river
1893 discharge in the Lena basin (Fig. 3d), this sub-optimal performance with regard to
1894 hydrology during August to October seeming to be the main cause of a substantial
1895 underestimation in simulated bulk DOC outflow. Another cause may simply be the lack
1896 of peat representation in the model, for which DOC flux concentrations in outflowing
1897 fluvial water can be very high (e.g. Frey et al., 2005; 2009: see Section 4.5.1).
1898

1899 In addition, the mean spring (June) discharge peak flows are slightly underestimated or
1900 out of phase in simulations (Figs. 3c, 4b) compared to observations (Ye et al., 2009): this
1901 is caused by a large amount of water throughput being simulated in May (~10,000 m³ s⁻¹)
1902 in excess of observed rates. Finally, during the winter low-flow period, it seems that
1903 the model consistently under-estimates water flow-through volumes reaching the river
1904 main stem (see Fig. 3c, winter months). Although this underestimate is not severe
1905 relative to annual bulk flows, the divergence is large as a percentage of observations
1906 (see right-hand axis, Fig. 3c), and may point to an issue in how ice is represented in the
1907 model, such as the fact that solid ice inclusions in the soil column are not represented, or
1908 the possibility that much slower groundwater dynamics than those represented in the
1909 model are feeding discharge.
1910

1911 In addition to this, the presence of a dam on the Vilui tributary of the Lena has been
1912 shown to reduce main stem winter low-flow rates by up to 90% (Ye et al., 2003), similar
1913 to the discrepancy of our low-flow rates: given that our model only simulates 'natural'
1914 hydrological flows and thus does not include dams, we expect that this effect is also at
1915 play. Evaluating these considerations, if presently possible, remains beyond the scope of
1916 this paper. We note that discharge simulations with ORCHIDEE MICT (Fig. 12 of
1917 Guimberteau et al. (2018)(Guimberteau et al., 2018)) performed with the same climate
1918 forcing over the basin are comparable with those from ORCHIDEE MICT-L, with similar
1919 overall seasonality and discharge peaks of ~60,000m³ s⁻¹ in the former over the period
1920 1981-2007. This indicates that the modifications made in Bowring et al. (Part 1)
1921 focussing on the DOC cycle did not degrade the hydrological performance of the model
1922 in this regard.
1923

1924 Our CTRL simulation shows that the yearly sum of DOC output to the Arctic Ocean has

1925 increased steadily over course of the 20th Century, from ~1.4Tg DOC-C yr⁻¹ in 1901 to
1926 ~4Tg DOC-C yr⁻¹ in 2007 (Fig. 4a). Smoothing the DOC discharge over a 30-year
1927 running mean shows that the increasing trend (Fig. 4a) over this averaging scale is
1928 almost linear, at ~0.11TgC per decade, or a net increase of 40% using this averaging
1929 scale. Empirically based estimates of total contemporary DOC entering the Laptev Sea
1930 from Lena river discharge vary around ~2.5-5.8 TgC-DOC (Cauwet and Sidorov, 1996;
1931 Dolman et al., 2012; Holmes et al., 2012; Lara et al., 1998; Raymond et al., 2007;
1932 Semiletov et al., 2011).

1933
1934 The red bar in Fig. 4a shows the average simulated DOC discharge of the last decade
1935 (1998-2007) of 3.2 TgC yr⁻¹, to be compared with estimates of 3.6 TgC yr⁻¹ (black bar)
1936 from Lara et al. (1998)(Lara et al., 1998) and 5.8 TgC yr⁻¹ (orange bar) from Raymond et
1937 al. (2007) and 5.7 TgC yr⁻¹ from Holmes et al. (2012). These estimates are based on
1938 different years, different data and different scaling approaches, whose veracity or
1939 accuracy are beyond the scope of this study to address or assess.

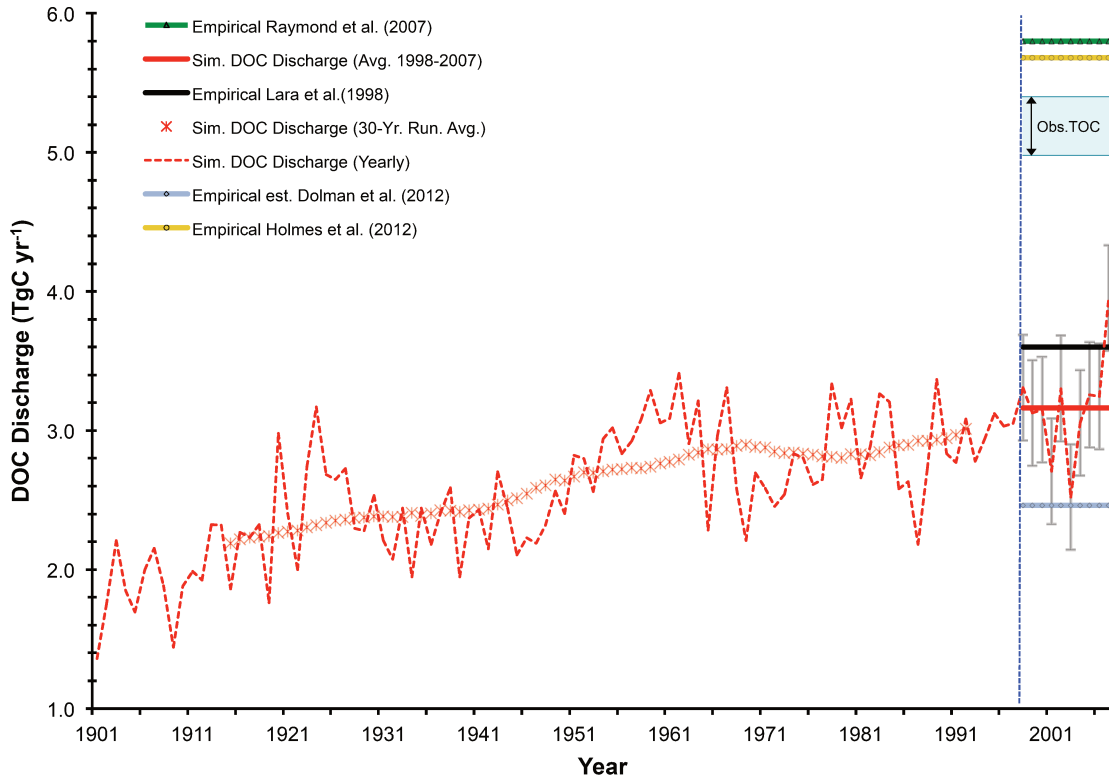
1940
1941 Nonetheless, the most recent and elaborate of those estimates is that of Holmes et al.
1942 (2012) who used a rating curve approach based on 17 samples collected from 2003 to
1943 2006 and covering the full seasonal cycle, which was then applied to 10 years of daily
1944 discharge data (1999-2008) for extrapolation. Given that their estimate is also based on
1945 Arctic-GRO-1/PARTNERS data (<https://www.arcticgreatrivers.org/data>), which stands
1946 as the highest temporal resolution dataset to date, we presume that their estimate can
1947 be taken to be the most accurate of the actual riverine discharge of DOC from the Lena
1948 basin. Compared to their average annual estimate of 5.7 Tg C yr⁻¹ then, our simulated
1949 DOC export is somewhat low, which can be due to multiple causes:

1950
1951 Firstly, as noted above, the model underestimates observed river discharge. We plot
1952 seasonal DOC discharge against river discharge for the Lena outflow grid cell (Kusur
1953 station –see Fig. 3a) over 1901-2007 in Fig. 3d, which shows a quasi-linear positive
1954 relationship between the two. This dependence is particular to the Arctic rivers, in
1955 which the DOC yield of rivers experiences disproportionately large increases in output
1956 with increases in discharge yield (Fig. 4, Raymond et al., 2007), relative to the same
1957 relationship in e.g. temperate rivers like the Mississippi (Fig. 3, Raymond et al., 2007),
1958 owing largely to the ‘flushing’ out of terrestrially fixed carbon from the previous year’s
1959 production by the massive runoff generated by ice and snow melt during the spring
1960 thaw.

1961
1962 Average river discharge almost doubled between the first and last decades of our
1963 simulation (Fig 4b), giving further credence to the relationship between DOC and water
1964 discharge. Comparing simulated annual mean discharge rate (m³ s⁻¹) with long-term
1965 observations(Ye et al., 2003) over years 1940-2000 (Fig. 4c) shows that though absolute
1966 discharge rates are underestimated by simulations, their interannual variation
1967 reasonably tracks the direction and magnitude of observations. Linear regressions
1968 through each trend yield very similar yearly increases of 29 vs 38 m³ s⁻¹ yr⁻¹ for
1969 simulations and observations, respectively, while the mean annual water discharge
1970 differential hovers at 30% (Fig. 4c), a fraction similar to that of the simulated and
1971 observed(Holmes et al., 2012; Raymond et al., 2007) bulk annual DOC discharge
1972 discrepancy (Fig. 4a). Figure 4b plots discharge over the first (1901-1910) and last

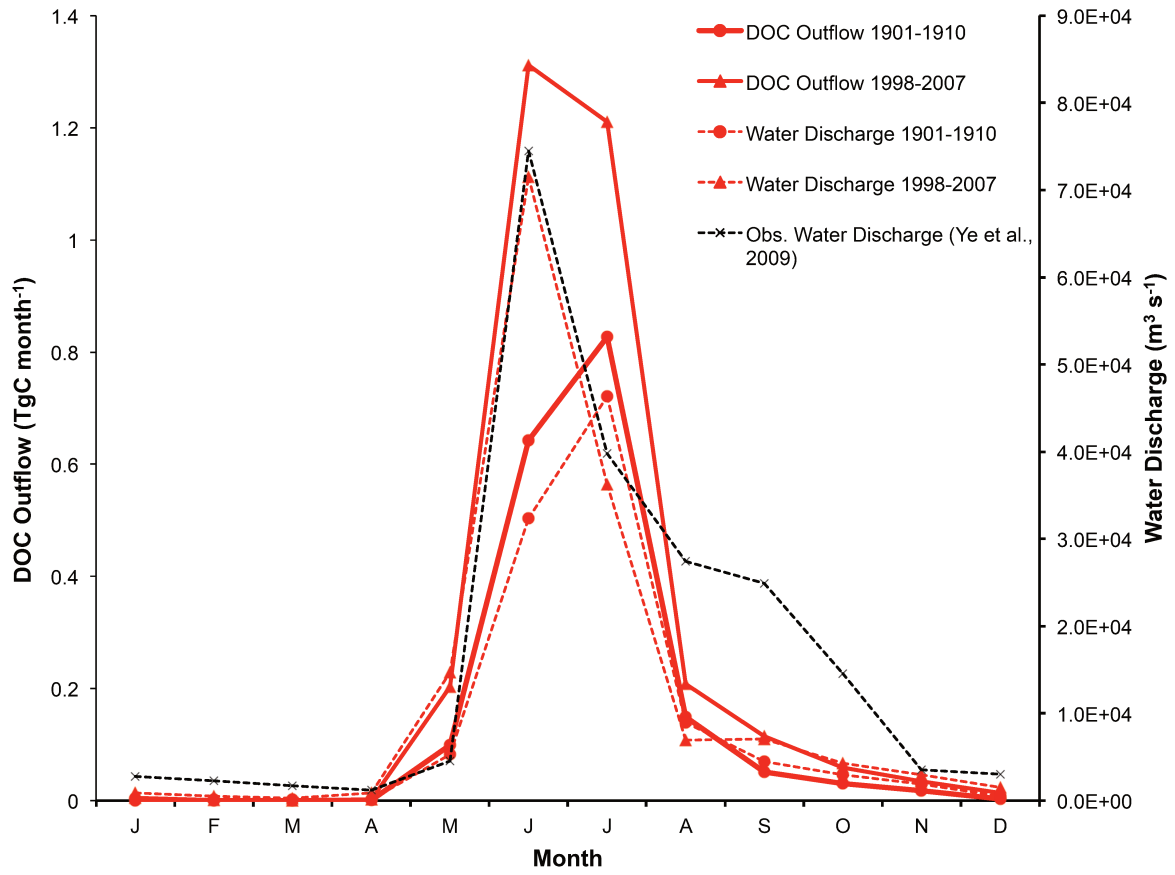
1973 (1998-2007) decades of simulated monthly DOC and river discharge with observed
 1974 river discharge. The bulk of the DOC outflow occurs during the spring freshet or
 1975 snow/ice-melting period of increased discharge, accounting for ~50-70% of the year's
 1976 total Lena outflow to the Arctic (Lammers et al., 2001; Ye et al., 2009), with peak river
 1977 discharge rates in June of ~80,000 m³ s⁻¹. DOC concentrations increase immensely at this
 1978 time, as meltwater flushes out DOC accumulated from the previous year's litter and SOC
 1979 generation (Kutscher et al., 2017; Raymond et al., 2007).
 1980
 1981

(a)



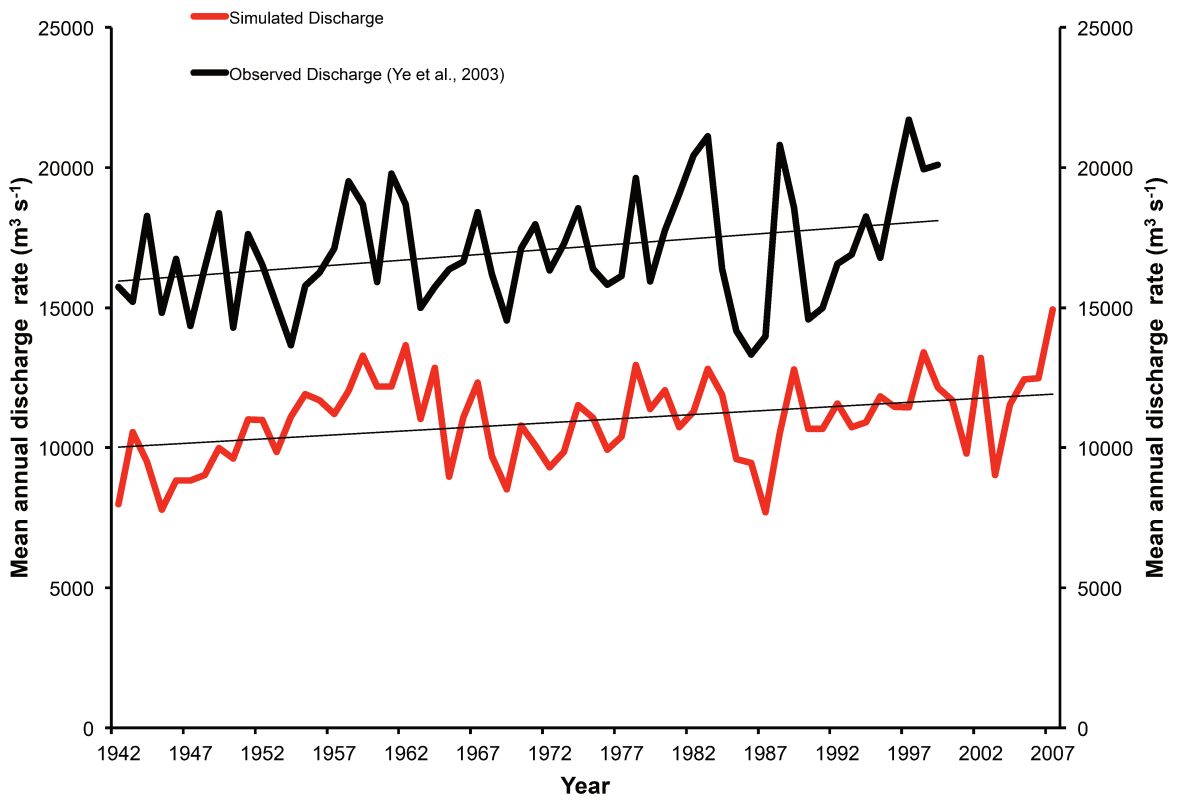
1982
 1983

(b)



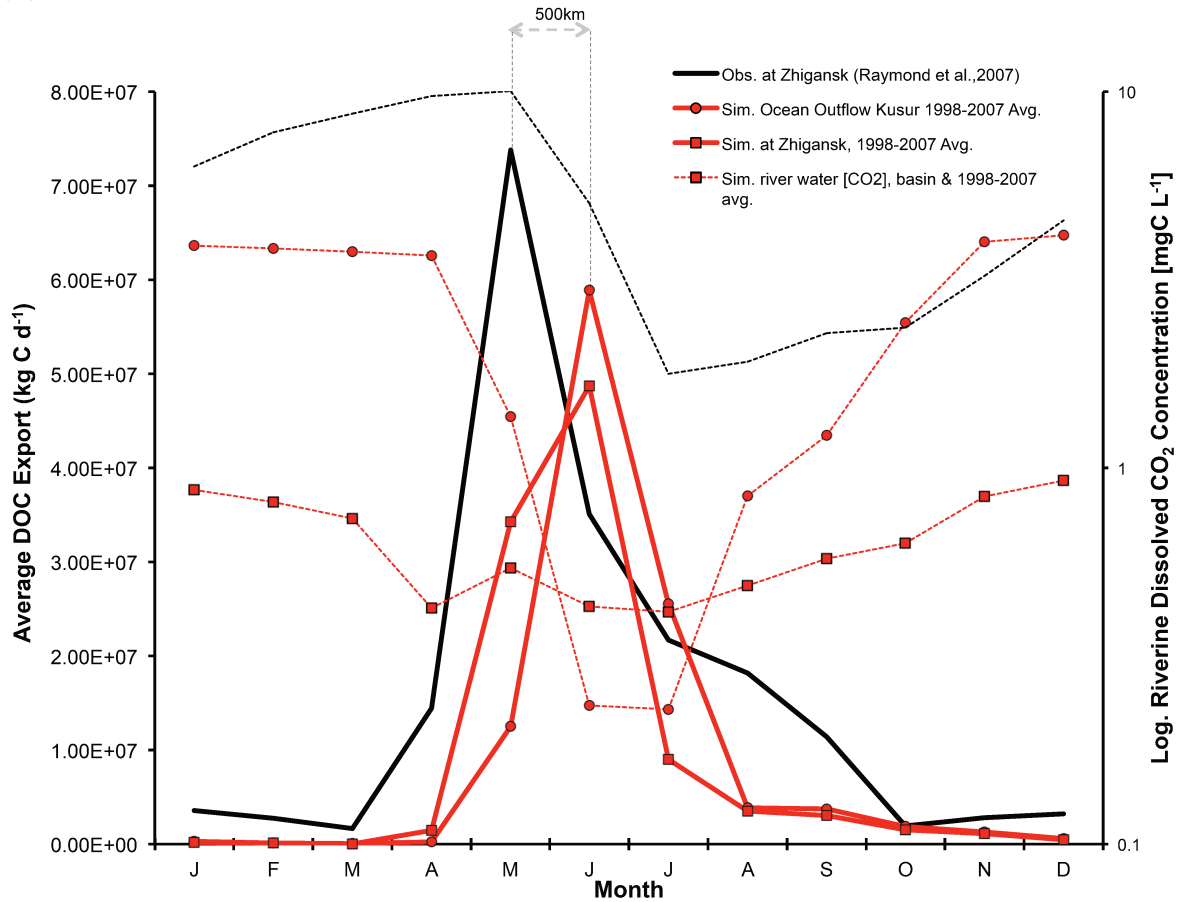
1984
1985

(c)



1986

1987 (d)



1988
1989
1990
1991
1992
1993
1994
1995
1996
1997
1998
1999
2000
2001
2002
2003
2004
2005
2006
2007
2008
2009
2010
2011
2012
2013
2014

Figure 4: (a) Yearly DOC discharged from the Lena river into the Laptev sea is shown here in tC yr^{-1} , over the entire simulation period (dashed red line), with the smoothed, 30-year running mean shown in asterisk. Observation based estimates for DOC discharge from Lara et al. (1998), Raymond et al. (2007), Dolman et al. (2012) and Holmes et al. (2012) are shown by the horizontal black, green triangle, blue diamond and yellow circle line colours and symbols, respectively, and are to be compared against the simulated mean over the last decade of simulation (1998-2007, horizontal red line), with error bars added in grey displaying the standard deviation of simulated values over that period. The range of estimates for total organic carbon discharged as shown in Lara et al. (1998) are shown by the blue bounded region, where TOC here refers to DOC+POC. (b) Average monthly DOC discharge (solid red, tC month^{-1}) and water discharge (dashed red, $\text{m}^3 \text{s}^{-1}$) to the Laptev Sea over the period averaged for 1901-1910 (circles) and 1997-2007 (squares) are compared, with modern maxima closely tracking observed values. Observed water discharge over 1936-2000 from R-ArcticNet v.4 (Lammers et al., 2001) and published in Ye et al. (2009) are shown by the dashed black line. (c) (d) Observed (black) and simulated (red) seasonal DOC fluxes (solid lines) and CO_2 discharge concentrations (dashed lines). Observed DOC discharge as published in Raymond et al. (2007) from 2004-2005 observations at Zhigansk, a site $\sim 500\text{km}$ upstream of the Lena delta. This is plotted against simulated discharge for: (i) the Lena delta at Kusur (red circles) and (ii) the approximate grid pixel corresponding to the Zhigansk site (red squares) averaged over 1998-2008. Observed CO_2 discharge from a downstream site (Cauwet & Sidorov, 1996; dashed black), and simulated from the outflow site (dashed circle) and the basin average (dashed square) are shown on the log-scale right-hand axis for 1998-2008.

This is reproduced in our simulations given that DOC discharge peak occurs at the onset of the growing season, meaning that outflow DOC is generated from a temporally prior stock of organic carbon. Simulation of the hydrological dynamic is presented in maps of

2015 river discharge through the basin in Fig. 3b, which show low-flows in April with
2016 substantial hydrographic flow from upstream mountainous headwaters and Lake Baikal
2017 inflow in the south, peak flow in June with substantial headwater input in the northern
2018 portion and a moderate flow through the mainstem with little headwater input in
2019 September.

2020
2021 In Fig. 4b we observe that (i) DOC discharge fluxes closely track hydrological fluxes
2022 (solid versus dashed lines); (ii) the simulated modern river discharge peak is very close
2023 to the historical observed discharge peak, however it slightly overestimates spring
2024 fluxes and substantially underestimates fluxes in the Autumn (dashed red versus black
2025 lines). Thus the discrepancy between simulated bulk DOC discharge fluxes and
2026 empirical estimates may largely be found in the simulated hydrology. (iii) The curve
2027 shape of discharge fluxes differs greatly between the first and last decades of simulation.

2028
2029 The difference between the first and last decades of the simulation in Fig. 4b is mostly
2030 attributable to a large increase in the DOC flux mobilised by spring freshet waters that
2031 culminate in the early summer outflow of DOC to the ocean, which generate the peaks in
2032 DOC flux. This suggests both greater peaks in simulated DOC flux and a shift to earlier
2033 peak timing, owing to an increase in river discharge indicative of an earlier spring and a
2034 progressively warmer environment. (iv) The maximum modeled modern monthly DOC
2035 flux rate of $\sim 1.3 \text{ TgC month}^{-1}$ (Fig. 4b, solid red line) is comparable to the mean
2036 maximum DOC flux rate measured in a recent study, which showed that the aggregate
2037 carbon discharge flux of the Lena River over its 2-month peak period in 2013 was 3.5
2038 TgC, giving a mean flux of $1.75 \text{ TgC month}^{-1}$ (Kutscher et al., 2017, Fig. 2(Kutscher et al.,
2039 2017)).

2040
2041 The monthly pattern of DOC discharge approximates the seasonal pattern found in an
2042 empirical Pan-Arctic DOC discharge study by Raymond et al. (2007), which they take to
2043 represent total Lena river DOC discharge. The latter study, which looks at Pan-Arctic
2044 DOC discharge rates, finding them to be 15-20% higher than in prior estimates, gives
2045 discharge maxima in May, whereas our simulated maxima are in June. We compare the
2046 Raymond et al. (2007) modern DOC outflow (Fig. 4d, solid black line) from the Lena
2047 river at Zhigansk (Raymond et al., 2007) against simulated DOC outflow from the
2048 Zhigansk site as well as from the river outflow site (Kusur) 500km downstream (Fig. 4d,
2049 solid blue and solid red lines, respectively).

2050
2051 Simulated DOC flux is underestimated for both sites. Peakflow at Zhigansk seems to be
2052 attenuated over May and June in simulations, as opposed to May peakflow in
2053 observations, while peakflow at Kusur is definitively in June. This suggests that
2054 simulated outflow timing at Zhigansk may slightly delayed, causing a split in peak
2055 discharge when averaged in the model output. Thus the aggregation of model output to
2056 monthly averages from calculated daily and 30 minute timesteps can result in the
2057 artificial imposition of a normative temporal boundary (i.e. month) on a continuous
2058 series. This may cause the less distinctive 'sharp' peak seen in Fig. 4d (solid blue), which
2059 is instead simulated at the downstream Kusur site, whose distance some 500km away
2060 from Zhigansk more clearly explains the delay difference in seasonality.

2061

2062 We further evaluate our DOC discharge at the sub-basin scale, to see if the simulated
2063 aggregate flux exiting the Lena river mouth is composed of a coarsely realistic
2064 breakdown of source matter geography. In other words, whether the fractional
2065 contribution of different DOC flows from rivers draining the simulated Lena basin
2066 correspond to those in the observed basin. This comparison is depicted in Fig. 5, where,
2067 again using data from Kutscher et al., (2017)(Kutscher et al., 2017), the observed and
2068 simulated percentage DOC contributions of the Aldan, Vilui, and Upper and Lower Lena
2069 sub-basins to total flux rates are 19 (24)%, 20(10%), 33 (38%) and 30 (28)% in
2070 simulations (observations) for the four basins, respectively.

2071
2072 While deviations between simulation and observation can be expected given the
2073 difference in magnitude and timing of DOC discharge previously discussed, in addition
2074 to interannual variability, the nearly twofold value mismatch of the Vilui basin likely has
2075 its roots in the fact in its real-world damming, not represented here. On the other hand,
2076 we cannot explain the ~5% discrepancies in other sub-basin fluxes, particularly for the
2077 Aldan.

2078
2079 Of the shortcomings in our model with respect to observations, year-on-year variations
2080 over the decade 1998-2007 may be of significance, given that the Holmes et al. (2012)
2081 and Raymond et al. (2007) DOC discharge values are significantly higher than total
2082 organic carbon (DOC+POC) outflow estimates ($\sim 5.0\text{-}5.4 \text{ TgC yr}^{-1}$, Fig. 4a blue boundary)
2083 as presented in Lara et al. (1998)(Lara et al., 1998). To this we can add scale-related
2084 inaccuracies in the routing protocol that can lead to small geographic inconsistencies in
2085 simulated versus observed phenomena, as well as the exclusion of explicit peatland
2086 formation and related dynamics in this model, which is the subject of further model
2087 developments within the ORCHIDEE-MICT envelope(Qiu et al., 2018) that have yet to be
2088 included in this iteration. With peatlands thought to cover ~17% of the Arctic land
2089 surface (Tarnocai et al., 2009), and with substantially higher leaching concentrations,
2090 this may be a significant omission from our model's representation of high latitude DOC
2091 dynamics.

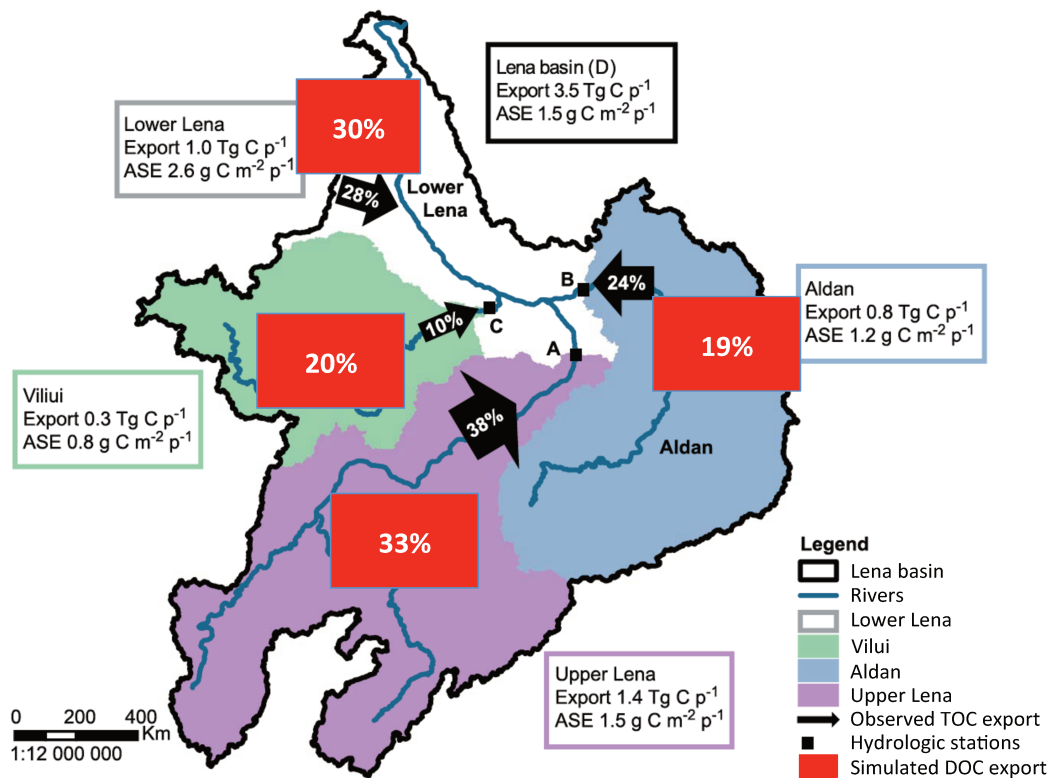


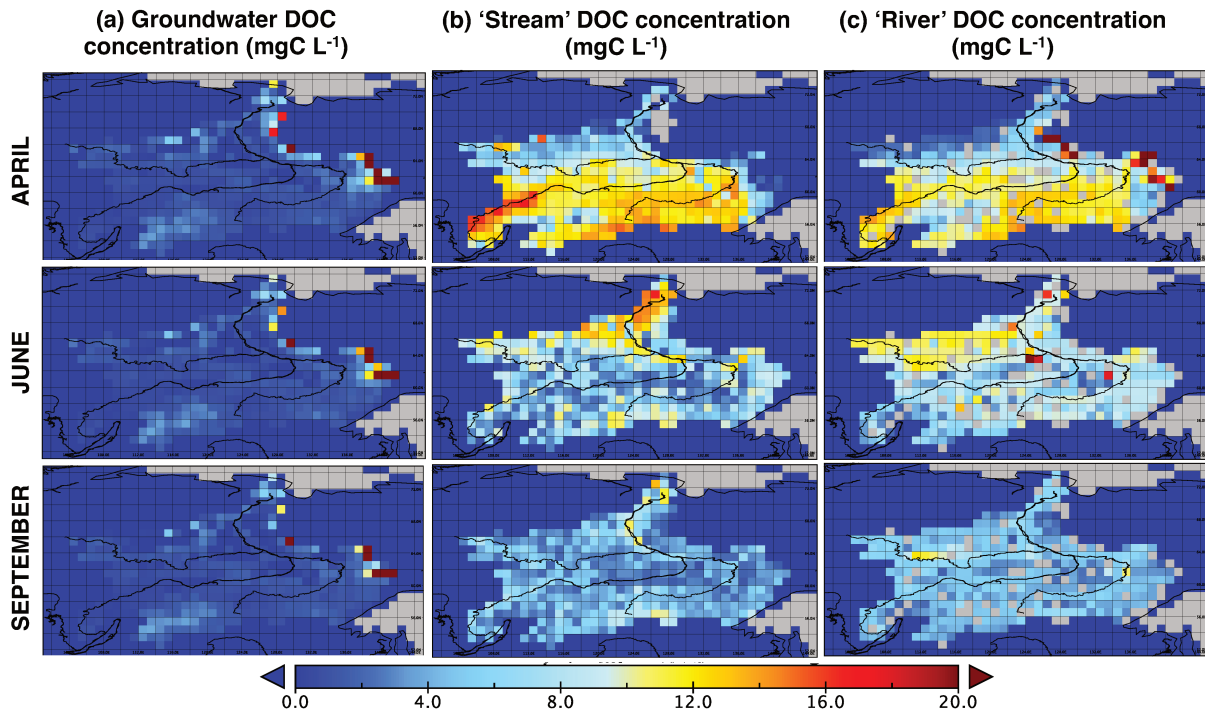
Figure 5: Map adapted from Fig. 2 in Kutscher et al. (2017) showing proportional sub-basin contributions of TOC outflow to total TOC discharge in 2012-2013 as observed in Kutscher et al., 2017 (black arrows), and DOC export contributions as simulated over the period 1998-2007 by ORCHIDEE MICT-L (red boxes). Simulation pixels used in the calculation are correlates of the real-world sampling locations unless the site coordinates deviated from a mainstem hydrographic flowpath pixel –in which case a nearest ‘next-best’ pixel was used. Here the percentages are out of the summed mean bulk DOC flow of each tributary, not the mean DOC discharge from the river mouth, because doing so would negate the in-stream loss of DOC via degradation to CO₂ while in-stream.

4.3 DOC Concentrations in lateral transport

The range of simulated riverine DOC concentrations approximates those found in the literature for the Lena and other Eurasian high-latitude river basins (e.g. Arctic-GRO 1 (<https://www.arcticgreatrivers.org/data>); and refs.(Denfeld et al., 2013; Mann et al., 2015; Raymond et al., 2007; Semiletov et al., 2011)). In those for the Lena, observed average DOC concentrations hover at ~10mgC L⁻¹. Likewise, simulated DOC concentrations mostly lie in the range of 0-10 mgC L⁻¹, with monthly grid cell maxima of 1-200 mgC L⁻¹, and on flow-weighted average exhibit the observed seasonal range and amplitude. Figure 6 summarises some of this simulated output, showing maps of mean monthly DOC concentration for stream water, river water and groundwater (Fig. 6a,b,c, respectively) in April, June and September –the beginning, middle and end of the non-frozen period in the basin, respectively, over 1998-2007.

For both the stream and river water reservoirs, DOC concentrations appear to have spatio-temporal gradients correlated with the flux of water over the basin during the thaw period, with high concentrations of 10-15 mgC L⁻¹ as the snow and ice melts in April in the upstream portions of the basin, these high concentrations moving

2121 northward to the coldest downstream regions of the basin in June. Lower DOC
 2122 concentrations of $\sim 5 \text{ mgC L}^{-1}$ dominate the basin in September when the bulk of
 2123 simulated lateral flux of DOC has dissipated into the Laptev Sea, bearing in mind that we
 2124 underestimate the river discharge flux in the Autumn. In contrast, groundwater DOC
 2125 concentrations are generally stable with time, although some pixels appear to
 2126 experience some 'recharge' in their concentrations during the first two of the three
 2127 displayed thaw months. Significantly, highest groundwater DOC concentrations of up to
 2128 20 mgC L^{-1} are focussed on the highest elevation areas of the Lena basin on its Eastern
 2129 boundary, which are characterized by a dominance of Podzols (SI, Fig. 2b).



2130
 2131
 2132 **Figure 6:** Maps of (a) DOC concentrations (mgC L⁻¹) in groundwater ('slow' water pool),
 2133 (b) stream water pool, (c) river water pool in April, June and September (first to third
 2134 rows, respectively), averaged over the period 1998-2007. The coastal boundary and a
 2135 water body overlay have been applied to the graphic in black, and the same scale applies
 2136 to all diagrams.

2137
 2138
 2139 **Table 2:** Mean observed groundwater CO₂ and DOC concentrations for global permafrost regions
 2140 subdivided by biogeographic province and compiled by Shvartsev (2008) from over 9000 observations.
 2141

	Permafrost Groundwater Provinces			Average	Average (-Swamp)
	Swamp	Tundra	Taiga		
CO ₂ (mgC L ⁻¹)	12.3	14	10.8	12.4	12.4
DOC (mgC L ⁻¹)	17.6	10.1	9.3	12.3	9.7

2142
 2143
 2144 This region, the Verkhoyansk range, is clearly visible as the high groundwater DOC
 2145 concentration ($2\text{-}20 \text{ mgC L}^{-1}$) arc (in red) in Fig. 6a, as well as other high elevation areas

2146 in the south-western portion of the basin (see Fig. 3a for the basin grid cell mean
2147 topographic slope), while the central basin of very low mean topographic slope exhibits
2148 much smaller groundwater DOC concentrations ($0\text{-}2\text{mgC L}^{-1}$). The range of simulated
2149 groundwater DOC concentration comes close to those aggregated from the empirical
2150 literature by Shvartsev (2008)(Shvartsev, 2008) in his seminal review of global
2151 groundwater geochemistry, which finds from >9000 observations that groundwater in
2152 permafrost regions exhibit a mean concentration of $\sim 10\text{ mgC L}^{-1}$ after peatlands and
2153 swamps (not simulated here) are removed (Table 2).

2154
2155 The high groundwater reservoir DOC concentrations simulated in high altitude regions
2156 by ORCHIDEE MICT-L is related to the fact that, in the model, DOC is rapidly produced
2157 and infiltrated deep into soil above the permafrost table, to the point that it reaches the
2158 simulated groundwater pool relatively quickly, allowing it to enter this reservoir before
2159 being metabolised through the soil column –hence allowing for the relatively high
2160 groundwater concentrations found in mountain areas. Because of the prevailing low
2161 temperatures, this DOC is not quickly decomposed by microbes and instead feed the
2162 groundwater DOC pool.

2163 2164 **4.4 In-Stream CO₂ Production, Transport, Evasion**

2165
2166 In our model, the fate of DOC once it enters the fluvial system is either to remain as DOC
2167 and be exported to the ocean, or to be degraded to dissolved CO₂ (CO_{2(aq.)}), which is
2168 itself either also transported to the marine system or outgassed from the fluvial surface
2169 to the atmosphere (see Part 1, Section 2.10). The latter two outcomes also apply to
2170 CO_{2(aq.)} produced in the soil by organic matter degradation and subsequently
2171 transported by runoff and drainage flows to the water column. As shown in Fig. 2, a
2172 large proportion of DOC (38%, 2.1 TgC yr^{-1}) that enters the water column is degraded to
2173 CO_{2(aq.)} during transport, which adds to the 1.65 TgC yr^{-1} of direct CO_{2(aq.)} input from the
2174 terrestrial land surface. Of this bulk CO₂ exported into and generated within the water
2175 column, 3.6 TgC yr^{-1} evades from the water surface to the atmosphere before reaching
2176 the river delta. In what follows, we evaluate first inputs of CO_{2(aq.)} to the water column in
2177 terms of their seasonality, before evaluating CO₂ evasion rates and the relation of this to
2178 smaller and larger water bodies (river versus stream).

2179
2180 The seasonality of riverine dissolved CO₂ concentrations (CO_{2(aq.)}, mgC L^{-1}) is evaluated
2181 in Fig. 4d to compare CO_{2(aq.)} concentrations with DOC bulk flows, since CO_{2(aq.)}
2182 concentrations follow an inverse seasonal pattern to those of DOC, being highest during
2183 the winter baseflow period and lowest in summer due to dilution during its high
2184 discharge phase (Semiletov et al., 2011). The simulated flow of CO_{2(aq.)} at Kusur (Fig. 4d,
2185 dashed red) reproduces the seasonality of observations from Cauwet and Sidorov
2186 (1996)(Cauwet and Sidorov, 1996), who sampled the Lower Lena (ship-board, several
2187 sites in river delta region (see Fig. 3a)), but somewhat underestimates concentrations,
2188 this perhaps due to the absence of peat representation in our model, in combination
2189 with underestimated hydrological discharge. Also included in Fig. 4d is the basin
2190 average for all non-zero values, whose shape also tracks that of observations. Thus the
2191 model represents on the one hand increasing hydrological flow mobilising increasing
2192 quantities and concentrations of DOC while on the other hand those same increasing
2193 hydrological flows increasing the flux, but decreasing the concentration, of CO_{2(aq.)}

2194 throughput.

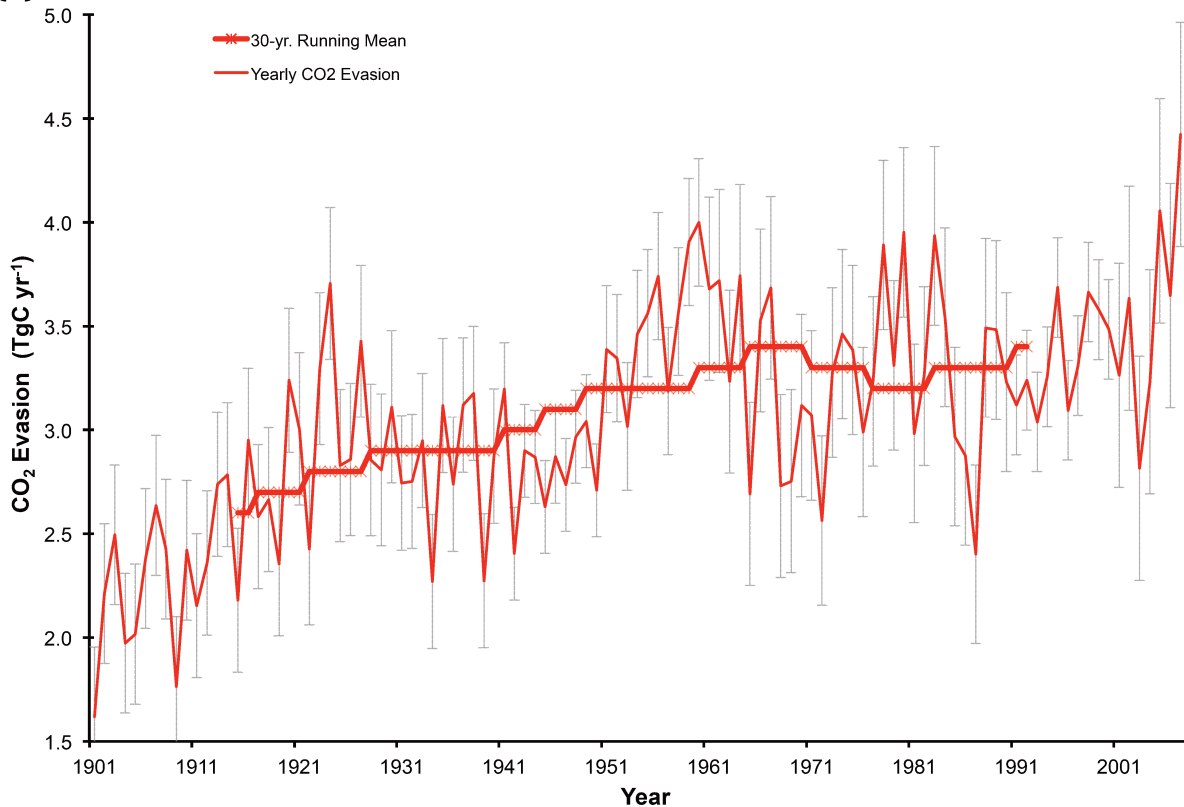
2195

2196 To our knowledge, no direct measurements for CO₂ evasion from the surface of the Lena
2197 river are available in the literature, presumably owing to the notorious difficulty in
2198 successfully obtaining such data. We refer to Denfeld et al. (2013)(Denfeld et al., 2013)
2199 for evaluating our evasion flux results, since their basin of study, the Kolyma River, is the
2200 most geographically proximate existing dataset to the Lena, despite biogeographical
2201 differences between the two basins –namely that the Kolyma is almost entirely
2202 underlain by continuous permafrost. The Kolyma River CO₂ evasion study measured
2203 evasion at 29 different sites along the river basin (~158-163°E; 68-69.5°N), with these
2204 sites distinguished from one another as ‘main stem’, ‘inflowing river’ or ‘stream’ on the
2205 basis of reach length. The study showed that during the summer low-flow period
2206 (August), areal river mainstem CO₂ evasion fluxes were ~0.35 gC m⁻² d⁻¹, whereas for
2207 streams of stream order 1-3 (widths 1-19m), evasion fluxes were up to ~7 gC m⁻² d⁻¹,
2208 and for non-mainstem rivers (widths 20-400m) mean net fluxes were roughly zero
2209 (Table 3 of Denfeld et al., 2013). Thus, while small streams have been observed to
2210 contribute to roughly 2% of the Kolyma basin surface area, their measured percentage
2211 contribution to total basin-wide CO₂ evasion ~40%, whereas for the main stem the
2212 surface area and evasion fractions were ~80% and 60%, respectively.

2213

2214

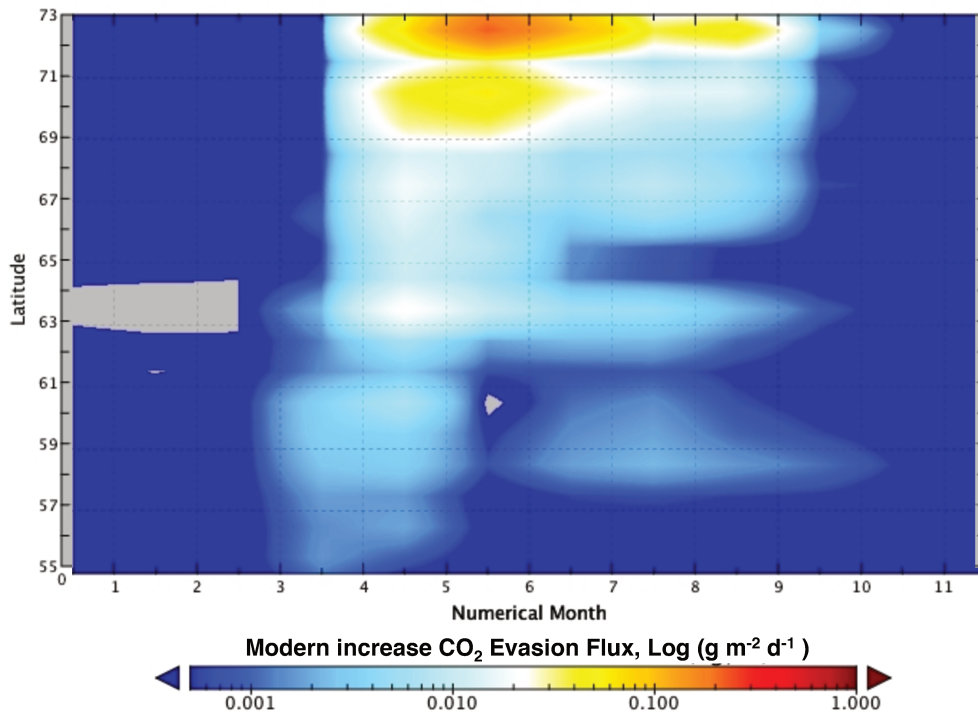
(a)



2215

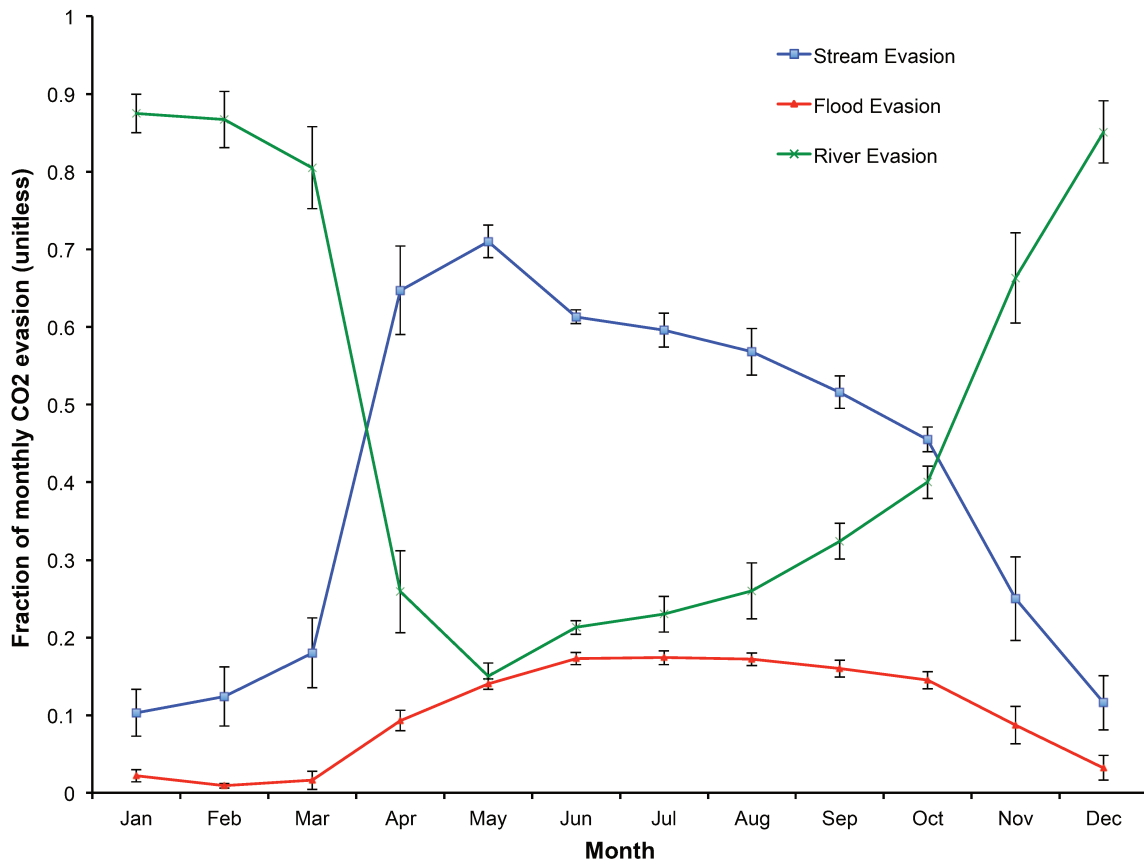
2216

(b)



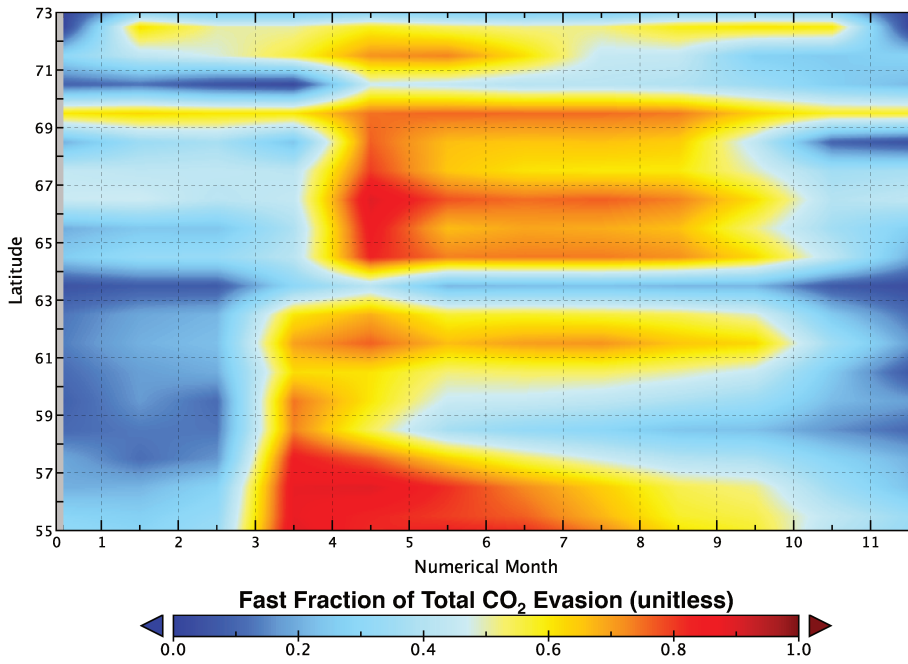
2217
2218

(c)

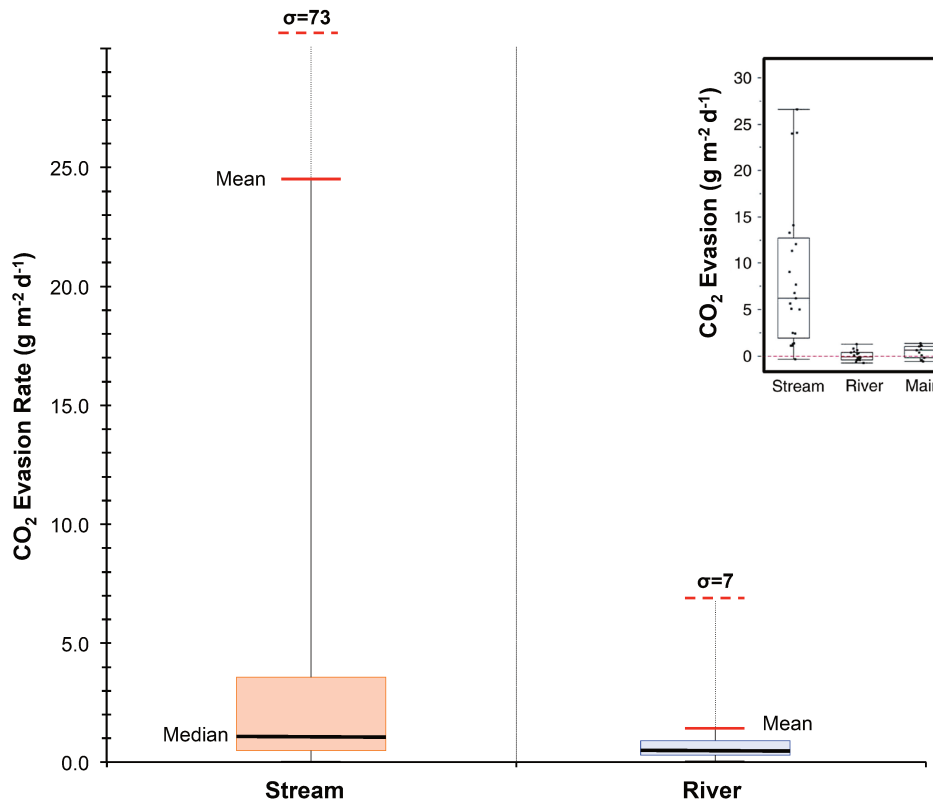


2219
2220

(d)



2221
2222 (e)
2223



2224
2225
2226
2227
2228
2229
2230
2231
2232

Figure 7: CO₂ evasion from stream, river, flood reservoirs. **(a)** Timeseries of total yearly CO₂ evasion (tC yr⁻¹) summed over the three hydrological pools (red line) with the 30-year running mean of the same variable overlain in thick red (asterisk). Error bars give the standard deviation of each decade (e.g. 1901-1910) for each data point in that decade. **(b)** Log-scale Hovmöller diagram plotting the longitudinally-averaged difference (increase) in total CO₂ evaded from the Lena River basin between the average of the periods 1998-2007 and 1901-1910, over each monthly timestep, in (log) gC m⁻² d⁻¹. Thus as the river drains northward the month-on-month difference in water-body CO₂ flux, between the beginning and end of the 20th Century is shown; **(c)** The fraction of total CO₂ evasion emitted from each of the

2233 hydrological pools for the average of each month over the period 1998-2007 is shown for river, flood and
2234 stream pools (blue, green and red lines, respectively), with error bars depicting the standard deviation of
2235 data values for each month displayed. **(d)** Hovmöller diagram showing the monthly evolution of the
2236 stream pool fraction (range 0-1) per month and per latitudinal band, averaged over the period 1998-2007.
2237 **(e)** Boxplot for approximate (see text) simulated CO₂ evasion (gC m⁻² d⁻¹) from the streamwater reservoir
2238 and river water reservoir averaged over 1998-2007. Coloured boxes denote the first and third quartiles
2239 of the data range, internal black bars the median. Whiskers give the mean (solid red bar) and standard
2240 deviation (dashed red bar) of the respective data. Empirical data on these quantities using the same scale
2241 for rivers, streams and mainstem of the Kolyma river from Denfeld et al., 2013 are shown inset.
2242

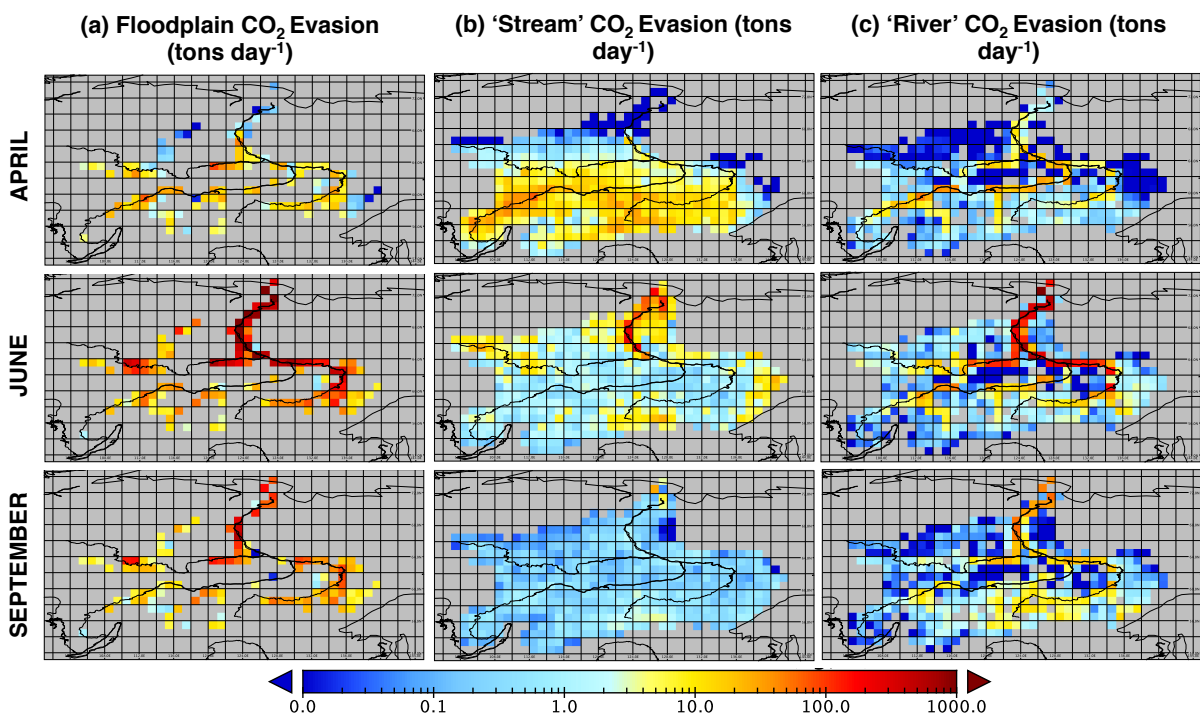
2243 Results such as these, in addition to permafrost soil incubation experiments (e.g. Drake
2244 et al., 2015; Vonk et al., 2013, 2015a) suggest that small streams, which represent the
2245 initial (headwater) drainage sites of these basins, rapidly process hydrologically leached
2246 carbon to the atmosphere, and that this high-reactivity carbon is a mix of recently
2247 thawed ancient permafrost material, as well as decomposing matter from the previous
2248 growth year. This is given as evidence that the total carbon processing of high-latitude
2249 rivers is significantly underestimated if only mainstem carbon concentrations are used
2250 in the accounting framework, since a large amount of carbon is metabolised to the
2251 atmosphere before reaching the site of measurement.
2252

2253 Figure 7 summarises some of the results from the simulated water body CO₂ outgassing
2254 flux. Year-on-year variation in basin-wide evasion from river, stream and floodplain
2255 sources combined exhibits a marked increasing trend over the course of the 20th
2256 Century, increasing from a minimum of ~1.6 TgCO₂-C yr⁻¹ in 1901 to a maximum of ~4.4
2257 TgCO₂-C yr⁻¹ in 2007, an increase of almost 300% (Fig. 7a). Smoothing the data over a 30
2258 year running average yields a dampened net increase in basin-wide evasion of ~30%
2259 over the historical period on this averaging scale (Fig. 7a). Thus yearly evasion flux is
2260 some 105% of yearly DOC discharge to the coast from the Lena basin and 51% of C
2261 exported from soils to headwaters as CO₂ or DOC. If we compare the mean yearly rate of
2262 increase in absolute (TgC yr⁻¹) CO₂ evasion and DOC discharge based on linear
2263 regression over the whole simulation period, it appears that the rate of increase of both
2264 fluxes has been strikingly similar over the simulated 20th Century, with mean increases
2265 of 11.1 GgC yr⁻¹ and 11.5 GgC yr⁻¹ per year for evasion and export, respectively.
2266

2267 The heterogeneity of CO₂ evasion from different sources in the model is most evident in
2268 terms of their geographic distribution and relative intensity, as shown in the evasion
2269 flux rate maps (tons grid cell⁻¹ d⁻¹) over floodplain, stream and river areas in April, June
2270 and September (Fig. 8a-c). Whereas floodplains (Fig. 8a) tend to have some of the
2271 highest evasion rates in the basin, their limited geographic extent means that their
2272 contribution to basinwide evasion is limited for the whole Lena. Stream evasion
2273 meanwhile (Fig.8b), tends to be broadly distributed over the whole basin, representing
2274 the fact that small streams and their evasion are the main hydrologic connectors outside
2275 of the main river and tributary grid cells, whereas river evasion (Fig. 8c) is clearly linked
2276 to the hydrographic representation of the Lena main stem itself, with higher total
2277 quantities in some individual grid cells than for the stream reservoir, yet distributed
2278 amongst a substantially smaller number of grid cells. Whereas the stream reservoir has
2279 greatest absolute evasion flux rates earlier in the year (April-May), maximum evasion
2280 rates occur later in the year and further downstream for the river reservoir, reflecting
2281 the fact that headwaters are first-order integrators of soil-water carbon connectivity,

2282 whereas the river mainstem and tributaries are of a secondary order. Note that the
 2283 September values must be interpreted with caution, given the underestimation in our
 2284 simulations of the river discharge during the Autumn period.
 2285

2286 The spatio-temporal pattern of increasing evasion over the simulation period is shown
 2287 in Fig. 7b as a Hovmöller difference plot, between the last and first decade, of log-scale
 2288 average monthly evasion rates per latitudinal band. This shows that the vast majority of
 2289 outgassing increase occurs between March and June, corresponding to the progressive
 2290 onset of the thaw period moving northwards over this timespan. Although relatively
 2291 small, outgassing increases are apparent for most of the year, particularly at lower
 2292 latitudes. This would suggest that the change is driven most acutely by relatively greater
 2293 temperature increases at higher latitudes ('Arctic amplification' of climate warming, e.g.
 2294 ref. (Bekryaev et al., 2010)) while less acute but more temporally homogenous evasion
 2295 is driven by seasonal warming at lower latitudes.



2296 **Figure 8:** Maps of CO₂ evasion from the surface of the three surface hydrological pools, (a) the floodplains,
 2297 (b) streams and (c) rivers in April, June and September. All maps use the same (log) scale in units of (tons
 2298 pixel⁻¹ d⁻¹).
 2299

2300
 2301
 2302 As previously discussed, the proportion of total basin-wide CO₂ evasion attributable to
 2303 headwater streams and rivers is substantially greater than their proportion of total
 2304 basin surface area. Figure 7c represents the mean monthly fractional contribution of
 2305 each surface hydrological water pool to the total evasion flux (unitless) over the period
 2306 1998-2007. This shows that over the entirety of the thaw period, the stream water pool
 2307 takes over from the river water pool as the dominant evasion source, particularly at the
 2308 height of the freshet period, where its fractional contribution rises to >75%.
 2309

2310 The stream fraction of August outgassing is roughly 57% of the annual total, which is
 2311 higher than the ~40% found for streams in the Denfeld et al. (2013) study. However,

2312 the values between the two studies are not directly comparable, different basins
2313 notwithstanding. This is because in ORCHIDEE MICT-L, the 'stream' water reservoir is
2314 water routed to the river network for all hydrologic flows calculated to not cross a 0.5
2315 degree grid cell boundary (the resolution of the routing module, explained in Part 1,
2316 Section 2.6), which may not be commensurate with long, <20m width streams in the
2317 real-world, that were used in the Denfeld et al. (2013) study. In addition, this 'stream'
2318 water reservoir in the model does not include any values for width or area in the model,
2319 so we cannot directly compare our stream reservoir to the <20m width criterion
2320 employed by Denfeld et al. (2013) in their definition of an observed stream. Thus our
2321 'stream' water reservoir encompasses substantially greater surface area and hydrologic
2322 throughput than that in the Denfeld et al. study. We also add the qualification that
2323 because of its coarse-scale routing scheme, ORCHIDEE isn't able to simulate stream
2324 orders lower than 4 or 5 thus missing a potentially substantial vector for the water-
2325 surface evasion of CO₂.

2326
2327 Significantly, also shown in Fig. 7c, is the gradual onset of evasion from the floodplain
2328 reservoir in April, as the meltwater driven surge in river outflow leads to soil inundation
2329 and the gradual increase of proportional evasion from these flooded areas over the
2330 course of the summer, with peaks in June-August as water temperatures over these
2331 flooded areas likewise peak. We stress the importance of these simulation results as
2332 they concur with large numbers of observational studies (cited above) which show
2333 smaller headwater streams' disproportionately large contribution to total outgassing
2334 (Fig. 7c), this being due to their comparatively high outgassing rates (Fig. 7e). In
2335 addition, the contribution of floodplains to evasion, an otherwise rarely studied feature
2336 of high latitude biomes, is shown here to be significant.

2337
2338 A Hovmöller plot (Fig. 7d) of the monthly longitude-averaged stream reservoir fraction
2339 of total evasion, gives some indication as to the spatio-temporal pattern under which
2340 evasion from this hydrological pool evolves over the course of the year. From this we
2341 can infer that: (i) The dominance of stream evasion begins in the most southern
2342 upstream headwaters in the lower latitude thaw period (April-May), and trickles
2343 northward over the course of the next two months, following the riverflow. (ii) The
2344 intensity of stream water evasion is greatest in the lower latitude regions of the basin,
2345 which we speculate is the result of higher temperatures causing a greater proliferation
2346 of small thaw water-driven flows and evasion. (iii) Areas where the stream fraction is
2347 not dominant or only briefly dominant during the summer (58-60°N, 63-64°N, 70-71°N)
2348 are all areas where floodplain CO₂ evasion plays a prominent role at that latitudinal
2349 band.

2350
2351 Although not directly comparable due to the previously mentioned issues arising from
2352 our model-derived representation of 'stream' water versus those in the real world, we
2353 evaluate the approximate rate of areal CO₂ efflux from the water surface against
2354 observations from Denfeld et al. (2013) in Fig. 7e. The 'approximate' caveat refers to the
2355 fact that model output doesn't define a precise surface area for the stream water
2356 reservoir, which is instead bundled into a single value representing the riverine fraction
2357 of a grid cell's total surface area. Thus, in order to break down the areal outgassing for
2358 the stream versus river water reservoirs, we derive an approximate value for the
2359 fractional area taken up by rivers and streams in a simple manner: we weight the total

2360 non-floodplain inundated area of each grid cell by the relative total water mass of each
2361 of the two hydrological pools, then divide the total daily CO₂ flux simulated by the model
2362 by this value. The per-pool areal estimate is an approximation since it assumes that
2363 rivers and streams have the same surface area: volume relationship. This is clearly not
2364 the case, since streams are generally shallow, tending to have greater surface area per
2365 increment increase in depth than rivers. Thus, our areal approximations are likely
2366 underestimated (overestimated) for streams (rivers), respectively.

2367
2368 The comparison of simulated results with those from Denfeld et al. (2013) are displayed
2369 in Fig.7e, which shows boxplots for simulated CO₂ evasion (gC m⁻² d⁻¹) from the stream
2370 water reservoir and river water reservoir averaged over 1998-2007. The empirical
2371 (Kolyma river) analog of this data, from which this plot is inspired (Fig. 4d in Denfeld et
2372 al., 2013), is shown inset in the figure, with whiskers in their case denoting measured
2373 maxima and minima. Median efflux was 1.1 (6) versus 0.4 (0.8) for stream and river,
2374 respectively, in simulations (observations). Like the observations, simulated stream
2375 efflux had a substantially greater interquartile range, mean (24.6) and standard
2376 deviation (73) than total river efflux (1.3 and 7.2, respectively). Note that from ~700
2377 non-zero simulation datapoints, 7 were omitted as 'outliers' from the stream reservoir
2378 efflux statistics described below, because very low stream:river reservoir values skewed
2379 the estimation of total approximate stream surface area values very low, leading to
2380 extreme efflux rate values of 1-3000gC m⁻² d⁻¹ and are thus considered numerical
2381 artefacts of the areal approximation approach used here.

2382
2383

2384 **4.5 Emergent Phenomena**

2385

2386 **4.5.1 DOC and mean annual air temperature**

2387 A key emergent property of DOC concentrations in soils and inland waters should be
2388 their positive partial determination by the temperature of the environment under which
2389 their rates of production occur, as has been shown in the literature on permafrost
2390 regions, most notably in Frey & Smith (2005) (Frey and Smith, 2005) and Frey &
2391 McClelland (2009)(Frey and McClelland, 2009).

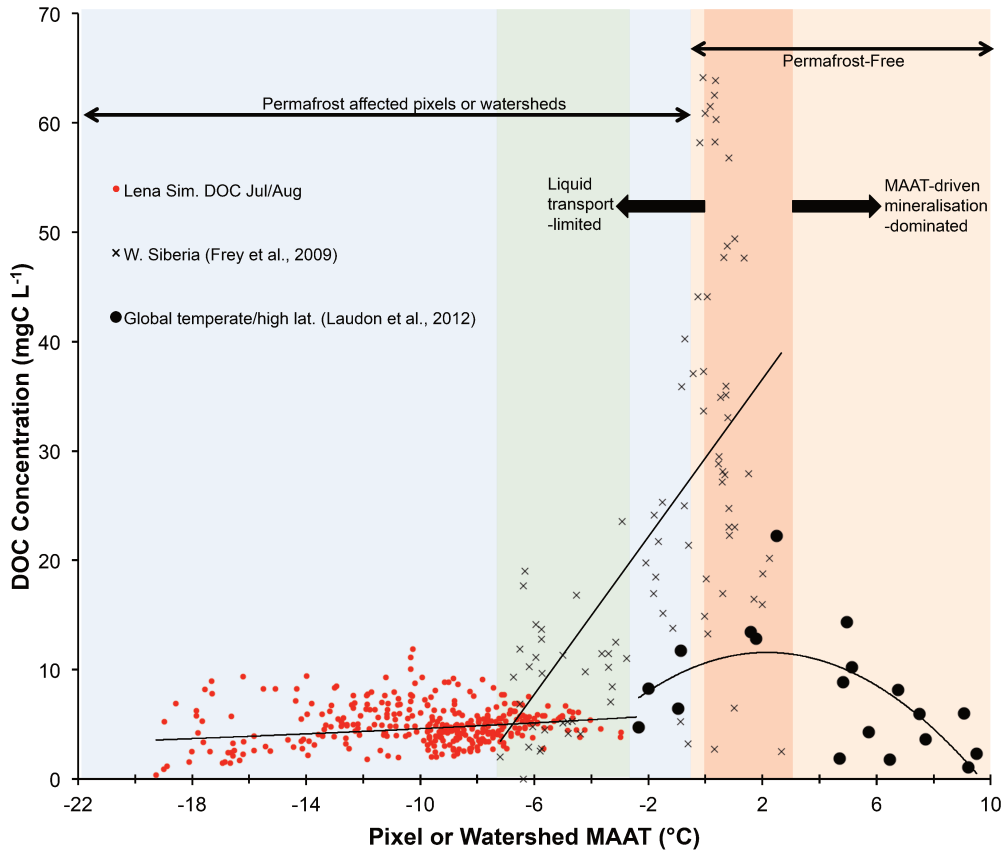
2392

2393 Increasing temperatures should lead to greater primary production, thaw,
2394 decomposition and microbial mobilisation rates, and hence DOC production rates,
2395 leading to (dilution effects notwithstanding) higher concentrations of DOC in thaw and
2396 so stream waters. Looking at this emergent property allows us to evaluate the soil-level
2397 production of both DOC and thaw water at the appropriate biogeographic and temporal
2398 scale in our model. This provides a further constraint on model effectiveness at
2399 simulating existing phenomena at greater process-resolution.

2400

2401 Figure 9 compares three datasets (simulated and two observational) of riverine DOC
2402 concentration (in mgC L⁻¹) plotted against mean annual air temperature (MAAT). The
2403 simulated grid-scale DOC versus MAAT averaged over July and August (for
2404 comparability of DOC with observational sampling period) of 1998-2007 is shown in
2405 red, and observed data compiled by Laudon et al. (2012)(Laudon et al., 2012) and Frey
2406 and Smith (2005) (Frey and Smith, 2005) for sites in temperate/cold regions globally
2407 and peatland-dominated Western Siberia, respectively. The Laudon et al. (2012) data

2408 are taken from 49 observations including MAAT over the period 1997-2011 from
 2409 catchments north of 43°N, and aggregated to 10 regional biogeographies, along with
 2410 datapoints from their own sampling; those in the Frey and Smith study are from 55-
 2411 68°N and ~65-85°E (for site locations, see Laudon et al. (2012), Table 1 and 2; Frey and
 2412 Smith (2005), Fig. 1).
 2413



2414
 2415 **Figure 9:** Mean summertime DOC concentrations (mgC L⁻¹) plotted against mean annual air temperature
 2416 (MAAT, °Celsius) for simulated pixels over the Lena river basin (red circles), and observations for largely
 2417 peat-influenced areas in western Siberia as reported in Frey et al., 2009 (black crosses), and observations
 2418 from a global non-peat temperate and high latitude meta-analysis (black circles) reported in Laudon et al.
 2419 (2012). The blue region represents permafrost-affected areas, while the orange region represents
 2420 permafrost-free areas. The green region bounds the area of overlap in MAAT between the observed and
 2421 simulated datasets. The dark red shaded area corresponds to the MAAT 'zone of optimality' for DOC
 2422 production and transport proposed by Laudon et al. (2012). Regression curves of DOC against MAAT for
 2423 each of the separate datasets are shown for each individual dataset.
 2424

2425
 2426 can be interpreted in a number of ways. First, this MAAT continuum spans the range of
 2427 areas that are both highly and moderately permafrost affected and permafrost free (Fig.
 2428 9, blue and green versus orange shading, respectively), potentially allowing us a glimpse
 2429 of the behaviour of DOC concentration as the environment transitions from the former
 2430 to the latter. Simulated Lena DOC concentrations, all in pixels with MAAT < -2°C and
 2431 hence all bearing continuous or discontinuous permafrost ('permafrost-affected' in the
 2432 figure), only exhibit a weakly positive response to MAAT on the scale used
 2433 ($y=6.05e^{0.03MAAT}$), although the consistent increase in DOC minima with MAAT is clearly
 2434 visible.

2435
2436 Second, the Laudon et al. (2012) data exhibit an increasing then decreasing trend over
2437 the range of MAAT (-2°C to 10°C) in their dataset, which they propose reflects an
2438 'optimal' MAAT range for the production and transport of DOC, occupying the 0°C to 3°C
2439 range (Fig. 9, red shading). Below this optimum range, DOC concentrations may be
2440 limited by transport due to freezing, and above this, smaller soil carbon pools and
2441 temperature-driven decomposition would suppress the amount of DOC within rivers.
2442 Third, the lower end of the Laudon et al. (2012) MAAT values correspond to a DOC
2443 concentration roughly in line with DOC concentrations simulated by our model at those
2444 temperatures.

2445
2446 Fourth, DOC concentrations in the Frey and Smith (2005) data exhibit a broad scattering
2447 in permafrost-affected sites, with concentrations overlapping those of our simulations
2448 (Fig. 9, green shading), before rapidly increasing to very high concentrations relative to
2449 the Laudon et al. (2012) data, as sites transition to permafrost-free (red shading,
2450 $y=3.6_{MAAT}+29.4$). Their data highlight the difference in DOC concentration regime
2451 between areas of high (Frey and Smith, 2005) and low (Laudon et al., 2012) peatland
2452 coverage and the different response of these to temperature changes. Fifth, because our
2453 simulation results largely correspond with the observed data where the MAAT ranges
2454 overlap (green shading), and because our model does not include peatland specific
2455 processes, we should expect our model to broadly follow the polynomial regression
2456 plotted for the Laudon et al. (2012) data as temperature inputs to the model increase.
2457 Figure 9 implies that this increase should be on the order of a doubling of DOC
2458 concentration as a system evolves from a MAAT of -2°C to 2°C. In addition, as the Arctic
2459 environment warms we should expect the response of DOC concentrations as a whole to
2460 reflect a mix of both observationally-derived curves, as a function of peatland coverage.

2461 2462 **4.5.2 DOC and topographic slope**

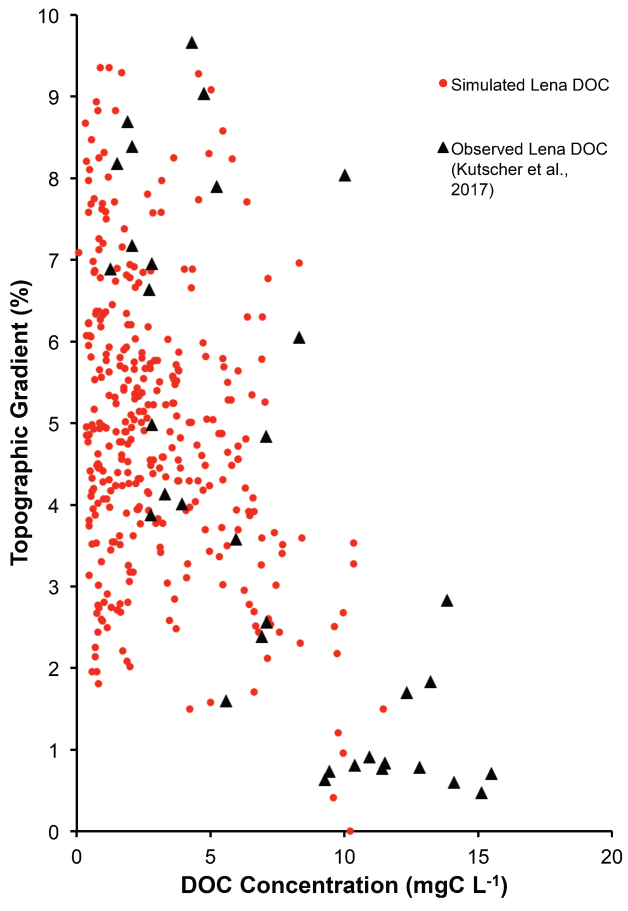
2463 Subsurface water infiltration fluxes and transformations of dissolved matter represent
2464 an important, if poorly understood and observationally under-represented
2465 biogeochemical pathway of DOC export to river main stems, involving the complex
2466 interplay of slope, parent material, temperature, permafrost material age and soil
2467 physical-chemical processes, such as adsorption and priming.

2468
2469 In the Lena basin, as in other permafrost catchments, topographic slope has been shown
2470 to be a powerful predictor for water infiltration depth, and concentration and age of
2471 dissolved organic carbon (Jasechko et al., 2016; Kutscher et al., 2017; McGuire et al.,
2472 2005), with deeper flow paths and older, lower DOC-concentrated waters found as the
2473 topographic slope increases. This relationship was shown in Fig. 4 of Kutscher et al.
2474 (2017) who surveyed DOC concentrations across a broad range of slope angle values in
2475 the Lena basin and found a distinct negative relationship between the two. We compare
2476 the Kutscher et al. (2017) values with our model output, by plotting stream and river
2477 DOC concentrations averaged per gridpoint over 1998-2007 against the topographic
2478 map used in the routing scheme, versus their empirically derived data (Fig. 10). As
2479 shown therein, a similar negative relationship between the two variables is clearly
2480 apparent.

2481

2482 A similar relationship was found in temperate rivers by Lauerwald et al.
2483 (2012)(Lauerwald et al., 2012), and a recent paper by Connolly et al. (2018)(Connolly et
2484 al., 2018), based on their observational data and a synthesis of Pan-Arctic empirical
2485 literature. They showed that for Arctic catchments in general, the relationship of DOC
2486 concentration in fluvial waters scaled in a consistent and strongly negative manner
2487 against topographic slope. This was found for all Arctic catchments, globally, prompting
2488 Connolly et al. to argue that topographic slope may be a type of 'master variable' for
2489 estimating fluvial DOC concentrations in the absence of viable *in situ* measurement
2490 programs.

2491
2492 The reasoning for the negative slope-DOC concentration relationship is that as elevation
2493 increases, temperature and primary production decreases. This leads to a thinner
2494 organic soil layer, meaning that mineral soil plays a stronger role in shallow hydrologic
2495 flowpaths, allowing for deeper infiltration and shorter residence time in a given soil
2496 layer. In addition, steeper terrain leads to a lower soil water residence time and lower
2497 moisture than in flat areas.
2498



2499 **Figure 10:** Variation of DOC concentrations versus topographic slope in Kutscher et al., 2017 (black
2500 triangles) and (red dots) as simulated and averaged for the summer months (JJA) over 1998-2007;
2501 observed values were measured during June and July 2012-2013.
2502

2503
2504 As a result, a given patch of soil matter will be exposed to leaching for less (residence)
2505 time, while the organic matter that is leached is thought to be adsorbed more readily to
2506 mineral soil particles, leading to either their re-stabilisation in the soil column or

2507 shallow retention and subsequent heterotrophic respiration in situ, cumulatively
2508 resulting in lower DOC concentrations in the hydrologic export (Kaiser and Kalbitz,
2509 2012; Klaminder et al., 2011). This line of reasoning was recently shown to apply also to
2510 deep organic permafrost soils (Zhang et al., 2017), although the degree to which this is
2511 the case in comparison to mineral soils is as yet unknown.

2512
2513 In addition, and as described in Part 1 (Section 2.5) of this study, MICT-L contains a
2514 provision for increased soil column infiltration and lower decomposition rates in areas
2515 underlain by Podzols and Arenosols. The map from the Harmonized World Soil Database
2516 (Nachtergaele, 2010), which is used as the input to this criterion, shows areas underlain
2517 by these soils in the Lena basin to also be co-incident with areas of high topographic
2518 slope (Fig. 3a, SI, Fig S2b). Their Podzol effect is to increase the rate of decomposition
2519 and infiltration of DOC, relative to all other soil types, thus also increasing the rate of
2520 DOC flux into groundwater (see Part 1 of this study, Section 2.5).

2521
2522 Our modelling framework explicitly resolves the processes involved in these
2523 documented dynamics –soil thermodynamics, solid vertical flow (turbation), infiltration
2524 as a function of soil textures and types, adsorption as a function of soil parameters (see
2525 Part 1 of this study, Section 2.11), DOC respiration as a function of soil temperature and
2526 hence depth (Part 1, Section 2.12), lagging of DOC vertical flow behind hydrological
2527 drainage flow (summary Figure in Part 1, Fig. 1). We thus have some confidence in
2528 reporting that the simulated negative relationship of DOC concentration with
2529 topographic slope may indeed emerge from the model. If generalisable to permafrost
2530 basins as a whole, this relationship may be an emergent process-based signal with
2531 which to evaluate the biogeographic performance of permafrost-region DOC modelling
2532 initiatives in the future, as was recently suggested by Connolly et al. (2018).

2533 2534 **4.6 DOC Reactivity Pools**

2535
2536 Here we examine the reactivity of DOC leached from the soil and litter to different
2537 hydrological export pools. Surface runoff DOC export is dominated by refractory carbon
2538 (Fig. 11a), with export rates largely following discharge rates as they drain the basin
2539 with an increasing delay when latitude increases. As the thaw period gets underway
2540 (April), the fraction of labile carbon in surface runoff DOC increases substantially from
2541 south to north, reflecting the hydrologic uptake of the previous year's undecomposed
2542 high-reactivity organic matter, as well as the addition of new inputs from the onset of
2543 the current year's growing season.

2544
2545 Refractory carbon-dominated drainage DOC export rates (Fig. 11a) are centered on the
2546 months June through October, with refractory export rate intensities per latitudinal
2547 band during this period largely consistent with the fraction of inundated area (Fig. S1)
2548 experienced by these bands during the course of the year, these centering on the areas
2549 bounded by 52-65N and 70-72N. The high refractory proportion of drainage flow is
2550 expected, as drainage leaches older, relict soil and litter matter. Because of its longer
2551 water residence time, labile DOC carried vertically downward through the soil
2552 infiltration flux will tend to be metabolised in situ before it can be exported to the
2553 hydrological network, thus further increasing the proportion of refractory carbon.

2554

2555 By contrast floodplain DOC export (Fig. 11a) is dominated by the labile carbon pool but
 2556 is composed of more nuanced mix of both reactivity classes, reflecting its relatively
 2557 greater dependence on the current year's 'fresh' biomass as source material (62% labile
 2558 DOC versus 38% refractory DOC, year-averaged) for carbon leaching. This can be
 2559 expected, since DOC and CO₂ production that would normally occur first in soil free DOC
 2560 concentrations before being gradually exported into surface runoff and drainage inputs
 2561 to the hydrological network are instead directly supplied to the water column as they
 2562 are generated, meaning that there is less of a time lag for the rapid decomposition of the
 2563 labile portion than through the other two hydrological export pathways.

2564
 2565 For both the river and stream pool, mean DOC concentrations are also dominated by
 2566 refractory carbon sources. Interestingly, very high concentrations in the stream
 2567 reservoir are maintained year-round in the northernmost reaches of the Lena basin, the
 2568 causes of which are not directly deducible from our data. Likely, very high stream
 2569 concentrations are obtained from the confluence of relatively low volumetric water
 2570 fluxes in these regions that owe themselves to the freezing temperatures, with these low
 2571 temperatures likewise retarding direct heterotrophic respiration of contemporary plant
 2572 litter and favouring instead their environmental mobilisation by hydrological leaching,
 2573 when liquid water is available for matter dissolution.

2574
 2575 When averaged over the year, the dominance of the refractory DOC carbon pool over its
 2576 labile counterpart is also evident for all DOC inputs to the hydrological routing except
 2577 for floodplain inputs, as well as within the 'flowing' stream and river pools themselves.
 2578 This is shown in Table 2, where the year-averaged percentage of each carbon
 2579 component of the total input or reservoir is subdivided between the 'North' and 'South'
 2580 of the basin, these splits being arbitrarily imposed as the latitudinal mid-point of the
 2581 basin itself (63N). This reinforces the generalised finding from our simulations that
 2582 refractory carbon dominates runoff and drainage inflows to rivers (89% refractory, on
 2583 average), while floodplains export mostly labile DOC to the basin (64%), these values
 2584 being effectively independent of this latitudinal sub-division (Table 3). This may be
 2585 expected, given that almost the entire basin is underlain by continuous permafrost,
 2586 whereas in areas with discontinuous or sporadic permafrost, the combination of higher
 2587 primary productivity and so litter input, with seasonal thaw of labile permafrost soil
 2588 matter may be expected to substantially increase the labile portion of the overall sum of
 2589 these quantities. Nonetheless, there appears to be a small consistent difference between
 2590 North and South in the stream and river water DOC makeup, in that the labile portion
 2591 decreases between North and South ; this may be an attenuated reflection of the portion
 2592 of labile DOC that is decomposed to CO₂ within the water column during its transport
 2593 northward, affecting the bulk average proportions contained within the water in each
 2594 'hemisphere'.

2595
 2596 **Table 3:** Summary of the average carbon reactivity types comprising the hydrological inputs to rivers and
 2597 streams (runoff, drainage and floodplain inputs), and within the rivers and streams themselves,
 2598 subdivided between the 'North' and 'South' of the Lena basin (greater or less than 63N, respectively).
 2599

Hydrological Source	Model Carbon Reactivity Pool	North	South
Runoff Input	Refractory	81%	83%
	Labile	19%	17%

Drainage Input	Refractory	96%	94%
	Labile	4%	6%
Flood Input	Refractory	36%	37%
	Labile	64%	63%
Streams	Refractory	91%	89%
	Labile	9%	11%
Rivers	Refractory	92%	90%
	Labile	8%	10%

2600

2601

2602

4.7 NPP and Soil Respiration

2603

2604

2605

2606

2607

2608

2609

2610

2611

2612

2613

2614

2615

2616

2617

2618

Rates of yearly net primary production (NPP) for Russian and Siberian forests have been inferred in situ from eddy flux and inventory techniques to range from 123-250 gC m⁻² yr⁻¹ (Beer et al., 2006; Lloyd et al., 2002; Roser et al., 2002; Schulze et al., 1999; Shvidenko and Nilsson, 2003). We likewise simulate a broad range of NPP carbon uptake rates, of 61-469 gC m⁻² yr⁻¹ averaged per grid cell over the Lena basin, with a mean value of 210 gC m⁻² yr⁻¹. NPP is heterogeneously distributed over space and between PFTs (SI, Fig. S4c), with forests averaging 90 gC m⁻² yr⁻¹ and grasslands averaging 104 gC m⁻² yr⁻¹ over the basin as a whole. Low values tended to originate in basin grid cells with elevated topography or high mean slope, while the maximum value was standalone, exceeding the next greatest by ~100 gC m⁻² yr⁻¹, and is most likely caused by the edge effects of upscaling a coastal gridcell's small fraction of terrestrial area where high productivity occurs in a small plot, to the grid cell as a whole. By evaluating NPP we are also evaluating at a secondary level litter production, which is at a third level a major component of DOC production.

2619

2620

2621

2622

2623

2624

Taken as a whole, gross primary production (GPP) was performed under simulations by four PFT groups, with the largest basin-wide bulk contributions coming from boreal needleleaf summer-green trees and C3 grasses (SI, Fig. S4a), the highest GPP uptake rates (3 TgC pixel⁻¹ yr⁻¹) generated by boreal needleleaf evergreen trees, and the remainder of GPP contributed by Boreal broad-leaved summer-green trees (SI, Fig. S4a).

2625

2626

2627

2628

2629

2630

2631

2632

2633

2634

2635

2636

2637

2638

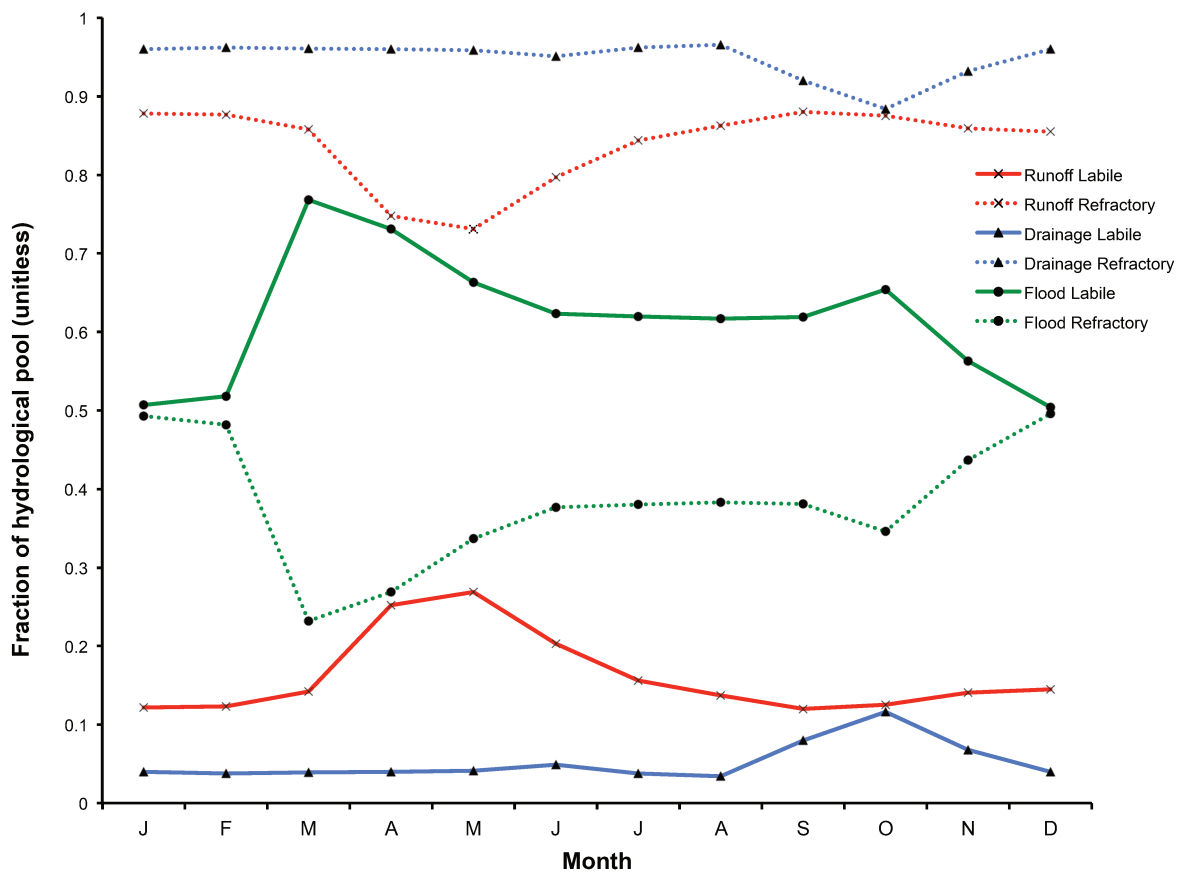
Soil respiration rates, of combined soil heterotroph and plant root respiration in our Control simulation, averaged 208 gC m⁻² yr⁻¹ (0.57 gC m⁻² d⁻¹) over the Lena basin over the period 1990-2000, which is somewhat higher than those found by Elberling (2007)(Elberling, 2007) in forest soils over Svalbard, of 103-176 gC m⁻² yr⁻¹ (0.28-0.48 gC m⁻² d⁻¹). Sawamoto, et al. (2000)(Sawamoto et al., 2000) measured in situ summertime soil respiration over the central Lena basin and found rates of 1.6-34 gC m⁻² d⁻¹, while Sommerkorn (2008)(Sommerkorn, 2008) observed rates of 0.1-3.9 gC m⁻² d⁻¹ at higher latitudes, these appearing to vary with vegetation and fire history, water table depth and temperature. Mean heterotrophic respiration rates of 1.6 gC m⁻² d⁻¹ are simulated here during July and August, in the range 0.05-2.2 gC m⁻² d⁻¹ for each of the above PFT groups. The spatial distribution of, and difference in respiration rates between PFT groups largely mirrors those for NPP (SI Fig. S4c), with maximum rates of 1.4 gC m² d⁻¹ over forested sites, versus a maximum of 2.2 gC m² d⁻¹ over grassland/tundra sites (SI, Fig. S4b).

2639
 2640
 2641
 2642
 2643
 2644
 2645
 2646
 2647
 2648
 2649
 2650
 2651
 2652
 2653
 2654
 2655
 2656
 2657
 2658
 2659
 2660
 2661
 2662

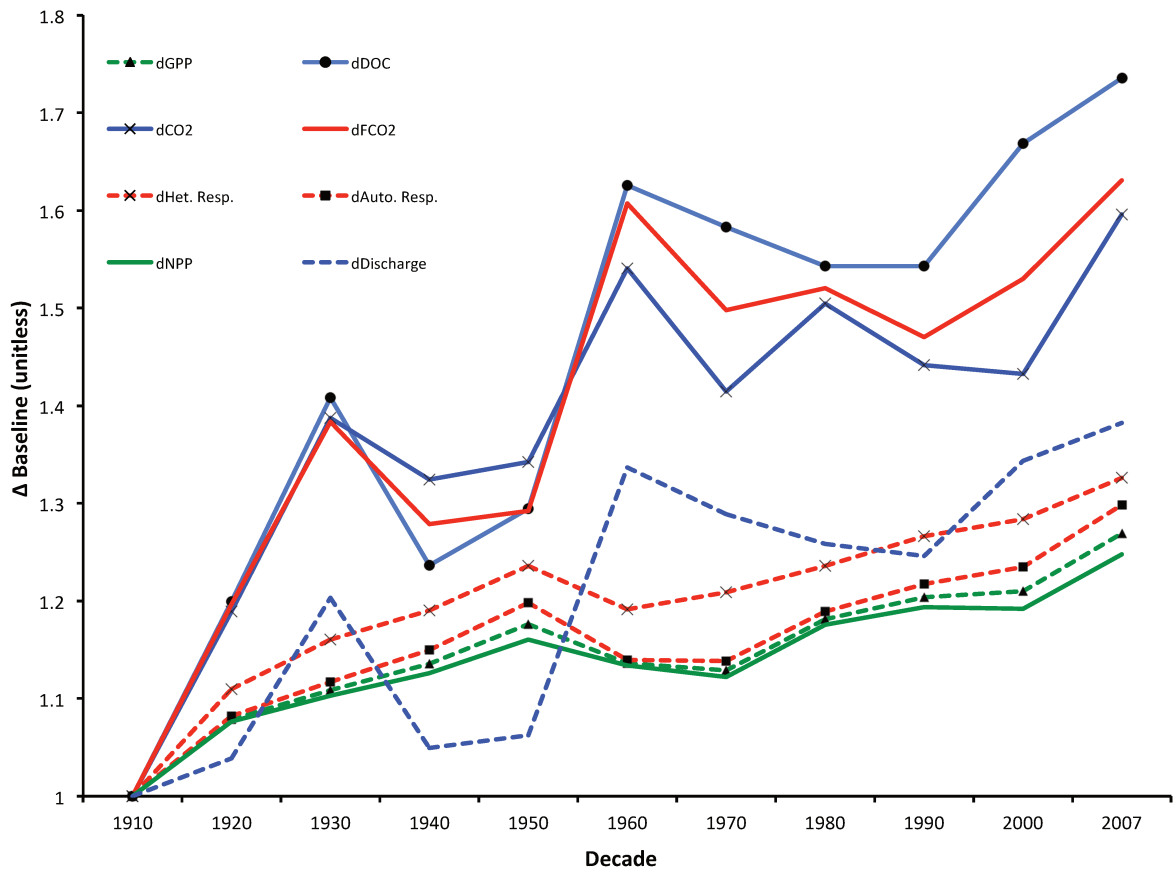
Aggregated over the basin, results show that increases over the course of the 20th Century were simulated for NPP, GPP, River Discharge, DOC, CO_{2(aq.)}, autotrophic and heterotrophic respiration and CO₂ evasion, with percentage changes in the last versus first decade of +25%, +27%, 38%, +73%, +60%, +30%, +33% and +63%, respectively. (Fig. 11b). It thus appears that rising temperatures and CO₂ concentrations disproportionately favoured the metabolisation of carbon within the soil and its transport and mineralisation within the water column, fed by higher rates of primary production and litter formation as well as an accelerated hydrological cycle (see Fig. 4b and 13a).

In Figure 11c we run linear regressions through scatter-plots of yearly DOC and CO₂ export and CO₂ evasion fluxes, versus rates of NPP (TgC yr⁻¹). These show that whereas bulk DOC flux appears most sensitive (steeper slope) to increases in NPP, it is also least coupled to it (more scattered, R²=0.42). CO₂ evasion is least sensitive yet most tightly coupled to NPP (R²=0.52), while CO₂ export is intermediate between the two for both (R²=0.43) –this is expected given that CO₂ export is also the intermediate state between DOC export and CO₂ evasion. The greater scattering of DOC:NPP compared to evasion:NPP is understandable, given that the initial of leaching is a covariate of both primary production and runoff, whereas the actual evasion flux is largely dependent on organic inputs (production) and temperature.

(a)

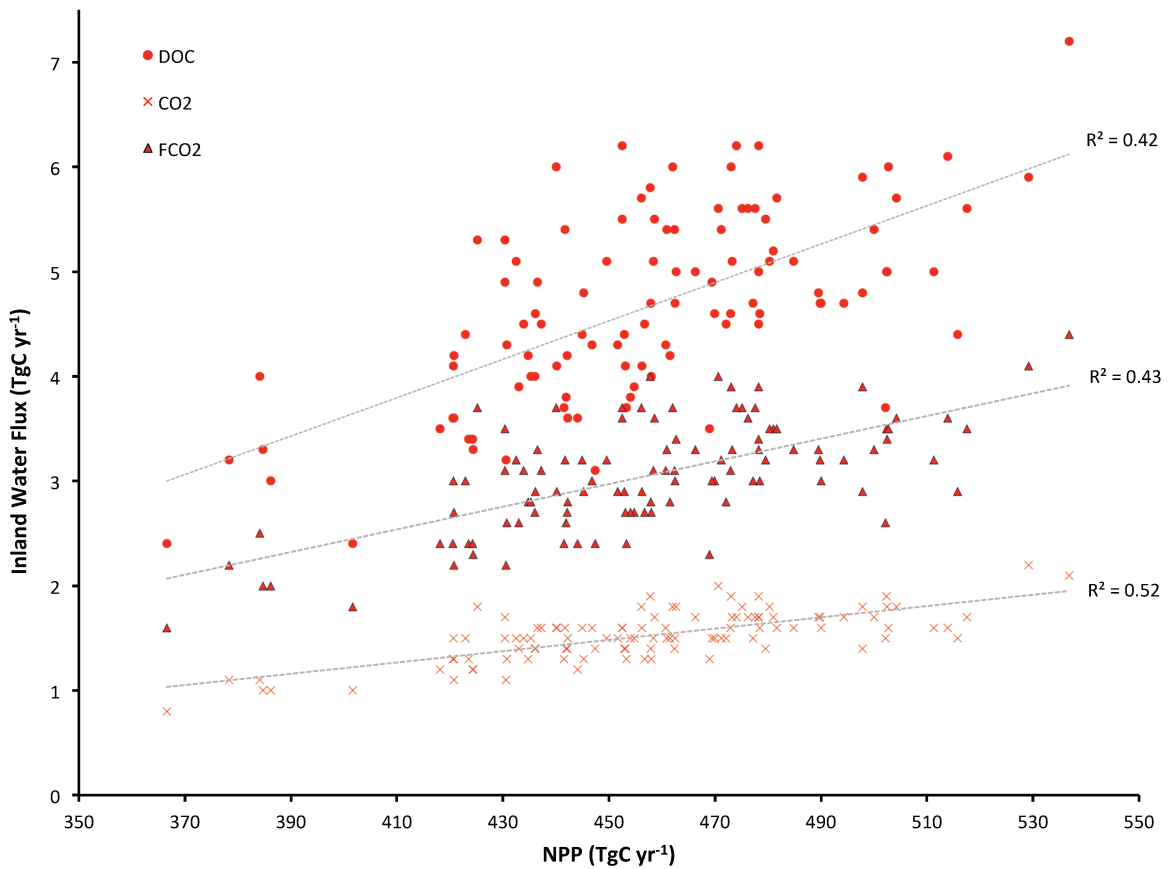


2663



2664
2665

(c)



2666

Figure 11: (a) The mean monthly fraction of each hydrological pool's (runoff, drainage, floodplains) carbon reactivity constituents (labile and refractory) averaged across the simulation area over 1998-2008. (b) Time series showing the decadal-mean fractional change in carbon fluxes normalised to a 1901-1910 average baseline (=1 on the y-axis) for NPP, GPP, autotrophic and heterotrophic respiration, DOC inputs to the water column, CO₂ inputs to the water column, CO₂ evasion from the water surface (FCO₂), and discharge. (c) Summed yearly lateral flux versus NPP values for DOC discharge, CO₂ discharge and CO₂ evasion (FCO₂) over the entire simulation period, with linear regression lines shown.

4.8 Land-Ocean Aquatic Continuum (LOAC)

4.8.1 LOAC Fluxes

Overall, our simulation results show that dissolved carbon entering the Lena river system is significantly transformed during its transport to the ocean. Taking the average throughput of carbon into the system over the last ten years of our simulation, our results show that whereas 7 TgC yr⁻¹ (after reinfiltration following flooding of 0.45 TgC yr⁻¹; see Fig. 2 'Return' flux) of carbon enters the Lena from terrestrial sources as dissolved carbon and CO₂, only 3.4 TgC yr⁻¹ is discharged into the Laptev Sea and beyond from the river mouth. The remainder (3.6TgC yr⁻¹) is metabolised in the water column during transport and evaded to the atmosphere (bottom panel, Fig. 12a). The terrestrial DOC inflow estimate is comparable to that made by Kicklighter et al. (2013)(Kicklighter et al., 2013), who estimated in a modelling study terrestrial dissolved carbon loading of the Lena is ~7.7 TgC yr⁻¹.

The relative quantities of carbon inflow, evasion and outflow in the river system that are presented for the Lena in Fig. 12a can be compared to the same relative quantities –that is, the ratios of evasion:in and out:in, where 'in' refers to dissolved terrestrial input, – from the global study by Cole et al. (2007)(Cole et al., 2007), who estimated these fluxes from empirical or empirically-derived data at the global scale. This is shown in the top panel of Fig. 12a, where we simplify the Cole et al. (2007) data to exclude global groundwater CO₂ flux from the coast to the ocean (because our basin mask has a single coastal pixel whereas coastal groundwater seepage is distributed along the entire continental boundary) and the POC fraction of in-river transport and sedimentation (since ORCHIDEE MICT lacks a POC erosion/sedimentation module) from their budget.

This gives global terrestrial dissolved carbon input of 1.45 PgC yr⁻¹, 0.7 PgC of which is discharged to the ocean, and the other 0.75 PgC evaded to the atmosphere. Taking the previously mentioned [evasion:in] and [out:in] ratios as a percentage, the outflow and evasion fluxes for the Lena versus the global aggregate are remarkably similar, at 48.6 vs. 48.3% and 51.4 vs 51.7%, for the two respective flows. Thus our results agree with the proposition that the riverine portion of the 'land-ocean aquatic continuum' (Regnier et al., 2013) or 'boundless carbon cycle' (Battin et al., 2009) is indeed a substantial reactor for matter transported along it.

4.8.2 LOAC drivers

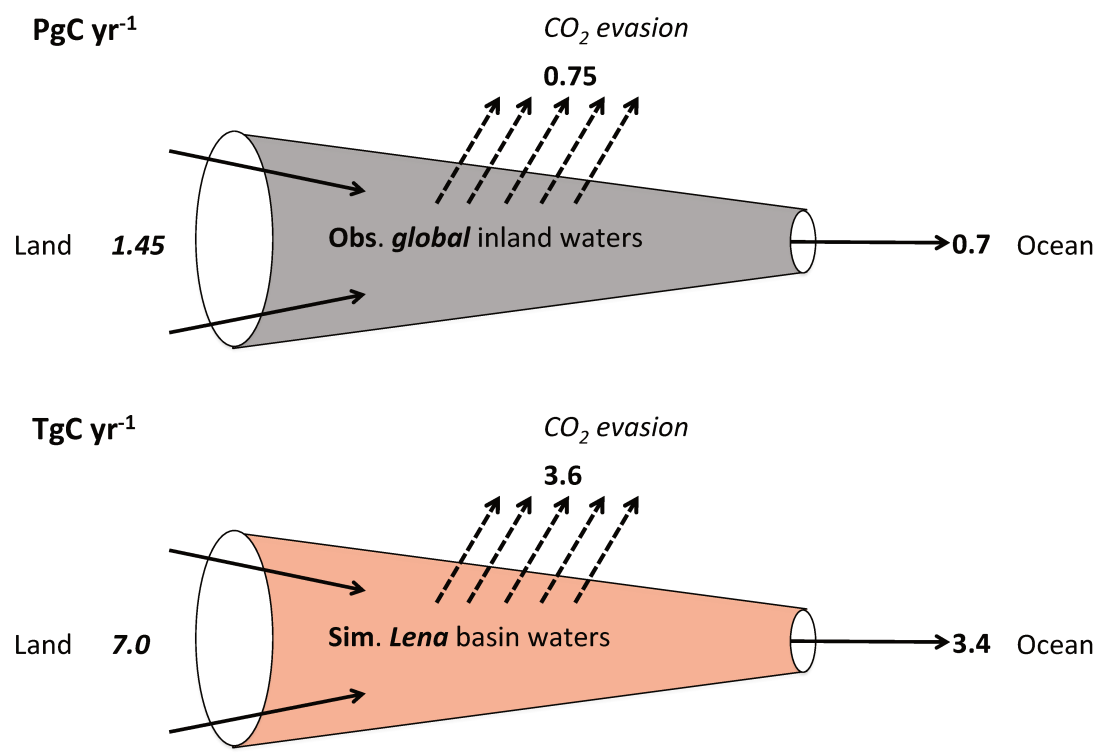
The constant climate (CLIM) and constant CO₂ (CO2) simulations were undertaken to assess the extent –and the extent of the difference –to which these two factors are drivers of model processes and fluxes. These differences are summarised in Figs. 12(b-

2716 c), in which we show the same 1998-2007 –averaged yearly variable fluxes as in the
2717 CTRL simulation, expressed as percentages of the CTRL values given in Fig. 2. A number
2718 of conclusions can be drawn from these diagrams.
2719

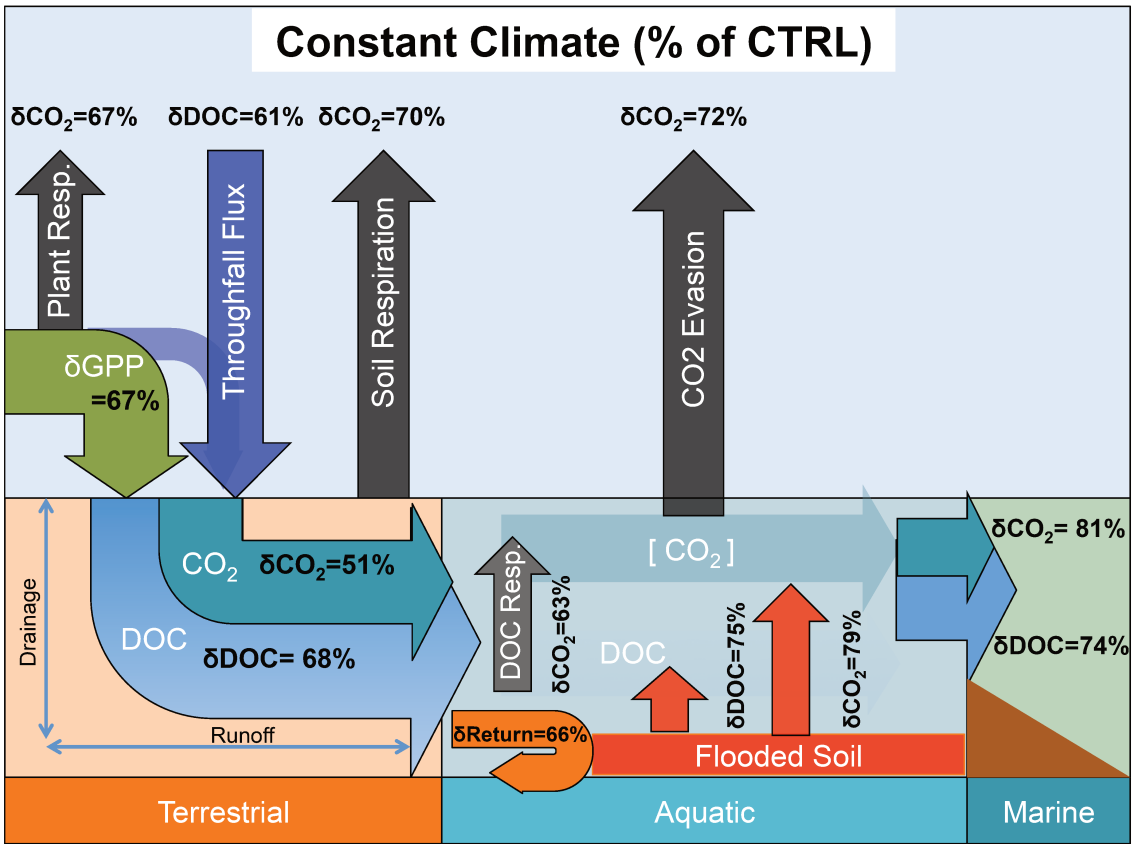
2720 First, all fluxes are lower in the factorial simulations, which can be expected due to
2721 lower carbon input to vegetation from the atmosphere (constant CO₂) and colder
2722 temperatures (constant climate) inhibiting more vigorous growth and carbon cycling.
2723 Second, broadly speaking, both climate and CO₂ appear to have similar effects on all
2724 fluxes, at least within the range of climatic and CO₂ values to which they have subjected
2725 the model in these historical runs. With regard to lateral export fluxes in isolation,
2726 variable climate (temperature increase) is a more powerful driver than CO₂ increase
2727 (see below). Third, the greatest difference between the constant climate and CO₂
2728 simulation carbon fluxes appear to be those associated with terrestrial inflow of
2729 dissolved matter to the aquatic network, these being more sensitive to climatic than CO₂
2730 variability. This is evidenced by a 49% and 32% decline in CO₂ and DOC export,
2731 respectively, from the land to rivers in the constant climate simulation, versus a 27%
2732 and 23% decline in these same variables in the constant CO₂ simulation. Given that the
2733 decline in primary production and respiration in both factorial simulations was roughly
2734 the same, this difference in terrestrial dissolved input is attributable to the effect of
2735 climate (increased temperatures) on the hydrological cycle, driving changes in lateral
2736 export fluxes.
2737

2738 This would imply that at these carbon dioxide and climatic ranges, the modelled DOC
2739 inputs are slightly more sensitive to changes in the climate rather than to changes in
2740 atmospheric carbon dioxide concentration and the first order biospheric response to
2741 this. However, while the model biospheric response to carbon dioxide concentration
2742 may be linear, thresholds in environmental variables such as MAAT may prove to be
2743 tipping points in the system's emergent response to change, as implied by Fig. 9,
2744 meaning that the Lena, as with the Arctic in general, may soon become much more
2745 temperature-dominated, with regard to the drivers of its own change.

2746 (a)



2747
2748 (b)



2749
2750 (c)

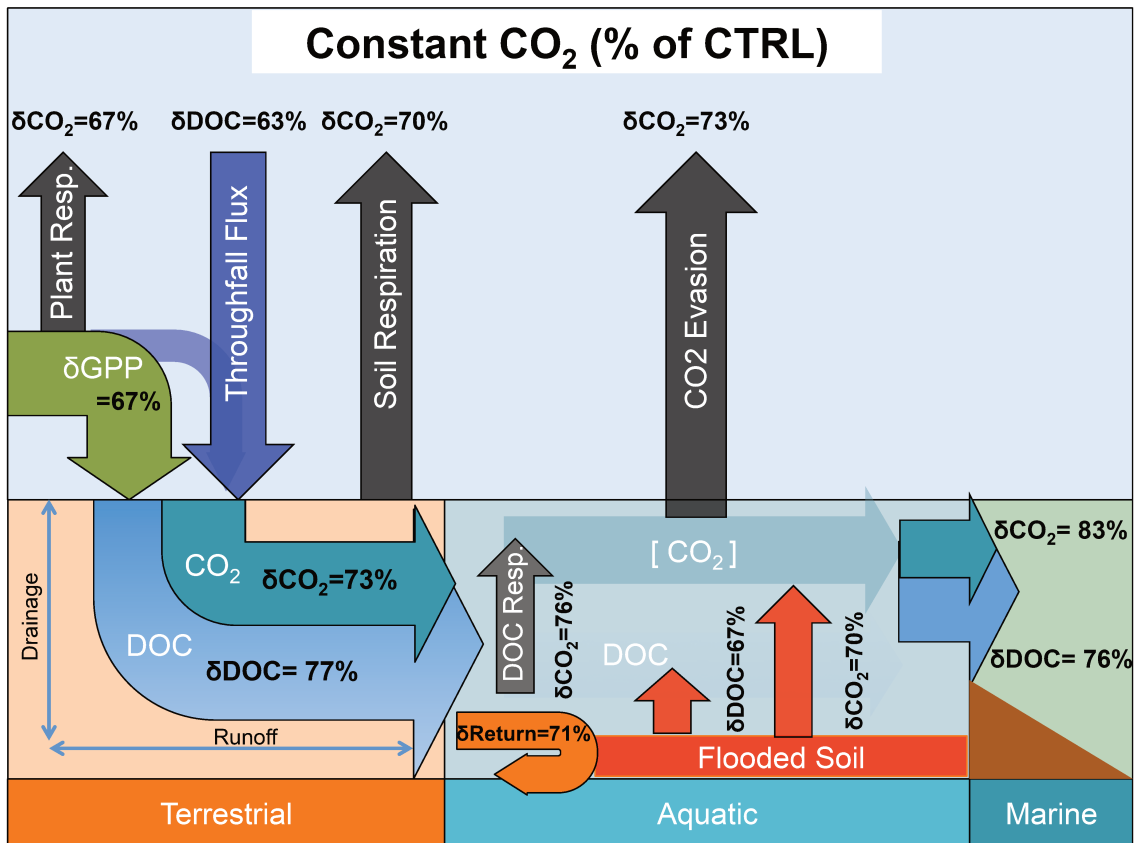


Figure 12: (a) Simplified 'leaky pipe' diagram representing the transport and processing of DOC within the land-ocean hydrologic continuum. The scheme template is taken from Cole et al. (2007), where we reproduce their global estimate of DOC and non-groundwater discharge portion of this flow in the top panel (PgC yr⁻¹), and the equivalent flows from our Lena basin simulations in TgC yr⁻¹ in the bottom panel. Thus easy comparison would look at the relative fluxes within each system and compare them to the other. **(b-c):** Schematic diagrams detailing the major yearly carbon flux outputs from simulations averaged over the period 1998-2007 as they are transformed and transported across the land-aquatic continuum. Figures **(b)** and **(c)** give the same fluxes as a percentage difference from the Control (CTRL-Simulation), for the constant climate and CO₂ simulations, respectively.

4.8.3 LOAC export flux considerations

Despite our simulations' agreement with observations regarding the proportional fate of terrestrial DOC inputs as evasion and marine export (Section 4.8.1, Fig. 12a), our results suggest substantial and meaningful differences in the magnitude of those fluxes relative to NPP in the Lena, compared to those estimated by other studies in temperate or tropical biomes. Our simulations' cumulative DOC and CO₂ export from the terrestrial realm into inland waters is equivalent to ~1.5 % of NPP.

This is considerably lower than Cole et al. (2007) and Regnier et al. (2013) who find lateral transfer to approximate ~5% (1.9PgC yr⁻¹) of NPP at the global scale, while Lauerwald et al. (2017)(Lauerwald et al., 2017) found similar rates for the Amazon. The cause of this discrepancy with our results is beyond the scope of this study to definitively address, given the lack of tracers for carbon source and age in our model. Nonetheless, our analysis leads us to hypothesise the following.

2778
2779 Temperature limitation of soil microbial respiration at the end of the growing season
2780 (approaching zero by October, SI Fig. S4d) makes this flux negligible from November
2781 through May (SI Fig. S4d). In late spring, mobilisation of organic carbon is performed by
2782 both microbial respiration and leaching of DOC via runoff and drainage water fluxes.
2783 However, because the latter are controlled by the initial spring meltwater flux period,
2784 which occurs before the growing season has had time to produce litter or new soil
2785 carbon (May-June, Fig. 4b), aggregate yearly DOC transport reactivity is characterised by
2786 the available plant matter from the previous year, which is overwhelmingly derived
2787 from recalcitrant soil matter (Fig. 11a) and is itself less available for leaching based on
2788 soil carbon residence times.

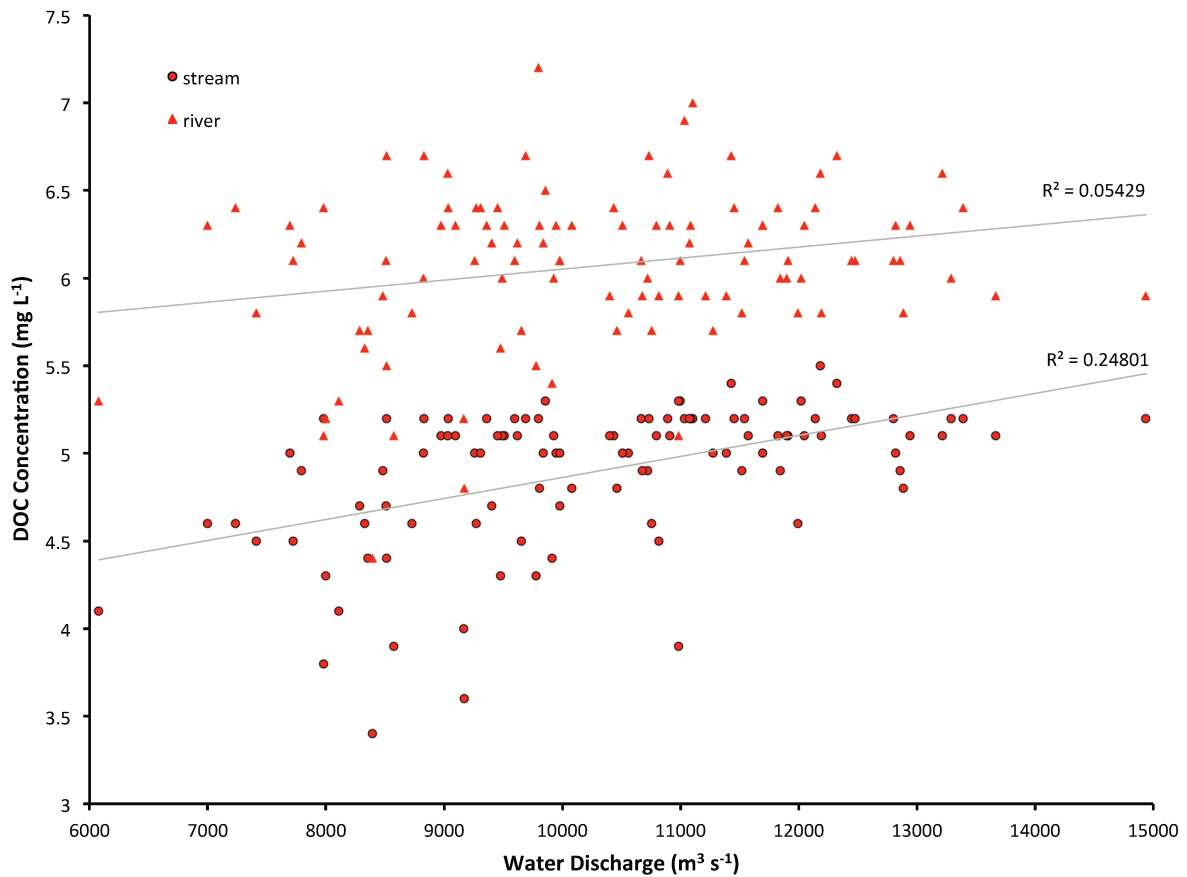
2789
2790 This causes relatively low leaching rates and riverine DOC concentrations (e.g. Fig. 9), as
2791 compared to the case of leaching from the same year's biological production.
2792 Highlighting this point are floodplains' domination by labile carbon sourced from that
2793 year's production with a mean DOC concentration of 12.4 mgC L⁻¹ (1998-2007 average),
2794 with mean riverine DOC concentrations around half that value (6.9 mgC L⁻¹).
2795 Nonetheless the May-June meltwater pulse period dominates aggregate DOC discharge.
2796 As this pulse rapidly subsides by late July, so does the leaching and transport of organic
2797 matter. Warmer temperatures come in conjunction with increased primary production
2798 and the temperature driven soil heterotrophic degradation of contemporary and older
2799 matter (via active layer deepening). These all indicate that transported dissolved matter
2800 in rivers, at least at peak outflow, is dominated by sources originating in the previous
2801 year's primary production, that was literally 'frozen out' of more complete
2802 decomposition by soil heterotrophs.

2803
2804 Further, we infer from the fact that all of our simulation grid cells fall within areas of low
2805 (<-2°C) MAAT, far below the threshold MAAT (>3°C) proposed by Laudon et al. (2012)
2806 for soil respiration-dominated carbon cycling systems (Fig. 9), that the Lena is
2807 hydrologically-limited with respect to DOC concentration and its lateral flux. Indeed, the
2808 seasonal discharge trend of the Lena –massive snowmelt-driven hydrological and
2809 absolute DOC flux, coupled with relatively low DOC concentrations at the river mouth
2810 (Fig. 4b, simulation data of Fig. 9), are in line with the Laudon et al. (2012) typology.

2811
2812 We therefore suggest that relatively low lateral transport (as %NPP) in our simulations
2813 compared to other biomes is driven by meltwater (vs. precipitation) dominated DOC
2814 mobilisation, which occurs during a largely pre-litter deposition period of the growing
2815 season. DOC is then less readily mobilised by being sourced from recalcitrant matter,
2816 leading to low leaching concentrations relative to those from labile material. As
2817 discharge rates decline, the growing season reaches its peak, leaving carbon
2818 mobilisation of fresh organic matter to be overwhelmingly driven by in situ
2819 heterotrophic respiration.

2820
2821 While we have shown that bulk DOC fluxes scale linearly to bulk discharge flows (Fig.
2822 3d), DOC concentrations (mgC L⁻¹) hold a more complex and weaker positive
2823 relationship with discharge rates, with correlation coefficients (R²) of 0.05 and 0.25 for
2824 river and stream DOC concentrations, respectively (Fig. 13). This implies that while
2825 increasing discharge reflects increasing runoff and an increasing vector for DOC

2826 leaching, particularly in smaller tributary streams, by the time this higher input of
 2827 carbon reaches the river main stem there is a confounding effect of dilution by increased
 2828 water fluxes which reduces DOC concentrations, explaining the difference between
 2829 stream and river discharge vs. DOC concentration regressions in the Figure. Thus, and
 2830 as a broad generalisation, with increasing discharge rates we can also expect somewhat
 2831 higher concentrations of terrestrial DOC input to streams and rivers. Over the
 2832 floodplains, DOC concentrations hold no linear relationship with discharge rates
 2833 ($R^2=0.003$, SI Fig. S5), largely reflecting the fact that DOC leaching is here limited by
 2834 terrestrial primary production rates more than by hydrology. To the extent that
 2835 floodplains fundamentally require flooding and hence do depend on floodwater inputs
 2836 at a primary level, we hypothesise that DOC leaching rates are not limited by that water
 2837 input, at least over the simulated Lena basin.
 2838



2839 **Figure 13:** Simulated basin-mean annual DOC concentrations (mg L^{-1}) for the stream and river water
 2840 pools regressed against mean annual simulated discharge rates ($\text{m}^3 \text{s}^{-1}$) at Kusur over 1901-2007. Linear
 2841 regression plots with corresponding R^2 values are shown.
 2842
 2843

2844 As discussed above simulated DOC and CO_2 export as %NPP was 1.5% over 1998-2007.
 2845 However, this proportion appears to be highly dynamic at the decadal timescale. As
 2846 shown in Fig. 11b, all lateral flux components in our simulations increased their relative
 2847 throughput at a rate double to triple that of NPP or respiration fluxes over the 20th
 2848 century, also doing so at a rate substantially higher than the rate increase in discharge.
 2849 In addition, differentials of these lateral flux rates with the rates of their drivers
 2850 (discharge, primary production) have on average increased over the century (Fig. 11b).

2851 This suggests that there are potential additive effects of the production and discharge
2852 drivers of lateral fluxes that could lead to non-linear responses to changes in these
2853 drivers as the Arctic environment transforms, as suggested by the Laudon et al.
2854 (2012)(Laudon et al., 2012) data plotted in Fig. 4. Acceleration of the hydrological cycle
2855 compounded by temperature and CO₂ -driven increases in primary production could
2856 therefore increase the amount of matter available for leaching, increase the carbon
2857 concentration of leachate, and increase the aggregate generation of runoff to be used as
2858 a DOC transport vector. Given that these causal dynamics apply generally to permafrost
2859 regions, both low lateral flux as %NPP and the hypothesised response of those fluxes to
2860 future warming may be a feature particular to most high latitude river basins.

2861

2862 **5. Conclusion**

2863

2864 This study has shown that the new DOC-representing high latitude model version of
2865 ORCHIDEE, ORCHIDEE MICT-LEAK, is able to reproduce with reasonable accuracy
2866 modern concentrations, rates and absolute fluxes of carbon in dissolved form, as well as
2867 the relative seasonality of these quantities through the year. When combined with a
2868 reasonable reproduction of real-world stream, river and floodplain dynamics, we
2869 demonstrate that this model is a potentially powerful new tool for diagnosing and
2870 reproducing past, present and potentially future states of the Arctic carbon cycle. Our
2871 simulations show that of the 34 TgC yr⁻¹ remaining after GPP is respired autotrophically
2872 and heterotrophically in the Lena basin, over one-fifth of this captured carbon is
2873 removed into the aquatic system. Of this, over half is released to the atmosphere from
2874 the river surface during its period of transport to the ocean, in agreement with previous
2875 empirically-derived global-scale studies. Both this transport and its transformation are
2876 therefore non-trivial components of the carbon system at these latitudes that we have
2877 shown are sensitive to changes in temperature, precipitation and atmospheric CO₂
2878 concentration. Our results, in combination with empirical data, further suggest that
2879 changes to these drivers –in particular climate –may provoke non-linear responses in
2880 the transport and transformation of carbon across the terrestrial-aquatic system's
2881 interface as change progresses in an Arctic environment increasingly characterised by
2882 amplified warming.

2883

2884

2885

2886

2887

2888

2889

2890

2891

2892

2893

2894

2895

2896

2897

2898

Chapter 4

Arctic lateral carbon fluxes decline with future warming³.

Summary

Release of dissolved organic carbon (DOC) from Arctic soils has been the focus of extensive empirical work over the last decade, with results suggesting that the future thawing of permafrost soils may increase the export of DOC by rivers to Arctic seas. However, to date no studies have reconciled theory and observation with *predictions* of Arctic lateral transport response to anthropogenic forces, owing to the lack of global climate models able to address the complexities of both permafrost soil physics and the mechanics of carbon lateral transport.

Using ORCHIDEE MICT-LEAK, a global-scale land surface model built specifically for addressing this omission (Chapter 1), and successfully evaluated previously for a single permafrost-region river basin (the Lena –Chapter 2), we conduct simulations spanning the 20th and 21st centuries (1898-2099) over the entire Pan-Arctic region (> 45°N), under the Intergovernmental Panel on Climate Change (IPCC) ‘RCP 6.0’ future (intermediate-range) warming scenario, at a one degree grid-cell resolution. Unlike in Chapter 2, which uses a reanalysis data product to drive the model, future simulations require simulated future climate, land cover and vegetation data to drive them, and are thus necessarily modelling product-driven. This results in some differences in simulated outputs compared with output driven by data used in Chapter 2, driven largely by hydrological and primary production differences. Nonetheless, the model again broadly reproduces modern day bulk riverine DOC fluxes and concentrations that exist in the sparse data record for these regions.

Over the 21st century, our simulations project that mean annual air temperature, CO₂ and precipitation increases relative to the mean of 1996-2005 drive large-scale changes in primary production, biome-scale respiration and soil carbon losses, consistent with the notions that warming will lead to widespread metabolisation of permafrost carbon, and that the latter exceeds increases in carbon uptake by vegetation. Despite this strengthening of the carbon and water cycle, we show that contrary to first-order empirical expectations arising from their trends, lateral carbon flows over the Pan-Arctic decline under RCP6.0 by 2100. This is caused by the complex interaction of temperature with precipitation, soil hydrology and leaching substrate, causing DOC flux temperature response to oscillate in magnitude and sign.

The causes of this result are complex, but are generally driven by deepening hydrological flowpaths resulting from thaw of the permafrost ‘cap’ on drainage water flows with increases in temperature. Thaw allows drainage of water to depth, which, coupled with increasing soil temperatures, permits increasing water infiltration into the soil, higher rates of soil respiration at depth, and subsequently lower concentrations of carbon in the water-leachate fluxes produced by the deeper hydrological flowpaths. By

³ Manuscript being prepared for submission to *Nature Climate Change*.

2944 partitioning the aggregate precipitation water flux in favour of infiltration flows, these
2945 flows are further exposed to leaching substrate with a lower carbon concentration than
2946 those that exist at the soil surface, which correspond to recently-produced soil and litter
2947 matter. Finally, despite an increase in overall precipitation, we hypothesise that the
2948 timing and phase-state of precipitation, drives decreases in DOC flux. Decreasing
2949 snowfall in winter and increasing rainfall in late summer demote and promote the
2950 massive post-winter leaching flux of contemporary carbon, and that of deeper, lower
2951 carbon concentration matter, owing to the deeper active layer and water infiltration
2952 regime during this time, respectively, also driving a decline in bulk lateral carbon fluxes.
2953 This result appears to be a general result of warming of the permafrost region, and
2954 further justifies the necessity of using a model specifically created for representing high-
2955 latitude conditions in making these projections. Indeed, whereas the temperature
2956 sensitivity of soil carbon release from the Arctic is unequivocally positive, our
2957 simulations show that for lateral carbon fluxes the temperature sensitivity increases and
2958 decreases in both magnitude and sign, owing to the response of carbon mobilisation to
2959 threshold changes in active layer depth that promote hysteresis as an emergent
2960 response.

2961
2962
2963
2964
2965
2966
2967
2968
2969
2970
2971
2972
2973
2974
2975
2976
2977
2978
2979
2980
2981
2982
2983
2984
2985
2986
2987
2988
2989
2990
2991

Chapitre 4

Les flux de carbone latéraux dans l'Arctique diminuent avec le réchauffement futur.

Résumé

La libération de carbone organique dissous (COD) des sols arctiques a fait l'objet de nombreux travaux empiriques depuis une décennie environ avec des résultats suggérant que le dégel futur des sols de pergélisol pourrait accroître les exportations de COD par les rivières vers les mers arctiques. Cependant, à ce jour, aucune étude n'a concilié théorie et observation avec les prévisions de la réponse du transport latéral arctique aux forces anthropiques, en raison de l'absence de modèles climatiques globaux capables de traiter les complexités de la physique des sols du pergélisol et de la mécanique du transport latéral du carbone.

En utilisant ORCHIDEE MICT-LEAK, un modèle de surface terrestre à l'échelle mondiale construit spécifiquement pour remédier à cette omission (chapitre 1) et déjà évalué avec succès pour un seul bassin hydrographique de la région de pergélisol (Lena –Chapitre 2), nous effectuons des simulations couvrant la 20^{ième} et 21^{ième} siècles (1898-2099) sur l'ensemble de la région panarctique ($> 45^\circ \text{N}$), dans le cadre du scénario de réchauffement futur du Groupe d'experts intergouvernemental sur l'évolution du climat (GIEC) 'RCP 6.0'. Contrairement au chapitre 2, qui utilise un produit de réanalyse pour piloter le modèle, les simulations futures nécessitent des données simulées sur le climat, la couverture terrestre et la végétation pour les piloter, et sont donc nécessairement modélisées à partir de produits. Cela entraîne certaines différences dans les résultats simulés par rapport aux résultats tirés des données utilisées au chapitre 2, en grande partie dus aux différences hydrologiques et de production primaire. Néanmoins, le modèle reproduit à nouveau de manière générale les flux et les concentrations de COD fluviales modernes de ces régions.

Au 21^{ième} siècle, nos simulations prévoient que la température moyenne annuelle de l'air, les émissions de CO_2 et les précipitations augmentent par rapport à la moyenne de 1996-2005, entraînant des changements à grande échelle dans la production primaire, la respiration à l'échelle du biome et les pertes de carbone du sol, conformément aux notions de réchauffement, entraînera une métabolisation généralisée du carbone du pergélisol, et que ce dernier dépasserait l'augmentation de l'absorption de carbone par la végétation. Malgré ces accélérations des cycles du carbone et de l'eau, nous montrons que, contrairement aux attentes empiriques de premier ordre découlant de leurs tendances, les flux de carbone latéraux serait stable sous un scénario RCP6.0 d'ici 2100. Ceci est dû à l'interaction complexe des températures avec les précipitations, l'hydrologie du sol et le substrat de lessivage, entraînant une variation de la réponse de la température du flux de COD en amplitude et en signe.

Les causes de ce résultat sont complexes, mais sont généralement dues à l'approfondissement des voies hydrologiques résultant du dégel de pergélisol et son impact sur les eaux de drainage lorsque la température augmente. Le dégel permet de drainer l'eau en profondeur, ce qui, associé à l'augmentation de la température du sol, permet une infiltration croissante de l'eau dans le sol, un taux plus élevé de respiration du sol en profondeur et, par la suite, une diminution des concentrations de carbone dans les flux de lixiviat d'eau produits par les

3040 sillons hydrologiques plus profonds. . En diminuant en proportion les flux de ruissèlement de
3041 surface par rapport aux flux de drainage, ces flux d'eau sont en outre exposés à un substrat
3042 présentant une concentration en carbone inférieure à celle existant à la surface du sol, ce qui
3043 correspond au sol et à la litière récemment produits. Enfin, malgré une augmentation des
3044 précipitations globales, nous émettons l'hypothèse que le moment et l'état de phase des
3045 précipitations entraînent une diminution du flux de COD. La diminution des chutes de neige
3046 en hiver et des précipitations croissantes en fin d'été rétablit et favorise le flux de lixiviation
3047 massif post-hiver du carbone contemporain, ainsi que celui des matières à plus faible
3048 concentration de carbone, en raison de la couche active plus profonde et du régime
3049 d'infiltration d'eau pendant cette période, respectivement, entraînant également une
3050 diminution des flux de carbone latéraux massifs.

3051
3052 Ce résultat semble être un résultat général du réchauffement de la région de pergélisol et
3053 justifie en outre la nécessité d'utiliser un modèle créé spécifiquement pour représenter les
3054 conditions de haute latitude lors de la réalisation de ces projections. En effet, alors que la
3055 sensibilité à la température du dégagement de carbone du sol de l'Arctique est très positive,
3056 nos simulations montrent que, pour les flux de carbone latéraux, la sensibilité à la température
3057 augmente et diminue en valeur et en signe, en raison de la réponse de la mobilisation du
3058 carbone à des changements de seuil dans la couche active, profondeur qui favorise l'hystérésis
3059 en tant que réponse émergente.

3060
3061
3062
3063
3064
3065
3066
3067
3068
3069
3070
3071
3072
3073
3074
3075
3076
3077
3078
3079
3080
3081
3082
3083
3084
3085
3086
3087

3088 **Introduction**

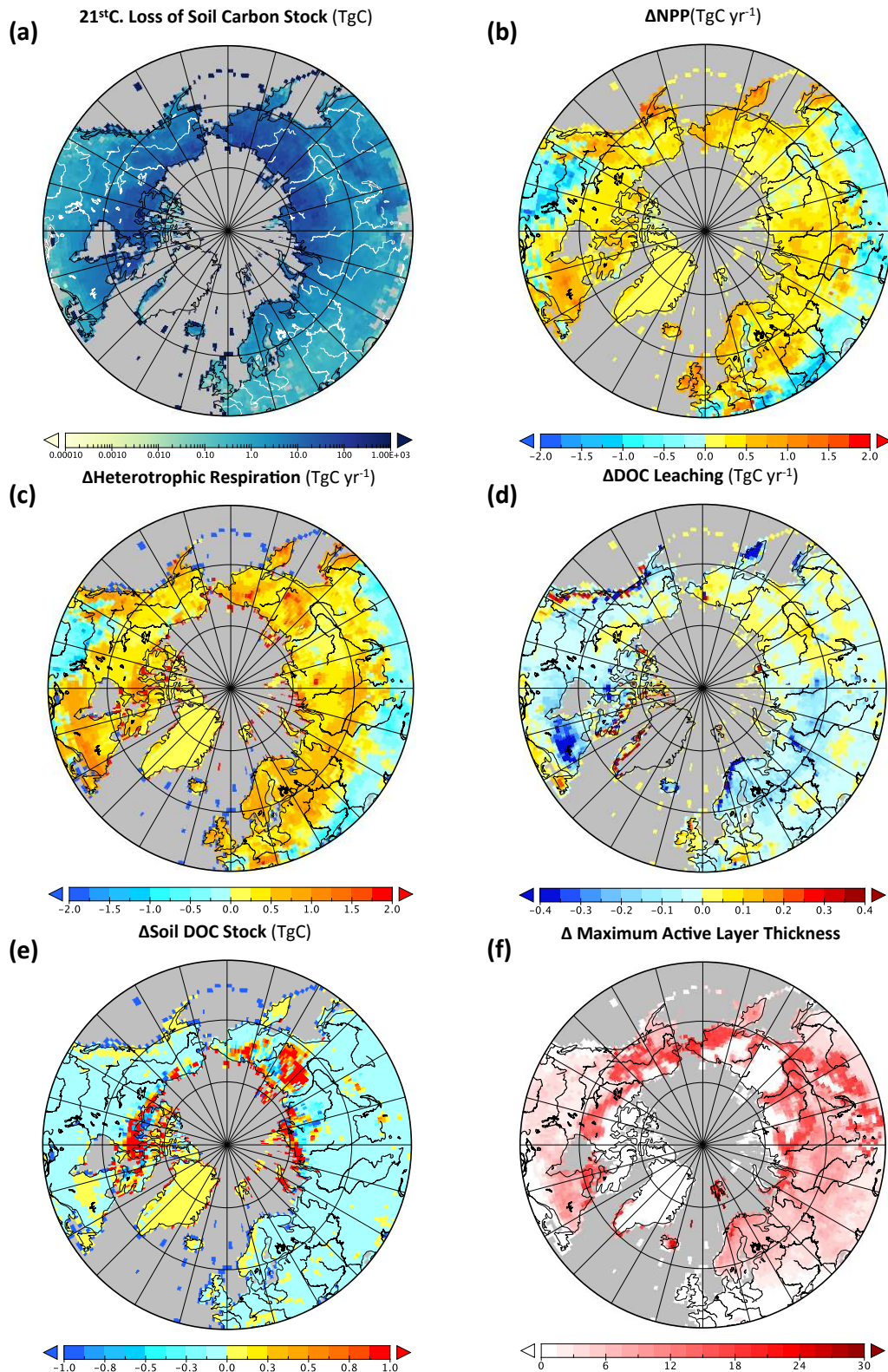
3089
3090 High-latitude permafrost soils contain large amounts of frozen, often ancient and
3091 relatively reactive carbon down to depths of over 30m. Permafrost profoundly affects
3092 Arctic river hydrology. A permanently frozen soil layer acts as a barrier to groundwater,
3093 so that surface and shallow sub-surface runoff dominates basin-scale waterflow,
3094 increasing the inter-seasonal variability of river discharge(Ye et al., 2009). This
3095 concentration of water volume near the surface during the thawing season is
3096 exacerbated by the accumulation of snow and ice in winter that subsequently melt
3097 during the spring freshet(Drake et al., 2015; Spencer et al., 2015) and cause intense
3098 leaching of DOC from the topsoil(O'Donnell et al., 2016). The spring pulse of DOC
3099 contains mostly modern river carbon(Aiken et al., 2014) and dominates the bulk annual
3100 DOC flux(Holmes et al., 2012) to the Arctic Ocean (25-36 TgC yr⁻¹)(McClelland et al.,
3101 2008). The pronounced seasonality in river flow also drives the summertime inundation
3102 of the floodplain regions(Smith and Pavelsky, 2008), whose subsequent recession spurs
3103 the lateral transport of terrestrial carbon(Zubrzycki et al., 2013). These dynamics may
3104 be subject to amplification by recent and future climate change(Frey and McClelland,
3105 2009; Tank et al., 2018). It is generally expected that rising temperature and enhanced
3106 precipitation(Peterson et al., 2002) will increase streamflow and total energy
3107 flux(Lammers et al., 2007) and drive an earlier onset of discharge peak(Van Vliet et al.,
3108 2012, 2013).

3109
3110 Soil warming can be expected to destabilize soil carbon stocks(Schuur et al., 2015) as
3111 active layer deepening exposes old/ancient soil horizons to leaching and
3112 transport(Spencer et al., 2015; Vonk et al., 2015c); once mobilised, these carbon
3113 compounds appear to be rapidly metabolized in headwater streams(Drake et al., 2015),
3114 and may constitute a significant fraction of CO₂ evasion (40-84 TgC yr⁻¹(McGuire et al.,
3115 2009)) from Arctic rivers(Vonk et al., 2013). Increasing trends in temperature, soil
3116 moisture/snow thaw(McClelland et al., 2004) and microbial activity(Hollesen et al.,
3117 2015; Schuur et al., 2009) may converge to raise soil leaching and dissolved
3118 organic(Frey and Smith, 2005) and inorganic carbon(Drake et al., 2018; Tank et al.,
3119 2012c) export rates into the future. The resulting increase in dissolved and particulate
3120 carbon delivery to the Arctic Ocean could lead to local decreases in ocean CO₂
3121 uptake(Manizza et al., 2011) and seawater acidification(Semiletov et al., 2016),
3122 conversely contributing to local primary production(Le Fouest et al., 2018): factors all
3123 amplified by the Arctic Ocean's high surface area:volume ratio(Jakobsson, 2002).

3124
3125 Despite its importance as both a vehicle for permafrost carbon mobilisation and its
3126 effects on the Arctic Ocean, to date, no attempt has been made to mechanistically
3127 quantify the Pan-Arctic response of permafrost-region litter/soil carbon leaching and
3128 subsequent lateral transport/evasion to rising temperatures. This omission owes itself to
3129 the complexity of representing the interacting processes alluded to above at large scale,
3130 which would have to include vegetation and physical processes for high latitude cryo-
3131 phenomena, and the leaching and cycling of DOC and CO₂, along the terrestrial-aquatic
3132 continuum. This study fills that gap by subjecting a state-of-the-art global land surface
3133 model (ORCHIDEE MICT-LEAK) built and evaluated specifically for representing these
3134 processes (see Methods and Bowring et al. (2019a, 2019b)), to historical and future

3135 climate change under the IPCC RCP6.0 (“no mitigation”) scenario over the Arctic (45-
3136 90N) at 1° resolution.
3137
3138

Results



3139
3140 **Figure 1:** Maps of changes in variables over the 21st century. **(a)** Aggregate loss (TgC) of soil carbon over
3141 2000-2099; **(b-f):** changes in variables between the mean of (2090-2099) subtracted by that of (1996-

3142 2005) in each pixel for **(b)** NPP (TgC yr⁻¹) **(c)** Heterotrophic soil respiration (TgC yr⁻¹), **(d)** DOC leaching,
 3143 (TgC yr⁻¹) **(e)** Soil DOC stock (TgC) **(f)** Maximum active layer thickness (m).

3144

3145 **21st Century changes and annualised outflow**

3146 Over the course of the 21st Century, simulations show that whereas bulk soil carbon loss
 3147 is concentrated over the coldest regions of the northern hemisphere (Fig. 1a),
 3148 heterotrophic respiration increases are greatest in warmer (and fastest-warming (SI,
 3149 Fig.S5e,f) areas like Sweden and western Siberia (Fig. 1c). This spatial difference arises
 3150 from large increases in net primary production (NPP) in the warmer regions (Fig. 1b)
 3151 and therefore higher litter production rates. DOC leached from the soil to rivers (Fig.
 3152 1d) generally increases in the in northern N. America and Eastern Siberia, where
 3153 permafrost coverage is highest and temperatures are lower, but decreases substantially
 3154 in western Siberia, Sweden and Eastern Canada. Indeed, where the change in annual-
 3155 mean ‘active layer’ (thawed soil) thickness was near zero (Fig.1f), the soil column
 3156 experienced large-scale increases in DOC stock over the 21stC, decreasing almost
 3157 everywhere else (Fig.1e). Furthermore, areas of negligible soil thawing are bounded on
 3158 the southern edges by regions that experienced huge increases in annualised thaw
 3159 depth over the century. This suggests that the transition from ‘continuous’ to
 3160 discontinuous or sporadic permafrost responds in a highly non-linear manner to
 3161 climatic change, for which soil thermodynamics appear to hold a threshold in reponse,
 3162 examined in greater detail below.

3163

3164

3165 **Table 1:** Simulated and observation-based estimates(Holmes et al., 2012) of DOC discharge by the ‘Big
 3166 Six’, and ‘Medium 9’ river basins. as well as discharge from the remaining Arctic watershed to give the
 3167 Pan-Arctic river outflow (see Methods). All values are in TgC yr⁻¹. Also shown are the mean annual sum of
 3168 soil and floodplain DOC and CO₂ input to the Big Six rivers, and CO₂ evasion from their respective water
 3169 surfaces. Simulated values encompass the mean of the temporal range covering the turn of the millenium
 3170 (1996-2005) and the last decade of simulation (2090-2099).

	Simulated		Observed	Simulated
	DOC to Ocean (1996-2005)	DOC to Ocean (Holmes et al., 2012)	DOC to Ocean (Holmes et al., 2012)	DOC to Ocean (2090-2099)
Big Six	Kolyma	1.12 ±0.24	0.82	1.19±0.26
	Lena	4.14 ±0.30	5.68	4.27 ±0.43
	Yenisei	5.66 ±0.80	4.65	4.78 ±0.42
	Ob	5.07 ±0.70	4.12	2.38 ±0.61
	Mackenzie	2.19 ±0.27	1.38	1.67 ±0.23
	Yukon	1.19 ±0.14	1.47	1.11 ±0.22
	Total	19.36	18.11	15.40
Medium 9	Pechora	1.64 ±0.21	n/a	1.16 ±0.19
	Pyasina	0.76 ±0.13	n/a	0.75 ±0.17
	Verkhnyaya-Taymyra	0.49 ±0.10	n/a	0.37 ±0.07
	Khatanga	1.16 ±0.18	n/a	1.18 ±0.21
	Olenek	0.46 ±0.07	n/a	0.44 ±0.10
	Yana	0.21 ±0.05	n/a	0.21 ±0.06
	Indigirka	0.38 ±0.10	n/a	0.42 ±0.19
	Anadyr	0.77 ±0.13	n/a	0.94 ±0.13
	Kuskokwin	0.40 ±0.07	n/a	0.34 ±0.08
Total	6.27	n/a	5.80	
Remaining				
Total	6.43	n/a	6.44	
Pan-Arctic				
Total	32.06	34.04	27.64	

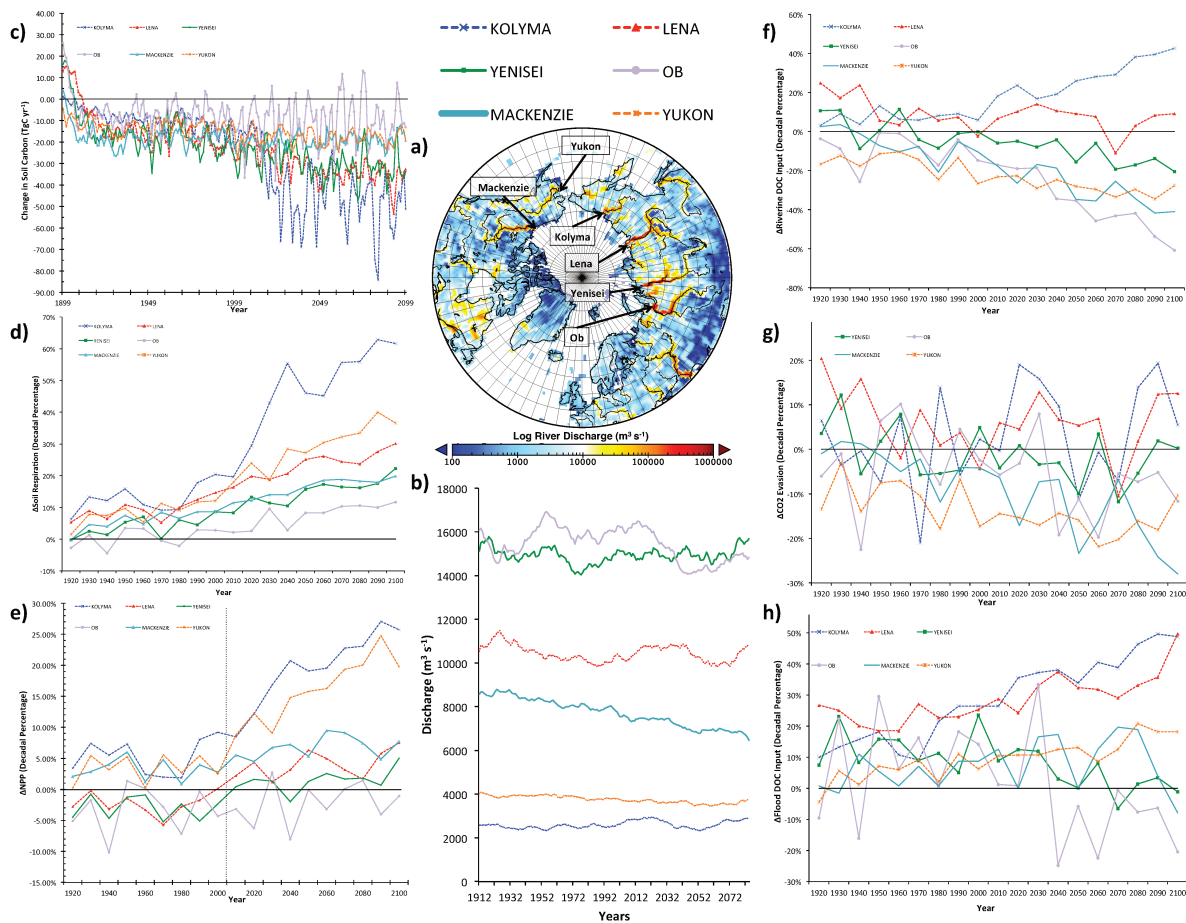
3171

3172

3173 Simulated modern annual DOC flux to the Arctic Ocean, a first order evaluation
 3174 constraint on model adequacy in representing dissolved carbon dynamics, is in broad
 3175 agreement with the existing observational literature(Holmes et al., 2012) (Table 1).

3176 Mean DOC discharge over the present day (1996-2005) for each of the Big Six rivers
 3177 (TgC yr⁻¹) is simulated (observed) to be 1.12 ±0.24 (0.82) for the Kolyma, 4.14 ±0.3
 3178 (5.68) for the Lena; 5.66 ±0.8 (4.65) for the Ob; 2.19±0.27 (1.38) for the Mackenzie; and
 3179 1.19 ±0.14 (1.47) for the Yukon. With the exception of the Lena and Mackenzie, our
 3180 model output falls within two standard deviations of observed fluxes. Simulations show
 3181 that DOC discharge of the 9 next-largest basins ('Medium 9', Table 1), which are largely
 3182 un-sampled for this metric, is about a third that of the Big 6 (~6 vs.~19 TgC yr⁻¹). For the
 3183 Pan-Arctic as a whole we estimate similar DOC discharge to that found in Holmes et al
 3184 (2012),(Holmes et al., 2012) of ~32 vs 34 TgC yr⁻¹, for simulations vs. observations. The
 3185 Supplement contains the full inland water budget breakdown for each basin (SI Fig.S2).
 3186

3188 Over the six basins, DOC discharge represents on average 55% (varying from 41-62%)
 3189 of total dissolved carbon input from the soil to streamflow
 3190 (runoff+drainage+floodplain), while the combined 'dissolved CO₂' (CO_{2(aq.)})+DOC
 3191 outflow (Table 1, Supplement Table S2) increases that fraction to 60%. On average,
 3192 31% (11-38%) of modelled dissolved C inputs are evaded to the atmosphere as CO₂ in
 3193 streams and rivers, with the remainder returning to the soil as 'reinfiltration'. This
 3194 evasion flux as a proportion of carbon inputs from soils is significantly lower than
 3195 global-scale estimates (~52%)(Cole et al., 2007), a consequence of the temperature-
 3196 dependence of CO₂ evasion(Lauerwald et al., 2015). Likewise, simulated dissolved
 3197 carbon influx to streamflow represents only 0.7% (range 0.5-0.9%) of NPP, substantially
 3198 lower than the global (5% of NPP(Cole et al., 2007; Regnier et al., 2013)) estimate.



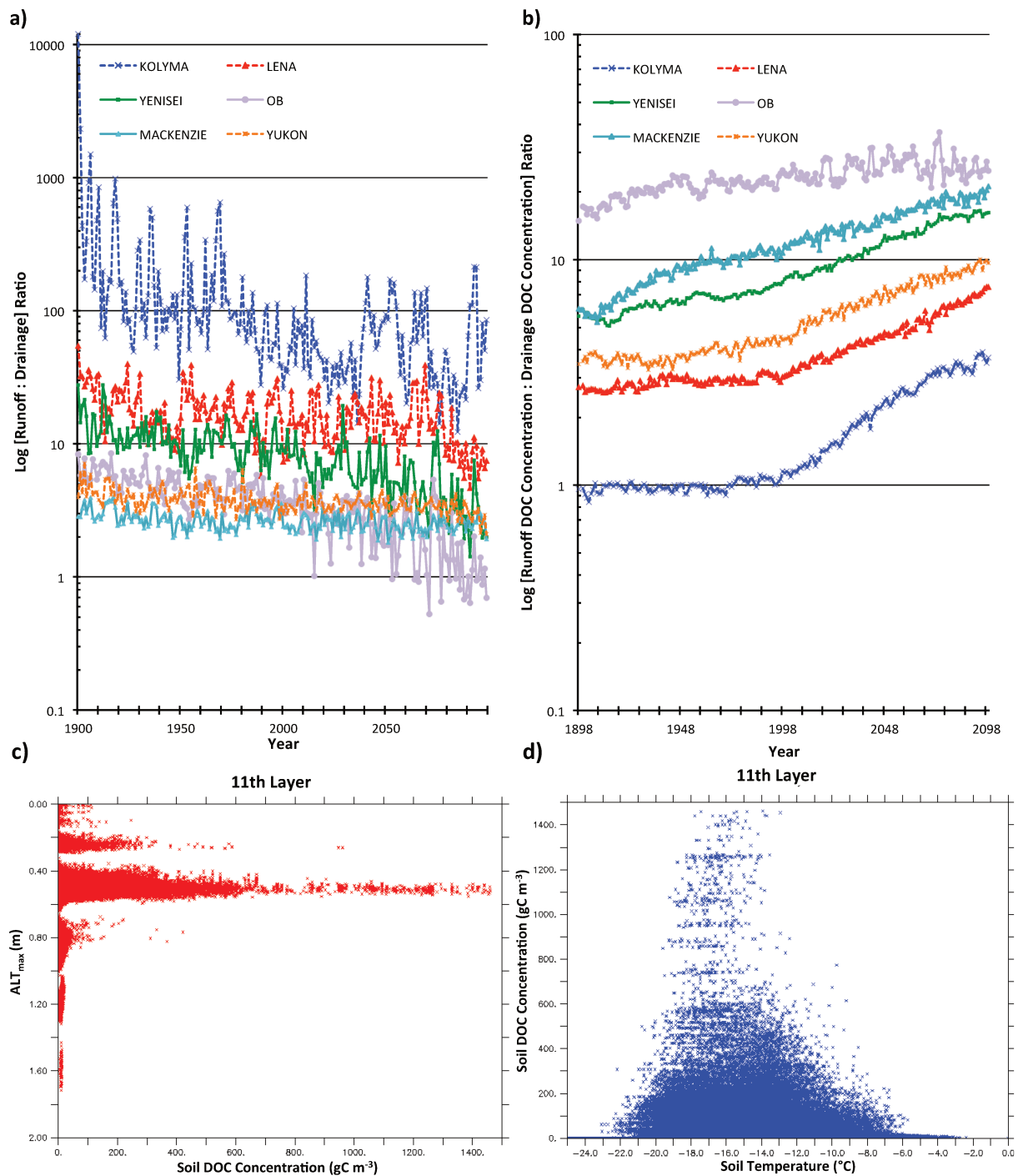
3199

3200 **Figure 2:** Basin-disaggregated timeseries of variables (periphery) and **(a)** a map of the Pan-Arctic
3201 (centre) with major river satellite overlay and mean river discharge plotted, and the Big Six river basins
3202 identified by outflow grid cell. **(b)** 30-year moving average of river discharge per basin ($\text{m}^3 \text{yr}^{-1}$); **(c)**
3203 Yearly change in total soil organic carbon (SOC) for each basin (TgC yr^{-1}); **(d-h):** These plots show the
3204 decadal-mean deviation (%) from a baseline of the first simulation decade (1901-1910), for each decade,
3205 for: **(d)** Soil respiration; **(e)** Net primary production (NPP); **(f)** Soil DOC inputs from runoff and drainage
3206 fluxes; **(g)** CO_2 evasion from the river surface; **(h)** Floodplain DOC input to the river.

3207
3208 Simulated future (2090-99, Table 1) DOC discharge relative to present day values
3209 increases slightly for the Kolyma (+7%) and Lena (+3%) basins, but declines
3210 significantly for the Yukon (-7%) and more substantially for the Yenisei (-16%), Ob (-
3211 53%) and Mackenzie (-37%). On average, this amounts to a decline of -13% for the Big
3212 6 and -13% for the PanArctic as a whole, over the 21st century. The following examines
3213 this general decline.

3214 **More carbon–less DOC**

3216
3217 From the first (1901-1910) to last (2090-2099) decade of the simulation, net primary
3218 production (NPP) increased for all basins except the Ob (Fig. 2e). Soil carbon respiration,
3219 changes that are proportionally 2-3 times that of NPP (Fig. 2d, Fig. S4), are partially
3220 explained by an increase of soil carbon decomposition inducing a loss in soil carbon
3221 stocks across basins (Fig. 2c). These flux trends point towards an accelerated Arctic soil
3222 carbon cycle, in line with expectations that increases in primary productivity will be
3223 more than outbalanced by increases in biome-scale respiration (Abbott et al., 2016).
3224 However, this does not translate into an increasing trend in riverine export of DOC from
3225 the soil (Fig. 2f), which generally decreases, except for in the case of the Kolyma basin.
3226 The Kolyma may carry the signal of substantial increases in permafrost soil carbon
3227 mobilisation, consistent with empirical data (Feng et al., 2017). Marked export decreases
3228 can be seen in the Ob, Yukon and Yenisei. Conversely, riverine DOC inputs from flooded
3229 regions either carry no trend (Ob, Yenisei) or clearly increase (Kolyma, Lena, Yukon),
3230 reflecting this fluxes' dependence on direct litter inputs and primary production.
3231 Previous studies have shown that DOC concentration and bulk flow scale positively with
3232 discharge (Lauerwald et al., 2017). These are largely volatile, bar a decrease in the
3233 Mackenzie (Fig. 2b, Fig. S8). Water discharge trends for the N. American and W. Siberian
3234 high latitudes are consistent with those from weighted predictions using global climate
3235 model ensembles (Yang et al., 2017). The high signal volatility of the Yenisei and Lena
3236 basins has also been suggested by the ensemble model output, however these also
3237 mostly suggest a modest discharge increase (<5-10%, RCP4.5-8.5, respectively) in these
3238 areas in the future. This discrepancy may arise from either reduced precipitation in the
3239 model forcing data, or in the enhanced evaporation and evapotranspiration arising from
3240 increased temperatures and primary production, respectively.



3241
 3242 **Figure 3:** Basin-disaggregated timeseries of (a) the yearly mean ratio of (runoff: drainage) water flux over
 3243 the basin; (b) yearly mean ratio of (runoff: drainage) DOC concentrations in those fluxes over the basin. (c-
 3244 d) The soil DOC concentration (gC m⁻³) at the model's 11th(2m) layer for each grid cell underlain by
 3245 continuous permafrost are plotted against (c) maximum active layer depth over the pixel and (d) mean
 3246 annual soil temperature.

3247
 3248 Where DOC fluxes purely controlled by runoff and river discharge in our simulations,
 3249 their trends would follow those of the hydrograph. Instead, a more subtle phenomenon
 3250 is at play. Over 1901-2099, Pan-Arctic soils warmed, permitting an increase in active
 3251 layer depth and the sudden onset of subsoil water intrusion (drainage) previously
 3252 inhibited by permafrost shielding. All Arctic basins experienced an order of magnitude

3253 increase in drainage relative to runoff water fluxes over the 200 years (Fig. 3a), where
3254 the absolute value of the ratio (runoff:drainage) positively reflects per-basin permafrost
3255 coverage. Simultaneously, the relative concentration of DOC in runoff relative to
3256 drainage water experienced a similar, ~5-fold increase (Fig. 3b) over that time, spurred
3257 by an increase in NPP (+runoff concentration), increased respiration of DOC with depth
3258 of its entrainment (drainage concentration decrease of -55 – -74%/200 yrs.), and
3259 changes in the seasonal precipitation phase and regime (+runoff). Absolute runoff DOC
3260 concentration ratio scales with relative basin permafrost coverage, while its rate of
3261 increase accelerates suddenly around the turn of the millenium for the Kolyma and Lena
3262 (most permafrost), indicating a basin-wide threshold in active layer thaw and drainage
3263 intrusion.

3264
3265 As the mean annual maximum active layer thickness (ALT_{max}) deepens, annual mean soil
3266 DOC concentrations at a depth of 2m initially increase (Fig. 3c) up to a thaw depth of
3267 ~50cm, before rapidly declining. Correspondingly, the 2m soil DOC concentration
3268 responds first positively then negatively to increases in the mean annual soil surface
3269 temperature (Fig. 3d), indicating that with increasing temperature, the soil DOC
3270 available for lateral transport declines as it is metabolised to CO_2 during the transport
3271 into the soil column. Furthermore, lower drainage DOC concentrations scale with lower
3272 soil particulate carbon concentrations at 2m depth (the depth at which lateral drainage
3273 flows occurs) compared to the top 40cm, where runoff DOC fluxes are generated (SI,
3274 Fig.S9). This lower substrate concentration leads to a lower leachate concentrations,
3275 while carbon concentrations are preferentially depressed at greater soil depths as
3276 warming proceeds over the 21st century. Similar dependencies between subsoil carbon
3277 fluxes and carbon concentration of their parent material have been found for lateral
3278 fluxes of permafrost particulate carbon (Feng et al., 2013).

3279
3280 Increased drainage input to rivers and lower relative concentration of DOC in drainage
3281 water combine to lower bulk DOC flow, despite a strengthened carbon cycle, aided by
3282 shifting precipitation dynamics. The rain:snowfall ratio increases substantially (SI, Fig.
3283 S12a), driven largely by the rain fraction (SI, Fig. S10). This increase largely occurs in
3284 mid-late summer (July-October, Fig. S13a-d), with two consequences for DOC: First, it
3285 amplifies soil and litter degradation where this is moisture-limited, decreasing the
3286 carbon pool build-up normally made available to DOC leaching in the spring snowmelt
3287 period, thus decreasing potential DOC input and outflow. Second, late summer
3288 corresponds to timing of maximum active layer depth, promoting increased soil water
3289 infiltration (feeding massive increases in wintertime groundwater flow (SI, Fig. S14) and
3290 lower bulk DOC outflow relative to the case of increased rainfall in e.g. spring (SI,
3291 Figs.S12,S13). The relationship of DOC export to rivers with snow and rainfall differs
3292 substantially between areas underlain by continuous and discontinuous permafrost (SI,
3293 Figs. S12c-f). In permafrost areas, DOC inputs generally increase with rain and snowfall
3294 and are more responsive to snowfall (SI, Figs.12c-d). In non-continuous permafrost
3295 gridcells, there is no correlation to snowfall and a strong correlation to rainfall (SI,
3296 Figs.12e-f). The inference is that the frozen soil layer and cold temperatures in general
3297 inhibit DOC flow up until a certain moment in time (late spring/early summer) when the
3298 thaw season permits a carbon 'flush'. This is why snow has no relationship with DOC
3299 inputs in non-permafrost areas, since DOC-mobilisation isn't limited by the thawing of a
3300 massive snowmelt-derived water flux.

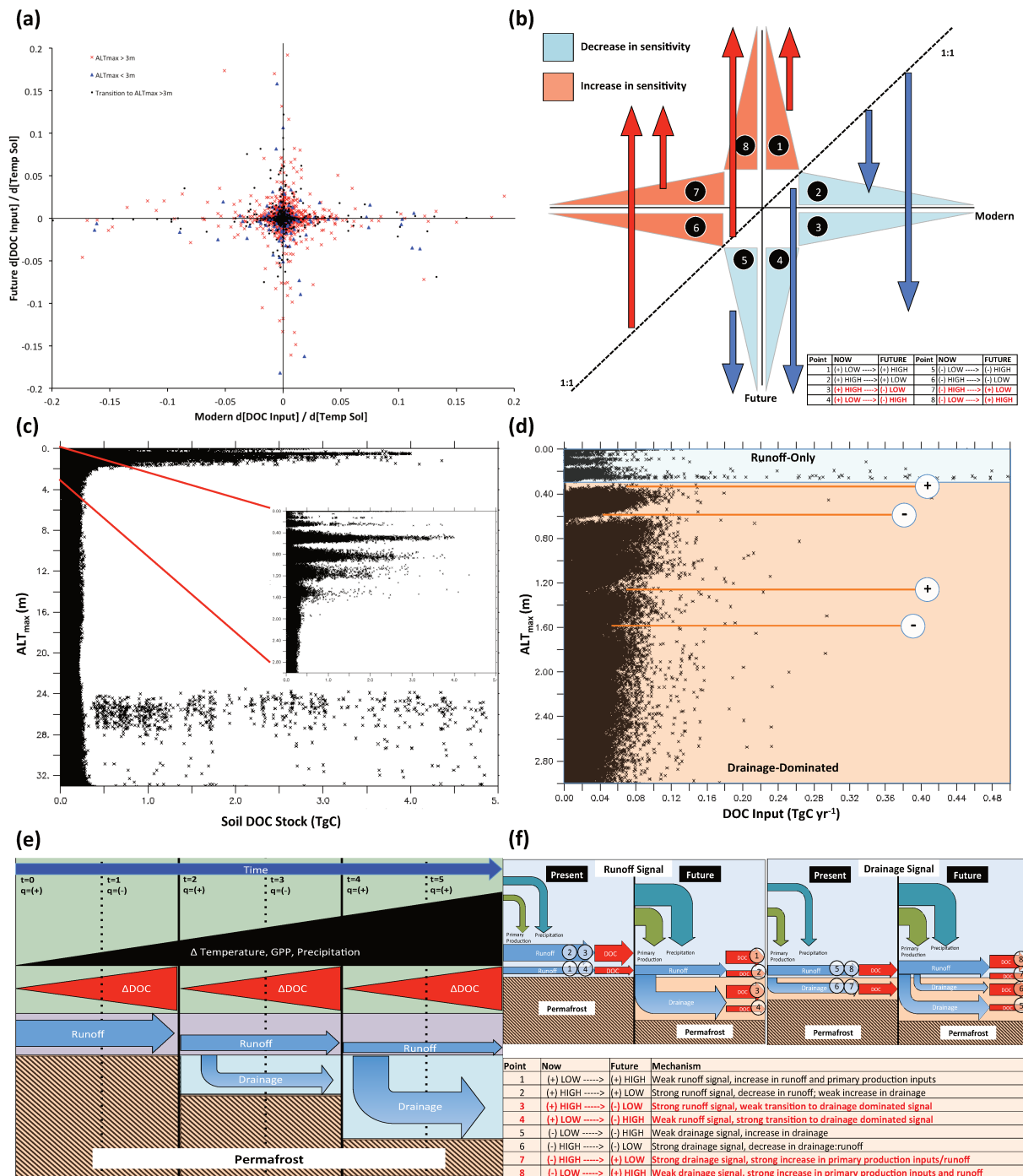
3301
3302
3303
3304
3305
3306
3307
3308
3309
3310
3311
3312
3313
3314
3315
3316
3317
3318
3319
3320
3321
3322
3323
3324
3325
3326
3327
3328
3329
3330
3331
3332
3333
3334
3335
3336
3337
3338
3339
3340
3341
3342
3343
3344
3345
3346
3347

DOC climate sensitivity

Soil-to-river dissolved carbon flux integrates a complex signal, dependent on the interactions between permafrost extent, precipitation, active layer thickness, soil carbon stock, soil type, topography and NPP. These dependencies vary strongly in both strength (R^2) and sign between basins (SI, Fig.S11), highlighting the differing combinations of their interaction. Whereas some basins (e.g., Ob) appear to be clearly driven over the entire simulation period in DOC and CO_2 input by the hydrologic and leaching effects of active layer deepening (SI, Fig.S11b,c,d), others like the Lena appear to lack any response to a full spectrum of drivers ($R^2 < 0.1$, SI, Fig.S11a-d) over the whole basin.

This signal between and within catchments is examined with respect to the prime driver of land surface changes, temperature. Sensitivity of combined runoff and drainage DOC exports to temperature for each grid cell grouped under 'permafrost' ($ALT_{max} < 3m$), 'non-permafrost' ($ALT_{max} > 3m$) and 'transitional' (transition from the former to latter over the 21stC, (SI, Fig.S4a) and averaged over the 'modern' (1996-2005) and 'future' (2020-2099)) are plotted against each other (Fig. 4a). DOC input temperature sensitivity between present and future does not follow any distinct pattern between the 3 permafrost groups, although the overall signal appears dominantly controlled by drainage response (SI, Fig. S15a,c). The fractal 'star'-shaped response space that results is broken down into an idealised present-future typology (Fig. 4b) to show why such distinct present versus future sensitivity pairings occur. Essentially, the response space indicates high volatility in temperature sensitivity between time periods, in which sensitivity either experiences a change in sign and strong or weak change in value (Fig. 4b, nodes 3,4,7,8), or no change in sign and strong or weak change in value (Fig. 4b, nodes 1,2,5,6).

The DOC input temperature sensitivity is captured by the response of DOC to changes in non-frozen soil or 'active layer' thickness. As temperatures increase, the active layer (ALT_{max}) deepens, causing greater entrainment of water and carbon into the soil. ALT_{max} represents both a temperature and 'DOC-mobilised' soil depth metric. Response of the soil DOC stock and DOC river input (the former the precursor to the latter) to active layer thickness is thus equivalent to a temperature response. This is sinusoidal as the active layer deepens for riverine DOC input and its precursor soil DOC (Figs. 4c,d), reflecting the temperature sensitivity space shown in Fig.4 a-b. The cause for the temperature sensitivity volatility is due to sequential changes in land surface dynamics idealised in Fig. 4e. As temperature, GPP, precipitation and soil carbon loss increase over time in areas underlain by continuous permafrost (no drainage), DOC inputs increase and sensitivity (q) is positive (Fig. , $t=0 \rightarrow t=1$), but at a temperature threshold ($t=2$), one soil layer thaws, permitting drainage and causing reduced bulk DOC flux ($q=(-)$). As the system re-equilibrates, increasing vegetative inputs may cause the sign to switch again ($t=3$), until a new temperature threshold is reached that thaws another layer of soil ($t=4$), permitting further diversion of water to drainage another reversal in sensitivity sign, and so on.



3348
 3349
 3350
 3351
 3352
 3353
 3354
 3355
 3356
 3357
 3358
 3359
 3360

Figure 4: (a) Scatter plots showing the year-averaged temperature sensitivity (ground temperature) of DOC inputs to the river (TgC °Celsius⁻¹) in the 'modern' (1996-2005 average) versus 'future' (2020-2099 average) era for 'permafrost' (blue), 'non-permafrost' (red) and 'transitional' (black) grid cells. (b) Schematic plot explaining how the 'star'-shaped pattern in (a) results from temperature sensitivity pairs, with each segment of the shape assigned a number and colour. Numbers build a typology of modern versus future temperature sensitivity of DOC (table inset), colours denote an change in sensitivity over time. Arrows indicate the absolute magnitude of change in temperature sensitivity in the future. Red highlights in the inset table indicate changes of sensitivity sign. (c) Variation of the summed per-pixel soil DOC stock with the year-mean ALT_{max} for each pixel and year over the entire simulation period, with inset magnification of the 3m thaw depth. (d) Variation of the summed per-pixel DOC input to rivers with the annualised ALT_{max} for each pixel and year over the entire simulation period, to an ALT_{max} value of 3m. (e) Schematic explaining the change in sign and magnitude of total DOC input temperature-sensitivity shown

3361 in (a-b). **(e)** As temperature increases with time GPP inputs with high runoff can cause positive
3362 temperature sensitivity ($q=+$); at a temperature threshold, a given permafrost soil layer thaws (middle
3363 panel), permitting drainage and causing an abrupt shift in sign of temperature sensitivity to negative ($t=2$)
3364 before regaining positive momentum from runoff and GPP inputs ($t=3$), etc. **(f)**: Specific causal processes
3365 explaining the changes in magnitude and sign in (b) with linkages between above and below -ground
3366 processes before and after warming (left (LH) and right hand (RH) panels, respectively). **LH panel**
3367 corresponds to a situation in which a no-drainage flux soil transitions to one with drainage; **RH panel**
3368 corresponds to a situation in which drainage flux increases further with warming. The specific DOC
3369 outcomes of warming (red arrows in each right hand panel) map onto the specific modern/future
3370 temperature sensitivity pairs in a-b, with an explanation of the potential mechanism for each of these
3371 typologies given in the lower panel table.

3372
3373 Expanding on this, we illustrate how each of the temperature sensitivity typology pairs
3374 (Fig. 4b) can transition from one side of the pair (present) to the other (future) under
3375 second-order environmental drivers, depending on initial conditions (drainage versus
3376 no drainage) in Fig.4b,c,d. Thus, nodes (1-4) are cells with no drainage, with DOC input
3377 a function of low(1,4)/high(2,3) runoff (Fig. 4f, LHS), and depend on the differing and
3378 relative impacts of precipitation, NPP and runoff:drainage to arrive at the specific DOC
3379 input outcomes (Fig.4f, RHS) corresponding to the present-future DOC sensitivity pair in
3380 Fig. 4b.

3381
3382 These results suggest that despite enhanced water and carbon inputs, bulk DOC outflow
3383 to the Arctic Ocean may decline in a warmer future as a result of dynamic water flow
3384 paths, their timing, and interaction with a dynamic leaching substrate. This aggregate
3385 result is underpinned by substantial divergence between basins in the response of DOC
3386 leaching to different variables, which is itself the cause of a necessary volatility, in
3387 magnitude and sign, of the temperature sensitivity of DOC leaching between time
3388 periods. Given the counter-intuitive nature of these results, we suggest that greater
3389 emphasis should be placed on understanding the many non-vegetative interactions from
3390 which they emerge.

3391
3392
3393
3394
3395
3396
3397
3398
3399
3400
3401
3402
3403
3404
3405
3406
3407
3408
3409
3410
3411
3412
3413
3414

Chapter 5

CO₂ Uptake By Weathering Increasingly Exceeds CO₂ Evasion From Rivers As Permafrost Thaws ⁴

Summary

The potential significance of the rock weathering system to the high latitude inland water and biome-scale carbon cycle has come under increasing recognition in the literature on the topic. In the high latitudes, high carbonate concentrations in bedrock lithologies, their thermal protection from weathering due to the prevalence of permafrost throughout the soil column, and increasing temperatures, soil thaw depths and precipitation caused in part by the amplification of CO₂-driven radiative forcing in high latitude regions, appear on course to combine and drive large-scale increases in CO₂-uptake by chemical weathering. Indeed, recent publications have shown that fluxes of bicarbonate being discharged from major Arctic rivers –a symptomatic measure of rock weathering –have increased on the order of 50-100% in the last few decades alone, with major implications for how the permafrost-region carbon cycle should be viewed and its fate projected into the future. With this in mind, and given the preceding work in this thesis regarding the importance of lateral organic carbon fluxes to the permafrost region, this study integrates a simple simulation module of atmospheric CO₂ uptake by chemical rock weathering and carbonate alkalinity generation and export to ocean through rivers in the permafrost region into the land surface component (ORCHIDEE) of an Earth system model (IPSL). To do so, we apply simplified mathematical expressions from the literature relating weathering related CO₂ consumption and alkalinity fluxes to bedrock lithology, surface and subsurface runoff rates and soil temperature. While surface and subsurface runoff rates and soil temperature are simulated by ORCHIDEE at a 30 minute time-step, bedrock lithology is read from a forcing file. After calibrating our model against observed alkalinity fluxes, we are able to reproduce the observed seasonal dynamics in river alkalinity fluxes for present day and to project the long-term evolution of weathering rates and their effect on the CO₂ budget of Arctic watersheds and the exports of carbonate alkalinity to the Arctic Ocean over the 21st century.

To our knowledge, this is the first global-scale model that integrates the specifics of permafrost region soil-thaw dynamics and land-to-river-to-ocean lateral flux tracers to simulate the overland transfer of lithogenically-sourced carbon. Furthermore, by simulating the soil export rate of bicarbonate alkalinity, we are able to estimate the rate of atmospheric carbon dioxide uptake by the chemical weathering process, using some simple literature-derived factors as applied to a lithology map, coupled to the model-generated alkalinity export. All calculated variables are available at daily, monthly or yearly timestep, and at 0.5-2 degree resolution, providing the opportunity to both evaluate and break down the dynamics of these fluxes into their spatial and temporal components and compare them to empirical data. The resulting model version is then subjected to historical and future climatological forcing data to drive simulations of past and future carbonate weathering and alkalinity fluxes for the Pan-Arctic to 2100, under the high/intermediate-warming scenario of RCP-6.0. We show that the model underestimates alkalinity discharge relative to observations by *%. Nevertheless these

⁴ Manuscript being prepared for submission to *Global Biogeochemical Cycles*.

3460 flows of DIC (bicarbonates) are similar to DOC fluxes in the present day, and exceed
3461 them in projections of the future. Furthermore, and despite the weathering flux
3462 underestimate for the current period, CO₂ uptake by chemical weathering is found to
3463 exceeds CO₂ evasion from river surfaces across the six largest Arctic rivers, and indeed is
3464 nearly double the flux of evasion by the last decade of the 21st C. The upshot of this
3465 result is that by including weathering-generated alkalinity fluxes into the calculus of
3466 carbon fluxes, the inland water carbon cycle loop including DOC and DIC and their
3467 impacts on surface-atmosphere CO₂ fluxes, moves from a net source (via evasion) to a
3468 net sink (via chemical weathering uptake) of carbon, and does so increasingly in the
3469 future. Furthermore, by including this process, lateral carbon fluxes more than double
3470 to ~16% of net biome productivity. Given the shortcomings of both the model and the
3471 input data used to drive them, we suggest that this number underestimates the lateral
3472 flux contribution by at least a factor of two.

3473
3474
3475
3476
3477
3478
3479
3480
3481
3482
3483
3484
3485
3486
3487
3488
3489
3490
3491
3492
3493
3494
3495
3496
3497
3498
3499
3500
3501
3502
3503
3504
3505
3506
3507

Chapitre 5

L'absorption de CO₂ par altération des roches dépasse de plus en plus le relargage de CO₂ des rivières à mesure que le pergélisol dégèle

Résumé

L'importance potentielle du système d'altération des roches pour le cycle du carbone des eaux intérieures et des biomes à haute latitude est de plus en plus reconnue dans la littérature sur le sujet. Dans les hautes latitudes, les concentrations élevées en carbonates dans les lithologies du substrat rocheux, leur protection thermique contre les intempéries due à la prévalence du pergélisol dans la colonne de sol, ainsi que l'augmentation des températures, des profondeurs de dégel du sol et des précipitations provoquées en partie par l'amplification du forçage radiatif induit par le CO₂ dans les régions à haute latitude semblent bien vouloir se combiner et entraîner une augmentation à grande échelle de l'absorption de CO₂ par les intempéries. En effet, des publications récentes ont montré que les flux de bicarbonate rejetés par les principaux fleuves arctiques - une mesure symptomatique de l'altération des roches - ont augmenté de l'ordre de 50-100% au cours des dernières décennies seulement, avec des implications majeures sur la façon dont la région du pergélisol le cycle du carbone doit être examiné et son devenir projeté dans le futur. Dans cet esprit, et compte tenu des travaux précédents de cette thèse concernant l'importance des flux de carbone organiques latéraux pour la région du pergélisol, cette étude intègre un module de simulation simple de l'absorption de CO₂ atmosphérique par l'altération chimique des roches et la production d'alcalinité des carbonates et son exportation dans les océans via des rivières de la région du pergélisol dans la composante de surface terrestre (ORCHIDEE) d'un modèle de système terrestre (IPSL). Pour ce faire, nous appliquons des expressions mathématiques simplifiées tirées de la littérature reliant la consommation de CO₂ liée à l'altération et les flux d'alcalinité à la lithologie du substrat rocheux, aux taux de ruissellement superficiel et souterrain et à la température du sol. Alors que les taux de ruissellement en surface et sous la surface et la température du sol sont simulés par ORCHIDEE à un intervalle de temps de 30 minutes, la lithologie du substrat rocheux est lue dans un fichier de forçage. Après avoir calibré notre modèle en fonction des flux d'alcalinité observés, nous sommes en mesure de reproduire la dynamique saisonnière observée dans les flux d'alcalinité des rivières et de projeter l'évolution à long terme des taux d'altération et de leurs effets sur le bilan en CO₂ des bassins versants arctiques et les exportations des produits en question sur l'alcalinité carbonatée dans l'océan Arctique au XXI^e siècle.

À notre connaissance, il s'agit du premier modèle à l'échelle mondiale qui intègre les spécificités de la dynamique sol-dégel des régions du pergélisol et des traceurs de flux latéraux de rivières à océan afin de simuler le transfert terrestre de carbone provenant de sources lithogènes. En outre, en simulant le taux d'exportation d'alcalinité en bicarbonate dans le sol, nous pouvons estimer le taux d'absorption de dioxyde de carbone dans l'atmosphère par le processus d'altération chimique, à l'aide de simples facteurs dérivés de la littérature, appliqués à une carte lithologique, couplés aux

3555 modèles générés par le modèle sur exportation d'alcalinité. Toutes les variables
3556 calculées sont disponibles à des intervalles de temps quotidiens, mensuels ou annuels et
3557 à une résolution de 0,5 à 2 degrés, ce qui permet d'évaluer et de décomposer la
3558 dynamique de ces flux en leurs composantes spatiales et temporelles et de les comparer
3559 à des données empiriques. La version du modèle résultante est ensuite soumise à des
3560 données de forçage climatologiques historiques et futures pour piloter des simulations
3561 de flux d'altération et d'alcalinité carbonatés passés et futurs pour le Pan-Arctique
3562 jusqu'à 2100, selon le scénario de réchauffement élevé / intermédiaire de RCP-6.0. Nous
3563 montrons que le modèle sous-estime le débit d'alcalinité par rapport aux observations
3564 de *. Néanmoins, ces flux de bicarbonates sont similaires aux flux de COD actuels et les
3565 dépassent dans les projections sur l'avenir. En outre, et malgré le sous-estimé du flux
3566 d'altération climatique pour la période actuelle, l'absorption de CO₂ due à l'altération
3567 chimique dépasse l'évasion de CO₂ de la surface des rivières sur les six plus grands
3568 fleuves arctiques, et représente en fait presque le double du flux d'évasion de la dernière
3569 décennie du 21^{ème} siècle. Ainsi, en intégrant les flux d'alcalinité générés par les
3570 intempéries dans le calcul des flux de carbone, le cycle du carbone des eaux intérieures
3571 comprenant DOC et DIC et leurs impacts sur les flux de CO₂ passe d'une source nette
3572 vers un puits de carbone, avec un effet amplifié à l'avenir. De plus, en intégrant ce
3573 processus, les flux de carbone latéraux représentent plus du double, pour atteindre
3574 environ 16% de la productivité nette du biome. Étant donné les lacunes du modèle et
3575 des données d'entrée utilisées pour les piloter, nous suggérons que ce nombre sous-
3576 estime la contribution du flux latéral d'au moins un facteur de deux.

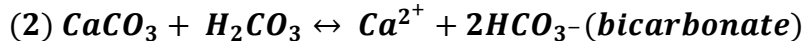
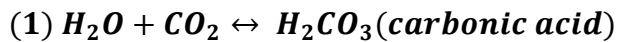
3577
3578
3579
3580
3581
3582
3583
3584
3585
3586
3587
3588
3589
3590
3591
3592
3593
3594
3595
3596
3597
3598
3599
3600
3601
3602

3603 **1 Introduction**

3604 Chemical weathering of the land surface represents a global CO₂ sink of ~0.26-0.29 PgCyr⁻¹
3605 (Amiotte Suchet et al., 2003; Gaillardet et al., 1999). This sink is balanced on oceanic
3606 turnover (10⁴) or geologic (10⁷) -year timescales, depending on whether the weathering
3607 product is precipitated in the ocean or outgassed in volcanic activity, respectively (Beaulieu et
3608 al., 2012). Fluvial export of weathering products and carbonate precipitation in the coastal
3609 ocean have been the primary sink for atmospheric CO₂ over Earth's history and are the reason
3610 why today the largest carbon storage term on Earth lies in carbonate rocks, followed by fossil
3611 fuel hydrocarbons –themselves partially derived from sedimentation of fluvial organic carbon
3612 fluxes (Kump, L.R., Kasting, J.F., Crane, 2010).

3613
3614 In the ocean, the carbonate alkalinity products of weathering (carbonate and
3615 bicarbonate) remain important for the contemporary state of the carbon cycle, their
3616 input rate and concentration determining the calcium carbonate saturation state of
3617 ocean water on which biogenic calcification, including that of many marine primary
3618 producers (PP), depend for survival (Feely et al., 2004). Transport by rivers and streams
3619 control this oceanic input with weathering reactions occurring in soils over the
3620 terrestrial landscape. The chemical products of weathering substantially affect the
3621 carbonate alkalinity of terrestrial runoff waters (hereafter referred to as 'alkalinity')
3622 through inputs of carbonate and bicarbonate (alkalinity = Σ[HCO₃⁻, CO₃²⁻]), which are
3623 likewise a major component of aggregate dissolved inorganic carbon (DIC, = Σ[CO₂,
3624 HCO₃⁻, CO₃²⁻]) fluxes to the ocean. Weathering is driven by the following idealised
3625 reactions:

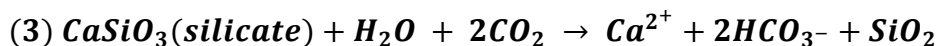
3626

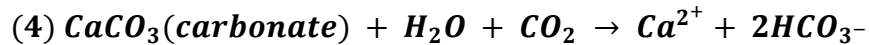


3627

3628 Rainwater dissolution of CO₂ in the root zone (this CO₂ being of atmospheric origin since
3629 it was initially fixed by photosynthesis) is converted into HCO₃⁻ upon weathering of
3630 carbonate rocks, which reduces its chemical susceptibility to atmospheric release
3631 (Brantley et al., 2011). Likewise, the vertical percolation of water through the soil
3632 column allows for the fixation of CO₂ of atmospheric origin residing in soil pore space as
3633 HCO₃⁻. Equation 2 acts on short time scales, in that the reaction is reversible, whereby
3634 carbonates can also be precipitated in solution in soils, rivers or the ocean, releasing
3635 CO₂. The link between freshwater alkalinity and DIC in inland water systems is through
3636 carbonate buffering of reaction kinetics, in which high alkalinity waters (pH ~8) cause a
3637 small fraction of dissolved CO₂ (H₂CO₃) to dissociate to H⁺ + HCO₃⁻, reducing the air-
3638 water CO₂ partial pressure gradient (Stets et al., 2017) and so the river surface flux of
3639 CO₂ to the atmosphere, which globally totals ~1.8 PgC yr⁻¹ (Raymond et al., 2013). In the
3640 high alkalinity case, the HCO₃⁻ produced by dissociation of carbonic acid is excluded
3641 from the summed HCO₃⁻ in the alkalinity metric defined above, as it is counterbalanced
3642 by the proton instead of a base cation. In practice, the weathering substrate responsible
3643 for CO₂ uptake is dominated by two globally-prevalent mineral rock sources, silicate and
3644 carbonate, similarly weathered as follows for the idealised carbonate and 'silicate'
3645 (wollastonite) reactions:

3646





3647
3648
3649
3650
3651
3652
3653
3654
3655
3656
3657
3658

Eqs. (3-4) show that whereas alkalinity (2HCO_3^- above) generated by silicate weathering is fully sourced from atmospheric CO_2 (or in practice free CO_2 in the soil (Calmels et al., 2014)), carbonate alkalinity is equally derived from the atmosphere (50%) and lithogenic source (50%). Soil free CO_2 , is mediated by soil microbial activity and root respiration that provide CO_2 and organic acid protons used in the weathering reaction (Kuzyakov, 2006). However, whereas weathering in Eqs. (1-2) uses carbonic acid, the presence of sulphides (pyrite) in parent material (e.g. shales), or in acid rain caused by the burning of sulfur-bearing fuels, can produce weathering via sulphuric acid without consumption of CO_2 , and is thus carbon-neutral on short, or a carbon source on ocean turnover, timescales (Tank et al., 2016; Zolchos et al., 2018), e.g. :



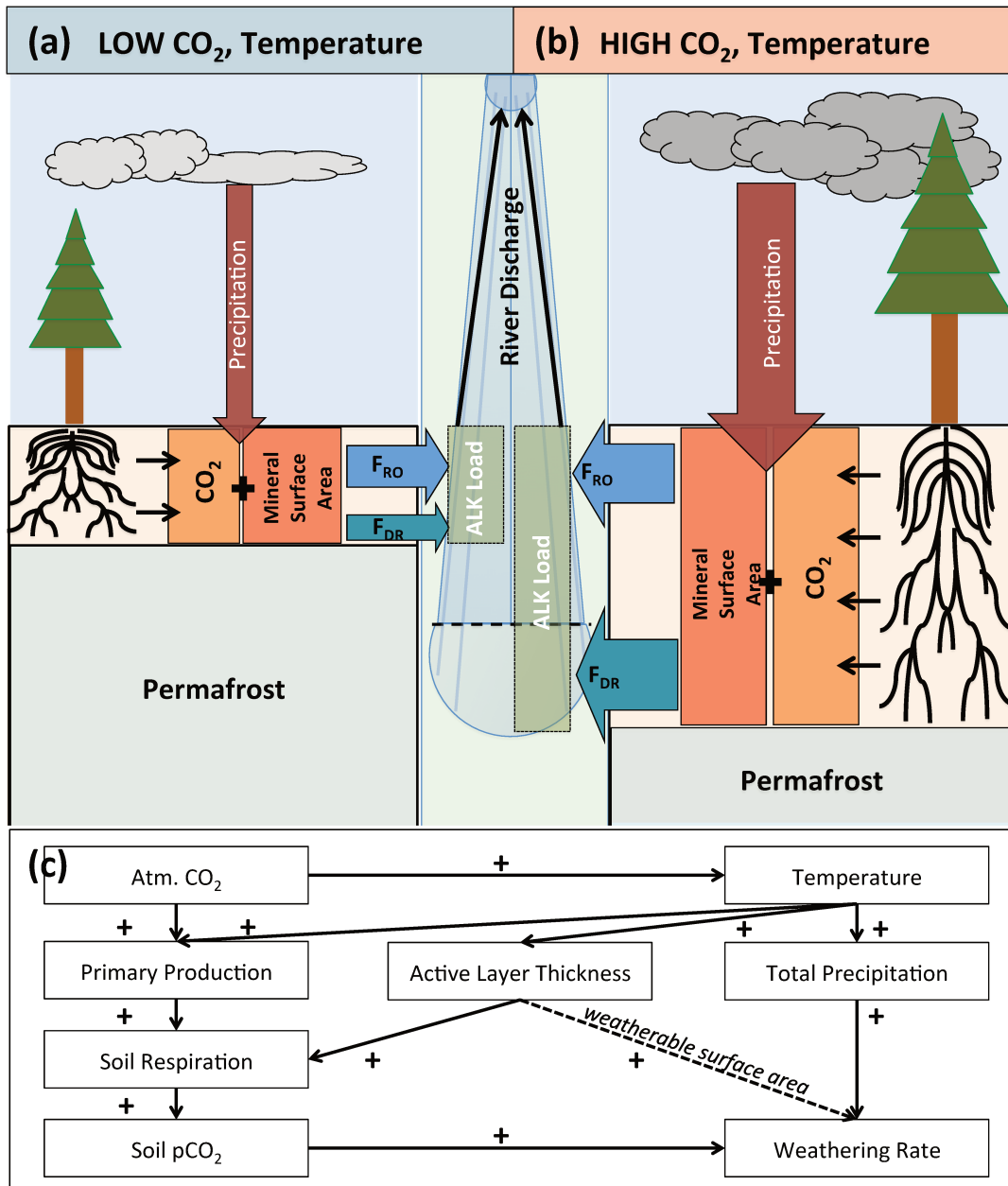
3659
3660
3661
3662
3663
3664
3665
3666
3667
3668
3669
3670
3671
3672
3673
3674
3675
3676
3677
3678

As suggested, the first-order control on weathering rates are the 'supply' of weatherable minerals -the quantity with which they exist on the land surface and soil (this global distribution driven initially by topographic uplift followed by other 'supply-side' factors like erosion) -and the 'demand' for those weatherable minerals by weathering agents (protons), themselves controlled by atmospheric CO_2 concentrations and the existence of soil flora and fauna for the production of CO_2 and organic acids. The reaction rate between these two is itself sensitive to other environmental drivers. Generally, weathering rates scale positively with temperature (Dessert et al., 2003; Raymond, 2017) due to the knock-on effects on solubility and reaction rates. However, there have been suggestions that the temperature dependence of weathering is limited by hydrological flux -if low, weathering may not be sensitive to temperature (Raymond, 2017; White and Blum, 1995). Likewise, when water throughput is low (residence times long), weathering will equilibrate with the soil solution more quickly, causing it to be 'transport limited' (Maher, 2010; Raymond and Hamilton, 2018) i.e. it will increase with increasing throughput (decreasing residence time) -until a peak is reached at which weathering is reaction-limited. By comparison, dissolved organic carbon (DOC) leaching rates scale positively with runoff but negatively with flowpath length (Maher and Chamberlain, 2014; Millot et al., 2003; Mulholland, 1997).

3679
3680
3681
3682
3683
3684
3685
3686
3687
3688
3689
3690
3691
3692

Globally, the inorganic carbon cycle in cold regions ($>50^\circ\text{N}$) can be characterised by physical and chemical weathering processes, including the grinding action of glaciers and annual freeze-thaw cycles, whose effect is to increase the effective mineral surface area exposed to the weathering reactant. Weathering in these high latitude regions is subject to substantial change due to anthropogenic climate warming. Glacial melting (Gislason et al., 2009) and permafrost thaw and subsequently enhanced soil-water interactions (Tank et al., 2016; Tank, Raymond, et al., 2012a), coupled with increased primary production via higher atmospheric CO_2 and thus biogenic soil CO_2 inputs (Striegl et al., 2007), may all increase weathering and hence riverine alkalinity flux rates (Fig. 1). In addition, temperature increases will spur silicate solubility, enhance chemical reaction rates and, in the high latitudes, probably substantially increase surface and subsurface hydrological runoff, increasing weathering reaction rates. These are presented in idealized form in Figure 1. Such changes may substantially impact the aggregate strength of weathering CO_2 consumption (Drake et al., 2018) and may partly

3693 offset some of the substantial CO₂ release to the atmosphere from microbial
 3694 metabolisation of thawed permafrost soils projected for the future (Schädel et al., 2014).
 3695 To date, however, quantification of the high latitude weathering response to a changing
 3696 climate has been elusive. This is because its process-based representation requires, on
 3697 the one hand, resolving the nexus of hydro-lithological reaction kinetics with thermal
 3698 and biotic factors necessary for generating a dynamic above-ground weathering flux
 3699 rate. Although this has previously been achieved by the WITCH model (Beaulieu et al.,
 3700 2012), that model requires a very large number of data-based parameters as input, and
 3701 may thus be difficult to employ outside of extremely well-studied basins, of which very
 3702 few exist in the high latitudes.
 3703



3704
 3705 **Figure 1:** (a-b) Schematic diagram with simplified representation of the main state variables and
 3706 processes under low (a) and high (b) CO₂ and temperature may affect weathering rate and by extension
 3707 the alkalinity load ('ALK Load') entering into rivers within the permafrost region. In the diagram, the
 3708 'tree' represents primary production, the black lines underneath the rooting depth, 'CO₂' refers to the

3709 partial pressure of CO₂ in the soil, 'Mineral Surface Area' refers to the weatherable soil mineral surface
3710 area increasing with active layer), 'F_{RO}' and 'F_{DR}' refer to the surface/near-surface and subsurface/deep
3711 soil water flows. The relative size of arrows, boxes and forms is indicative of differences in the volume of
3712 these flows between the two states shown.(c) System diagram depicting the idealized chain of causality
3713 (sign shown) between changes in climatology and changes in weathering rate in a-b.

3714
3715 On the other hand, the complexities of permafrost soil thermodynamics and hydraulics
3716 need to be resolved to represent the belowground reaction of these to thaw. The
3717 subsequent, dynamic responses of surface and groundwater fluxes likewise determines
3718 the flowpath, timing and concentration of weathering products in rivers, these requiring
3719 accurate spatio-temporal representation of chemical species lateral transfer across the
3720 landscape through the hydrological network. Finally, understanding the response of
3721 weathering to environmental change is hampered by the lack of long-term time-series of
3722 riverine alkalinity discharge with which to track this response. Globally, only the
3723 Mississippi has such data over the 20th Century (Raymond et al., 2008), while in the
3724 high latitudes records span a maximum of 50 years, with large data gaps for the
3725 Eurasian rivers(Drake et al., 2018; Tank et al., 2012b, 2016; Zolkos et al., 2018). This
3726 study aims to address these three problems, by integrating a simple carbonate alkalinity
3727 (weathering) generation scheme into a global land surface model developed specifically
3728 for resolving permafrost region-specific physical, hydrological and biological dynamics,
3729 and the lateral transfer of dissolved species across its landscape, requiring only basic
3730 hydrological datasets (alkalinity discharge, river water discharge) for this task. This
3731 allows us to simulate seasonal, surface and subsurface fluxes of alkalinity at a 30 minute
3732 simulation timestep. High temporal resolution allows us to capture the daily and
3733 seasonal cycle of alkalinity fluxes, which are sensitive to short-term variation in the soil
3734 environment, rather than bulk annual fluxes. Further, the seasonal variation of
3735 terrestrial alkalinity (and CO₂) fluxes into the Arctic ocean of is of particular relevance to
3736 the marine realm, where these variations dramatically impact seawater acidification,
3737 carbonate saturation state and photosynthetic production (Semiletov et al., 2016).
3738 Finally, the ability of our model in reconstructing the interannual trend for those rivers
3739 where long-term data exist may give us some confidence in producing datasets of
3740 historical fluxes for those where data does not exist. In what follows, we describe the
3741 equations and models that were added to the land surface model ORCHIDEE M-L to
3742 simulate riverine alkalinity fluxes, as well as the sequence of steps taken for model
3743 calibration and optimisation.

3744 **2 Materials and Methods**

	Basalt	Granite		
Activation Energy (j/mol)	50000	60000	Diff.	Diff. %
Temperature (Kelvin)	Multiplier (F_T)	Multiplier (F_T)		
274.15	0.462	0.396	0.066	14%
276.15	0.542	0.479	0.063	12%
278.15	0.633	0.578	0.055	9%
280.15	0.739	0.696	0.043	6%
282.15	0.861	0.835	0.025	3%
284.15	1.000	1.000	0.000	0%
286.15	1.159	1.194	-0.035	-3%
288.15	1.342	1.423	-0.081	-6%
290.15	1.549	1.691	-0.142	-9%
292.15	1.785	2.005	-0.219	-12%
294.15	2.053	2.371	-0.318	-15%

3745 **Table 1:** Sensitivity of the temperature-dependent alkalinity flux multiplier (Eq. 6) to the upper and lower
 3746 bound of the activation energy (E_a) range (for granite and basalt lithologies, respectively) given by
 3747 Hartmann et al., (2014), calculated for a range of temperatures (1-21°C) against a reference temperature
 3748 of 10°C. Absolute and percentage difference of the multiplier (F_T) from the mean of the temperature range
 3749 are shown.
 3750

3751
 3752 **2.1 Global Land Surface Model Description**

3753
 3754 The land surface model that was adapted to generate alkalinity fluxes in the northern
 3755 hemisphere is a sub-version of the land surface component of the IPSL Earth System
 3756 model, ORCHIDEE (Organising Carbon and Hydrology in Dynamic Ecosystems (Krinner
 3757 et al., 2005)), given the name ORCHIDEE MICT-LEAK (Bowring et al., 2019a), hereafter
 3758 referred to as ORCHIDEE M-L, which has previously been presented and evaluated for
 3759 the Lena river basin (Bowring et al., 2019b) as well as the Pan-Arctic (Bowring et al.,
 3760 2019 in prep.). This model version essentially derives from two other subversions of
 3761 ORCHIDEE. The first, was specifically coded for representation of high latitude
 3762 phenomena and permafrost processes, called ORCHIDEE-MICT, has been presented and
 3763 evaluated for the Pan-Arctic (Guimberteau et al., 2018). Specifically, it includes
 3764 representation of permafrost soil C stocks and snow physics, and their thermodynamics,
 3765 to a depth of 38m, soil hydrology to a depth of 2m, explicit simulation of the active layer
 3766 and subsequent thermal and hydrologic shielding of sub-active layer soil.
 3767

3768 The second, ORCHILEAK (Lauerwald et al., 2017) incorporates production of DOC from
 3769 soil organic matter (Camino-Serrano et al., 2018), soil carbon ‘priming’ (ORCHIDEE-
 3770 PRIM (Guenet et al., 2016)) and the riverine transport and transformation of DOC and
 3771 CO₂, C and water exchanges with floodplains, and CO₂ evasion from rivers and wetlands
 3772 (Lauerwald et al., 2017). ORCHIDEE M-L thus resolves DOC and CO₂ production, and
 3773 DOC diffusion, within a vertically-discrete soil column representative of permafrost
 3774 region soil thermodynamics and snow physics, and their transport/transformation
 3775 within the inland water network. This combination of process representations is, to our
 3776 knowledge, unique amongst land surface models and provides the instrumental
 3777 rationale for using this model sub-version as the basis from which to simulate high
 3778 latitude alkalinity fluxes at the global scale.
 3779

3780 Key to representation of weathering is the explicit, vertically discretised soil column and
3781 the hydrological fluxes which flow through them. Hydrological carbon tracers, including
3782 alkalinity, are assigned to surface and subsurface water flows, where surface runoff
3783 flows are aggregated from the water fluxes that do not permeate below 0.045m while
3784 subsurface ‘drainage’ waters, which flow laterally at depth, are sourced from depths of
3785 0.045-2m. Thus in what follows the “surface runoff” which actually includes a small
3786 portion of subsurface flow (to 4.5cm), will be referred to as ‘surface runoff’, while the
3787 deep subsurface flow will be referred to as ‘drainage’. This ability to distinguish surface
3788 from subsurface flows is important because the seasonality of each is markedly different
3789 in the permafrost region. Whereas drainage flows can occur throughout the year in the
3790 unfrozen portion of the soil column, surface runoff is highly seasonal. At the same time,
3791 we expect alkalinity concentrations in the high latitudes to be substantially higher in
3792 drainage versus runoff water flows, given that these flows may currently be accessing
3793 parts of the soil column previously inaccessible to them due to soil freezing, as well as
3794 higher water residence times and the higher concentration of weatherable surface in the
3795 mineral subsoil.

3796
3797 Finally, the soil temperature at the near-surface versus at depth also differ considerably,
3798 being cooler at the surface and warmer at depth in the winter, and vice versa in the
3799 summer. These temperature differences can drive substantial shifts in the rate of
3800 weathering, and can be accounted for in our model. The combination of different timing
3801 and concentrations of the surface and subsurface flows and vertically discretised soil
3802 temperatures means that we can produce simulated alkalinity at a daily or seasonally
3803 and spatially (vertically) disaggregated scale.

3804

3805 **2.2 Weathering flux model**

3806

3807 Generating a carbonate and silicate weathering flux rate in ORCHIDEE MICT-LEAK
3808 required a number of separate steps, described in the following subsections. Our
3809 approach was to combine equations linking lithology/hydrological runoff and
3810 temperature with weathering, presented first by (Moosdorf et al., 2011) and (Hartmann
3811 and Moosdorf, 2012), respectively, who successfully applied these relationships to
3812 North America and the globe. We then add in a factor relating weathering to soil
3813 respiration (e.g. (Striegl et al., 2007)). Based on an underlying high resolution lithology
3814 map (Hartmann and Moosdorf, 2012), and the soil temperature, hydrology and soil
3815 respiration, generated by ORCHIDEE M-L, we simulate a weathering and alkalinity flux
3816 in the model which is then calibrated against observed data from Tank et al., (2012a) for
3817 the six largest Arctic rivers, and used to partition simulated alkalinity fluxes between
3818 surface and subsurface flows. The resulting model setup permits us to run long-term
3819 model simulations and projections of future weathering.

3820

3821 **2.2.1 Step 1: Bulk weathering annual soil solution bicarbonate concentrations**

3822

3823 First, to calculate an initial grid cell-specific annualised weathering flux rate, we assume
3824 that this flux is determined by hydrological runoff, defined here as the combination of
3825 surface and subsurface water flows, and underlying lithology, per the Runoff-Lithology
3826 (RoLi) model described in Eq. 2 of Moosdorf et al., (2011) (see Figure 2a). RoLi uses 16
3827 lithological classes to estimate annual alkalinity yield per unit runoff, calibrated over the

3828 entire North American continent, whereby a linear regression parameter for runoff and
3829 a exponential parameter for runoff per lithological class are used. Over the lithological
3830 classes, carbonate rocks have the highest alkalinity yield per unit increase in runoff,
3831 whereas granitic rocks have the lowest (see Fig. 5 in Moosdorf et al., 2011).

3832
3833 To obtain the two weathering drivers (runoff and lithology), we run ORCHIDEE-ML for
3834 30 years at 1° resolution, using the second Inter-Sectoral Impact Model Intercomparison
3835 Project (ISIMIP2b (Frieler et al., 2017; Lange, 2016, 2018)) climatology over 1975-2005,
3836 to simulate high-latitude (45-90°N) annual river 'total runoff' (surface runoff + drainage
3837 in the model) fluxes. The average of this per-grid-cell annual total runoff flux is
3838 combined with the high resolution global lithological map GLiM (Hartmann and
3839 Moosdorf, 2012) and applied to the equations used in the RoLi Model using ArcGIS
3840 10.6.1 (ESRI, 2018). The result is a high latitude map of mean annual bicarbonate
3841 alkalinity concentration (mgC L⁻¹) in runoff and drainage water, i.e. the total runoff (Fig.
3842 2). This methodological sequence is shown for the first three points of Fig. 2a.

3843 3844 **2.2.2 Step 2 – Temperature dependence**

3845
3846 ORCHIDEE M-L was adapted to read in this annual bicarbonate concentration map, and
3847 to allow the model to distribute this annual concentration map into fluxes of alkalinity in
3848 surface runoff and drainage fluxes at a 30-minute timestep. To include the sensitivity of
3849 weathering rates to temperature we apply a temperature-driven chemical weathering
3850 multiplier from Hartmann et al., (2014) to the alkalinity flux generated by the model
3851 (concentration*instantaneous hydrological flux) at a 30 minute timestep into its code:

$$3852 \quad (6) \quad F_{T,i} = \exp(-E_{a,i}/R*(1/T - 1/T_0))$$

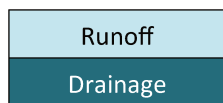
3853
3854 Where F_T is the temperature multiplier, R is the gas constant, T_0 is the reference
3855 temperature which is generated from average non-frozen soil temperature generated
3856 over the 20th century by the ORCHIDEE-ML at 45-90°N, T is the soil temperature per
3857 grid cell and soil layer and timestep (for each of the energy and water calculations
3858 module's 30 minutes timesteps) and E_a is the activation energy. Hartmann et al. (2014)
3859 give three lithology-dependent activation energies: one each for felsic, mafic, and
3860 pyroclastic rocks. For carbonate rocks, they assume that there is no temperature effect
3861 as increased weathering rates are counterbalanced by a decreased solubility of
3862 carbonates with increasing temperature. We use the mean of their activation energy
3863 range for basaltic and granitic rocks ($E_a=55000$ J mol⁻¹) as input to Eq. 6, justified by the
3864 fact that over a 20°C range of realistic non-zero temperatures in high latitudes (1-21°C),
3865 the temperature-dependent activation energy varies by a maximum of +/-15% across
3866 these two lithological classes (Table 1), while pyroclastic rocks are a relatively scarce
3867 underlying lithology, that are thus ignored here. Because ORCHIDEE M-L generates
3868 water losses to rivers at both the surface and subsurface, we determine a reference
3869 temperature (T_0 in Eq. 6) for each of the runoff and drainage fluxes, determined by the
3870 layer thickness-weighted average of the mean annual grid cell soil temperature, in the
3871 top five (top 0.045m, 283.2K) and bottom six hydrological soil layers (bottom 1.955m,
3872 280.15) over the 30-year model run period described above, averaged over all grid cells.

3873 **(a)**

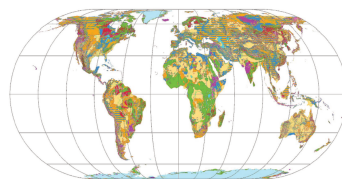
1. ORCHIDEE hydrological output (30yr)

2. Runoff-Lithology Model
Moosdorf (2011), trained on N. America

3. Global Lithological Map
Hartmann & Moosdorf (2012)

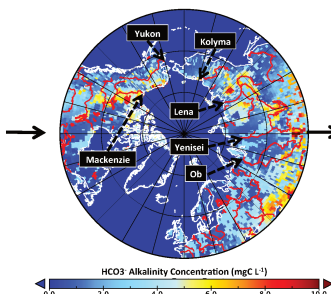


$$\text{RoLi-Model: } F\text{Alk}_i = b_0 * \sum (A_{ji} * q_i^{\text{HL}}) +$$



The new global lithological map database GLiM:
A representation of rock properties at the Earth surface

4. Create alk. Concentration Forcing
File Read by Model

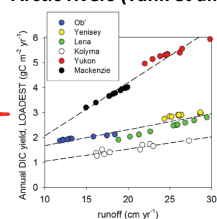


5. Incorporate weighted soil temperature sensitivity
Hartmann et al., (2014), trained on Japan

$$F_{T_s} = \exp(-E_a / R * (1/T - 1/T_0))$$

6. Add alkalinity flux sensitivity to whole soil respiration

7. Calibration Correction for alk. discharge from 6 largest Arctic rivers (Tank et al. 2012)



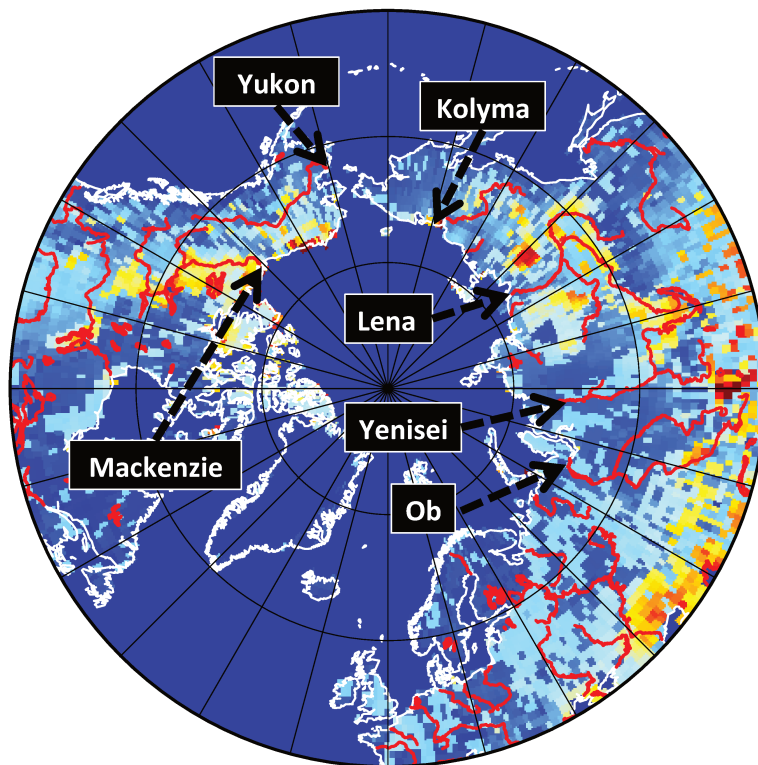
8. Add correction factor for differential runoff and drainage alkalinity flux concentrations

9. Create new alk. Concentration Forcing

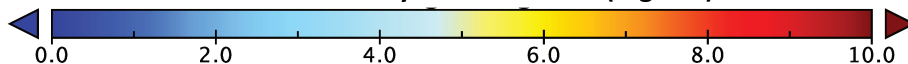
10. Run

3874
3875

(b)



HCO₃⁻ Alkalinity Concentration (mgC L⁻¹)



3876
3877
3878
3879
3880

Figure 2: (a) Schematic representation of the sequence of steps by which the simulation of alkalinity fluxes is generated by the model, as described in Section 2.2. (b) Average Pan-Arctic dissolved HCO₃⁻ alkalinity concentration (mgC L⁻¹) in runoff and drainage water fluxes used as a forcing file to run the

3881 model. Concentrations were calculated using the Moosdorf et al., (2011) Ro-Li model based on the
3882 Hartmann and Moosdorf, (2012) Global Lithological Map and the average runoff and drainage fluxes
3883 simulated over the years 1975-2005 by ORCHIDEE M-L under ISIMIP2-IPSL climatology. Names of the 'big
3884 six' Arctic river basins are given in black boxes, with arrows pointing to the river mouth of each basin.

3885

3886 **2.2.3 Step 3 –Respiration dependence of Weathering**

3887 As discussed, increases in CO₂ and temperature increase primary production and soil
3888 respiration, increasing the availability of the weathering agent (protons) and thus in
3889 theory the rate of weathering. To represent this, we scale simulated alkalinity fluxes in
3890 runoff and drainage waters to heterotrophic soil (R_{soil}), root (R_{root}), and belowground
3891 litter (R_{litt}), respiration, normalised by a reference respiration value (R_{ref}) taken from
3892 simulated output of these variables over the Big 6 basins for the approximate period
3893 during which most observational data have been gathered for these rivers (1996-2005).
3894 Runoff and drainage alkalinity fluxes in a grid cell at a given timestep is scaled to a
3895 dimensionless modifier (M) determined by the total soil respiration in that grid cell and
3896 timestep, normalised by the R_{ref} calculated, as in Eq. 7:

$$(7) M = \frac{R_{soil} + R_{root} + R_{litt}}{R_{ref}}$$

3897 Where R_{ref} depends on the input forcing data being used. Where ISIMIP (IPSL)
3898 climatology was fed into the model, $R_{ref} = 1.1 \text{ gC m}^{-2} \text{ d}^{-1}$, whereas for GSWP3 climatology
3899 (see Section 3.2) $R_{ref} = 0.69$.

3900

3901 **2.2.4 Step 4 –Calibrating Alkalinity Flows to Arctic River Data**

3902

3903 In the next step, we calibrated the model to obtain a reasonable ratio between surface
3904 runoff and drainage alkalinity concentrations, needed to simulate the seasonality in
3905 alkalinity concentrations, with lowest concentrations in late spring when contributions
3906 from surface runoff due to spring freshet are the highest, and higher concentrations
3907 when the river is mainly sourced by subsurface water flow (due to surface freezing). For
3908 this, we fitted the model-generated alkalinity fluxes sourced from both surface runoff
3909 and drainage to observation-based estimates of monthly average alkalinity loadings for
3910 the Big 6 Arctic Rivers. To obtain those observation-based estimates of monthly average
3911 alkalinity loads, we used for each river the rating curve representing the relationship
3912 between alkalinity flow and river discharge empirically found by Tank et al., (2012a),
3913 and applied them to the average monthly discharges simulated with ORCHIDEE M-L
3914 over the period 1976-2005. We preferred the so estimated monthly riverine alkalinity
3915 fluxes over the observed fluxes published in Tank et al., (2012a), as seasonality of
3916 alkalinity concentrations and discharge are tightly, functionally coupled and the slight
3917 but significant mismatch between simulated and observed seasonality and magnitude of
3918 discharge, which we had identified for our model results, would lead to erroneous,
3919 unrealistic calibrations of surface runoff versus drainage concentrations to compensate
3920 for the mismatch in discharge.

3921

3922 In order to calibrate a constant ratio between surface runoff and drainage concentration
3923 to be applied to all Arctic Rivers, we first performed a regression of modeled versus
3924 observation-driven monthly alkalinity concentrations for the 6 Arctic rivers (eq. 8,
3925 $n=72$). The observation-driven concentrations (C_{obs}) were calculated by dividing
3926 observation-driven monthly alkalinity fluxes (see above) by the simulated monthly

3927 discharge . The simulated annual concentrations $C_{sim,RUNOFF}$ and $C_{sim,DRAINAGE}$ were
3928 calculated by dividing the simulated surface runoff and drainage alkalinity flux,
3929 respectively, by the simulated mean discharge (1976-2005). That means that the sum of
3930 $C_{sim,RUNOFF}$ and $C_{sim,DRAINAGE}$ gives the total of simulated alkalinity concentration in the
3931 river.
3932

$$(8) C_{obs} = a1 * C_{sim,RUNOFF} + a2 * C_{sim,DRAINAGE}$$

3933
3934 The regression yields values for a1 and a2 of 0.58 and 1.22, respectively ($R^2=0.77$, p-
3935 value: $< 2.2e-16$). From this regression, we obtained a mean ratio of surface runoff to
3936 drainage alkalinity concentrations of 0.47. This ratio between surface runoff and
3937 alkalinity concentrations explains seasonal variations in alkalinity concentrations, with
3938 lowest values during the spring freshet when surface runoff is dominant, but also spatial
3939 variations in alkalinity concentrations. For example, areas with high permafrost
3940 coverage are dominated by surface runoff and thus exhibit low HCO_3^- concentrations
3941 (spatial feature), while during the spring thaw/high river discharge period (temporal
3942 feature), alkalinity concentrations plummet as the flux of weathered matter is diluted by
3943 the huge water flux at this time (Tank et al., 2012b, 2012c).
3944

3945 **2.2.5 Step 5 –Calibration Correction**

3946
3947 In the final step, we corrected the alkalinity concentration forcing, developed in Step 1
3948 (2.2.1), to account for the fact that the empirical model from which it is derived was
3949 mainly trained on temperate North American watersheds, and thus not necessarily
3950 representative of the high latitudes. We found a correction factor for each basin, by
3951 applying the [surface runoff:drainage alkalinity] concentration ratio of 0.47 to the
3952 surface runoff alkalinity fluxes generated from the alkalinity concentration forcing,
3953 while the drainage alkalinity fluxes were kept unchanged (eq. 9). Then, we summed both
3954 fluxes up to the simulated monthly fluvial alkalinity transports, which were regressed
3955 again against the observation-driven alkalinity fluxes.
3956

$$(9) Load_{obs} = b * (0.47 * Load_{sim,RUNOFF} + Load_{sim,DRAINAGE})$$

3957
3958 Where Load refers to annual alkalinity loading of a river ($kgC s^{-1}$), with right-hand-side
3959 subscripts referring to the source the simulated alkalinity flux and $Load_{obs}$ being the
3960 observation-based alkalinity flux. As mentioned above, we fitted that regression for the
3961 average monthly alkalinity fluxes for each basin, with regression results listed in Table
3962 S1. We applied the b-estimates from the regression as correction factors to the original
3963 alkalinity concentration forcing file. For areas outside the Big 6 river basins, we used the
3964 correction factor from the closest basin. Through this, we obtained a corrected forcing
3965 file representing the alkalinity concentration in the drainage fluxes per grid cell for a
3966 reference soil temperature of 280.15 K. The corresponding concentration in the surface
3967 runoff flow is calculated by applying the factor of 0.47 obtained above.
3968

3969 **2.3 Estimation of CO₂ Uptake by Chemical Weathering**

3970
3971 As described in the introduction, chemical weathering of carbonate and silicate rocks
3972 drives CO₂ uptake in the weathering reaction between water and carbonate and/or

3973 silicate -bearing rocks. Based on the rate of combined surface and subsurface
 3974 generation of dissolved product of this reaction (HCO_3^- in solution) –in other words, the
 3975 export rate of alkalinity from the soil – that is produced by the outputs of our model, we
 3976 can calculate the atmospheric CO_2 uptake rate associated with weathering, and the
 3977 spatially explicit changes in that rate over time. To do so, we use the lithology
 3978 dependent CO_2 uptake/alkalinity flux ratio found in Moosdorf et al. (2011) and apply it
 3979 to the total export (surface runoff + drainage) of alkalinity per grid cell and year of
 3980 simulation to arrive at a first-order CO_2 uptake rate per unit land surface area ($\text{gC m}^{-2} \text{yr}^{-1}$).
 3981

3982 3 Data and Simulation

3983 3.1 Simulation forcing with ISIMIP climatology

3984 The climatological forcing data used to drive ORCHIDEE-ML for historical and future
 3985 simulations was taken from bias-corrected projected output from the IPSL Earth System
 3986 Model under the second Inter-Sectoral Impact Model Intercomparison Project (ISIMIP2b
 3987 (Frieler et al., 2017; Lange, 2016, 2018)) rubric, following the ‘intermediate-warming’
 3988 trajectory of Representative Concentration Pathway 6.0 (RCP 6.0). This scenario
 3989 projects rising emissions through the 21st Century, which peak in 2080. Climatological
 3990 input data are at a daily temporal and 1 degree spatial resolution, covering the period
 3991 1960 to 2100. The input vegetation and land cover map was taken from the 5th Coupled
 3992 Model Intercomparison Project 5 (CMIP5-LUHa) output. As previously mentioned, we
 3993 derived a baseline weathering product concentration map which was read as input to
 3994 the model (Fig. 2a,b). This input is then mediated by the weighted mean soil
 3995 temperature experienced by the surface and subsurface water fluxes, as described in the
 3996 preceding subsections. The water height threshold, used to define the water level at
 3997 which floodplain inundation is triggered, is obtained statistically over multiple 30 year
 3998 (1976-2005) model runs using ORCHIDEE MICT-LEAK, in a stepwise procedure first
 3999 described in Lauerwald et al., (2017) and employed in Bowring et al. (2019).
 4000

<i>River Discharge (km³ yr⁻¹)</i>	Yukon	Mackenzie	Ob'	Yenisei	Lena	Kolyma
Observed 2000-2009	207	305	415	640	603	78
ISIMIP sim. 2000-2009	119	245	498	455	327	80
GSWP3 sim. 2000-2009	119	211	593	501	359	98
Observed 1990-1999	217	275	405	613	532	68
ISIMIP sim. 1990-1999	112	253	494	473	295	82
GSWP3 sim. 1990-1999	126	220	558	506	331	89
Observed 1980-1989	206	273	376	582	549	68
ISIMIP sim. 1980-1989	128	260	530	464	327	74
GSWP3 sim. 1980-1989	128	221	524	483	316	96
Observed 1970-1979	184	292	441	591	529	65
ISIMIP sim. 1970-1979	113	232	461	432	317	96
GSWP3 sim. 1970-1979	118	230	574	497	327	90

4001
 4002 **Table 2:** Observed vs. simulated river water discharge using the ISIMIP 2b and GSWP3
 4003 climatological forcing datasets. Shown are the decadal-mean simulated (ISIMIP 2b)
 4004 versus observed total annual river discharge ($\text{km}^3 \text{yr}^{-1}$); observations are taken from the
 4005 NOAA Arctic Report Card by Holmes et al., (2015).
 4006

4007 3.2 Rationale for simulation with GSWP3 climatology

4008
 4009 Previous studies (Bowring et al., *in prep.*) have shown that the ISIMIP 2b climatology
 4010 dataset, which we use to drive historical and future projections for alkalinity and

4011 weathering fluxes in our model, tends to underestimate hydrologic runoff when using
4012 ORCHIDEE, causing lower-than-observed bulk river fluxes and peak flows. Because
4013 bicarbonate weathering and transport rates are dependent on runoff, we are likely to
4014 underestimate these alkalinity fluxes in simulations using our model. On the other hand,
4015 when using another historical climatology dataset called GSWP3 ([http://hydro.iis.u-](http://hydro.iis.u-tokyo.ac.jp/GSWP3/)
4016 [tokyo.ac.jp/GSWP3/](http://hydro.iis.u-tokyo.ac.jp/GSWP3/)) -ORCHIDEE is able to more successfully reproduce observed Arctic
4017 river discharge flows (bulk and seasonal (Guimberteau et al., 2018)). The alkalinity
4018 model can be run using this 'optimal' dataset, from which we can compare model
4019 performance with respect to observations, and thus provide a yardstick against which to
4020 evaluate whether departures from observations are the result of suboptimal input data
4021 or suboptimal model representation. To this end, we repeat steps 1 to 3 using the
4022 GSWP3 dataset, and run the model over the historical simulation period (1901-2005).

4023 **4 Results**

4024 **4.1 Future Trends**

4025 Over the ISIMIP climatology-driven simulation period 1960-2099, bulk alkalinity basin-
4026 outflow trends for the 'Big Six' Arctic rivers increased markedly over Eurasia, with
4027 ambiguous trends in North America (Fig. 3). If river discharge of alkalinity is
4028 disaggregated by source of water flow –that is, if we discriminate between whether a
4029 given unit of alkalinity in the river entered the river via the soil surface (runoff) or
4030 subsurface (drainage) –as is done in Figure 3, the trend in alkalinity discharge is
4031 dominantly driven by large-scale increases in the drainage flux, against smaller
4032 increases (Lena, Yenisei, Kolyma) or no noticeable change in runoff fluxes (Ob,
4033 Mackenzie, Yukon). This dynamic is particularly apparent for the two largest and least
4034 permafrost-affected of the Eurasian rivers considered, the Ob and Yenisei, where the
4035 drainage alkalinity flux increases by ~3 (Ob) and ~6 (Yenisei) –fold over the simulation
4036 period, or from the order of $1 \rightarrow 3$ TgC yr⁻¹ and $0.2 \rightarrow 1.2$ TgC yr⁻¹ for each river
4037 respectively.

4038
4039 The massive increase in drainage water-sourced alkalinity discharge points to a large-
4040 scale increase in subsurface flows facilitated by permafrost thaw, a deeper active layer
4041 allowing increased vertical entrainment and flow of water from the surface-down.
4042 Permafrost thaw in this sense liberates the subsurface soil column from its previous
4043 thermal shielding, greatly expanding the surface area subjected to chemical weathering
4044 and the subsequent aggregate flux of the weathering product. Indeed, the increase in
4045 modeled drainage weathering corresponds with areas of greatest increases in
4046 temperature, drainage water flow and active layer depth. Further, the increased vertical
4047 distance of water flowpaths and their longer soil residence time (slower flow) converge
4048 to increase the concentration of weathered material in drainage flows, as represented in
4049 our simple weathering flux module, whose increase thus serves to further enhance the
4050 river discharge of alkalinity.

4051

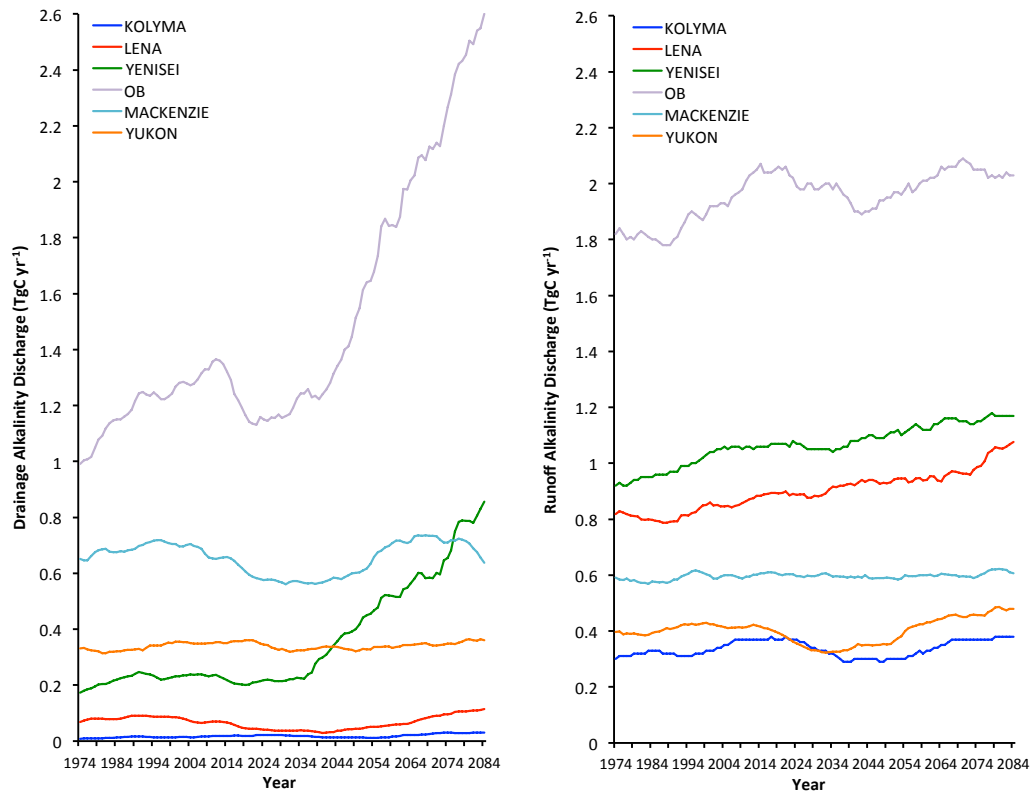
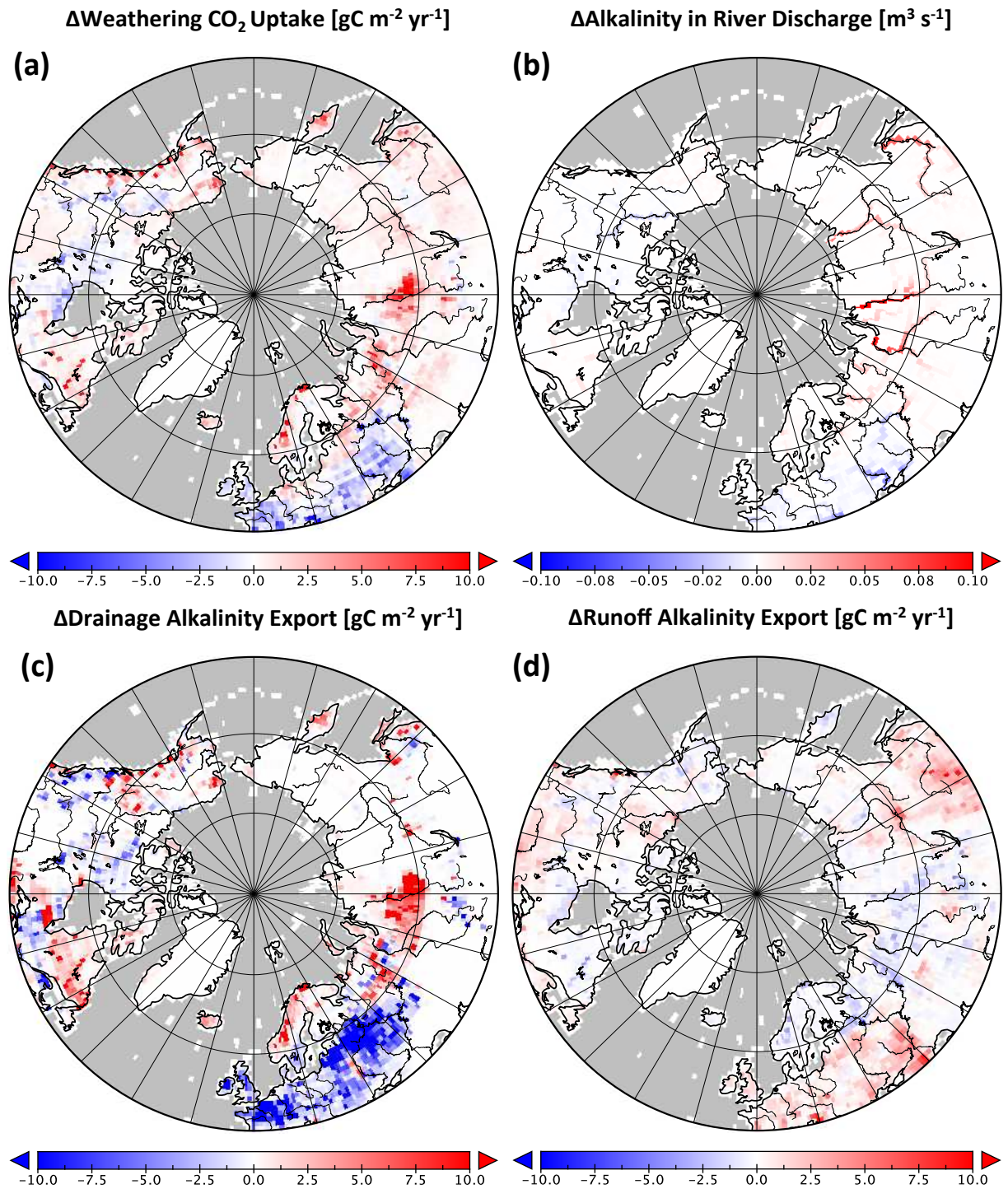


Figure 3: Drainage-sourced (left) and surface runoff-sourced (right) alkalinity discharge trends (TgC-eq. yr⁻¹) at basin outlet for each of the 'Big Six' rivers over the simulation period, with a 30-year moving average applied to each trendline.

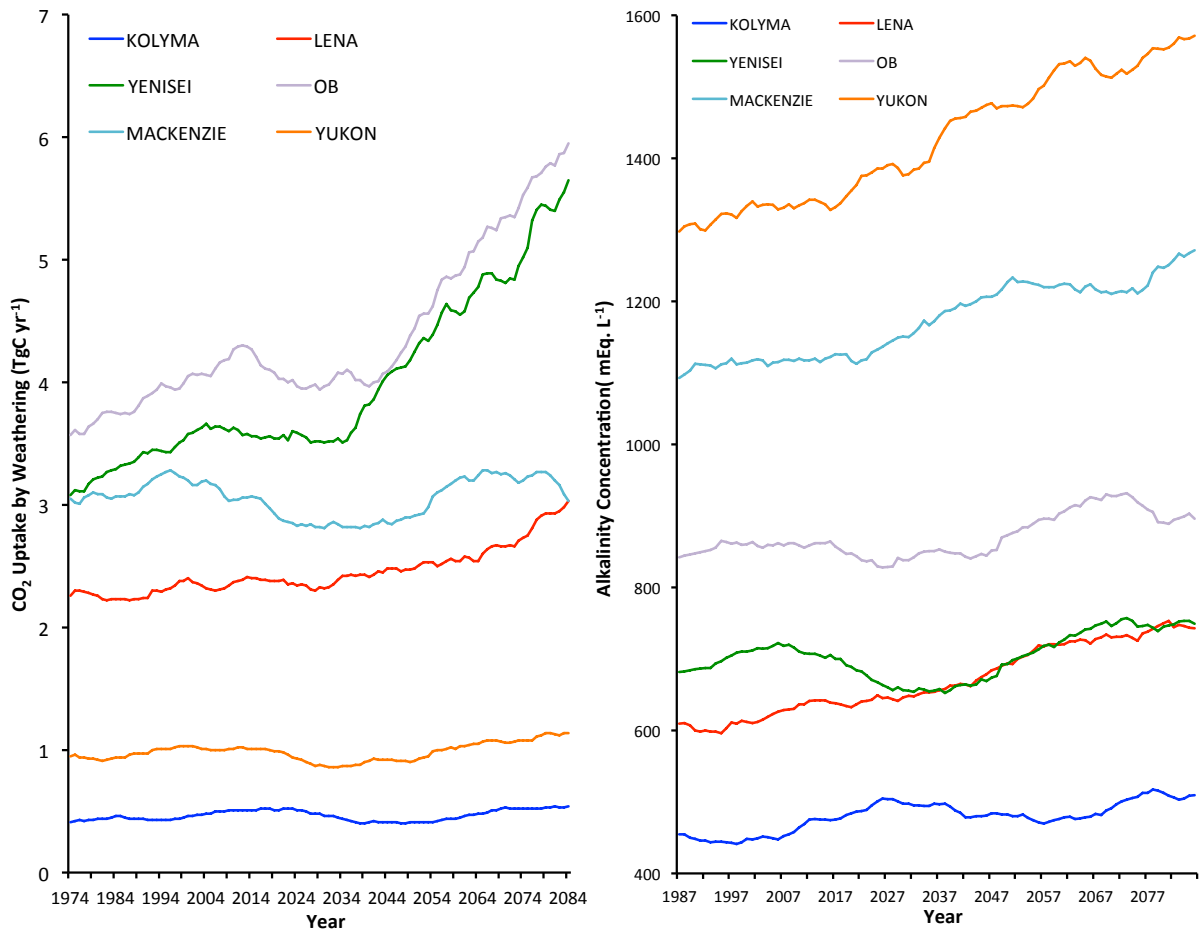
As described in the introduction, chemical weathering of carbonate and silicate rocks drives a net atmospheric CO₂ uptake. The change in this land-atmosphere CO₂ flux over the 21st Century is shown in Figure 4a. Carbon uptake rates decline in temperate Western Europe and the inland North American Arctic, but increase strongly in central-Western Siberia, Sweden and along the eastern and western boundaries of North America, and weakly in Eastern Siberia. These same regions correspond to areas of matching sign of changes in alkalinity discharge (Fig. 4b). At the same time, there is a strong spatial correlation (positive) of changes in weathering atmospheric CO₂-sink with changes in subsurface (drainage) soil alkalinity export (compare Fig. 4a and Fig. 4c), and a strong anti-correlation with changes in surface runoff alkalinity export (compare Fig. 4a and Fig. 4d). Thus, deeper vertical flow paths promote CO₂-weathering uptake, whereas an increased flux of water running over the land surface (runoff) is indicative of a shorter water residence time, less weathering per unit volume of water, which implies greater dilution of weathering products and a decrease in CO₂ uptake from weathering.

The trends of CO₂-weathering uptake, when extended to the Big Six rivers, underscore the magnitude of the change of this often-overlooked component of the terrestrial C cycle perturbed by climate change and human activities on short timescales, as well as its potential sensitivity to changes in environmental conditions. Fig. 5 (left) shows that the basin-summed CO₂-weathering uptake rate ranges from ~0.2 TgC yr⁻¹ (Kolyma) to up to ~10 TgC yr⁻¹ (Yenisei), a range very similar to the maxima and minima of dissolved organic carbon (DOC) export rates for each of the six basins predicted by the model. Like other alkalinity-related variables, the Eurasian basins tend to experience the highest

4080 rates of increase in weathering CO₂ uptake over the simulation period, owing, as
 4081 previously discussed for Fig. 4, to deeper subsurface flow paths.
 4082



4083 **Figure 4:** Maps of changes in alkalinity-related variables over the 21st Century, i.e. between the mean of
 4084 the last decade of simulation (2090-2099) and (1996-2005), for **(a)** weathering-driven CO₂ uptake, **(b)**
 4085 total alkalinity transport in river discharge, **(c)** drainage and **(d)** runoff alkalinity export from the soil
 4086 column.
 4087

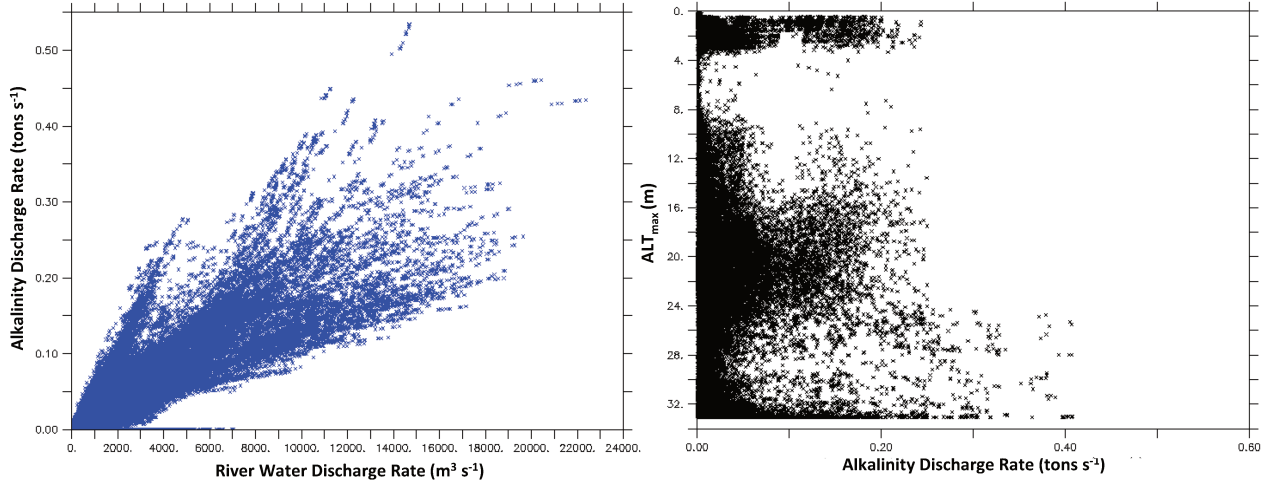


4088 **Figure 5:** 30-year moving average of (left) basin-aggregated CO₂ uptake by weathering (TgC yr⁻¹) and
 4089 (right) annual alkalinity concentrations (mEq L⁻¹) in outlet discharge, for each of the Big Six river basins.
 4090
 4091

4092 Whereas the bulk fluxes of terrestrial alkalinity export and discharge previously
 4093 described are strongly dependent on bulk inputs of precipitation and subsequent
 4094 surface runoff and drainage water flows, the input of alkalinity made available to each
 4095 volumetric unit of water flowing from the land surface (mEq L⁻¹) is a measure of the
 4096 concentration of alkalinity made available by the underlying lithology and soil
 4097 temperature. The per-basin trends in this alkalinity concentration are shown in Fig. 6
 4098 (right) and differ somewhat in magnitude and trend from the other alkalinity variables
 4099 in this analysis, with highest concentrations in the Mackenzie, Yukon and Ob basins,
 4100 reflecting the bedrock lithology, and greatest rates of change occurring in the Yukon and
 4101 Mackenzie, reflecting the whole-soil-column changes in temperature and hence
 4102 weathering associated with permafrost thaw.
 4103

4104 Characteristic features of alkalinity concentration seasonality in permafrost regions are
 4105 captured by the model output (Figs. 6-8). These include high concentration values in
 4106 autumn and winter (Fig. 7), as freezing of the top soil hampers runoff flow and facilitates
 4107 only slow subsurface flow with high concentrations as long as the bottom soil is not yet
 4108 frozen, followed by an abrupt collapse in concentration values in spring when the
 4109 freshet or thaw period causes a massive flushing of snow from the land surface whose
 4110 rapid runoff strongly dilutes concentrations. In the summer, concentrations pick up
 4111 again as the active layer deepens, causing deeper entrainment of the weathering

4112 reactant and subsequent access to a larger surface area of weatherable material (Fig. 6,
 4113 right hand side), leading to higher concentrations and fluxes of alkalinity. As expected,
 4114 alkalinity discharge rates are in proportion with river discharge rates (Fig. 6, left)
 4115 although it appears that there are clusters of different response rates to river discharge,
 4116 most likely driven by differing lithology and/or extent of permafrost coverage. These
 4117 dynamics have been found and explained in greater detail by several studies (Drake et
 4118 al., 2018; Tank et al., 2012a, 2016).
 4119

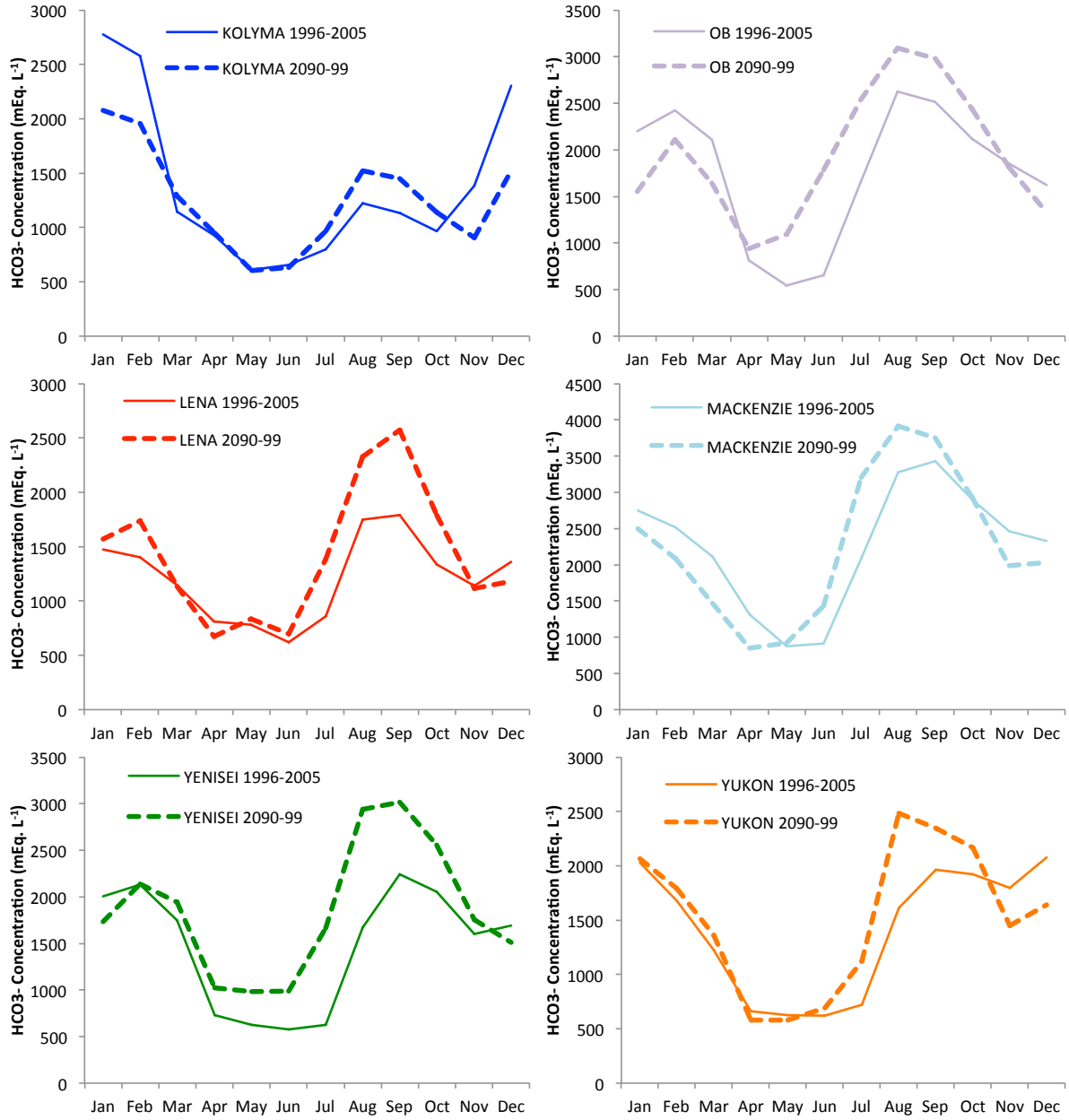


4120
 4121 **Figure 6:** Scatter plots of model output under ISIMIP 2b forcing, where each point represents a given grid
 4122 cell for a given year over the entire simulation period for the Big 6 rivers combined, to show the variation
 4123 of bulk alkalinity discharge rate flowing through rivers (tons s⁻¹) with **(left)** annual mean river discharge
 4124 rate, and **(right)** mean annual maximum active layer depth.
 4125

4126 As shown in Fig. 7, the Big 6 basins share common changes in the seasonality of
 4127 alkalinity concentrations between the end of the 20th and 21st centuries. Generally, the
 4128 whole seasonal cycle is shifted earlier by one or two months, as warmer temperatures
 4129 drive ice melt and peak river flow (corresponding to the concentration minimum)
 4130 earlier in the year. The summertime concentration peak (~Jul-Aug to ~Sept-Oct)
 4131 increases in magnitude for all rivers as warming deepens the active layer and combines
 4132 with late summer rain to increase the high-concentration drainage flux of alkalinity. In
 4133 addition, wintertime concentration peaks (~Dec-Feb) decline in magnitude for all rivers.
 4134 This suggests that wintertime baseflow rates in river discharge increase in the future,
 4135 leading to a suppressive dilution effect on alkalinity concentrations.
 4136

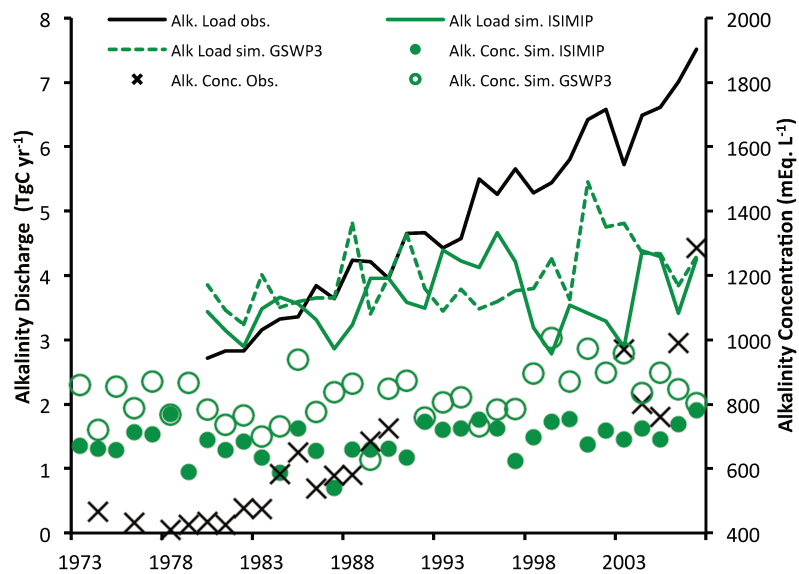
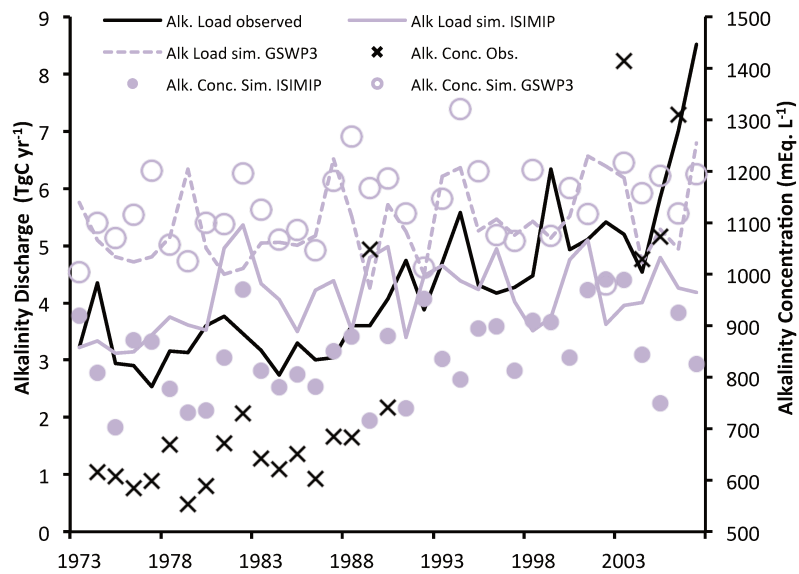
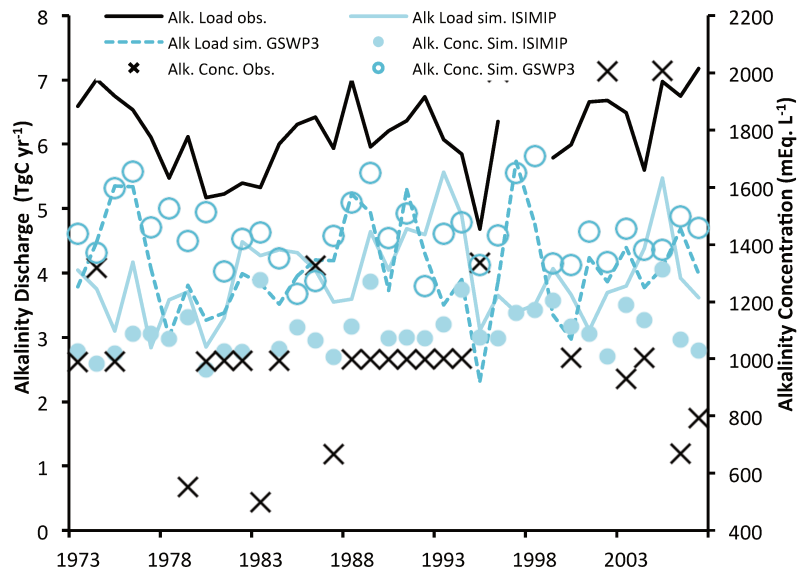
4137 **4.2 Comparing observations with model output per climate input dataset**

4138 Previous studies have suggested that weathering rates and attendant riverine alkalinity
 4139 loading are dominantly driven by runoff and lithology, rather than temperature
 4140 (Eiriksdottir et al., 2011). At the same time, the climatological datasets from which our
 4141 models run generally lead to underestimations (with the exception of the Ob) of runoff
 4142 and river discharge in the Arctic (Table 2), and with a greater negative bias under ISIMIP
 4143 climatology. Thus by comparing observations of seasonal and inter-annual variations in
 4144 bulk fluxes and concentrations with simulations performed using two separate datasets,
 4145 we gain some heuristic grip on the extent to which model-simulation discrepancies
 4146 reflect issues relating to the forcing data, or issues relating to process-representation in
 4147 our simple alkalinity-generating module.



4149
 4150
 4151
 4152

Figure 7: Simulated seasonal variation in alkalinity concentration in the over the decade 1996-2005 (solid) and 2090-2099 (dashed) for the Big Six rivers at outflow grid cell, under ISIMIP 2b forcing.

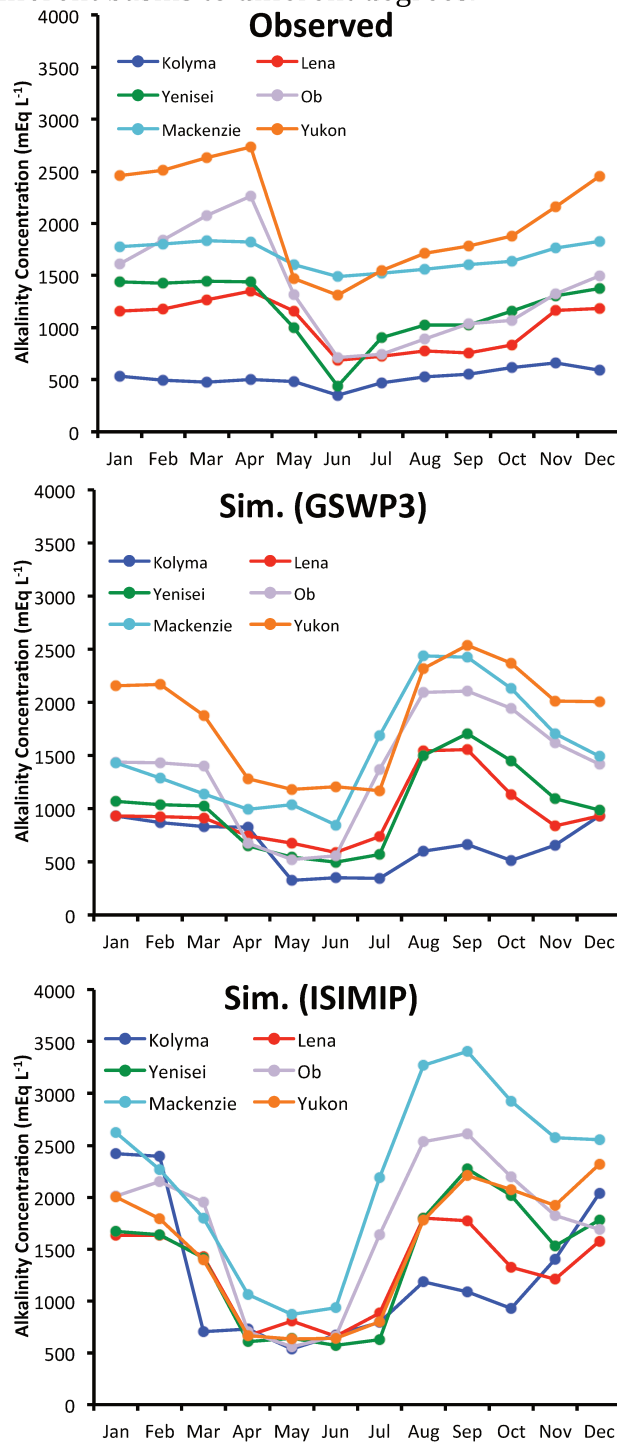


4154 **Figure 8:** Timeseries of bulk annual alkalinity discharge rates at outflow for **(top)** the Ob, **(middle)**
4155 Yenisei and **(bottom)** Mackenzie basins, in simulations (solid) and from empirically-determined
4156 estimates (dotted) in Drake et al. (2018) and Tank et al. (2016), respectively.
4157

4158 Generally, Figure 8 shows that our model does reasonably well in capturing the
4159 magnitude and inter-annual variability of annual alkalinity discharge for the period
4160 ~1973-2007 over the Yenisei, Ob (Drake et al. 2018) and Mackenzie (Tank et al. 2016)
4161 rivers (those Arctic rivers for which long-term data exist in the published literature).
4162 Where the simulated annual river water discharge is low compared to observations
4163 (Yenisei, Mackenzie (Table 2)), so too is the simulated alkalinity discharge. Where bulk
4164 water outflow is overestimated (Ob under GSWP3 climatology), so the alkalinity
4165 discharge is likewise overestimated, suggesting the dominance of runoff as determinant
4166 of weathering flux rates. Inter-annual variations in alkalinity discharge appear to be
4167 reasonably well captured by our model, particularly for the Ob and Mackenzie, however
4168 in Fig. 8 our simulations fail to capture the multi-decadal trends for the two Siberian
4169 rivers: a pronounced increase in alkalinity loading (Drake et al., 2018). However, the
4170 Drake et al. study did not propose explicit causal mechanisms for the dramatic rise in
4171 alkalinity loading, complicating our ability to interpret the apparent shortcomings of our
4172 model. It may be that the temperature sensitivity or the weathering correction for soil
4173 respiration of the model (see Methods, Step 2) are too low or that it uses too low an
4174 activation energy. Similarly, our omission of peat processes or peatland coverage may be
4175 significant due to the high areal coverage of peatland in, particularly, West Siberia (for
4176 example, Zakharova et al. (2007) show that this can be up to 50% of total watershed
4177 area), which may have a significant impact on weathering rates either due to very low-
4178 pH soil waters or due to the comparatively low availability of weatherable material in
4179 peat soils. Speculatively therefore, changes in this areal peat coverage
4180 (expansion/contraction with increasing temperatures) may play a role in long-term
4181 weathering rates and alkalinity loading in rivers. On the other hand, the steep alkalinity
4182 increases seen in the Siberian region may also reflect changes in human production and
4183 consumption systems (e.g. liming or alterations to industrial production and related
4184 energy sources). The model is capable of approximating mean annual alkalinity
4185 concentrations (Fig. 8). Because simulations driven by the ISIMIP dataset lead to even
4186 lower river discharge flows than those driven by GSWP3, alkalinity concentrations tend
4187 to be correspondingly higher in the former compared to the latter simulations. For the
4188 two Siberian rivers, the model overestimates concentrations for the period preceding
4189 1990, and underestimates them for the period following year 2000. This is unsurprising,
4190 given that as previously discussed, our alkalinity model does not reproduce the ~300%
4191 increase in alkalinity loading recorded for these two rivers since the 1970s.
4192

4193 Because of this, and because river discharge in West Siberia has not greatly increased
4194 over that same time period, the observed increases necessarily ascribe to very large
4195 increases in alkalinity concentration. In addition across all rivers, where mean annual
4196 alkalinity concentrations are overestimated, this also partly owes itself to the
4197 underestimation of summertime river flow in both GSWP3 and ISIMIP climatologies
4198 (Fig. 9). This low discharge reduces what would otherwise be a dilution effect,
4199 correspondingly raising the mean annual concentration value simulated. Both simulated
4200 alkalinity load and concentration suffer from an inability to capture the importance and

4201 extent of other, non temperature/runoff/lithology -related processes which could be
 4202 important in different basins to different degrees.



4203 **Figure 9:** Monthly alkalinity concentrations for the Big Six rivers at coastal outflow as reconstructed from
 4204 observations in Tank et al. (2012) averaged over the period 2003-2009 and calibrated by river discharge
 4205 data over 2000-2009 (**top**), and the average simulated by our model over the period 2000-2007 using
 4206 (**middle**) ISIMIP 2b and (**bottom**) GSWP3 climatological data.

4207
 4208
 4209 For example, the impact of glacial processes and glacial thaw, the cracking exposure of
 4210 weatherable material caused by repeated freeze-thaw cycles and the prevalent exposure
 4211 of bare rock and soil to precipitation in mountainous Arctic regions are high latitude-

4212 specific factors which by nature would have a high temperature sensitivity that would
4213 increase the amount of alkalinity transported in runoff. But the importance of such
4214 changes to these fluxes is not known and this is not considered here.

4215

4216 **4.3 Alkalinity and weathering in Arctic lateral-flux carbon budgets**

4217

4218 To our knowledge, ORCHIDEE M-L is the first and currently only land surface model to
4219 include carbonate alkalinity in the geological loop of the carbon cycle perturbed by
4220 climate change in the past and future century. This may be a substantial issue for C cycle
4221 models. Figure 10 explains why. Our model output suggests that over the Big 6 rivers
4222 combined, alkalinity input from soils to rivers in the present day are of the same order
4223 as DOC inputs, in C equivalent terms (23.1 vs 27.3, respectively). Likewise, the uptake of
4224 CO₂ from weathering in the present day exceeds outgassing from riverine CO₂ evasion
4225 (12.1 vs 15.6), which is the major C loss term for the inland-water C cycle, while
4226 alkalinity outflow to the Arctic Ocean also exceeds DOC outflow (19.4 vs 23.1). The
4227 relative importance of the alkalinity generation/flux and weathering CO₂ uptake only
4228 increases in a warmer future, as both processes increase their flux rates by around one-
4229 third, while DOC fluxes across the Big Six decline in aggregate. In particular, CO₂ uptake
4230 from weathering increases to 180% of evasion, meaning that the inclusion of lateral
4231 fluxes that themselves include alkalinity generation shift the inland water C cycle from a
4232 status of net C source to net C sink.

4233

4234 Furthermore, while both DOC fluxes and alkalinity fluxes have been shown to be
4235 underestimated by our modeling scheme, the former largely due to the poor
4236 representation of precipitation in the forcing files and the exclusion of peat in peat-rich
4237 basins, the latter also due to the precipitation issue as well as poor representation of
4238 some high latitude weathering processes, the factor of this underestimation is
4239 substantially higher for alkalinity fluxes, implying that its real importance relative to the
4240 organically-generated C fluxes may likewise be significantly higher. At the biome scale,
4241 the combined lateral flux process representation enabled by our inclusion of the
4242 relevant organic and inorganic dynamics involved in them in the land surface
4243 component of an Earth System model suggest that far from being a minor component of
4244 the C cycle, the combined lateral flows constitute 16% of net biosphere productivity
4245 (51/324 TgC yr⁻¹), or NPP –heterotrophic respiration, in the present day. This is likely
4246 an underestimate by a factor of at least two, given the shortcomings of our modeling
4247 approach and forcing data inputs used to generate them, when these are compared to
4248 empirical data. From this we can conclude that the inland water system offers a C sink to
4249 buffer the effect of increased temperatures in permafrost regions, since on the one hand
4250 the processes that promote the lateral flux of organic carbon (DOC) tend to decline with
4251 warming, decreasing the potential amount of carbon available to be outgassed as
4252 evasion to the atmosphere, while on the hand promoting the lateral flux of
4253 lithogenically-sourced C, increasing atmospheric C uptake.

4254 **5 Conclusions**

4255 Despite the shortcomings of this simple alkalinity generation module described above,
4256 we have shown that for some Arctic basins it remains capable of reproducing first order
4257 bulk alkalinity discharge fluxes as well as their seasonality and concentration. In

4258 addition, we have shown that far from being a minor component of the Arctic C cycle,
 4259 weathering and alkalinity fluxes are major constituents of it.
 4260

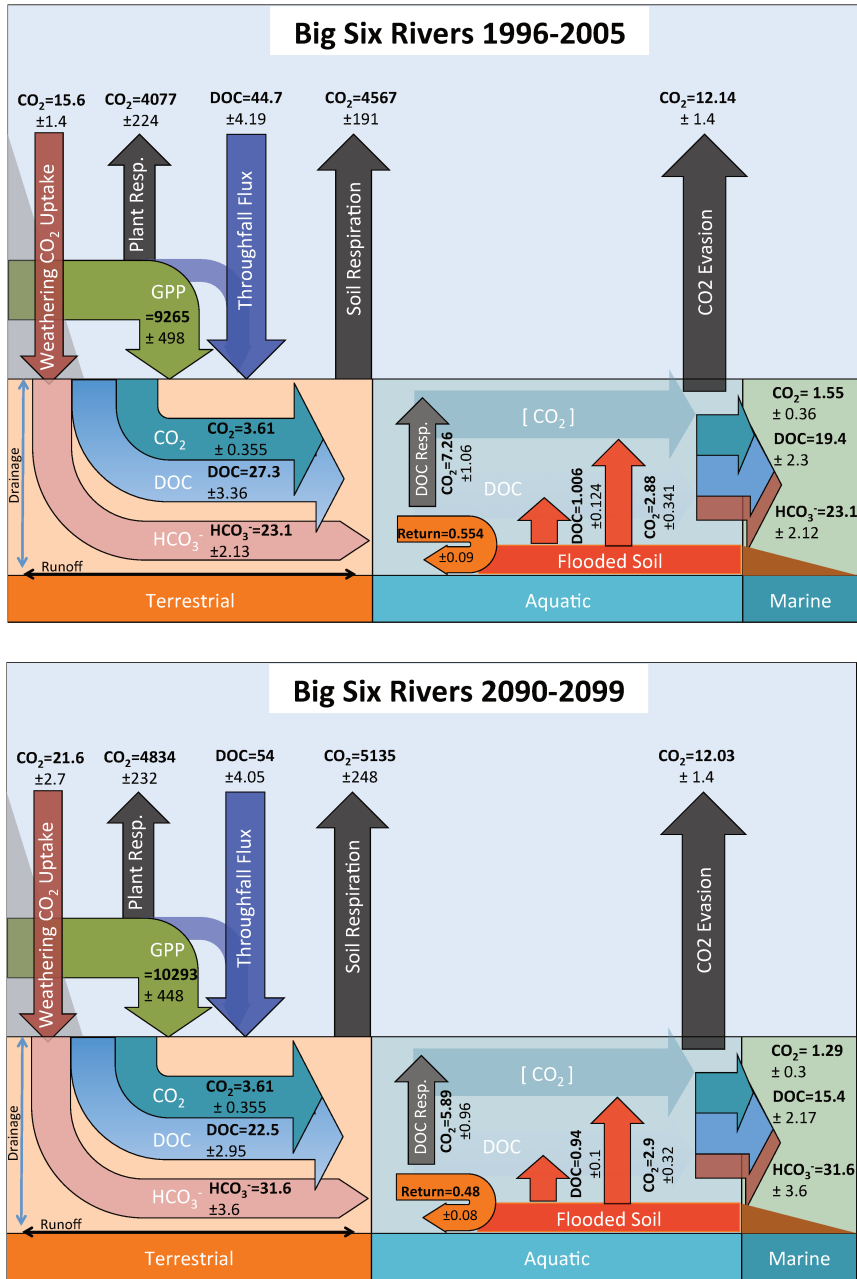


Figure 10: Major carbon fluxes (TgC yr⁻¹) over the terrestrial-aquatic continuum for the Big 6 Arctic rivers combined, averaged over (top) 1996-2005 and (bottom) 2090-2099.

4261
 4262
 4263
 4264
 4265
 4266
 4267
 4268
 4269
 4270
 4271
 4272

4273
4274
4275
4276
4277
4278
4279
4280
4281
4282
4283
4284
4285
4286
4287
4288
4289
4290
4291
4292
4293
4294
4295
4296
4297
4298
4299
4300
4301
4302
4303
4304
4305
4306
4307
4308
4309
4310
4311
4312
4313
4314
4315
4316
4317
4318
4319

Chapter 6: Perspective and Outlook

General Summary

This thesis and the studies of which it is comprised have sought to trace the development of a model that is able to simulate at a broad spatial and temporal scale the dynamics of biogenic and lithogenically -generated lateral carbon (DOC, CO₂ and alkalinity) transfer in permafrost ecosystems. Having described a new DOC-generating model fully coupled to hydrology and terrestrial carbon cycling and evaluated its ability to adequately represent these dynamics at a high spatial, temporal and, for an Earth system model, process resolution in Chapters 2 and 3, respectively, Chapter 4 uses the tool to project the response of the lateral flux system to future changes in the Arctic until the end of the 21st Century. Our simulation results in that study suggest that, contrary to first-order empirical expectations, the response of lateral fluxes to warming in the absence of large scale increases in precipitation-driven runoff, actually decrease the total throughput of carbon to inland waters. Chapter 5 then describes a new, simple module added into ORCHIDEE M-L for the simulation of alkalinity fluxes and shows it is able to broadly simulate present day alkalinity discharge fluxes for the 'Big 6' Arctic rivers, and further, that these fluxes increase substantially in the future when the model is forced by projections of future climatic conditions. Crucially, Chapter 5 also shows that by including the weathering uptake of CO₂, the land inland water lateral carbon transfer system switches from being a net source to a net sink of carbon as weathering carbon uptake exceeds CO₂ evasion from the river surface, even without the representation of autochthonous (in-stream) primary production in our model. Overall, this cumulative work represents a novel and substantial addition to the existing body of research and modelling products available to address such questions. Nonetheless, as with all endeavours in numerical modelling, ours suffers from substantial omission in process representation. In addition the lack of spatio-temporally representative empirical data that would enable greater theoretical understanding, improved input data and stronger baseline for evaluating the model on a Pan-Arctic scale is particularly acute for permafrost-affected areas, owing to the practical and logistical difficulties in acquiring such data. In what follows we summarise some of these data gaps, followed by gaps in the modelling scheme, how these two relate to one another, and discuss the plausible effects of their availability/inclusion.

The Data Gap

The carbon budget of Arctic rivers is poorly constrained with regard to both stocks and fluxes, with land surface flux data at the catchment scale particularly lacking. This limits the ability to understand and predict the amplified surface warming caused by future permafrost thaw and CO₂ release, with current estimates of cumulative terrestrial permafrost-sourced atmospheric loading standing at 65-240 PgC by 2100(Schuur et al., 2015). Given the region's geographical remoteness and the complexity of interacting snow, ice, soil and biology, ground observations are sparse and yet utterly critical for

4320 our understanding. Narrowing gaps will require better understanding of hydrological
4321 and biogeochemical dynamics (surface and subsurface) for all watersheds, in particular
4322 those outside the 'Big Six' rivers, which feed substantial volumes of Arctic Ocean
4323 discharge(Holmes et al., 2012) yet display different dynamics (e.g. base-flow of zero)
4324 due to the fact that they are at present entirely underlain by continuous permafrost.
4325 Indeed, our simulation output in Chapter 3 shows that the 'Medium 9' –the 9 next-
4326 largest rivers after the 'Big 6' –discharge about a third the quantity of DOC as the Big 6,
4327 despite proportionally lower water discharge, and that this fraction increases over the
4328 21st Century (Chapter 3, Table 1).

4329
4330 Current estimates for Arctic and boreal region CO₂ evasion are likely to be strong
4331 underestimates, given that empirical studies tend to sample from the river main stem
4332 over limited time periods, whereas extremely high DOC concentrations and CO₂ evasion
4333 rates found in both boreal and Arctic headwater streams are consistently under-
4334 sampled (e.g. refs.(Drake et al., 2015; Teodoru et al., 2009)). The current inland water
4335 evasion estimate over the high latitudes is around 40-84 TgC yr⁻¹ being emitted from
4336 Arctic lakes and rivers, of which 15-30 TgC yr⁻¹ is thought to be from rivers
4337 alone(Mcguire et al., 2009). Our modern-day evasion estimates from the Big 6 rivers
4338 alone total 12.14 TgC yr⁻¹, and bring our estimates for that flux close to the mid-range of
4339 the first order estimates (20.1 TgC yr⁻¹). Nonetheless, *despite being the dominant*
4340 *pathway for laterally exported carbon*(Drake et al., 2017), the fact that even a river the
4341 size of the Lena has, to our knowledge, never been the subject of a CO₂ evasion
4342 measurement campaign on either main stem, tributary or headwater scale highlights the
4343 extent of what is missing from empirical literature.

4344
4345 In addition, further hydrological data (volumes, timing, temperature) across the
4346 spectrum of small and large rivers, upstream, downstream and across the extent of their
4347 floodplains and coastlines, on connectivity of lakes (including thermokarst) with each
4348 other and to rivers via surface and subsurface flows, as well as higher spatio-temporal
4349 resolution maps of subsurface ice content are urgently needed. Without these, reliable
4350 estimates of carbon and nutrient transport rates, respective residence times and
4351 associated uptake and metabolization pathways and their subsequent flux rates, cannot
4352 be generated with much certainty.

4353
4354 Likewise, we recommend further pilot studies exploring the dynamics of POC and DOC
4355 parent material, in-stream burial and reaction rates along the length of the river reach.
4356 Basin-wide rates of organic carbon mobilization and their relative age, their processing
4357 within the aquatic continuum and how all of these factors vary seasonally and with
4358 multi-year temperature differentials remains somewhat speculative, despite some
4359 progress(O'Donnell et al., 2016). The impact of microbial or photo-degradation
4360 'priming' (De Baets et al., 2016) that might arise from mixing water and or soil masses
4361 with constituents of different sources and ages (e.g. ref.(Guenet et al., 2010)) requires
4362 comprehensive investigation. In lieu of existing basin-scale data, modeling studies
4363 might in the meantime make use of emergent properties such as the scaling relationship
4364 found between water retention time and carbon decay rate(Catalán et al., 2016), to
4365 derive carbon decomposition in complex Arctic hydro-systems.

4366

4367 Perhaps the most glaring gap in empirical data and process understanding concerns the
4368 terrestrial-marine transition zone (the continental shelf), and the effect of lateral fluxes
4369 on this region. While the drivers of organic matter outflow from rivers and the coast to
4370 the Arctic Ocean are relatively well established, little is known regarding its transport
4371 and fate along the Arctic continental shelf, particularly in the East Siberian Arctic
4372 Shelf(Semiletov et al., 2012). There, terrestrially-derived DOC behaves non-
4373 conservatively(Alling et al., 2010), causing high $p\text{CO}_2$ in, and acidification of, the near-
4374 shore zone, a phenomenon previously ascribed to surface water uptake of
4375 anthropogenic CO_2 (Biastoch et al., 2011; Semiletov et al., 2016). Acidification in
4376 addition to changes in riverine OC outflows, may in turn alter the composition of
4377 primary producers and heterotrophs along the shelf and beyond (Findlay et al., 2015b)
4378 In addition, little is known of marine permafrost stocks and fluxes
4379 ($\sim 1000 \pm 500 \text{PgC}$ (Shakhova et al., 2010)) –their extent, distribution, thickness, thermic
4380 conductivity, composition – and the response of these to both terrestrial heat and
4381 density (freshwater) fluxes over both short and long timescales(Archer, 2015; Janout et
4382 al., 2016; Nicolsky et al., 2012; Overduin et al., 2015; Sapart et al., 2017; Shakhova et al.,
4383 2014, 2015; Shakhova and Semiletov, 2007).

4384
4385 Finally, the Arctic and boreal land-ocean-aquatic continuum involve a wide range of
4386 methane stocks, methane-producing conditions, and transformative processes. These
4387 occur across the landscape, from thawing soils, thermokarst formations, lakes and
4388 inland waters, to the estuarine and shelf environments. Methane (CH_4) may contribute
4389 $\sim 40\%$ of total CO_2 -equivalent evasion from boreal rivers(Campeau et al., 2014; Campeau
4390 and Del Giorgio, 2014). CH_4 emissions occur dominantly in the winter (post-August) as
4391 the active layer is retained despite subzero air temperatures, through snow insulation
4392 and the thermal mass of soil water. Significantly, observed emissions are most acute in
4393 least inundated areas(Zona et al., 2015), contrary to previous theory(Bohn et al., 2015).
4394 Thus methane emissions from tundra wetlands of $16\text{-}27 \text{Tg CH}_4\text{yr}^{-1}$ (Bruhwiler et al.,
4395 2014; McGuire et al., 2012)are comparable to those from non-inundated tundra (23Tg
4396 $\text{CH}_4 \text{yr}^{-1}$ (Zona et al., 2015))and are likely to increase as Arctic winters warm. CH_4
4397 concentrations (and evasion) have been shown to co-vary significantly with those of
4398 CO_2 , suggesting common nodes of regulation or origin, despite markedly differing
4399 pathways of transformation. Unlike CO_2 concentrations, $p\text{CH}_4$ appears to be tightly
4400 coupled to temperature, with a Q_{10} of 4.1, suggesting that emissions therein may
4401 increase significantly ($\sim 30\text{-}100\%$) in the future(Campeau and Del Giorgio, 2014) In
4402 particular, Boreal lakes and ponds have been assessed as ‘hot spots’ for methane
4403 emissions(Bastviken et al., 2011; Tranvik et al., 2009) and thermokarst lakes and subsea
4404 methane deposits are thought to play an increasing role under warming
4405 conditions(Shakhova et al., 2010). These have been under-represented in the literature,
4406 and have a significant role to play in future pilot studies.

4407

4408 **The modelling gap**

4409

4410 This set of studies has sought to include a wide range of organic and inorganic carbon
4411 production, transformation and flux processes from permafrost-specific regions into a
4412 global climate model. The resulting product has permitted subsequent analysis and
4413 breakdown of the key drivers of this system, as well as their response to change.

4414 However, as it stands the configuration of this broad-scale process representation in our
4415 model is far from complete, with multiple areas of potentially substantial impact on the
4416 land-ocean-aquatic continuum with respect to permafrost thaw fully omitted from the
4417 current scheme.

4418
4419 As discussed in Chapter 3, the exclusion in our model of primary production by
4420 bryophytes (mosses, liverworts) as the dominant carbon uptake force in certain high
4421 latitude wetland regions (e.g. parts of the Ob river watershed) leads to the exclusion of
4422 peatlands, which are formed from these organisms, as well as attendant impacts on soil
4423 and soil-water dynamics. Due to their relative inhibition of oxidative decomposition
4424 from to soil water saturation, peatland areas tend to be characterised by much higher
4425 DOC concentrations, which are readily mobilised to rivers and streams if they are
4426 connected to the river network. If not directly connected, as in the aforementioned
4427 lakes and ponds, this high concentration can translate into large emissions of CH₄ from
4428 the water surface. This gap in process representation is, however, likely to be closed in
4429 the near future, given that a recent model version under the high-latitude ORCHIDEE
4430 umbrella (Guimberteau et al., 2018; Koven et al., 2013a; Qiu et al., 2018) has been coded
4431 to represent precisely these ecosystems, and thus awaits a relatively simple merger with
4432 our DOC-producing version to be included.

4433
4434 The anaerobic respiration of organic matter that occurs as a result of water inundation
4435 of that matter generally promotes methane as the dominant by-product of respiration.
4436 The methane cycle is not represented in our model, and would likely further increase
4437 the CO₂-equivalent respiration of the permafrost region, were it included. The process
4438 of methane generation is not spatially static, however, in that permafrost thaw over
4439 areas of high ice volume can lead to rapid local collapse of the soil column and the
4440 formation of depressions overlying carbon-rich soil, known as thermokarst.
4441 Thermokarst formation in turn promotes the formation of small, interconnected lakes,
4442 which have been shown to be hotspots of both CO₂ and methane emissions, but this
4443 phenomenon is as yet omitted from representation in our model, despite it being a
4444 characteristic dynamic of permafrost thaw systems. Nonetheless, we are not
4445 conceptually far from being able to include them in ORCHIDEE, given the progress and
4446 leg-work previously undertaken by (Lee et al., 2014) to include this in the Community
4447 Land Model earth system model.

4448
4449 While the high level of CO₂ evasion in headwater streams of permafrost watersheds
4450 demonstrated by a large number of empirical studies is likewise evident in our
4451 simulation of the high latitudes, as documented in Chapter 3, analysis of this dynamic is
4452 hampered by two shortcomings of our model scheme. Firstly, the model lacks explicit
4453 representation of 'stream' surface area at the sub-grid scale. This hampers
4454 determination of the real CO₂ flux rate, which we have inferred only from the relative
4455 size of the cumulative stream versus river water volumes boxes in our model output.
4456 Further, given that the surface area:depth or surface area:water volume ratios of small
4457 streams versus large rivers are likely to differ substantially, the methodology used in
4458 Chapter 3 likely greatly underestimates the true evasion rate being simulated.
4459 Furthermore, given that high headwater evasion rates are thought to be related to the
4460 mobilisation of once-thermally shielded reactive soil carbon, the lack of a tracer
4461 dimension relating a given carbon flux vector to a given soil or litter pool reactivity

4462 source and age remains a significant limitation on evaluating both the model's
4463 performance and for understanding what is being mobilised into lateral fluxes in greater
4464 proportion in a warmer Arctic: contemporary, CO₂-boosted litter inputs, or newly-
4465 exposed, ancient soil matter from the permafrost layer?

4466
4467 Although the fraction of carbon discharged by high latitude rivers in particulate form is
4468 relatively small(Raymond et al., 2007), this fraction differs strongly between basins, and
4469 is affected by a host of processes including glacial action, bank erosion, and thermokarst.
4470 As noted in the Introduction, the exposure of soil matter due to thaw is likely to result in
4471 either lateral transport or atmospheric release. If eroded, and passed on to streams,
4472 POC may end up being deposited into river or sea bed sediments, removing it once more
4473 from the pool of carbon available to metabolism in the short-term. Thus, the
4474 exclusion of this erosive flux, in conjunction with thermokarst processes in the model
4475 omit a potentially significant buffering factor with regard to the carbon released in
4476 lateral fluxes over the Arctic. This will likely be remedied in the future with the
4477 inclusion to this model of a soil erosion emulator that has already been made consistent
4478 with the ORCHIDEE soil carbon scheme(Naipal et al., 2018).

4479
4480 Finally, parallel to all the land surface dynamics represented or discussed in the
4481 preceding sections and chapters, yet absent from the model code or indeed the context
4482 of the discussion thus far, is the role that other nutrients have to play in regulating the
4483 carbon cycle, in particular that of nitrogen (N) and phosphorous (P). Additional to the
4484 clear benefits of including the cycling of these primary production-limiting elements in
4485 any vegetation or land surface model is the expectation that with high latitude warming
4486 and permafrost thaw will come the substantial liberation of these nutrients from soil
4487 carbon stocks previously under the protection of the permafrost shield. This release
4488 may in turn cause previously nutrient-limited production to increase, countering carbon
4489 losses implicit in permafrost thaw (Koven et al., 2015). Indeed, this thaw-induced
4490 nutrient release has been documented (Keuper et al., 2012) in northern peatland soils,
4491 which are N-limited, and may be a major feedback in the Arctic carbon cycle.

4492
4493 While ORCHIDEE incorporates a module that probabilistically simulates fire events and
4494 the subsequent combustion of large areas of biomass stock (Yue et al., 2016), this
4495 module has not been activated in the simulations documented here. The subsequent
4496 lateral transfer of burned material as DOC and POC into rivers, which may constitute a
4497 substantial proportion of total bulk DOC discharge(Myers-Pigg et al., 2015), is thus
4498 negated from the present modelling framework. Including it will entail some
4499 substantive additions to the soil carbon and fire modules, in order to incorporate both
4500 the highly stable pyrogenic soil carbon as well as the leaching of DOC from that soil pool.

4501
4502 Despite the above limitations, we remain confident in the broad conclusions drawn from
4503 this sequence of studies.

4504
4505
4506
4507
4508
4509

Appendices

Appendix 1

Appendix to Chapter 2:

ORCHIDEE MICT-LEAK (r5459), a global model for the production, transport and transformation of dissolved organic carbon from Arctic permafrost regions, Part 2: Model evaluation over the Lena River basin.

Table S1: Data type, name and sources of data files used to drive the model in the study simulations.

Data Type	Name	Source
Vegetation Map	ESA CCI Land Cover Map	Bontemps et al., 2013
Topographic Index	STN-30p	Vörösmarty et al., 2000
Stream flow direction	STN-30p	Vörösmarty et al., 2000
River surface area		Lauerwald et al., 2015
Soil texture class		Reynolds et al. 1999
Climatology	GSWP3 v0, 1 degree	http://hydro.iis.u-tokyo.ac.jp/GSWP3/
Potential floodplains	Multi-source global wetland maps	Tootchi et al., 2018
Poor soils	Harmonized World Soil Database map	Nachtergaele et al., 2010
Spinup Soil Carbon Stock	20ky ORCHIDEE-MICT soil carbon spinup	Based on config. in Guimberteau et al. (2018)

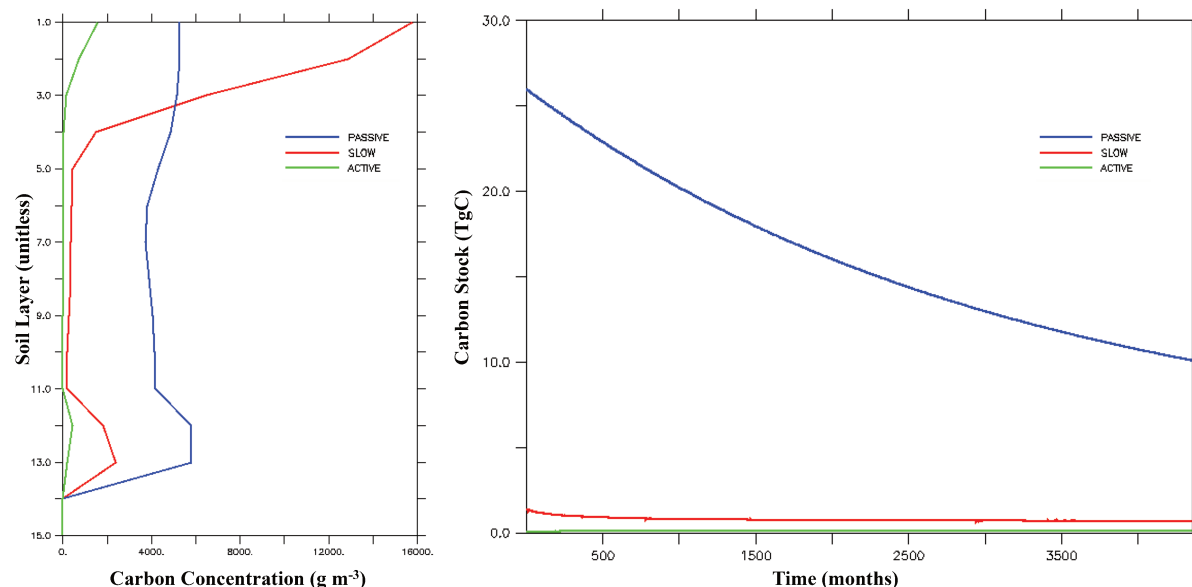
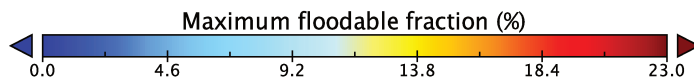
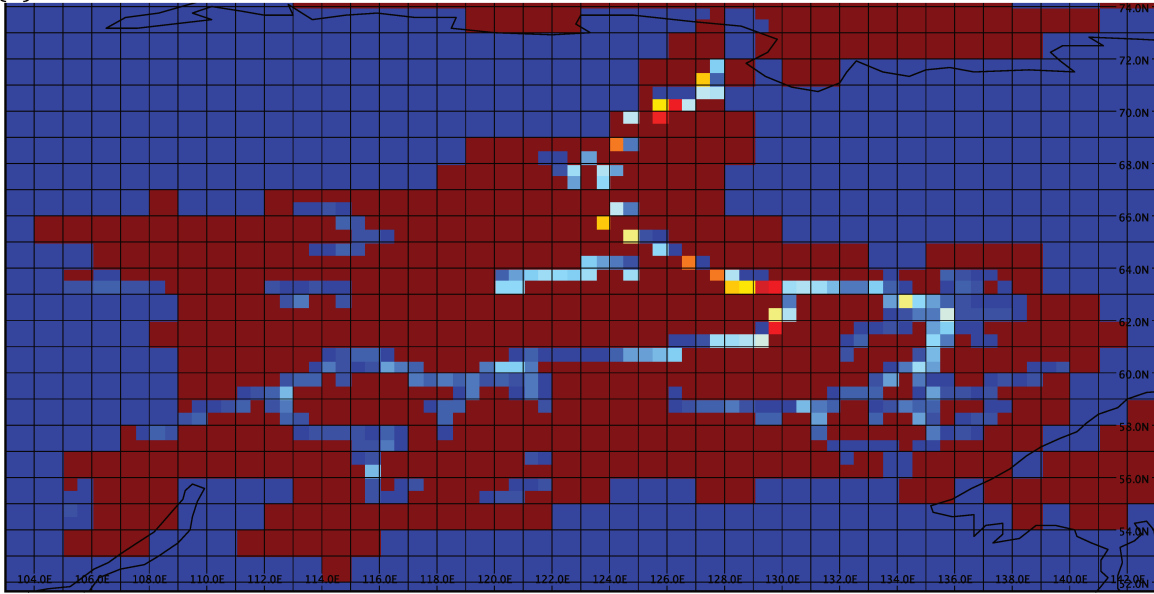


Figure S1: (Left) Soil carbon concentrations per depth level for each soil carbon reactivity pool at the end of the spinup period. (Right) Evolution of each soil carbon pool over the course of the 400-year spinup quasi-equilibration period.

4532

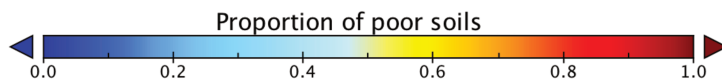
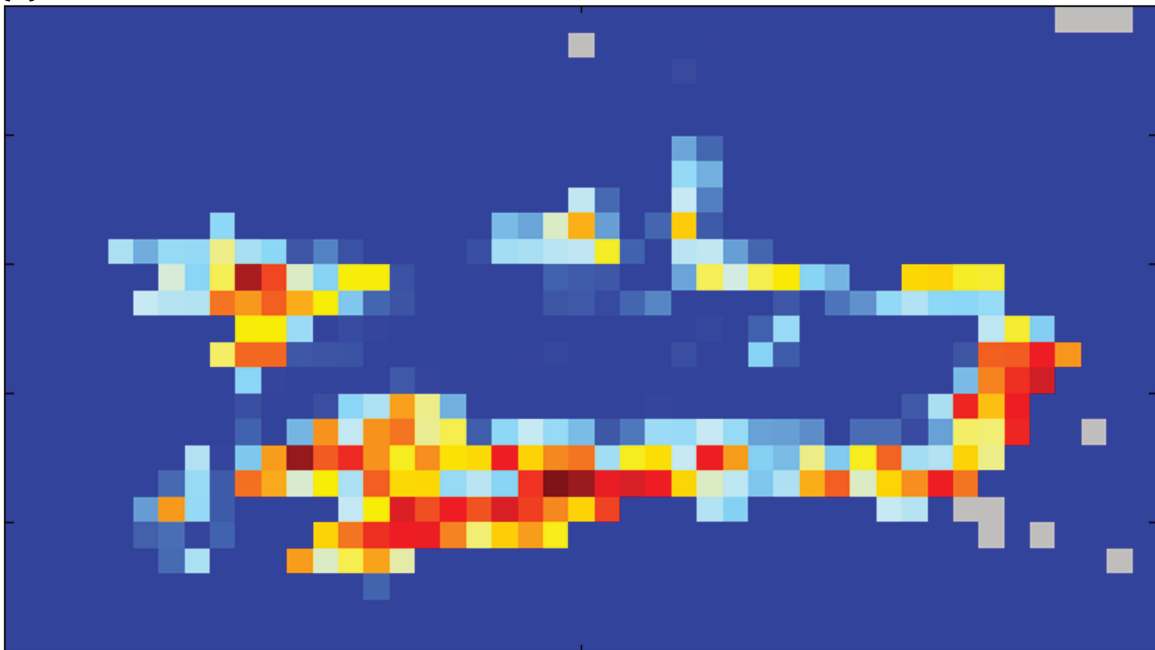
(a)



4533

4534

(b)



4535

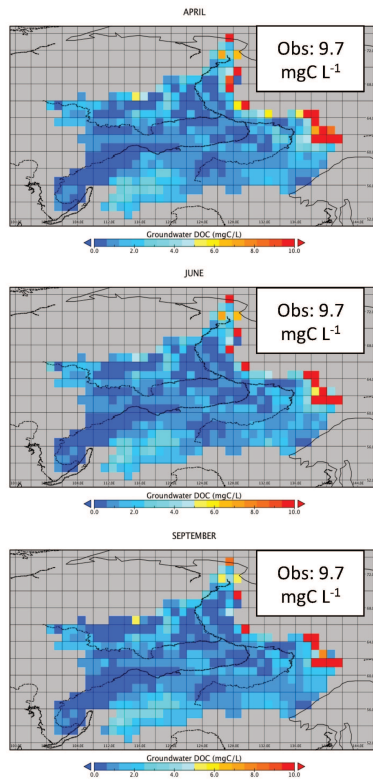
4536

4537

4538

4539

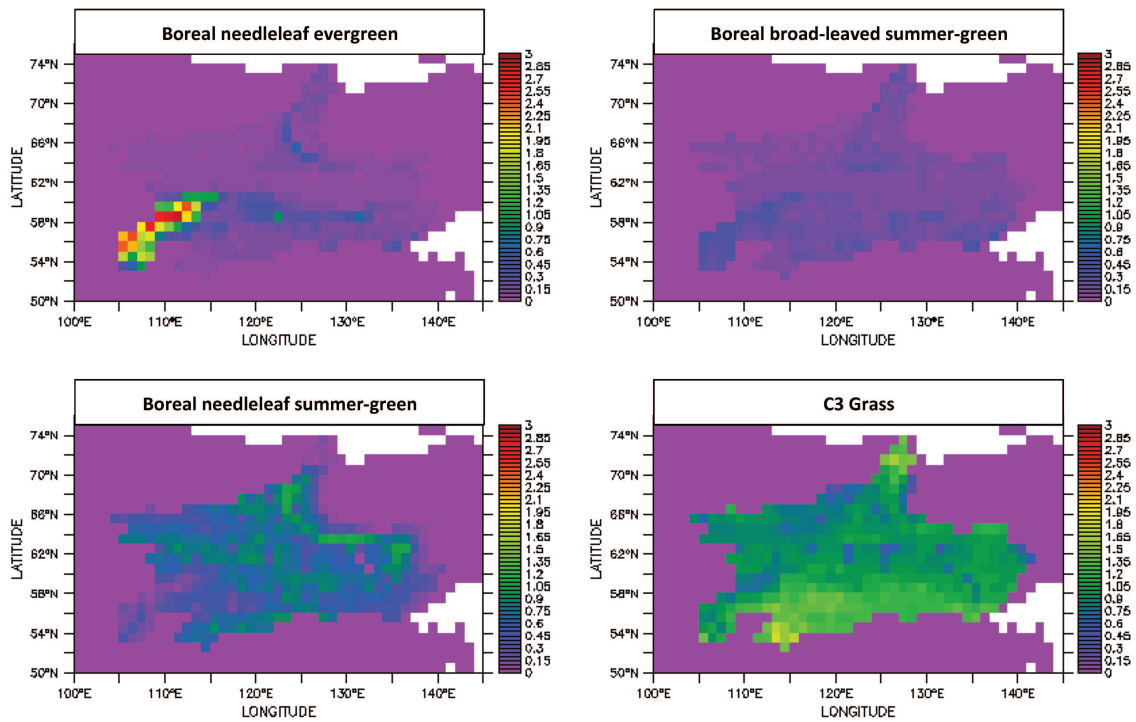
Figure S2: (a) Maximum floodable fraction of grid cells for the Lena basin per the input map from Tootchi et al. (2018). (b) Podzol and Arenosol map (Nachtergaele, 2010) used as input to the 'poor soils' module.



4540
4541
4542
4543
4544
4545

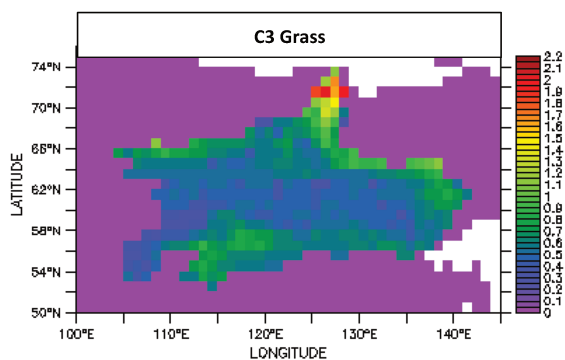
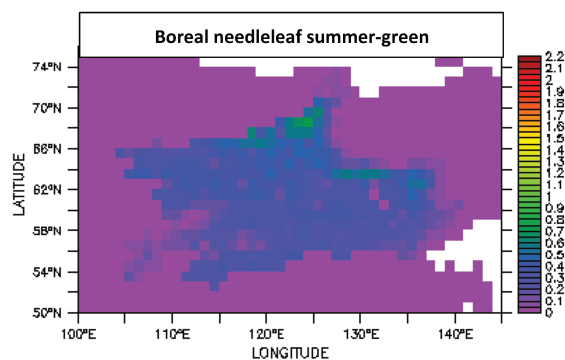
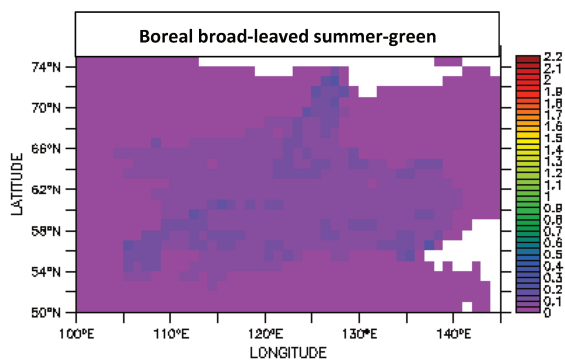
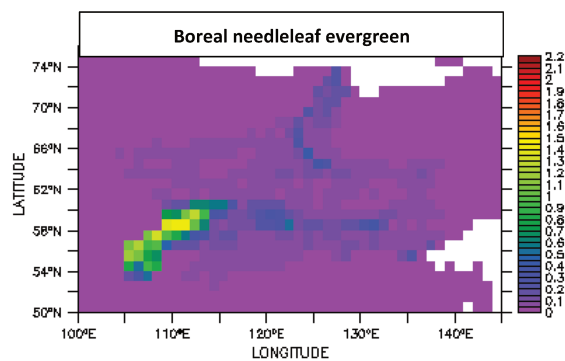
Figure S3: Groundwater DOC concentrations over the Lena basin for April, June and September averaged over 1998-2007, with mean observed concentrations for permafrost groundwater inset.

(a)



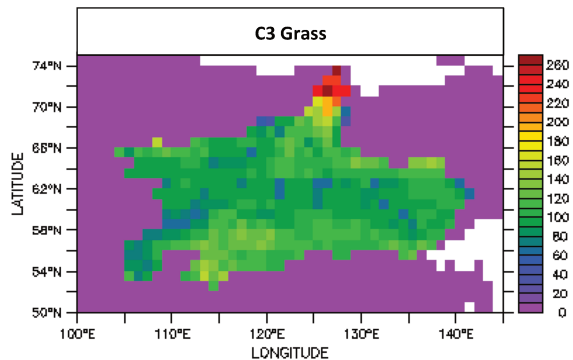
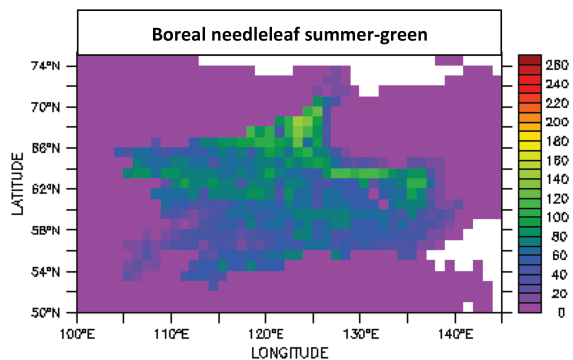
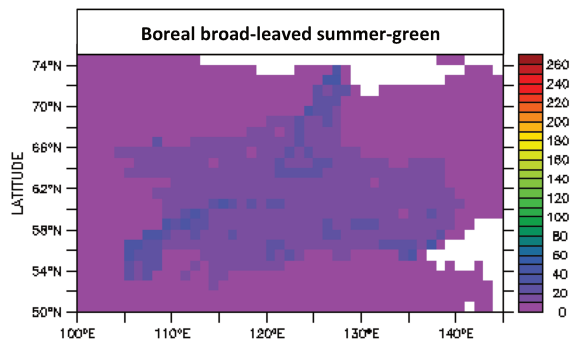
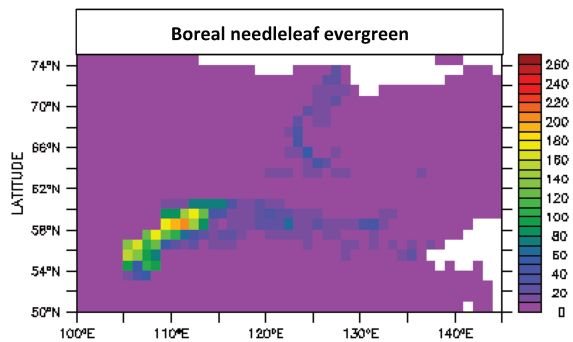
4546
4547

(b)



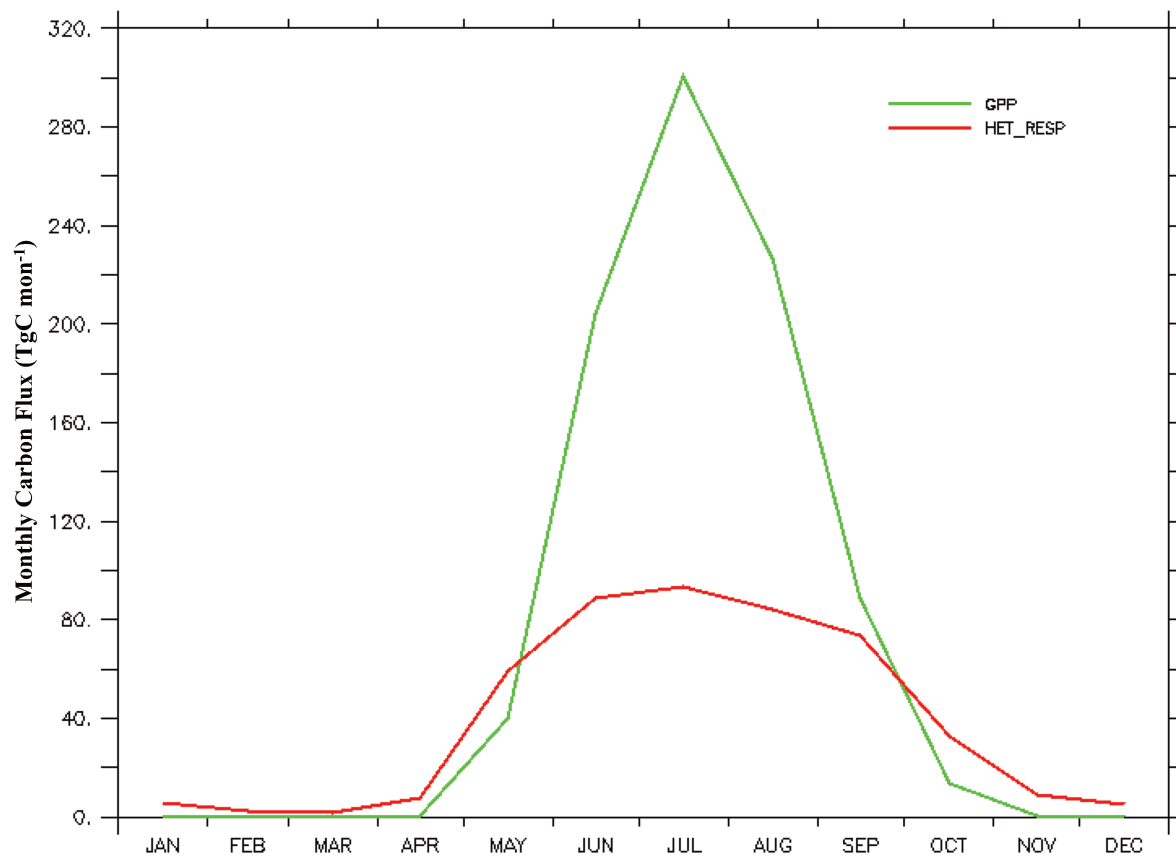
4548
4549

(c)

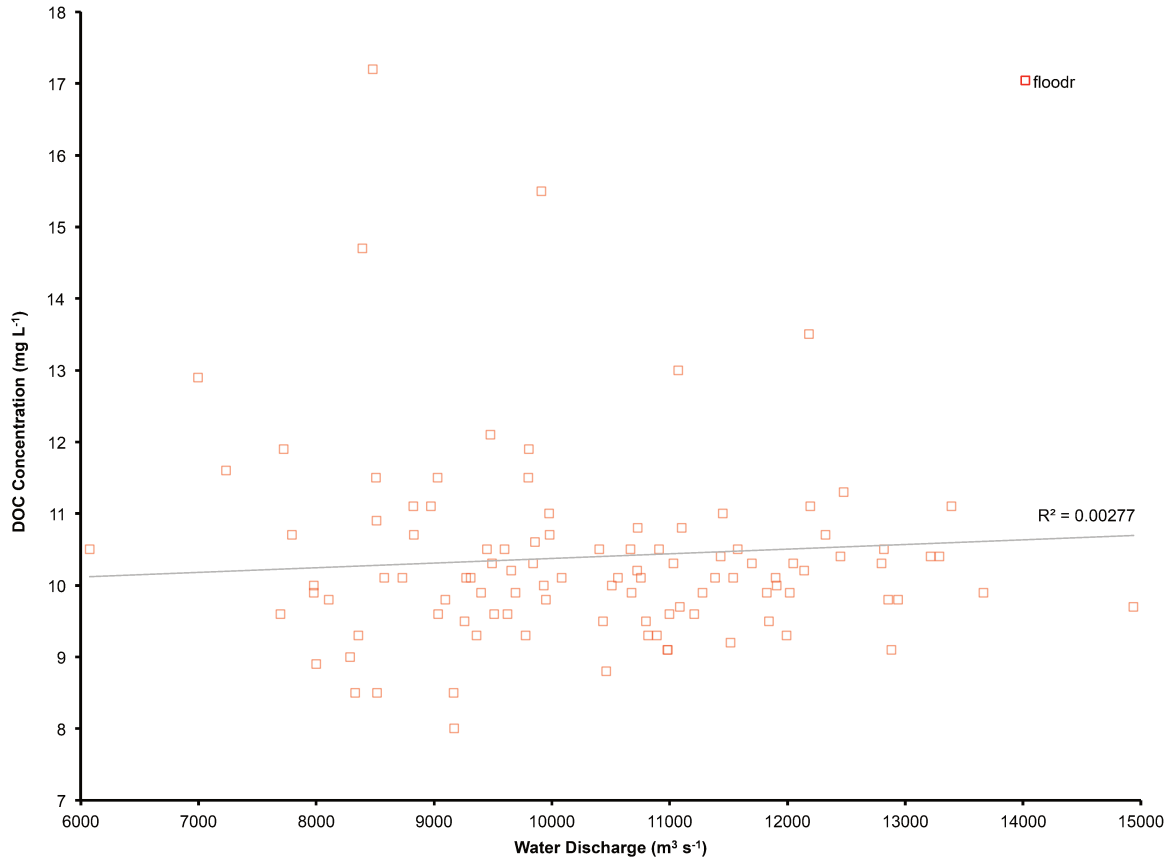


4550
4551

(d)



4552
 4553 **Figure S4:** (a) Absolute yearly gross primary productivity (GPP, TgC yr⁻¹) for the four
 4554 relevant PFT groups over the Lena basin, averaged over 1998-2007. (b) Mean July and
 4555 August soil heterotrophic respiration rates (g m² d⁻¹) for the same PFT groups as in (a),
 4556 during the period 1998-2007. (c) Average yearly NPP (gC m² yr⁻¹) averaged over the
 4557 period 1998-2007. (d) Mean monthly carbon uptake (GPP) versus its heterotrophic
 4558 respiration from the soil (Het_Resp) in TgC per month, over the period 1998-2007.
 4559



4560
 4561
 4562
 4563
 4564
 4565
 4566
 4567
 4568
 4569
 4570
 4571
 4572
 4573
 4574
 4575
 4576
 4577
 4578
 4579
 4580
 4581
 4582
 4583
 4584

Figure S5: Simulated basin-mean annual DOC concentrations (mg L⁻¹) for the floodplain water pool regressed against mean annual simulated discharge rates at Kusur (m³ s⁻¹) over 1901-2007. A linear regression with R² value is plotted.

4585 **Appendix 2**
4586 **Appendix to Chapter 4:**
4587 **Arctic lateral carbon fluxes decline with warming.**

4588
4589

4590 **Methods**

4591

4592 **Model description**

4593

4594 This study uses a new branch version of the land surface model ORCHIDEE (Organising
4595 Carbon and Hydrology in Dynamic Ecosystems(Krinner et al., 2005)), the terrestrial
4596 component of the IPSL Earth System Model (IPSL-ESM). This model version (ORCHIDEE
4597 MICT-LEAK, revision r5459) brings together a recent DOC production module(Camino-
4598 Serrano et al., 2018) and DOC and dissolved CO₂ lateral transport module(Lauerwald et
4599 al., 2017) with the high latitude-specific ORCHIDEE version(Guimberteau et al., 2018),
4600 which includes novel routines and representations of cold region phenomena for snow,
4601 ice, soil carbon and permafrost. This new model version has been recently described in
4602 detail and evaluated over the Lena River basin ((Bowring et al., 2019a, 2019b)). No
4603 changes to the code post-dating those publications were made for the simulations
4604 undertaken in this study.

4605

4606 **Forcing Data**

4607

4608 The climatological forcing data used to drive the model for historical and future
4609 simulations was taken from reconstructed and projected output from the IPSL Earth
4610 System Model under the second Inter-Sectoral Impact Model Intercomparison Project
4611 (ISIMIP2b(Frieler et al., 2017; Lange, 2016, 2018)) rubric, following the trajectory of
4612 Representative Concentration Pathway 6.0 (RCP 6.0). Climatological input data are at a
4613 daily temporal and 1 degree spatial resolution, covering the period 1898 to 2100. The
4614 input vegetation and land cover map was taken from the 5th Coupled Model
4615 Intercomparison Project 5 (CMIP5-LUHa) output. The water height threshold, used to
4616 define the water level at which floodplain inundation is triggered, is obtained
4617 statistically over multiple 30 year (1976-2005) model runs using ORCHIDEE MICT-
4618 LEAK, in a stepwise procedure first described in ref. ((Lauerwald et al., 2017)) and
4619 employed in (Bowring et al., 2019b). The remaining input forcing data for topographic
4620 index, stream flow direction, river surface area, soil texture, potential floodplains, bulk
4621 density, pH, 'poor soils' and soil carbon spinup (refs. (Guimberteau et al., 2018;
4622 Lauerwald et al., 2015; Nachtergaele, 2010; Reynolds et al., 2000; Tootchi et al., 2019;
4623 Vorosmarty et al., 2000), respectively) are summarised in Table 1 of the Supplement.

4624

4625 **Simulation Setup**

4626

4627 As detailed in (Bowring et al., 2019b, 2019a)the soil carbon stock used to represent the
4628 Pan-Arctic permafrost soil carbon stock in our simulation was reconstituted from the
4629 20,000 year carbon stock derived from a soil carbon spinup looped over 1961-1990 (to
4630 coarsely approach a warmer mid-Holocene climate) of an ORCHIDEE-MICT simulation
4631 used in (Guimberteau et al., 2018). This was run to quasi-steady state equilibrium for
4632 the Active and Slow carbon pools over 500 years. (Supplement, Fig. 1), by looping over

4633 the years 1901-1930 and the first year (1901) of the prescribed land cover map. Where
4634 possible, the parameter configuration remained faithful to that used in the original
4635 ORCHIDEE-MICT spinup simulations, to avoid excessive drift from the original soil
4636 organic carbon (SOC) state. This is equilibrium simulation is performed to allow the soil
4637 carbon state to adjust to a new equilibrium under the different, DOC and lateral
4638 transport-generating soil carbon scheme used by the model branch employed here.
4639 After some adjustment simulations to account for differing read/write norms between
4640 ORCHIDEE-MICT and this model version, the model was then run in transient mode
4641 under historical climate, land cover and atmospheric CO₂ concentrations for the period
4642 1898-2005, and a separate simulation restarted from the latter point over the 'future'
4643 period 2006-2099, using the input forcing data under RCP 6.0 described in the
4644 preceding section. A summary of the step-wise procedure for simulation setup described
4645 is given graphically in Figure 1 of the Supplement. Modules calculating floodplain
4646 inundation, water and carbon reinfiltration, poor soils filtration, organic matter priming,
4647 canopy and precipitation DOC, all of which have been previously described in
4648 detail(Bowring et al., 2019a; Lauerwald et al., 2017)), were all activated for the
4649 historical and future simulations.

4650

4651 **Simulation Output Analysis and Postprocessing**

4652

4653 Output analysis was largely conducted on a basin-by-basin basis for comparison with
4654 observational data and to facilitate interpretation of the results with respect to coarse
4655 biogeography. In Eurasia, the gradient east-west coarsely corresponds to the gradient
4656 pairs colder-warmer, or more-less permafrost. With the exception of the results shown
4657 in Table 1, our analysis was restricted to the 'Big Six' Arctic river basins, namely (from
4658 East to West) the Kolyma, Lena, Yenisei, Ob, Mackenzie and Yukon. The 'Medium Nine'
4659 basins referred to in Table 1 are the nine next-largest basins in the study region. Basins
4660 dominantly underlain by continuous or discontinuous permafrost (the Kolyma, Lena and
4661 Yukon) are denoted in timeseries graphics by a dotted line (versus solid for the
4662 remainder). The 'Pan-Arctic' DOC discharge values referred to in Table 1 include all
4663 non-Big Six or Medium Nine, non-island coastal grid cells from the western United States
4664 to Hudson Bay in North America, and northern Sweden to the northern boundary of the
4665 Kamchatka Peninsula, to coarsely match those areas of coastal outflow that correspond
4666 to proximate seawater inflow regions of the Arctic Ocean.

4667

4668 Discharge grid cells for each basin were determined from output using the coastal
4669 outflow grid cell for each basin. For each basin, these grid cells are as follows (lon,lat):
4670 Kolyma (161.5, 69.5); Lena (127.5, 73.5); Yenisei (82.5, 71.5); Ob (69.5, 66.5); Mackenzie
4671 (-134.5, 69.5); Yukon (-163.5, 62.5); Pechora (54.5, 68.5); Pyasina (86.5, 73.5);
4672 Verkhnyaya-Taymyra (98.5, 76.5); Khatanga (106.5, 73.5); Olenek (119.5, 72.5); Yana
4673 (135.5, 72.5); Indigirka (149.5, 71.5); Anadyr (177.5, 64.5); Kuskokwin (-162.5, 60.5).

4674

4675 When referring to standalone values for variables, unless otherwise stated, these are the
4676 average for that variable over the period 1996-2005. This same time bracket is used to
4677 denote the 'present' or 'modern' period as it marks the last 10 years of the historical
4678 (reconstructed) climatological input data used (the 'future' forcing data begin in 2006).
4679 Reference to the 'Future', however, implies any time after but including the year 2020.
4680 Timeseries displayed in both the main text body and the Supplement use a variety of

4681 aggregation metrics. Most employ a 'decadal-mean percentage change' from a baseline
4682 of the 1901-1910 average for a given variable, to enable easy comparison between
4683 basins with large differences in variable absolute values. Other metrics, including
4684 temperature sensitivities, regressions, 30-year running means, and absolute values for
4685 certain variables, are also included in the analysis. The 'present' and 'future' DOC input
4686 temperature sensitivities refer to those calculated for the mean of 1996-2005 and 2020-
4687 2099, respectively.

4688
4689 Carbon budget closure for the land-ocean-aquatic continuum is determined by the sum
4690 of inflows and outflow from a given system (basin), the relevant flows displayed in the
4691 Supplement (Fig. S1).

4692
4693 For the inland water carbon cycle of a given basin,

4694
4695 Budget Closure(=0) = [(Soil DOC + CO₂ Input) + (Floodplain DOC + CO₂ Input)] -
4696 [(Returnflow + CO₂ Evasion + (DOC+ CO₂ Ocean Outflow)].

4697 4698 **Code availability**

4699 The source code for ORCHIDEE MICT-LEAK revision 5459 is available online, but its
4700 access is restricted. Consequently, one is required to communicate with the
4701 corresponding author for a username and password. The source code can be found at
4702 the following address:
4703 `svn://forge.ipsl.jussieu.fr/orchidee/branches/publications/ORCHIDEE_MICT-`
4704 `LEAK_r5459`

4705 Primary data and scripts used in the analysis and other supplementary information that
4706 may be useful in reproducing the author's work can be obtained by contacting the
4707 corresponding author.

4708
4709 This software is governed by the CeCILL license under French law and abiding by the
4710 rules of distribution of free software. You can use, modify and/or redistribute the
4711 software under the terms of the CeCILL license as circulated by CEA, CNRS and INRIA at
4712 the following URL: <http://www.cecill.info>.

4713 4714 **Authors' contribution**

4715 SB coded this model version, conducted the simulations and wrote the main body of the
4716 paper. RL gave consistent input to the coding process and made several bug fixes. BG
4717 advised on the study design and model configuration; DZ gave input on the modelled soil
4718 carbon processes and model configuration. PC oversaw all developments leading to the
4719 publication of this study. All authors contributed to suggestions regarding the final
4720 content of the study.

4721 4722 **Competing interests**

4723 The authors declare no competing financial interests.

4724 4725 **Acknowledgements**

4726 Simon Bowring acknowledges funding from the European Union's Horizon 2020
4727 research and innovation program under the Marie Skłodowska-Curie grant agreement
4728 No. 643052, 'C-CASCADES' program. Simon Bowring received a PhD grant. RL

4729 acknowledges funding from the European Union's Horizon 2020 research and
 4730 innovation program under grant agreement no.703813 for the Marie Skłodowska-Curie
 4731 European Individual Fellowship "C-Leak".

4732
 4733
 4734
 4735
 4736
 4737

Table S1: Model forcing files used as input for the simulations.

Data Type	Name	Source
Vegetation Map	IPCC AR5 LUHa / IPCC AR5 RCP6.0 AIM	IPCC, 2014
Topographic Index	STN-30p	Vörösmarty et al., 2000
Stream flow direction	STN-30p	Vörösmarty et al., 2000
River surface area	River surface area	Lauerwald et al., 2015
Soil texture class	Soil texture class	Reynolds et al. 1999
Climatology	ISIMIP v2 IPSL-CM5A	Frieler et al., 2017; Lange, 2016,2018.
Potential floodplains	Multi-source global wetland maps	Tootchi et al., 2018
Poor soils	Harmonized World Soil Database map	Nachtergaele et al., 2010
Spinup Soil Carbon Stock	20ky ORCHIDEE-MICT soil carbon spinup	Based on config. in Guimberteau et al. (2018)
Floodwater height	Model vars: floodh_nth, streamr_nth, floodh	Statistically generated from model output
Atmospheric CO2	IPCC AR5 RCP 6.0	IPCC, 2014

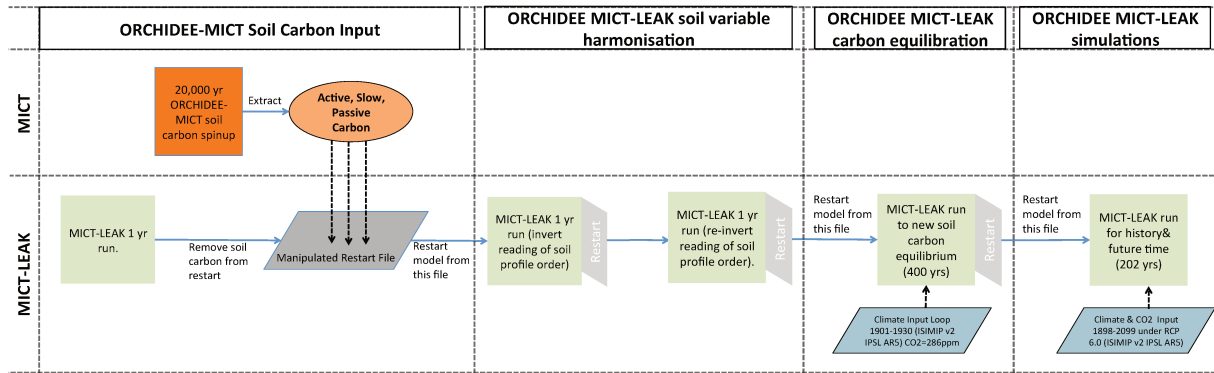
4738
 4739
 4740
 4741
 4742

Table S2: Simulated present day (1996-2005) and future (2090-2099) CO₂ discharge from the Big Six and Medium Nine river basins into the Arctic.

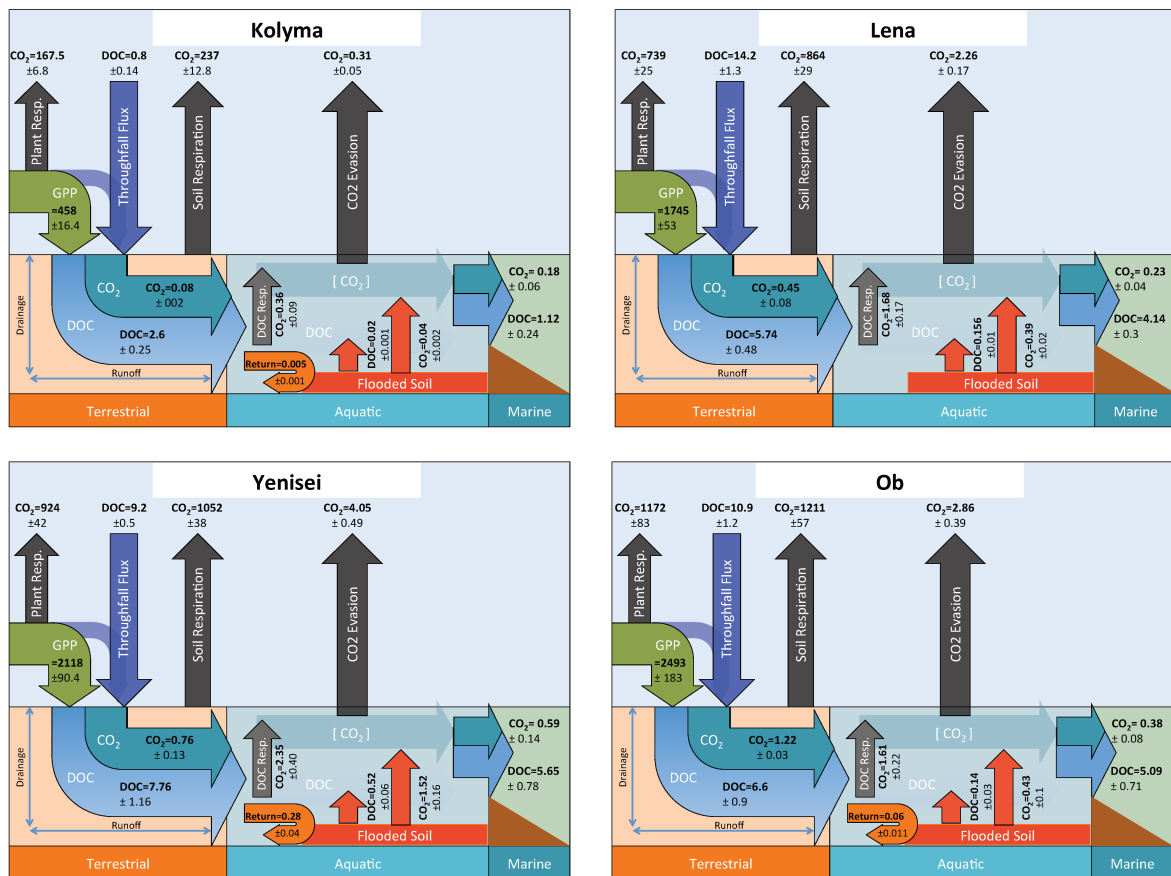
Big Six		CO2 to Ocean (1996-2005)		CO2 to Ocean (2090-2099)	
		s.d.	s.d.	s.d.	s.d.
	Kolyma	0.180	0.062	0.184	0.057
	Lena	0.203	0.041	0.211	0.043
	Yenisei	0.604	0.198	0.518	0.103
	Ob	0.376	0.111	0.235	0.066
	Mackenzie				
	Yukon	0.049	0.009	0.051	0.014
	SUM	1.412	/	1.199	/
Medium 9		CO2 to Ocean (1996-2005)		CO2 to Ocean (2090-2099)	
	Pechora	0.120	0.027	0.077	0.016
	Pyasina	0.121	0.032	0.108	0.044
	Verkhnyaya-Taymyra	0.050	0.012	0.045	0.019
	Khatanga	0.204	0.049	0.195	0.065
	Olenek	0.060	0.023	0.051	0.018
	Yana	0.028	0.010	0.023	0.009
	Indigirka	0.050	0.019	0.055	0.037
	Anadyr	0.092	0.023	0.114	0.020
	Kuskokwin	0.023	0.008	0.027	0.013
	SUM	0.748	/	0.695	/

4743
 4744
 4745
 4746
 4747

Figures:



4748
 4749 **Figure S1:** Flow diagram illustrating the step-wise protocol required to set up the model, up to and including the historical and future final simulation runs. The first (left)
 4750 'Soil Carbon Input' column refers to the initial steps taken to input permafrost-like soil
 4751 carbon stocks into our model. The next 'variable harmonisation' column refers to the fact that the restart inputs from ORCHIDEE-MICT are read by our model in inverse
 4752 order, so that one year must be run in which an activated flag reads it properly, before
 4753 the reading of soil profile restarts is re-inverted for all subsequent years. 'Carbon
 4754 equilibration' refers to the quasi-steady state carbon stock subsequently obtained, while
 4755 'simulation' refers to the final historical and future simulations whose output is
 4756 presented in this study.
 4757
 4758
 4759
 4760



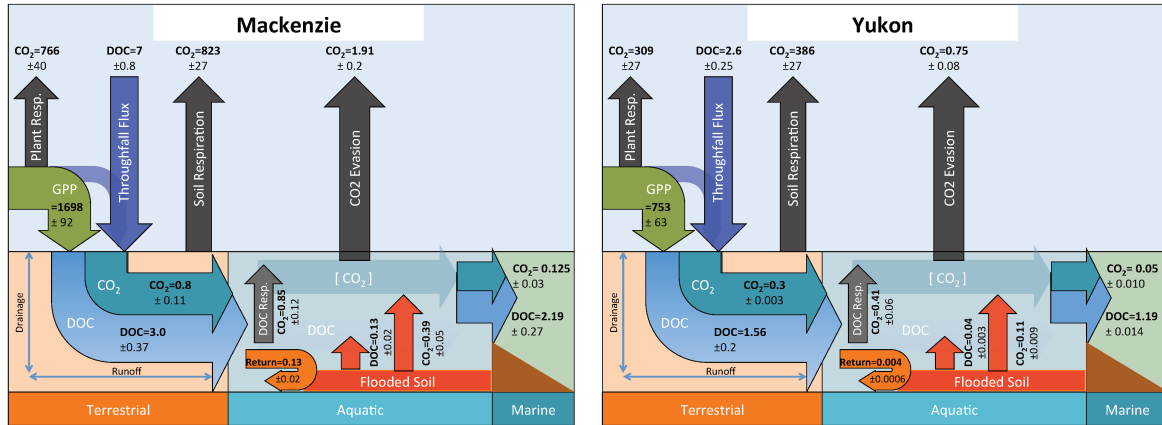


Figure S2: Schematic diagrams detailing the major yearly carbon flux model outputs for each of the Big Six river basins as they are transformed and transported across the land-ocean aquatic continuum (LOAC) for the average of the period 1996-2005. All values represent yearly sums of carbon fluxes in TgC yr⁻¹.

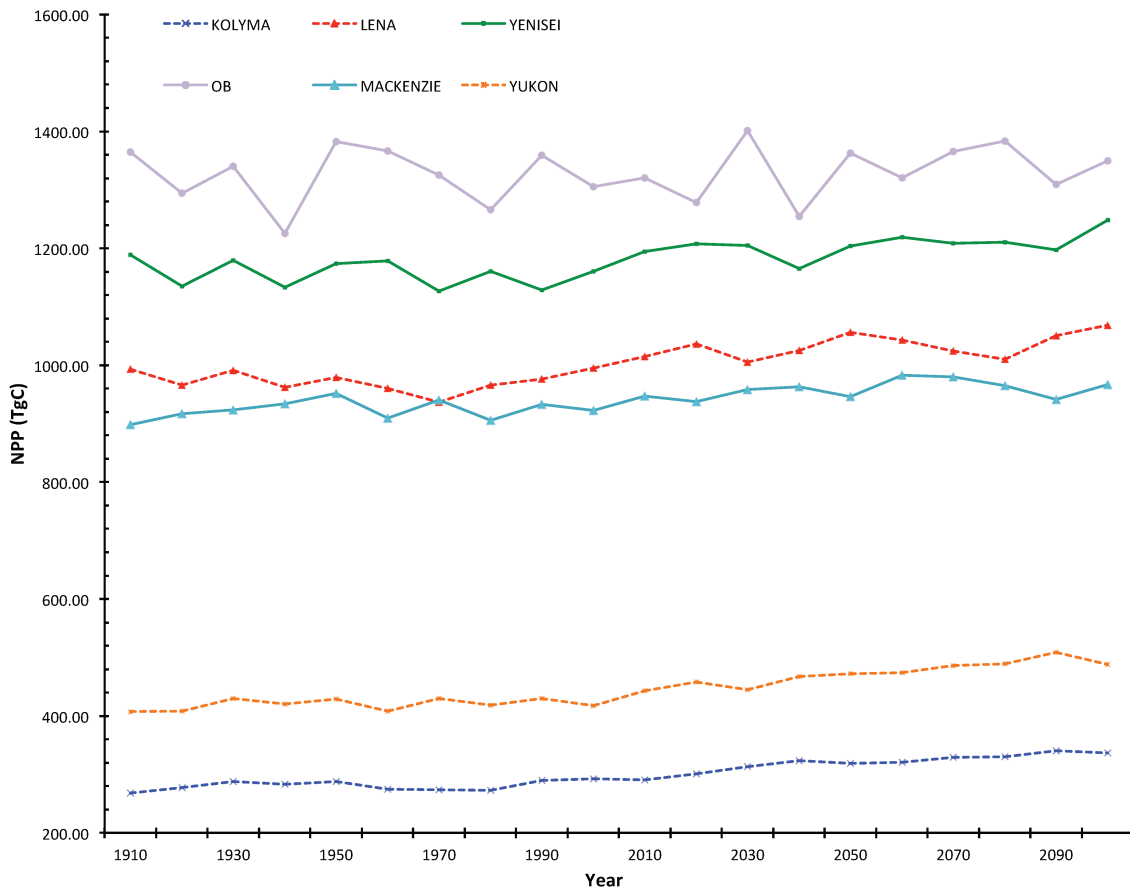
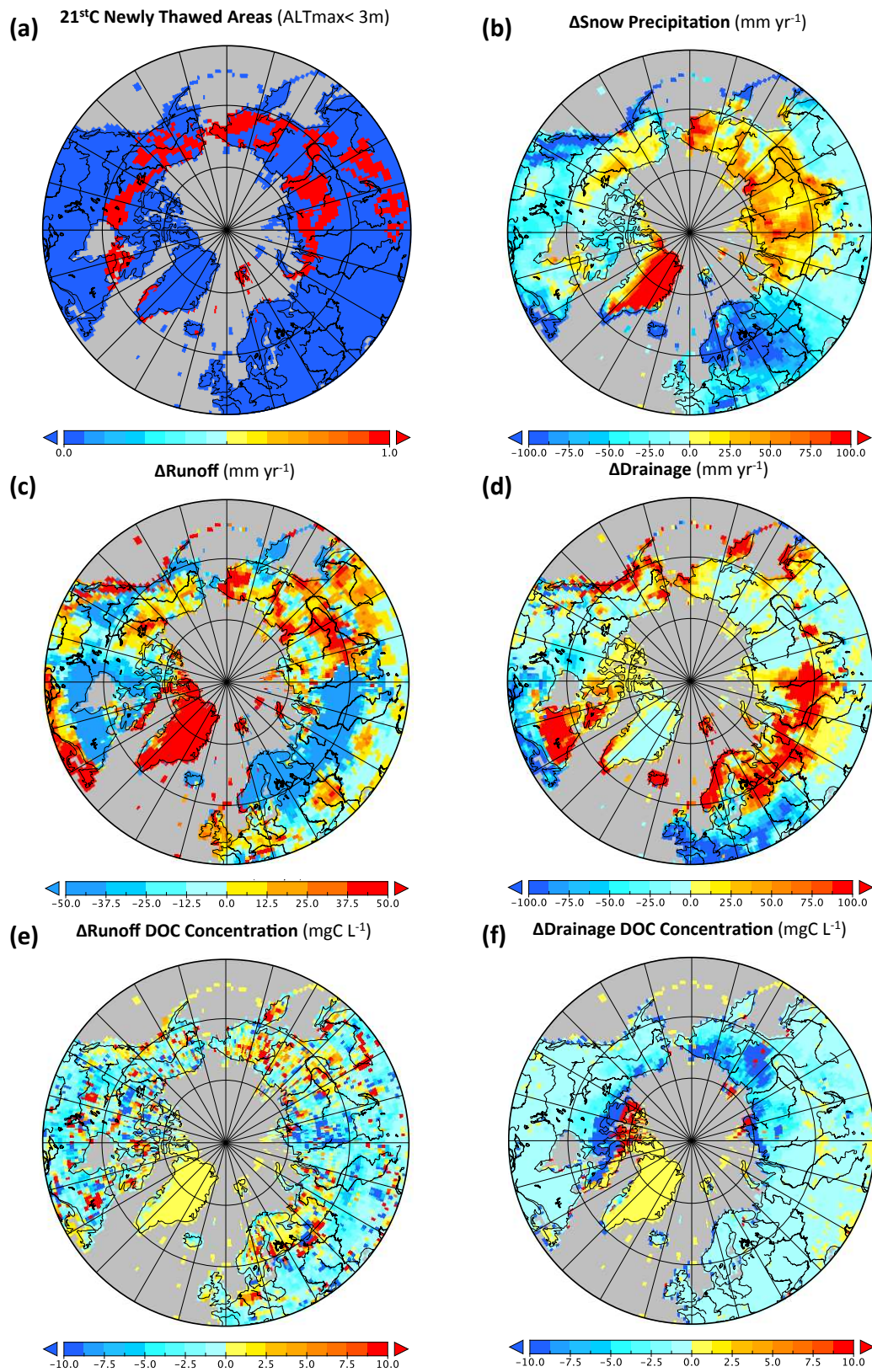


Figure S3: Decadal-averaged annual Net Primary Production (NPP) in TgC yr⁻¹ for each of the Big Six basins over the entire simulation period.

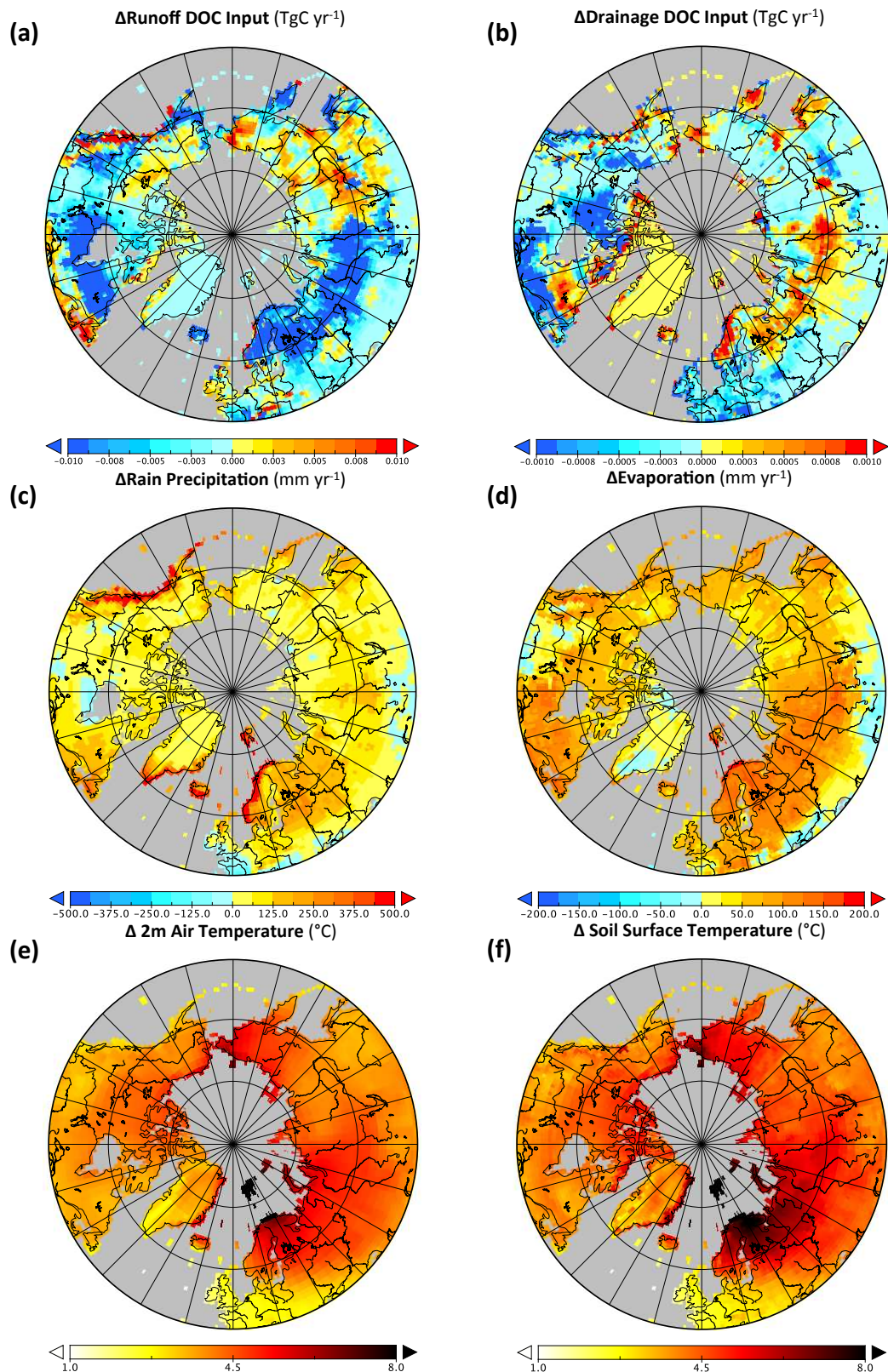
4762
4763
4764
4765
4766
4767

4768
4769
4770
4771
4772



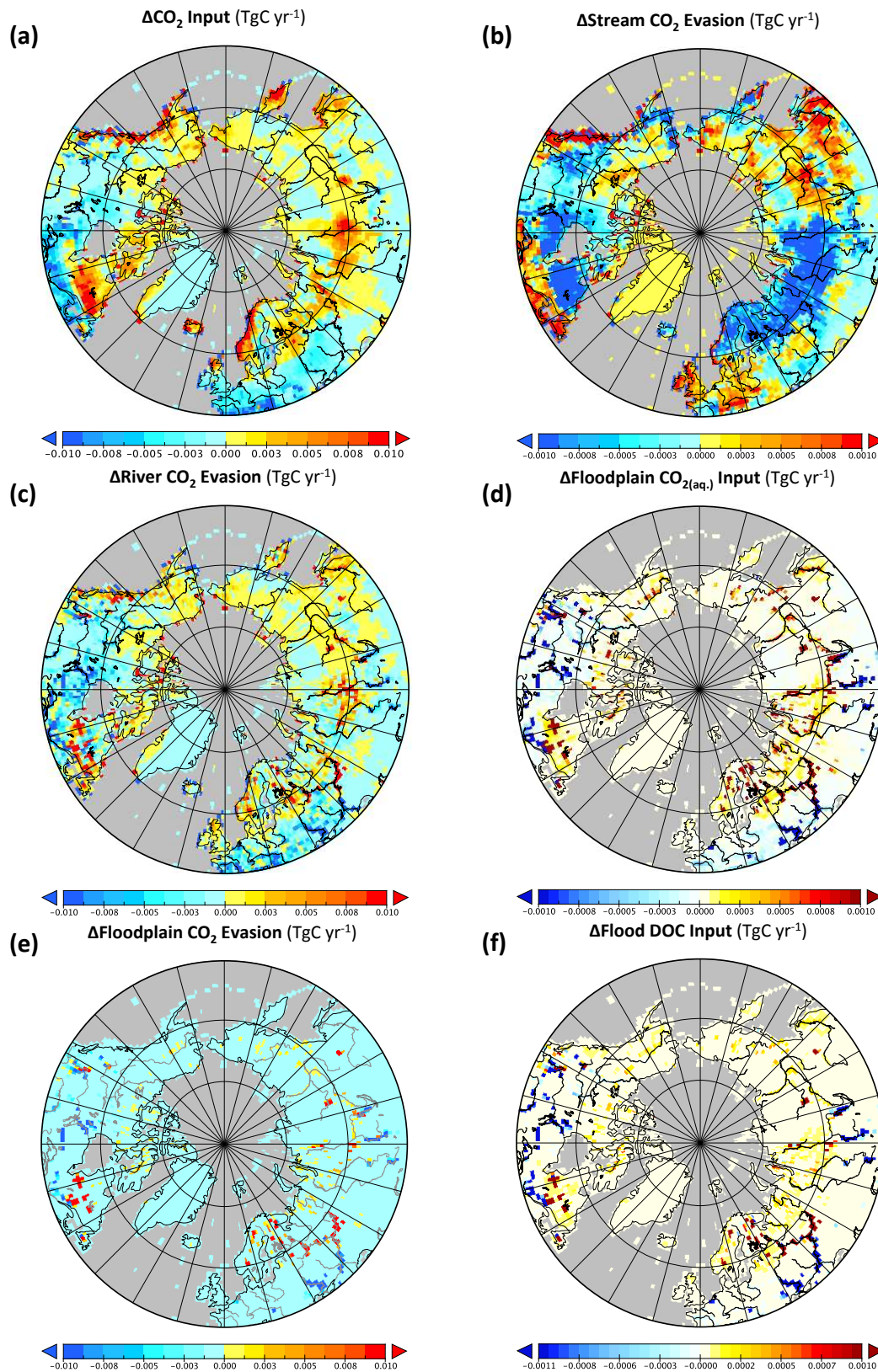
4773
 4774
 4775
 4776
 4777

Figure S4: Maps of changes in variables between the mean of (2090-2099) subtracted by that of (1996-2005) in each pixel for. **(a)** Newly thawed permafrost areas; **(b)** Snowfall (mm yr⁻¹) **(c)** Surface runoff (mm yr⁻¹), **(d)** Subsurface drainage (mm yr⁻¹) **(e)** Runoff DOC concentration (mgC L⁻¹) **(f)** Drainage DOC concentration (mgC L⁻¹).



4778
 4779
 4780
 4781
 4782
 4783

Figure S5: Maps of changes in variables between the mean of (2090-2099) subtracted by that of (1996-2005) in each pixel for. **(a)** Surface runoff DOC input to rivers (TgC yr⁻¹); **(b)** Drainage DOC input to rivers (TgC yr⁻¹) **(c)** Rain precipitation (mm yr⁻¹), **(d)** Evaporation (mm yr⁻¹) **(e)** 2 metre air temperature (Celsius) **(f)** Soil surface temperature (Celsius)..



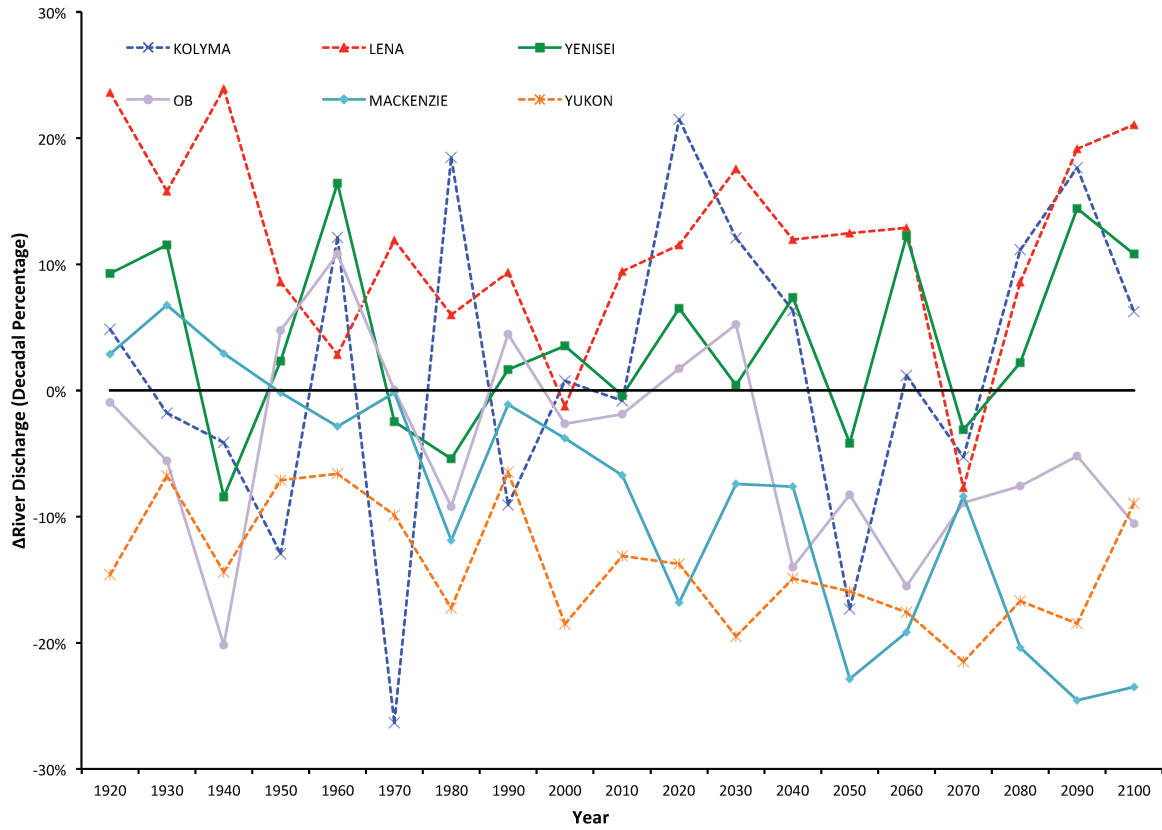
4784
4785
4786
4787
4788

Figure S6: Maps of changes in variables between the mean of (2090-2099) subtracted by that of (1996-2005) in each pixel for. **(a)** CO₂ input to rivers (TgC yr⁻¹); **(b)** Stream water CO₂ evasion (TgC yr⁻¹) **(c)** River water surface CO₂ evasion (TgC yr⁻¹); **(d)** Floodplain CO₂ input (TgC yr⁻¹) **(e)** CO₂ evasion from flooded areas (TgC yr⁻¹) **(f)** Floodplain DOC inputs (TgC yr⁻¹).



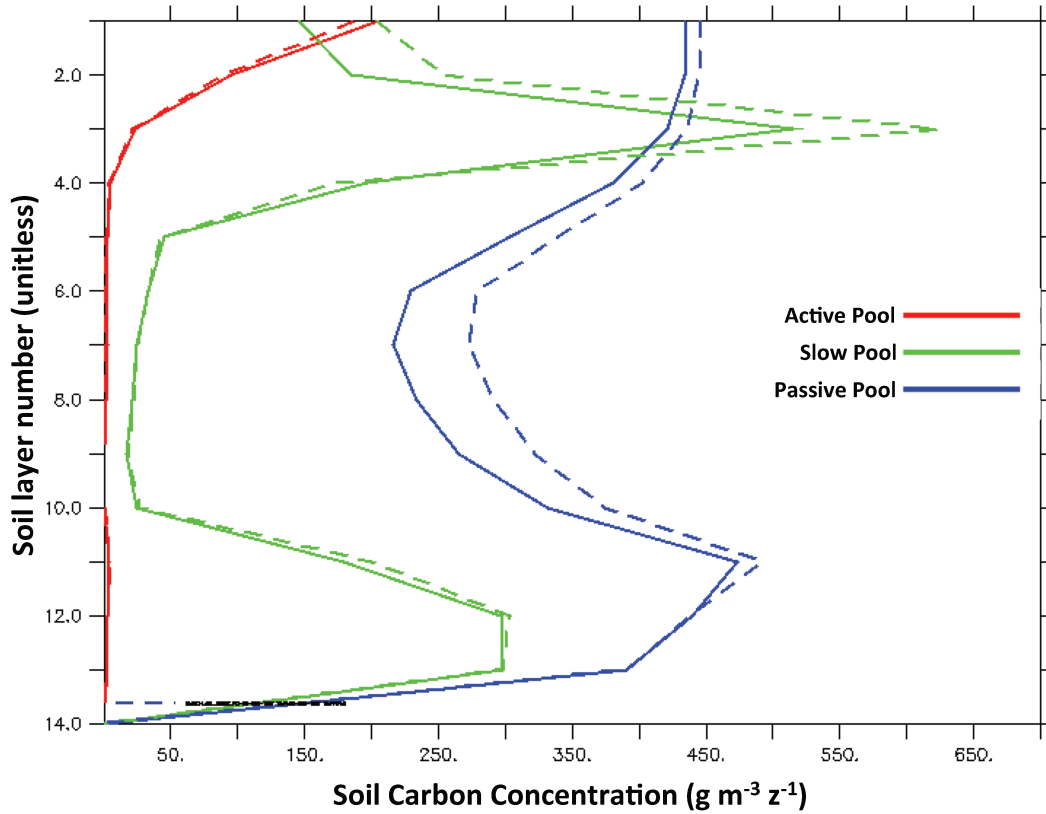
4789
4790
4791
4792

Figure S7: Decadal-average percentage change in Gross Primary Production (GPP) for each of the Big Six basins from a 1901-1910 baseline.

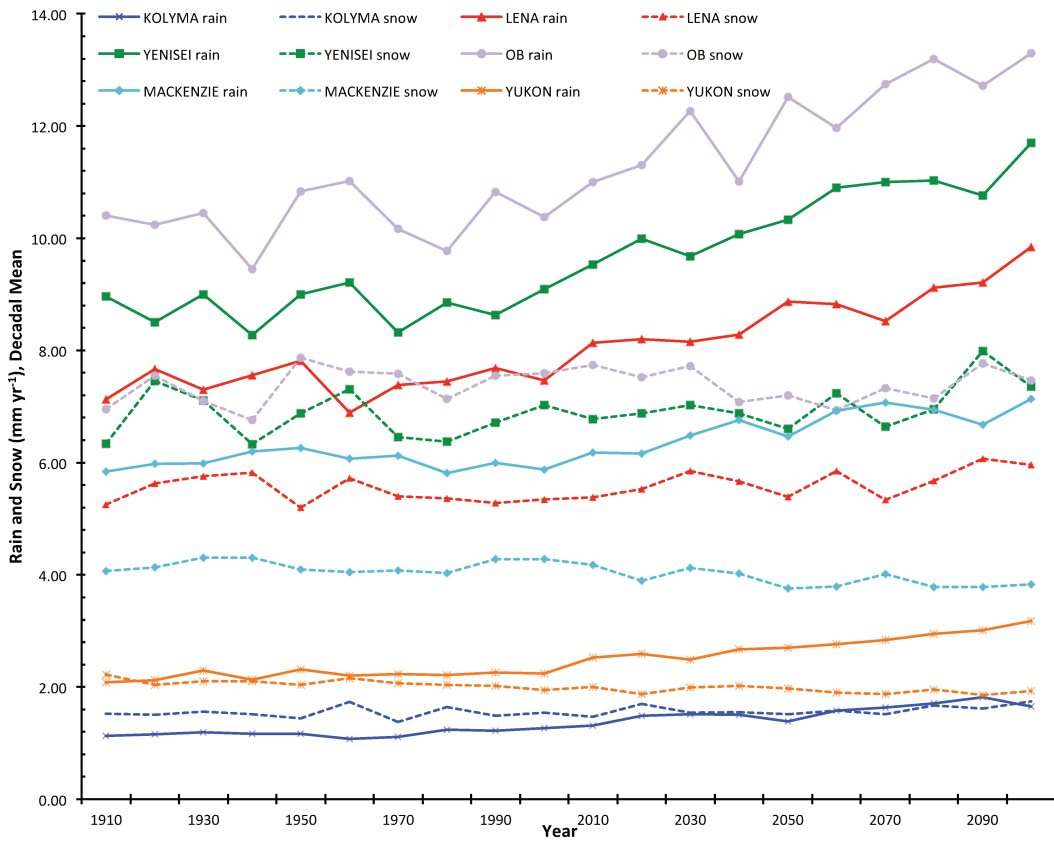


4793

4794 **Figure S8:** Decadal-averaged percentage change in river discharge for each of the Big Six basins from a
 4795 1901-1910 baseline.
 4796

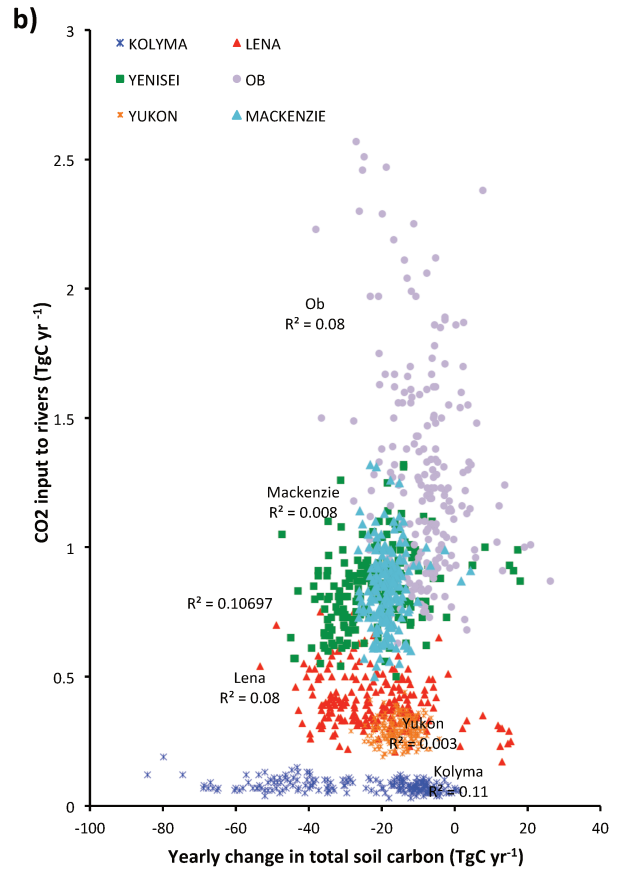
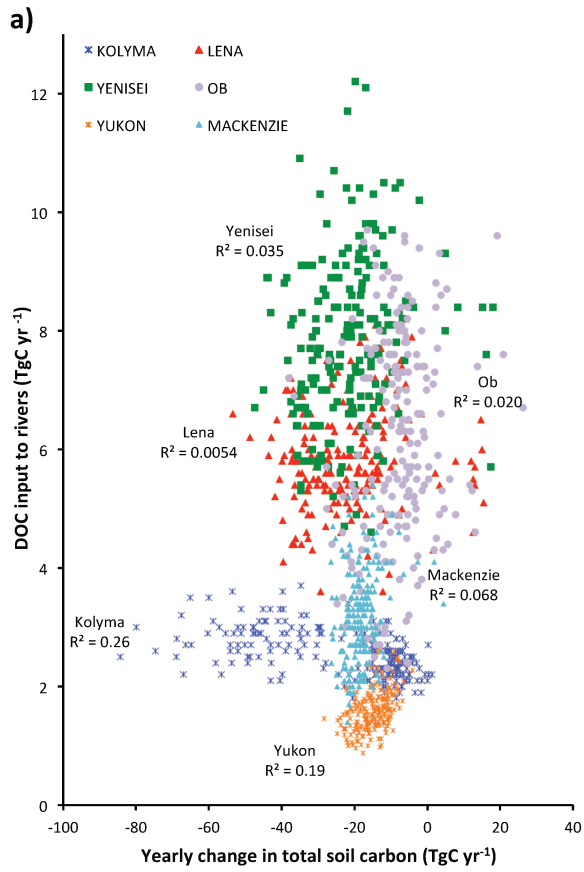


4797 **Figure S9:** Mean permafrost region soil carbon concentration profiles for each layer in the model soil
 4798 column (noting that layer thickness increases geometrically from layer 1), for each of the soil carbon pools
 4799 simulated by the model. Dashed lines are the profiles averaged over 1901-1910, solid lines those
 4800 averaged over 1996-2005.
 4801

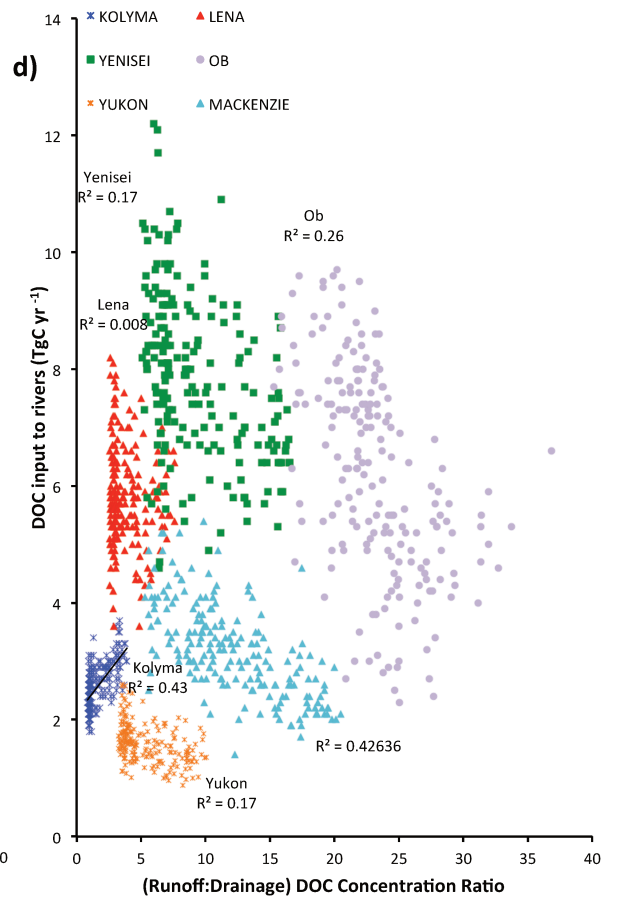
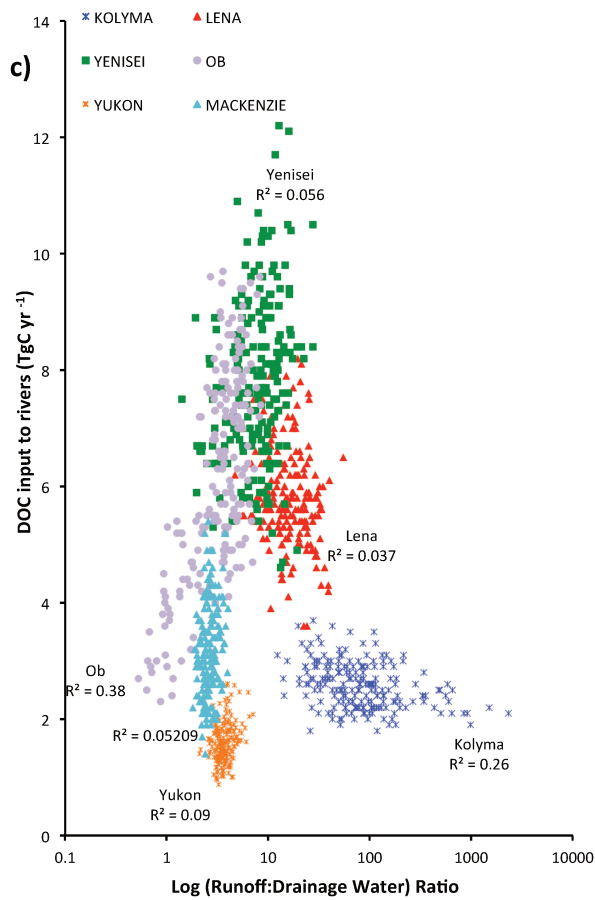


4802
4803
4804
4805

Figure S10: Timeseries for the decade-averaged annual precipitation (mm yr⁻¹) as rain (solid) and snowfall (dashed), given as a grid cell average over each of the basins for the entire simulation period.



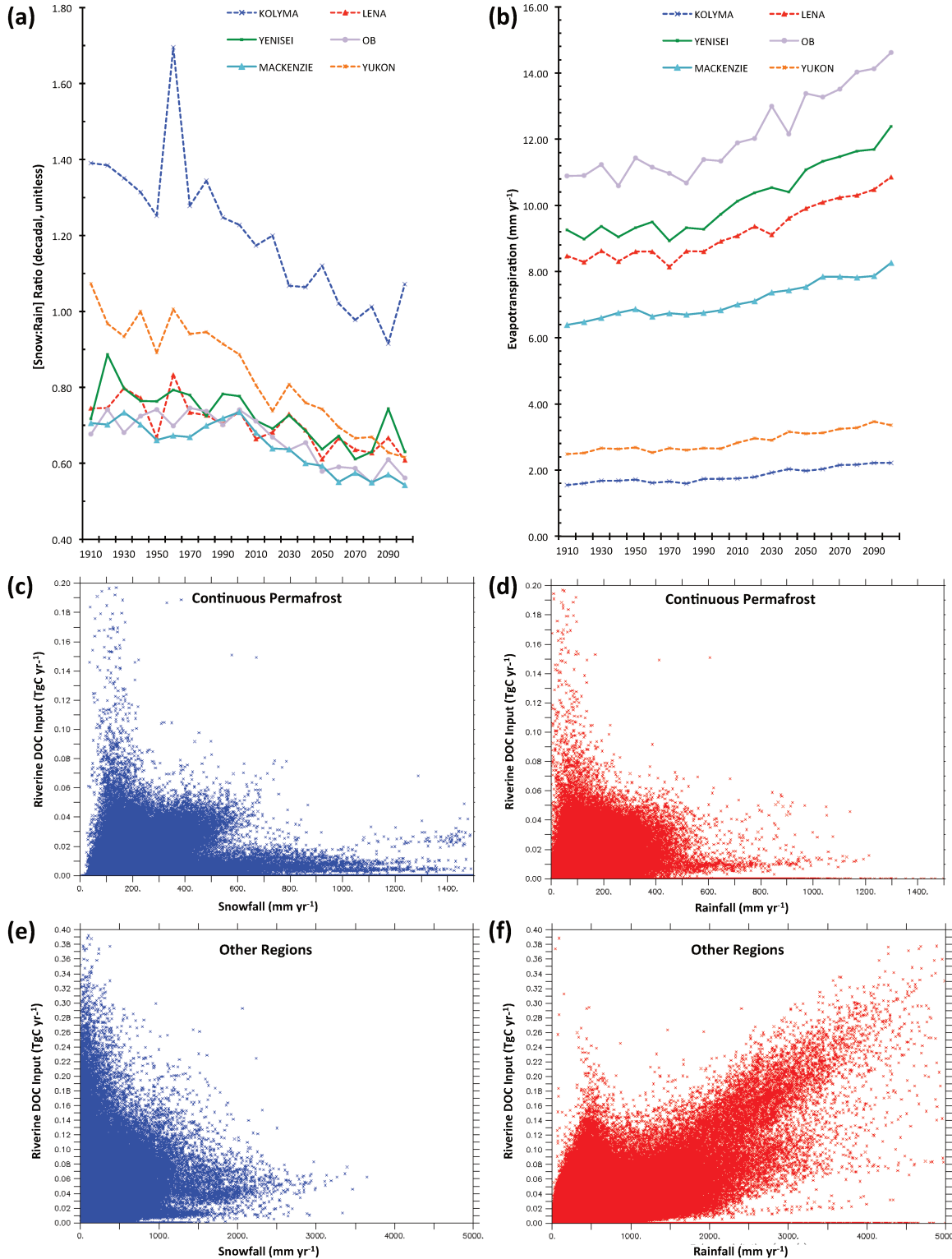
4806



4807

4808
 4809
 4810
 4811
 4812
 4813

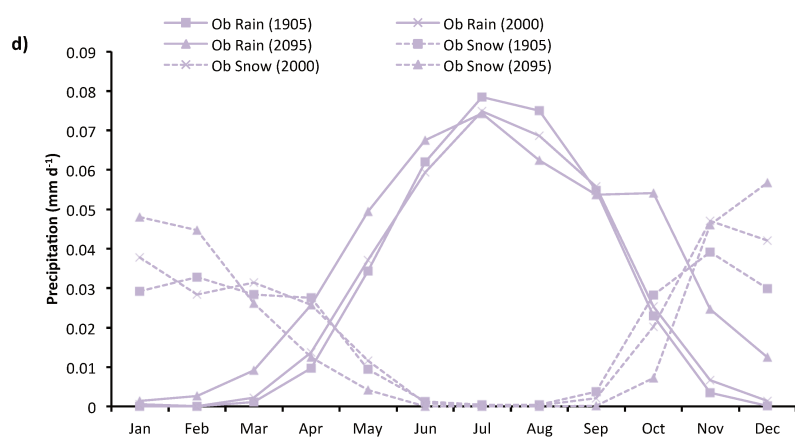
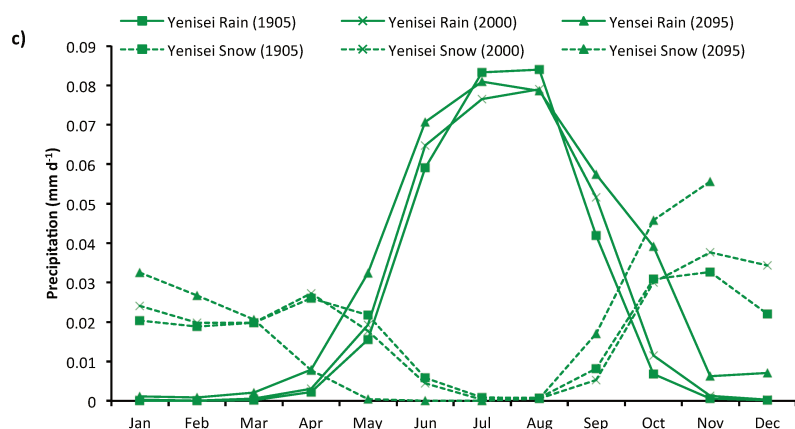
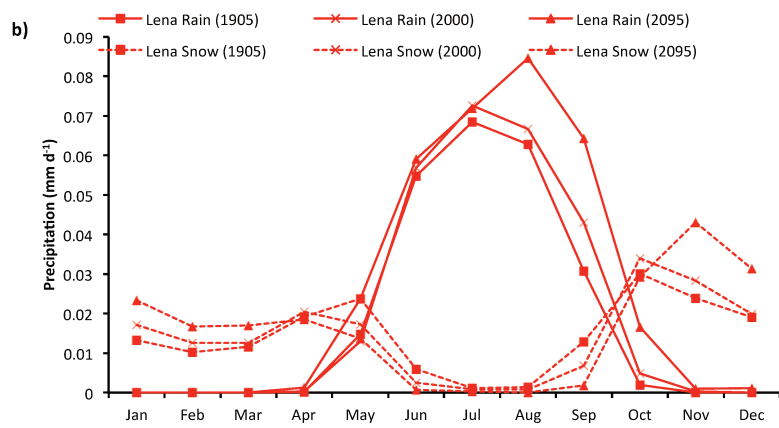
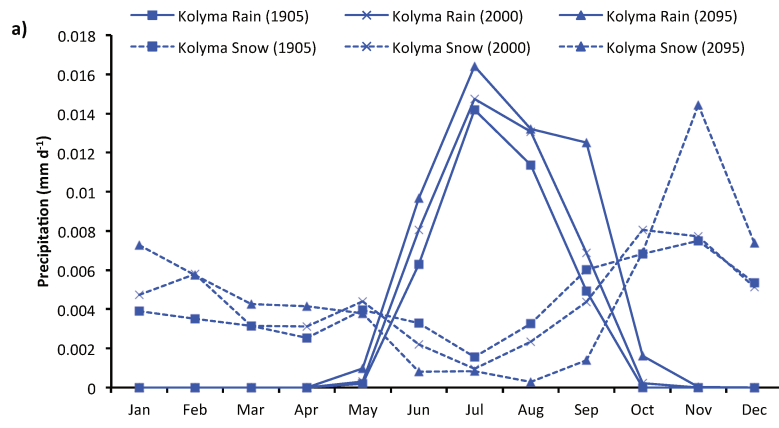
Figure S11: Basin-disaggregated regression scatter plots. Each point represents the aggregate over the entire basin for a given year, and thus for each basin the scattering reflects the temporal variability of the plotted variables. **(a)** DOC and **(b)** CO₂ inputs to rivers (TgC yr⁻¹) plotted against yearly basinwide changes in soil organic carbon (TgC yr⁻¹); and DOC input to rivers against the ratio of **(c)** runoff:drainage water flux; and **(d)** DOC concentrations in runoff and drainage (runoff:drainage).



4814
 4815
 4816

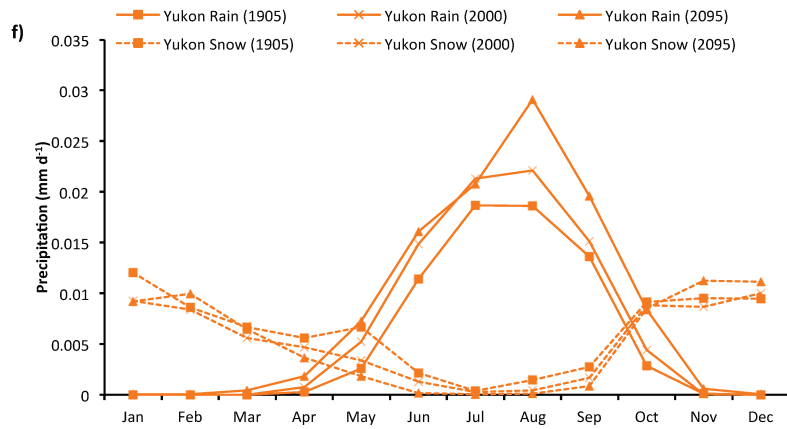
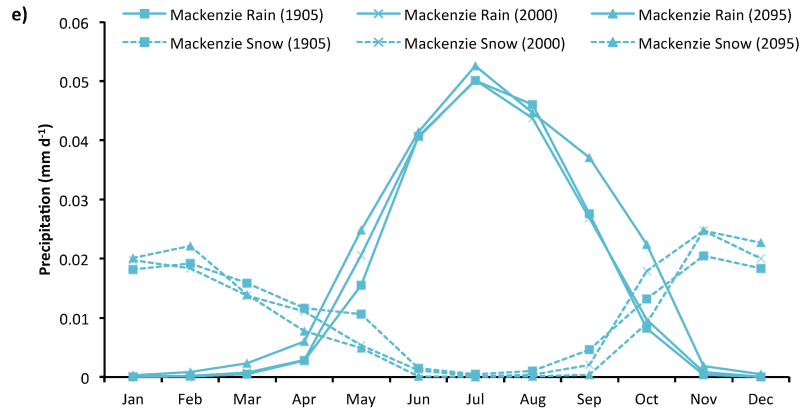
Figure S12: Basin-disaggregated timeseries of **(a)** Decadal-mean (snow:rain) ratio; **(b)** Decadal-mean evapotranspiration rates averaged over each basin. (c-f): Scatter plot of riverine DOC inputs to total

4817 annual snowfall (c,d) and rainfall (d,f) over 'continuous permafrost' and 'non-continuous-permafrost' or
4818 'other', regions, for each grid cell over the entire simulation period.
4819



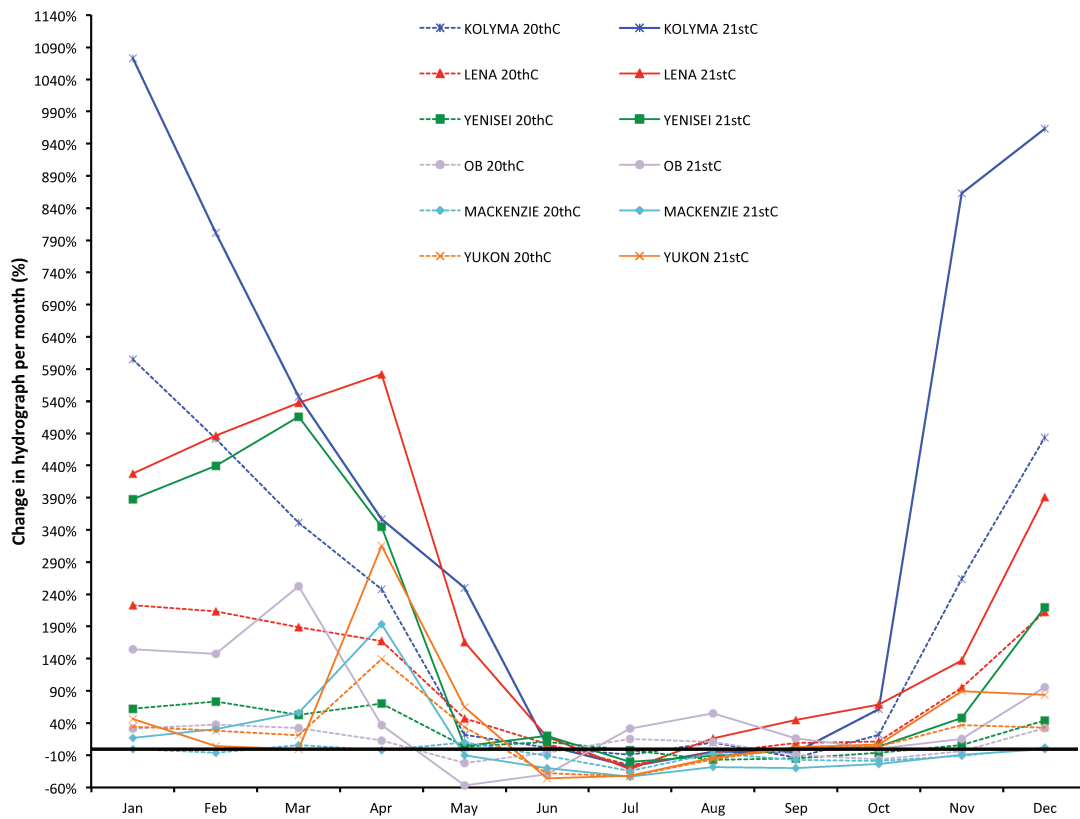
4820

4821



4822
4823
4824
4825
4826

Figure S13: Mean monthly rain (solid) and snow (dashed) in mm d⁻¹ averaged over the decades 1901-1910 (squares), 1996-2005 (crosses) and 2090-2099 (triangles) for the average of each of the Big Six basins (a-f). The legend shows the midpoint year of each of the decades concerned.



4827
 4828
 4829
 4830
 4831
 4832

Figure S14: Timeseries of the percentage change in mean monthly river discharge from a baseline of the 1901-1910 average, for the decades 1996-2005 (dashed) and 2090-2099 (solid), for each of the Big 6 rivers. Discharge is taken from the river outflow grid cell (see Methods) of each basin.

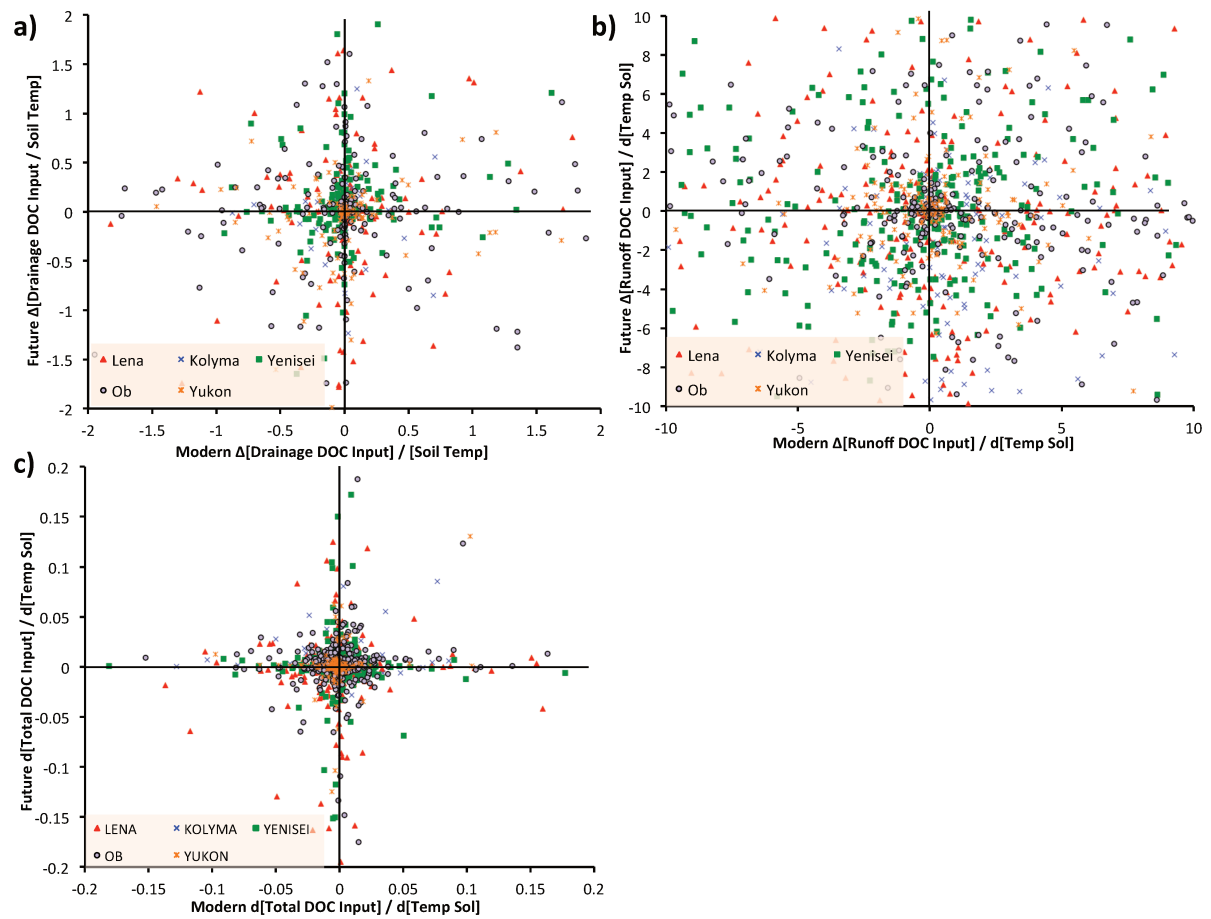


Figure S15: Scatter plots (a-c) showing the year-averaged temperature sensitivity (ground temperature) of carbon inputs to the river ($\text{TgC } ^\circ\text{Celsius}^{-1}$) in the 'modern' (1996-2005 average) versus 'future' (2020-2099 average) era, for (a) drainage DOC inputs, (b) runoff DOC inputs and (c) total DOC input. Basins are disaggregated by colour, with each point representing the mean future/modern temperature sensitivity pair of an individual grid cell.

4833
 4834
 4835
 4836
 4837
 4838
 4839
 4840
 4841
 4842
 4843
 4844
 4845
 4846
 4847
 4848
 4849
 4850
 4851
 4852
 4853
 4854
 4855
 4856
 4857

4858 **Appendix 3**
4859 **Appendix to Chapter 5:**
4860 **CO₂ Uptake By Weathering Increasingly Exceeds CO₂ Evasion From Rivers As**
4861 **Permafrost Thaws**

4862
4863 **Introduction**

4864 The content of this Supporting Information document covers in greater detail some of
4865 the steps taken in the Methods of this paper. Specifically, in Supporting Text S1, we
4866 explicitly give the rating curves used for estimating the alkalinity loading of a given river
4867 from discharge and, in case of the Ob river, the point in the seasonal cycle. In Table S1,
4868 we cover the regression statistics used in estimating a correction factor for per basin
4869 alkalinity flux (see 2.2.4 in main text).

4870 **Text S1: Per-Basin Calibration Using Tank et al. (2012) Rating Curve**

4871
4872 The rating curves set-up by Tank et al. include pre-set ‘models’ for alkalinity discharge,
4873 which differ from basin to basin. The predictor variable in this regression is monthly
4874 discharge, and in one case the time in the seasonal cycle (Ob), as predictor, with
4875 different models (M) following the following schemes for the Kolyma, Yenisei,
4876 Mackenzie and Yukon in Model 1, the Lena in Model 2 and the Ob in Model 4a (here we
4877 follow the model numbering convention used in Tank et al.).

4878
(1) $\ln(\text{Load}) = a_0 + a_1 * \ln(\text{discharge})^2$ (M1)
(2) $\ln(\text{Load}) = a_0 + a_1 * \ln(\text{discharge}) + a_2 * \ln(\text{discharge})^2$ (M2)
(3) $\ln(\text{Load}) = a_0 + a_1 * \ln(\text{discharge}) + a_2 * \sin(2 * \delta\text{time}) +$
4879 $a_3 * \cos(2\pi\delta\text{time})$ (M4a)

4880
4881 where ‘Load’ is alkalinity load [kgC d⁻¹], discharge is river discharge in m³s⁻¹ and ‘dtime’
4882 = decimal time - center of decimal time from the empirical data.

4883 Instead of directly using the rating curves established by Tank et al, we simplified those
4884 rating curves when information loss was limited. For this, we used the daily discharges
4885 and the predicted daily HCO₃⁻ fluxes from Tank et al., 2012, and performed a regression
4886 of these daily HCO₃⁻ fluxes against daily discharge values.

4887 For the Mackenzie, Yukon, Kolyma, and Yenisei Rivers, we reproduced the original rating
4888 curves of the form M1 (see above). Also for the Lena, for which the original rating curve
4889 followed the second-order polynomial equation M2, we chose a linear regression of the form
4890 M1 instead, as the difference in R² and root mean square error (RMSE) between each form
4891 was negligible. Only for the Ob River, for which the original rating curve followed form M4
4892 (see above), we removed the time variant and refitted a second-order polynomial equation of
4893 the form M2, using as well only discharge a independent variable. This simplified all basins’
4894 regression equation except for the Ob to the form in M1, with a₀= 7.424, 9.131, 12.84,
4895 22.924, 8.523, and 9.951, and a₁=7.424, 0.762, 0.397, -1.915, 0.881, 0.722, for the Kolyma,
4896 Lena, Yenisei, Ob, Yukon and Mackenzie, respectively. For the Ob polynomial, a₂=0.1294.

4897
4898

4899 **Table S1:** Regression statistics for the regression calculations undertaken in Section
 4900 2.2.4 of the main text, using the following regression equation
 4901 $Load_{obs} = b * (0.47 * Load_{sim,RUNOFF} + Load_{sim,DRAINAGE})$.
 4902 and solved for the factor b for each basin.
 4903

River	b	std	R^2	RMSE	p
Mackenzie	1.542	0.175	0.87	50%	2.54E-06
Yukon	2.472	0.165	0.95	30%	1.16E-08
Kolyma	0.664	0.012	1.00	14%	1.20E-14
Lena	1.032	0.053	0.97	28%	7.20E-10
Yenisei	1.050	0.105	0.89	39%	7.55E-07
Ob	1.077	0.110	0.89	44%	9.18E-07

4904
 4905
 4906
 4907
 4908
 4909
 4910
 4911
 4912
 4913
 4914
 4915
 4916
 4917
 4918
 4919
 4920
 4921
 4922
 4923
 4924
 4925
 4926
 4927
 4928
 4929
 4930
 4931
 4932
 4933
 4934
 4935
 4936
 4937
 4938

References

- 4939
4940
4941 Abbott, B. W., Jones, J. B., Godsey, S. E., Larouche, J. R. and Bowden, W. B.: Patterns and
4942 persistence of hydrologic carbon and nutrient export from collapsing upland
4943 permafrost, *Biogeosciences*, doi:10.5194/bg-12-3725-2015, 2015.
4944 Abbott, B. W., Jones, J. B., Schuur, E. A. G., Chapin, F. S., Bowden, W. B., Bret-Harte, M. S.,
4945 Epstein, H. E., Flannigan, M. D., Harms, T. K., Hollingsworth, T. N., Mack, M. C., McGuire, A.
4946 D., Natali, S. M., Rocha, A. V., Tank, S. E., Turetsky, M. R., Vonk, J. E., Wickland, K. P., Aiken,
4947 G. R., Alexander, H. D., Amon, R. M. W., Benscoter, B. W., Bergeron, Y., Bishop, K.,
4948 Blarquez, O., Bond-Lamberty, B., Breen, A. L., Buffam, I., Cai, Y., Carcaillet, C., Carey, S. K.,
4949 Chen, J. M., Chen, H. Y. H., Christensen, T. R., Cooper, L. W., Cornelissen, J. H. C., De Groot,
4950 W. J., Deluca, T. H., Dorrepaal, E., Fetcher, N., Finlay, J. C., Forbes, B. C., French, N. H. F.,
4951 Gauthier, S., Girardin, M. P., Goetz, S. J., Goldammer, J. G., Gough, L., Grogan, P., Guo, L.,
4952 Higuera, P. E., Hinzman, L., Hu, F. S., Hugelius, G., Jafarov, E. E., Jandt, R., Johnstone, J. F.,
4953 Karlsson, J., Kasischke, E. S., Kattner, G., Kelly, R., Keuper, F., Kling, G. W., Kortelainen, P.,
4954 Kouki, J., Kuhry, P., Laudon, H., Laurion, I., MacDonald, R. W., Mann, P. J., Martikainen, P.
4955 J., McClelland, J. W., Molau, U., Oberbauer, S. F., Olefeldt, D., Paré, D., Parisien, M. A.,
4956 Payette, S., Peng, C., Pokrovsky, O. S., Rastetter, E. B., Raymond, P. A., Reynolds, M. K.,
4957 Rein, G., Reynolds, J. F., Robards, M., Rogers, B. M., Schdel, C., Schaefer, K., Schmidt, I. K.,
4958 Shvidenko, A., Sky, J., Spencer, R. G. M., Starr, G., Striegl, R. G., Teisserenc, R., Tranvik, L. J.,
4959 Virtanen, T., Welker, J. M., et al.: Biomass offsets little or none of permafrost carbon
4960 release from soils, streams, and wildfire: An expert assessment, *Environ. Res. Lett.*,
4961 doi:10.1088/1748-9326/11/3/034014, 2016.
4962 Aiken, G. R., Spencer, R. G. M., Striegl, R. G., Schuster, P. F. and Raymond, P. A.: Influences
4963 of glacier melt and permafrost thaw on the age of dissolved organic carbon in the Yukon
4964 River basin, *Global Biogeochem. Cycles*, doi:10.1002/2013GB004764, 2014.
4965 Aitkenhead-Peterson, J. A., McDowell, W. H. and Neff, J. C.: Sources, Production, and
4966 Regulation of Allochthonous Dissolved Organic Matter Inputs to Surface Waters, in
4967 *Aquatic Ecosystems.*, 2003.
4968 Alling, V., Sanchez-Garcia, L., Porcelli, D., Pugach, S., Vonk, J. E., Van Dongen, B., Mörth, C.
4969 M., Anderson, L. G., Sokolov, A., Andersson, P., Humborg, C., Semiletov, I. and Gustafsson,
4970 Ö.: Nonconservative behavior of dissolved organic carbon across the Laptev and East
4971 Siberian seas, *Global Biogeochem. Cycles*, doi:10.1029/2010GB003834, 2010.
4972 Amiotte Suchet, P., Probst, J.-L. and Ludwig, W.: Worldwide distribution of continental
4973 rock lithology: Implications for the atmospheric/soil CO₂ uptake by continental
4974 weathering and alkalinity river transport to the oceans , *Global Biogeochem. Cycles*,
4975 doi:10.1029/2002gb001891, 2003.
4976 Archer, D.: A model of the methane cycle, permafrost, and hydrology of the Siberian
4977 continental margin, *Biogeosciences*, doi:10.5194/bg-12-2953-2015, 2015.
4978 Aufdenkampe, A. K., Mayorga, E., Raymond, P. A., Melack, J. M., Doney, S. C., Alin, S. R.,
4979 Aalto, R. E. and Yoo, K.: Riverine coupling of biogeochemical cycles between land, oceans,
4980 and atmosphere, in *Frontiers in Ecology and the Environment.*, 2011.
4981 De Baets, S., Van de Weg, M. J., Lewis, R., Steinberg, N., Meersmans, J., Quine, T. A., Shaver,
4982 G. R. and Hartley, I. P.: Investigating the controls on soil organic matter decomposition in
4983 tussock tundra soil and permafrost after fire, *Soil Biol. Biochem.*,
4984 doi:10.1016/j.soilbio.2016.04.020, 2016.
4985 Bardy, M., Derenne, S., Allard, T., Benedetti, M. F. and Fritsch, E.: Podzolisation and
4986 exportation of organic matter in black waters of the Rio Negro (upper Amazon basin,

4987 Brazil), Biogeochemistry, doi:10.1007/s10533-010-9564-9, 2011.

4988 Bastviken, D., Tranvik, L. J., Downing, J. A., Crill, P. M. and Enrich-Prast, A.: Freshwater

4989 methane emissions offset the continental carbon sink, *Science* (80-.),

4990 doi:10.1126/science.1196808, 2011.

4991 Battin, T. J., Luysaert, S., Kaplan, L. A., Aufdenkampe, A. K., Richter, A. and Tranvik, L. J.:

4992 The boundless carbon cycle, *Nat. Geosci.*, doi:10.1038/ngeo618, 2009.

4993 Bauch, D., Hölemann, J. A., Nikulina, A., Wegner, C., Janout, M. A., Timokhov, L. A. and

4994 Kassens, H.: Correlation of river water and local sea-ice melting on the Laptev Sea shelf

4995 (Siberian Arctic), *J. Geophys. Res. Ocean.*, doi:10.1002/jgrc.20076, 2013.

4996 Beaulieu, E., Goddëris, Y., Donnadieu, Y., Labat, D. and Roelandt, C.: High sensitivity of the

4997 continental-weathering carbon dioxide sink to future climate change, *Nat. Clim. Chang.*,

4998 doi:10.1038/nclimate1419, 2012.

4999 Beer, C., Lucht, W., Schimmlus, C. and Shvidenko, A.: Small net carbon dioxide uptake by

5000 Russian forests during 1981-1999, *Geophys. Res. Lett.*, doi:10.1029/2006GL026919,

5001 2006.

5002 Bekryaev, R. V., Polyakov, I. V. and Alexeev, V. A.: Role of polar amplification in long-term

5003 surface air temperature variations and modern arctic warming, *J. Clim.*,

5004 doi:10.1175/2010JCLI3297.1, 2010.

5005 Berezovskaya, S., Yang, D. and Hinzman, L.: Long-term annual water balance analysis of

5006 the Lena River, *Glob. Planet. Change*, doi:10.1016/j.gloplacha.2004.12.006, 2005.

5007 Bergkvist, B. O. and Folkesson, L.: Soil acidification and element fluxes of a *Fagus sylvatica*

5008 forest as influenced by simulated nitrogen deposition, *Water, Air, Soil Pollut.*,

5009 doi:10.1007/BF00482753, 1992.

5010 Biastoch, A., Treude, T., Rpk, L. H., Riebesell, U., Roth, C., Burwicz, E. B., Park, W., Latif,

5011 M., Böning, C. W., Madec, G. and Wallmann, K.: Rising Arctic Ocean temperatures cause

5012 gas hydrate destabilization and ocean acidification, *Geophys. Res. Lett.*,

5013 doi:10.1029/2011GL047222, 2011.

5014 Bohn, T. J., Melton, J. R., Ito, A., Kleinen, T., Spahni, R., Stocker, B. D., Zhang, B., Zhu, X.,

5015 Schroeder, R., Glagolev, M. V., Maksyutov, S., Brovkin, V., Chen, G., Denisov, S. N., Eliseev,

5016 A. V., Gallego-Sala, A., McDonald, K. C., Rawlins, M. A., Riley, W. J., Subin, Z. M., Tian, H.,

5017 Zhuang, Q. and Kaplan, J. O.: WETCHIMP-WSL: Intercomparison of wetland methane

5018 emissions models over West Siberia, *Biogeosciences*, doi:10.5194/bg-12-3321-2015,

5019 2015.

5020 Bontemps, S., Defourny, P., Radoux, J., Van Bogaert, E., Lamarche, C., Achard, F., Mayaux,

5021 P., Boettcher, M., Brockmann, C., Kirches, G., Zülkhe, M., Kalogirou, V., Seifert, F. . and

5022 Arino, O.: Consistent global land cover maps for climate modelling communities: current

5023 achievements of the ESA' and cover CCI, in *ESA Living Planet Symposium 2013.*, 2013.

5024 Borges, A. V., Darchambeau, F., Teodoru, C. R., Marwick, T. R., Tamooch, F., Geeraert, N.,

5025 Omengo, F. O., Guérin, F., Lambert, T., Morana, C., Okuku, E. and Bouillon, S.: Globally

5026 significant greenhouse-gas emissions from African inland waters, *Nat. Geosci.*,

5027 doi:10.1038/ngeo2486, 2015.

5028 Bowring, S. P. K., Lauerwald, R., Guenet, B., Zhu, D., Guimberteau, M., Tootchi, A.,

5029 Ducharne, A. and Ciais, P.: ORCHIDEE MICT-LEAK (r5459), a global model for the

5030 production, transport and transformation of dissolved organic carbon from Arctic

5031 permafrost regions, Part 1: Rationale, model description and simulation protocol,

5032 *Geosci. Model Dev. Discuss.*, 1–29, doi:10.5194/gmd-2018-320, 2019a.

5033 Bowring, S. P. K., Lauerwald, R., Guenet, B., Zhu, D., Guimberteau, M., Regnier, P., Tootchi,

5034 A., Ducharne, A. and Ciais, P.: ORCHIDEE MICT-LEAK (r5459), a global model for the

5035 production, transport and transformation of dissolved organic carbon from Arctic
5036 permafrost regions, Part 2: Model evaluation over the Lena River basin, *Geosci. Model*
5037 *Dev. Discuss.*, 1–45, doi:10.5194/gmd-2018-322, 2019b.

5038 Brantley, S. L., Megonigal, J. P., Scatena, F. N., Balogh-Brunstad, Z., Barnes, R. T., Bruns, M.
5039 A., Van Cappellen, P., Dontsova, K., Hartnett, H. E., Hartshorn, A. S., Heimsath, A.,
5040 Herndon, E., Jin, L., Keller, C. K., Leake, J. R., Mcdowell, W. H., Meinzer, F. C., Mozdzer, T. J.,
5041 Petsch, S., Pett-Ridge, J., Pregitzer, K. S., Raymond, P. A., Riebe, C. S., Shumaker, K., Sutton-
5042 Grier, A., Walter, R. and Yoo, K.: Twelve testable hypotheses on the geobiology of
5043 weathering, *Geobiology*, doi:10.1111/j.1472-4669.2010.00264.x, 2011.

5044 Bruhwiler, L., Dlugokencky, E., Masarie, K., Ishizawa, M., Andrews, A., Miller, J., Sweeney,
5045 C., Tans, P. and Worthy, D.: CarbonTracker-CH₄: An assimilation system for estimating
5046 emissions of atmospheric methane, *Atmos. Chem. Phys.*, doi:10.5194/acp-14-8269-
5047 2014, 2014.

5048 Calmels, D., Gaillardet, J. and François, L.: Sensitivity of carbonate weathering to soil
5049 CO₂ production by biological activity along a temperate climate transect, *Chem. Geol.*,
5050 doi:10.1016/j.chemgeo.2014.10.010, 2014.

5051 Camino-Serrano, M., Gielen, B., Luysaert, S., Ciais, P., Vicca, S., Guenet, B., Vos, B. De,
5052 Cools, N., Ahrens, B., Altaf Arain, M., Borcken, W., Clarke, N., Clarkson, B., Cummins, T.,
5053 Don, A., Pannatier, E. G., Laudon, H., Moore, T., Nieminen, T. M., Nilsson, M. B., Peichl, M.,
5054 Schwendenmann, L., Siemens, J. and Janssens, I.: Linking variability in soil solution
5055 dissolved organic carbon to climate, soil type, and vegetation type, *Global Biogeochem.*
5056 *Cycles*, doi:10.1002/2013GB004726, 2014.

5057 Camino-Serrano, M., Guenet, B., Luysaert, S., Ciais, P., Bastrikov, V., De Vos, B., Gielen, B.,
5058 Gleixner, G., Jornet-Puig, A., Kaiser, K., Kothawala, D., Lauerwald, R., Peñuelas, J.,
5059 Schrumppf, M., Vicca, S., Vuichard, N., Walmsley, D. and Janssens, I. A.: ORCHIDEE-SOM:
5060 Modeling soil organic carbon (SOC) and dissolved organic carbon (DOC) dynamics along
5061 vertical soil profiles in Europe, *Geosci. Model Dev.*, doi:10.5194/gmd-11-937-2018,
5062 2018.

5063 Campeau, A. and Del Giorgio, P. A.: Patterns in CH₄ and CO₂ concentrations across
5064 boreal rivers: Major drivers and implications for fluvial greenhouse emissions under
5065 climate change scenarios, *Glob. Chang. Biol.*, doi:10.1111/gcb.12479, 2014.

5066 Campeau, A., Lapierre, J. F., Vachon, D. and Del Giorgio, P. A.: Regional contribution of
5067 CO₂ and CH₄ fluxes from the fluvial network in a lowland boreal landscape of Québec,
5068 *Global Biogeochem. Cycles*, doi:10.1002/2013GB004685, 2014.

5069 Catalán, N., Marcé, R., Kothawala, D. N. and Tranvik, L. J.: Organic carbon decomposition
5070 rates controlled by water retention time across inland waters, *Nat. Geosci.*,
5071 doi:10.1038/ngeo2720, 2016.

5072 Cauwet, G. and Sidorov, I.: The biogeochemistry of Lena River: Organic carbon and
5073 nutrients distribution, in *Marine Chemistry*, 1996.

5074 Clarke, N., Wu, Y. and Strand, L. T.: Dissolved organic carbon concentrations in four
5075 Norway spruce stands of different ages, *Plant Soil*, doi:10.1007/s11104-007-9384-4,
5076 2007.

5077 Cole, J. J., Prairie, Y. T., Caraco, N. F., McDowell, W. H., Tranvik, L. J., Striegl, R. G., Duarte,
5078 C. M., Kortelainen, P., Downing, J. A., Middelburg, J. J. and Melack, J.: Plumbing the global
5079 carbon cycle: Integrating inland waters into the terrestrial carbon budget, *Ecosystems*,
5080 doi:10.1007/s10021-006-9013-8, 2007.

5081 Connolly, C. T., Khosh, M. S., Burkart, G. A., Douglas, T. A., Holmes, R. M., Jacobson, A. D.,
5082 Tank, S. E. and McClelland, J. W.: Watershed slope as a predictor of fluvial dissolved

5083 organic matter and nitrate concentrations across geographical space and catchment size
5084 in the Arctic, *Environ. Res. Lett.*, 13(10), 104015, doi:10.1088/1748-9326/aae35d, 2018.
5085 Cory, R. M., Ward, C. P., Crump, B. C. and Kling, G. W.: Sunlight controls water column
5086 processing of carbon in arctic fresh waters, *Science* (80-.),
5087 doi:10.1126/science.1253119, 2014.
5088 D'Orgeval, T., Polcher, J. and De Rosnay, P.: Sensitivity of the West African hydrological
5089 cycle in ORCHIDEE to infiltration processes, *Hydrol. Earth Syst. Sci.*, doi:10.5194/hess-
5090 12-1387-2008, 2008.
5091 DeLuca, T. H. and Boisvenue, C.: Boreal forest soil carbon: Distribution, function and
5092 modelling, *Forestry*, doi:10.1093/forestry/cps003, 2012.
5093 Denfeld, B., Frey, K. and Sobczak, W.: Summer CO₂ evasion from streams and rivers in
5094 the Kolyma River basin, north-east Siberia, *Polar ...*, doi:10.3402/polar.v32i0.19704,
5095 2013.
5096 Dery, S. J., Stadnyk, T. A., MacDonald, M. K. and Gauli-Sharma, B.: Recent trends and
5097 variability in river discharge across northern Canada, *Hydrol. Earth Syst. Sci.*,
5098 doi:10.5194/hess-20-4801-2016, 2016.
5099 Dessert, C., Dupré, B., Gaillardet, J., François, L. M. and Allègre, C. J.: Basalt weathering
5100 laws and the impact of basalt weathering on the global carbon cycle, *Chem. Geol.*,
5101 doi:10.1016/j.chemgeo.2002.10.001, 2003.
5102 Dolman, A. J., Shvidenko, A., Schepaschenko, D., Ciais, P., Tchepakova, N., Chen, T., Van
5103 Der Molen, M. K., Beileli Marchesini, L., Maximov, T. C., Maksyutov, S. and Schulze, E. D.:
5104 An estimate of the terrestrial carbon budget of Russia using inventory-based, eddy
5105 covariance and inversion methods, *Biogeosciences*, doi:10.5194/bg-9-5323-2012, 2012.
5106 Drake, T. W., Wickland, K. P., Spencer, R. G. M., McKnight, D. M. and Striegl, R. G.: Ancient
5107 low-molecular-weight organic acids in permafrost fuel rapid carbon dioxide production
5108 upon thaw, *Proc. Natl. Acad. Sci.*, doi:10.1073/pnas.1511705112, 2015.
5109 Drake, T. W., Raymond, P. A. and Spencer, R. G. M.: Terrestrial carbon inputs to inland
5110 waters: A current synthesis of estimates and uncertainty, *Limnol. Oceanogr. Lett.*,
5111 doi:10.1002/lol2.10055, 2017.
5112 Drake, T. W., Tank, S. E., Zhulidov, A. V., Holmes, R. M., Gurtovaya, T. and Spencer, R. G.
5113 M.: Increasing Alkalinity Export from Large Russian Arctic Rivers, *Environ. Sci. Technol.*,
5114 doi:10.1021/acs.est.8b01051, 2018.
5115 Ducharne, A., Golaz, C., Leblois, E., Laval, K., Polcher, J., Ledoux, E. and De Marsily, G.:
5116 Development of a high resolution runoff routing model, calibration and application to
5117 assess runoff from the LMD GCM, *J. Hydrol.*, doi:10.1016/S0022-1694(03)00230-0,
5118 2003.
5119 Eiriksdottir, E. S., Gislason, S. R. and Oelkers, E. H.: Does runoff or temperature control
5120 chemical weathering rates?, *Appl. Geochemistry*, doi:10.1016/j.apgeochem.2011.03.056,
5121 2011.
5122 Elberling, B.: Annual soil CO₂ effluxes in the High Arctic: The role of snow thickness and
5123 vegetation type, *Soil Biol. Biochem.*, doi:10.1016/j.soilbio.2006.09.017, 2007.
5124 Feely, R. A., Sabine, C. L., Lee, K., Berelson, W., Kleypas, J. A., Fabry, V. J. and Millero, F. J.:
5125 Impact of Anthropogenic CO₂ on the CaCO₃ System in the Oceans, *Science* (80-.),
5126 doi:10.1126/science.1097329, 2004.
5127 Feng, X., Vonk, J. E., van Dongen, B. E., Gustafsson, O., Semiletov, I. P., Dudarev, O. V.,
5128 Wang, Z., Montlucon, D. B., Wacker, L. and Eglinton, T. I.: Differential mobilization of
5129 terrestrial carbon pools in Eurasian Arctic river basins, *Proc. Natl. Acad. Sci.*,
5130 doi:10.1073/pnas.1307031110, 2013.

5131 Feng, X., Vonk, J. E., Griffin, C., Zimov, N., Montluçon, D. B., Wacker, L. and Eglinton, T. I.: ¹⁴
5132 C Variation of Dissolved Lignin in Arctic River Systems, ACS Earth Sp. Chem.,
5133 doi:10.1021/acsearthspacechem.7b00055, 2017.

5134 Findlay, H. S., Gibson, G., Kędra, M., Morata, N., Orchowska, M., Pavlov, A. K., Reigstad, M.,
5135 Silyakova, A., Tremblay, J.-É., Walczowski, W., Weydmann, A. and Logvinova, C.:
5136 Responses in Arctic marine carbon cycle processes: conceptual scenarios and
5137 implications for ecosystem function, Polar Res., doi:10.3402/polar.v34.24252, 2015a.

5138 Findlay, H. S., Gibson, G., Kedra, M., Morata, N., Orchowska, M., Pavlov, A. K., Reigstad, M.,
5139 Silyakova, A., Tremblay, J. É., Walczowski, W., Weydmann, A. and Logvinova, C.:
5140 Responses in Arctic marine carbon cycle processes: Conceptual scenarios and
5141 implications for ecosystem function, Polar Res., doi:10.3402/polar.v34.24252, 2015b.

5142 Fluet-Chouinard, E., Lehner, B., Rebelo, L. M., Papa, F. and Hamilton, S. K.: Development
5143 of a global inundation map at high spatial resolution from topographic downscaling of
5144 coarse-scale remote sensing data, Remote Sens. Environ., doi:10.1016/j.rse.2014.10.015,
5145 2015.

5146 Le Fouest, V., Matsuoka, A., Manizza, M., Shernetsky, M., Tremblay, B. and Babin, M.:
5147 Towards an assessment of riverine dissolved organic carbon in surface waters of the
5148 western Arctic Ocean based on remote sensing and biogeochemical modeling,
5149 Biogeosciences, doi:10.5194/bg-15-1335-2018, 2018.

5150 Frey, K. E. and McClelland, J. W.: Impacts of permafrost degradation on arctic river
5151 biogeochemistry, Hydrol. Process., doi:10.1002/hyp.7196, 2009.

5152 Frey, K. E. and Smith, L. C.: Amplified carbon release from vast West Siberian peatlands
5153 by 2100, Geophys. Res. Lett., doi:10.1029/2004GL022025, 2005.

5154 Frieler, K., Lange, S., Piontek, F., Reyer, C. P. O., Schewe, J., Warszawski, L., Zhao, F., Chini,
5155 L., Denvil, S., Emanuel, K., Geiger, T., Halladay, K., Hurtt, G., Mengel, M., Murakami, D.,
5156 Ostberg, S., Popp, A., Riva, R., Stevanovic, M., SuzGBRi, T., Volkholz, J., Burke, E., Ciais, P.,
5157 Ebi, K., Eddy, T. D., Elliott, J., Galbraith, E., Gosling, S. N., Hattermann, F., Hickler, T.,
5158 Hinkel, J., Hof, C., Huber, V., Jägermeyr, J., Krysanova, V., Marcé, R., Müller Schmied, H.,
5159 Mouratiadou, I., Pierson, D., Tittensor, D. P., Vautard, R., Van Vliet, M., Biber, M. F., Betts,
5160 R. A., Leon Bodirsky, B., Deryng, D., Frohking, S., Jones, C. D., Lotze, H. K., Lotze-Campen,
5161 H., Sahajpal, R., Thonicke, K., Tian, H. and Yamagata, Y.: Assessing the impacts of 1.5°C
5162 global warming - Simulation protocol of the Inter-Sectoral Impact Model
5163 Intercomparison Project (ISIMIP2b), Geosci. Model Dev., doi:10.5194/gmd-10-4321-
5164 2017, 2017.

5165 Fritz, M., Vonk, J. E. and Lantuit, H.: Collapsing Arctic coastlines, Nat. Clim. Chang.,
5166 doi:10.1038/nclimate3188, 2017.

5167 Fröberg, M., Berggren, D., Bergkvist, B., Bryant, C. and Mulder, J.: Concentration and
5168 fluxes of dissolved organic carbon (DOC) in three Norway spruce stands along a climatic
5169 gradient in Sweden, Biogeochemistry, doi:10.1007/s10533-004-0564-5, 2006.

5170 Gaillardet, J., Dupré, B., Louvat, P. and Allègre, C. J.: Global silicate weathering and
5171 CO₂ consumption rates deduced from the chemistry of large rivers, Chem. Geol.,
5172 doi:10.1016/S0009-2541(99)00031-5, 1999.

5173 Gislason, S. R., Oelkers, E. H., Eiriksdottir, E. S., Kardjilov, M. I., Gisladottir, G., Sigfusson,
5174 B., Snorrason, A., Elefsen, S., Hardardottir, J., Torssander, P. and Oskarsson, N.: Direct
5175 evidence of the feedback between climate and weathering, Earth Planet. Sci. Lett.,
5176 doi:10.1016/j.epsl.2008.10.018, 2009.

5177 Gouttevin, I., Menegoz, M., Dominé, F., Krinner, G., Koven, C., Ciais, P., Tarnocai, C. and
5178 Boike, J.: How the insulating properties of snow affect soil carbon distribution in the

5179 continental pan-Arctic area, *J. Geophys. Res. Biogeosciences*,
5180 doi:10.1029/2011JG001916, 2012.

5181 Graham, D. E., Wallenstein, M. D., Vishnivetskaya, T. A., Waldrop, M. P., Phelps, T. J.,
5182 Pfiffner, S. M., Onstott, T. C., Whyte, L. G., Rivkina, E. M., Gilichinsky, D. A., Elias, D. A.,
5183 MacKelprang, R., Verberkmoes, N. C., Hettich, R. L., Wagner, D., Wullschleger, S. D. and
5184 Jansson, J. K.: Microbes in thawing permafrost: The unknown variable in the climate
5185 change equation, *ISME J.*, doi:10.1038/ismej.2011.163, 2012.

5186 Guenet, B., Danger, M., Abbadie, L. and Lacroix, G.: Priming effect: Bridging the gap
5187 between terrestrial and aquatic ecology, *Ecology*, doi:10.1890/09-1968.1, 2010.

5188 Guenet, B., Moyano, F. E., Peylin, P., Ciais, P. and Janssens, I. A.: Towards a representation
5189 of priming on soil carbon decomposition in the global land biosphere model ORCHIDEE
5190 (version 1.9.5.2), *Geosci. Model Dev.*, doi:10.5194/gmd-9-841-2016, 2016.

5191 Guenet, B., Camino-Serrano, M., Ciais, P., Tifafi, M., Maignan, F., Soong, J. L. and Janssens,
5192 I. A.: Impact of priming on global soil carbon stocks, *Glob. Chang. Biol.*,
5193 doi:10.1111/gcb.14069, 2018.

5194 Guimberteau, M., Drapeau, G., Ronchail, J., Sultan, B., Polcher, J., Martinez, J. M., Prigent,
5195 C., Guyot, J. L., Cochonneau, G., Espinoza, J. C., Filizola, N., Fraizy, P., Lavado, W., De
5196 Oliveira, E., Pombosa, R., Noriega, L. and Vauchel, P.: Discharge simulation in the sub-
5197 basins of the Amazon using ORCHIDEE forced by new datasets, *Hydrol. Earth Syst. Sci.*,
5198 doi:10.5194/hess-16-911-2012, 2012.

5199 Guimberteau, M., Zhu, D., Maignan, F., Huang, Y., Yue, C., Dantec-N d lec, S., Ottl, C., Jornet-
5200 Puig, A., Bastos, A., Laurent, P., Goll, D., Bowring, S., Chang, J., Guenet, B., Tifafi, M., Peng,
5201 S., Krinner, G., Ducharne, A. s., Wang, F., Wang, T., Wang, X., Wang, Y., Yin, Z., Lauerwald,
5202 R., Joetzjer, E., Qiu, C., Kim, H. and Ciais, P.: ORCHIDEE-MICT (v8.4.1), a land surface
5203 model for the high latitudes: model description and validation, *Geosci. Model Dev.*,
5204 doi:10.5194/gmd-11-121-2018, 2018.

5205 Hartmann, J. and Moosdorf, N.: The new global lithological map database GLiM: A
5206 representation of rock properties at the Earth surface, *Geochemistry, Geophys.*
5207 *Geosystems*, doi:10.1029/2012GC004370, 2012.

5208 Hartmann, J., Moosdorf, N., Lauerwald, R., Hinderer, M. and West, A. J.: Global chemical
5209 weathering and associated p-release - the role of lithology, temperature and soil
5210 properties, *Chem. Geol.*, doi:10.1016/j.chemgeo.2013.10.025, 2014.

5211 Heim, B., Abramova, E., Doerffer, R., Günther, F., Hölemann, J., Kraberg, A., Lantuit, H.,
5212 Logina, A., Martynov, F., Overduin, P. P. and Wegner, C.: Ocean colour remote sensing
5213 in the southern laptev sea: Evaluation and applications, *Biogeosciences*, doi:10.5194/bg-
5214 11-4191-2014, 2014.

5215 Holgerson, M. A. and Raymond, P. A.: Large contribution to inland water CO₂ and
5216 CH₄ emissions from very small ponds, *Nat. Geosci.*, doi:10.1038/ngeo2654, 2016.

5217 Hollesen, J., Matthiesen, H., Møller, A. B. and Elberling, B.: Permafrost thawing in organic
5218 Arctic soils accelerated by ground heat production, *Nat. Clim. Chang.*,
5219 doi:10.1038/nclimate2590, 2015.

5220 Holmes, R.M., Shiklomanov, A. I., Tank, S. E., McClelland, J. W., Tretiakov, M.: Arctic
5221 Report Card 2016 Arctic Report Card 2016. <https://arctic.noaa.gov/Report-Card/Report-Card-2015/ArtMID/5037/ArticleID/227/River-Discharge>, *Arct. Rep. Card*
5222 *-River Disch.*, 2015.

5224 Holmes, R. M., McClelland, J. W., Peterson, B. J., Tank, S. E., Bulygina, E., Eglinton, T. I.,
5225 Gordeev, V. V., Gurtovaya, T. Y., Raymond, P. A., Repeta, D. J., Staples, R., Striegl, R. G.,
5226 Zhulidov, A. V. and Zimov, S. A.: Seasonal and Annual Fluxes of Nutrients and Organic

5227 Matter from Large Rivers to the Arctic Ocean and Surrounding Seas, *Estuaries and*
5228 *Coasts*, doi:10.1007/s12237-011-9386-6, 2012.

5229 Hugelius, G., Bockheim, J. G., Camill, P., Elberling, B., Grosse, G., Harden, J. W., Johnson, K.,
5230 Jorgenson, T., Koven, C. D., Kuhry, P., Michaelson, G., Mishra, U., Palmtag, J., Ping, C.-L.,
5231 O'Donnell, J., Schirrmeister, L., Schuur, E. A. G., Sheng, Y., Smith, L. C., Strauss, J. and Yu, Z.:
5232 A new data set for estimating organic carbon storage to 3m depth in soils of the
5233 northern circumpolar permafrost region, *EARTH Syst. Sci. DATA*, doi:10.5194/essd-5-
5234 393-2013, 2013.

5235 Hugelius, G., Strauss, J., Zubrzycki, S., Harden, J. W., Schuur, E. A. G., Ping, C. L.,
5236 Schirrmeister, L., Grosse, G., Michaelson, G. J., Koven, C. D., O'Donnell, J. A., Elberling, B.,
5237 Mishra, U., Camill, P., Yu, Z., Palmtag, J. and Kuhry, P.: Estimated stocks of circumpolar
5238 permafrost carbon with quantified uncertainty ranges and identified data gaps,
5239 *Biogeosciences*, doi:10.5194/bg-11-6573-2014, 2014.

5240 Jakobsson, M.: Hypsometry and volume of the Arctic Ocean and its constituent seas,
5241 *Geochemistry, Geophys. Geosystems*, doi:10.1029/2001GC000302, 2002.

5242 Janout, M., Håflemann, J., Juhls, B., Krumpfen, T., Rabe, B., Bauch, D., Wegner, C., Kassens,
5243 H. and Timokhov, L.: Episodic warming of near-bottom waters under the Arctic sea ice
5244 on the central Laptev Sea shelf, *Geophys. Res. Lett.*, doi:10.1002/2015GL066565, 2016.

5245 Jasechko, S., Kirchner, J. W., Welker, J. M. and McDonnell, J. J.: Substantial proportion of
5246 global streamflow less than three months old, *Nat. Geosci.*, doi:10.1038/ngeo2636, 2016.

5247 Kaiser, K. and Kalbitz, K.: Cycling downwards - dissolved organic matter in soils, *Soil*
5248 *Biol. Biochem.*, doi:10.1016/j.soilbio.2012.04.002, 2012.

5249 Kanevskiy, M., Shur, Y., Fortier, D., Jorgenson, M. T. and Stephani, E.: Cryostratigraphy of
5250 late Pleistocene syngenetic permafrost (yedoma) in northern Alaska, Itkillik River
5251 exposure, *Quat. Res.*, doi:10.1016/j.yqres.2010.12.003, 2011.

5252 Kaushal, S. S., Likens, G. E., Pace, M. L., Utz, R. M., Haq, S., Gorman, J. and Grese, M.:
5253 Freshwater salinization syndrome on a continental scale, *Proc. Natl. Acad. Sci.*,
5254 doi:10.1073/pnas.1711234115, 2018.

5255 Keuper, F., van Bodegom, P. M., Dorrepaal, E., Weedon, J. T., van Hal, J., van Logtestijn, R.
5256 S. P. and Aerts, R.: A frozen feast: Thawing permafrost increases plant-available nitrogen
5257 in subarctic peatlands, *Glob. Chang. Biol.*, doi:10.1111/j.1365-2486.2012.02663.x, 2012.

5258 Kicklighter, D. W., Hayes, D. J., McClelland, J. W., Peterson, B. J., McGuire, A. D. and Melillo,
5259 J. M.: Insights and issues with simulating terrestrial DOC loading of Arctic river
5260 networks, *Ecol. Appl.*, doi:10.1890/11-1050.1, 2013.

5261 Klaminder, J., Grip, H., Mörth, C. M. and Laudon, H.: Carbon mineralization and pyrite
5262 oxidation in groundwater: Importance for silicate weathering in boreal forest soils and
5263 stream base-flow chemistry, *Appl. Geochemistry*,
5264 doi:10.1016/j.apgeochem.2010.12.005, 2011.

5265 Koven, C., Friedlingstein, P., Ciais, P., Khvorostyanov, D., Krinner, G. and Tarnocai, C.: On
5266 the formation of high-latitude soil carbon stocks: Effects of cryoturbation and insulation
5267 by organic matter in a land surface model, *Geophys. Res. Lett.*,
5268 doi:10.1029/2009GL040150, 2009.

5269 Koven, C. D., Riley, W. J. and Stern, A.: Analysis of permafrost thermal dynamics and
5270 response to climate change in the CMIP5 earth system models, *J. Clim.*,
5271 doi:10.1175/JCLI-D-12-00228.1, 2013a.

5272 Koven, C. D., Riley, W. J., Subin, Z. M., Tang, J. Y., Torn, M. S., Collins, W. D., Bonan, G. B.,
5273 Lawrence, D. M. and Swenson, S. C.: The effect of vertically resolved soil biogeochemistry
5274 and alternate soil C and N models on C dynamics of CLM4, *Biogeosciences*,

5275 doi:10.5194/bg-10-7109-2013, 2013b.

5276 Koven, C. D., Lawrence, D. M. and Riley, W. J.: Permafrost carbon–climate feedback is
5277 sensitive to deep soil carbon decomposability but not deep soil nitrogen dynamics, Proc.
5278 Natl. Acad. Sci., doi:10.1073/pnas.1415123112, 2015.

5279 Krinner, G., Viovy, N., de Noblet-Ducoudré, N., Ogée, J., Polcher, J., Friedlingstein, P., Ciais,
5280 P., Sitch, S. and Prentice, I. C.: A dynamic global vegetation model for studies of the
5281 coupled atmosphere-biosphere system, *Global Biogeochem. Cycles*,
5282 doi:10.1029/2003GB002199, 2005.

5283 Kump, L.R., Kasting, J.F., Crane, R. G.: Kump, L.R., Kasting, J.F. and Crane, R.G., 2004. The
5284 Earth System 3rd edition (Vol. 432). Upper Saddle River, NJ: Pearson Prentice Hall., ,
5285 doi:10.1017/s0016756800243823, 2010.

5286 Kunkel, K. E., Robinson, D. A., Champion, S., Yin, X., Estilow, T. and Frankson, R. M.:
5287 Trends and Extremes in Northern Hemisphere Snow Characteristics, *Curr. Clim. Chang.*
5288 *Reports*, doi:10.1007/s40641-016-0036-8, 2016.

5289 Kutscher, L., Mörth, C. M., Porcelli, D., Hirst, C., Maximov, T. C., Petrov, R. E. and
5290 Andersson, P. S.: Spatial variation in concentration and sources of organic carbon in the
5291 Lena River, Siberia, *J. Geophys. Res. Biogeosciences*, doi:10.1002/2017JG003858, 2017.

5292 Kuzyakov, Y.: Sources of CO₂ efflux from soil and review of partitioning methods, *Soil*
5293 *Biol. Biochem.*, doi:10.1016/j.soilbio.2005.08.020, 2006.

5294 Lammers, R. B., Shiklomanov, A. I., Vörösmarty, C. J., Fekete, B. M. and Peterson, B. J.:
5295 Assessment of contemporary Arctic river runoff based on observational discharge
5296 records, *J. Geophys. Res. Atmos.*, doi:10.1029/2000JD900444, 2001.

5297 Lammers, R. B., Pundsack, J. W. and Shiklomanov, A. I.: Variability in river temperature,
5298 discharge, and energy flux from the Russian pan-Arctic landmass, *J. Geophys. Res.*
5299 *Biogeosciences*, doi:10.1029/2006JG000370, 2007.

5300 Lange, S.: Earth2Observe, WFDEI and ERA-Interim data Merged and Bias-corrected for
5301 ISIMIP (EWEMBI), GFZ Data Serv., doi:10.5880/pik.2016.004, 2016.

5302 Lange, S.: Bias correction of surface downwelling longwave and shortwave radiation for
5303 the EWEMBI dataset, *Earth Syst. Dyn.*, doi:10.5194/esd-9-627-2018, 2018.

5304 Lara, R. J., Rachold, V., Kattner, G., Hubberten, H. W., Guggenberger, G., Skoog, A. and
5305 Thomas, D. N.: Dissolved organic matter and nutrients in the Lena River, Siberian Arctic:
5306 Characteristics and distribution, *Mar. Chem.*, doi:10.1016/S0304-4203(97)00076-5,
5307 1998.

5308 Laudon, H., Buttle, J., Carey, S. K., McDonnell, J., McGuire, K., Seibert, J., Shanley, J.,
5309 Soulsby, C. and Tetzlaff, D.: Cross-regional prediction of long-term trajectory of stream
5310 water DOC response to climate change, *Geophys. Res. Lett.*, doi:10.1029/2012GL053033,
5311 2012.

5312 Lauerwald, R., Hartmann, J., Ludwig, W. and Moosdorf, N.: Assessing the nonconservative
5313 fluvial fluxes of dissolved organic carbon in North America, *J. Geophys. Res.*
5314 *Biogeosciences*, doi:10.1029/2011JG001820, 2012.

5315 Lauerwald, R., Laruelle, G. G., Hartmann, J., Ciais, P. and Regnier, P. A. G.: Spatial patterns
5316 in CO₂ evasion from the global river network, *Global Biogeochem. Cycles*,
5317 doi:10.1002/2014GB004941, 2015.

5318 Lauerwald, R., Regnier, P., Camino-Serrano, M., Guenet, B., Guimberteau, M., Ducharne,
5319 A., Polcher, J. and Ciais, P.: ORCHILEAK (revision 3875): A new model branch to simulate
5320 carbon transfers along the terrestrial-aquatic continuum of the Amazon basin, *Geosci.*
5321 *Model Dev.*, doi:10.5194/gmd-10-3821-2017, 2017.

5322 Lee, H., Swenson, S. C., Slater, A. G. and Lawrence, D. M.: Effects of excess ground ice on

5323 projections of permafrost in a warming climate, *Environ. Res. Lett.*, doi:10.1088/1748-
5324 9326/9/12/124006, 2014.

5325 Lindroos, A. J., Derome, J., Derome, K. and Smolander, A.: The effect of scots pine, norway
5326 spruce and silver birch on the chemical composition of stand throughfall and upper soil
5327 percolation water in northern Finland, *Boreal Environ. Res.*, 2011.

5328 Lloyd, J., Shibistova, O., Zolotoukhine, D., Kolle, O., Arneth, A., Wirth, C., Styles, J. M.,
5329 Tchebakova, N. M. and Schulze, E. D.: Seasonal and annual variations in the
5330 photosynthetic productivity and carbon balance of a central Siberian pine forest, *Tellus*,
5331 *Ser. B Chem. Phys. Meteorol.*, doi:10.1034/j.1600-0889.2002.01487.x, 2002.

5332 MacKelprang, R., Waldrop, M. P., Deangelis, K. M., David, M. M., Chavarria, K. L.,
5333 Blazewicz, S. J., Rubin, E. M. and Jansson, J. K.: Metagenomic analysis of a permafrost
5334 microbial community reveals a rapid response to thaw, *Nature*,
5335 doi:10.1038/nature10576, 2011.

5336 Maher, K.: The dependence of chemical weathering rates on fluid residence time, *Earth*
5337 *Planet. Sci. Lett.*, doi:10.1016/j.epsl.2010.03.010, 2010.

5338 Maher, K. and Chamberlain, C. P.: Hydrologic regulation of chemical weathering and the
5339 geologic, *Science (80-.)*, doi:10.1126/science.1250770, 2014.

5340 Manizza, M., Follows, M. J., Dutkiewicz, S., Menemenlis, D., McClelland, J. W., Hill, C. N.,
5341 Peterson, B. J. and Key, R. M.: A model of the Arctic Ocean carbon cycle, *J. Geophys. Res.*
5342 *Ocean.*, doi:10.1029/2011JC006998, 2011.

5343 Mann, P. J., Eglinton, T. I., McIntyre, C. P., Zimov, N., Davydova, A., Vonk, J. E., Holmes, R.
5344 M. and Spencer, R. G. M.: Utilization of ancient permafrost carbon in headwaters of Arctic
5345 fluvial networks, *Nat. Commun.*, doi:10.1038/ncomms8856, 2015.

5346 Manning, R.: On the Flow of Water in Open Channels and Pipes, *Trans. Inst. Civ. Eng. Irel.*,
5347 doi:10.1021/bi2010619, 1891.

5348 Manzoni, S., Taylor, P., Richter, A., Porporato, A. and Ågren, G. I.: Environmental and
5349 stoichiometric controls on microbial carbon-use efficiency in soils, *New Phytol.*,
5350 doi:10.1111/j.1469-8137.2012.04225.x, 2012.

5351 McClelland, J. W., Holmes, R. M., Peterson, B. J. and Stieglitz, M.: Increasing river
5352 discharge in the Eurasian Arctic: Consideration of dams, permafrost thaw, and fires as
5353 potential agents of change, *J. Geophys. Res. Atmos.*, doi:10.1029/2004JD004583, 2004.

5354 McClelland, J. W., Holmes, R. M., Peterson, B. J., Amon, R., Brabets, T., Cooper, L., Gibson, J.,
5355 Gordeev, V. V., Guay, C., Milburn, D., Staples, R., Raymond, P. A., Shiklomanov, I., Striegl,
5356 R., Zhulidov, A., Gurtovaya, T. and Zimov, S.: Development of Pan-Arctic database for
5357 river chemistry, *Eos (Washington. DC)*, doi:10.1029/2008EO240001, 2008.

5358 McClelland, J. W., Holmes, R. M., Dunton, K. H. and Macdonald, R. W.: The Arctic Ocean
5359 Estuary, *Estuaries and Coasts*, doi:10.1007/s12237-010-9357-3, 2012.

5360 McClelland, J. W., Holmes, R. M., Peterson, B. J., Raymond, P. A., Striegl, R. G., Zhulidov, A.
5361 V., Zimov, S. A., Zimov, N., Tank, S. E., Spencer, R. G. M., Staples, R., Gurtovaya, T. Y. and
5362 Griffin, C. G.: Particulate organic carbon and nitrogen export from major Arctic rivers,
5363 *Global Biogeochem. Cycles*, doi:10.1002/2015GB005351, 2016.

5364 McGuire, A. D., Anderson, L. G., Christensen, T. R., Scott, D., Laodong, G., Hayes, D. J.,
5365 Martin, H., Lorenson, T. D., Macdonald, R. W. and Nigell, R.: Sensitivity of the carbon cycle
5366 in the Arctic to climate change, *Ecol. Monogr.*, doi:10.1890/08-2025.1, 2009.

5367 McGuire, A. D., Anderson, L. G., Christensen, T. R., Dallimore, S., Guo, L., Hayes, D. J.,
5368 Heimann, M., Lorenson, T. D., Macdonald, R. W. and Roulet, N.: Sensitivity of the carbon
5369 cycle in the Arctic to climate change, *Ecol. Monogr.*, doi:10.1890/08-2025.1, 2009.

5370 McGuire, A. D., Christensen, T. R., Hayes, D., Heroult, A., Euskirchen, E., Kimball, J. S.,

5371 Koven, C., Lafleur, P., Miller, P. A., Oechel, W., Peylin, P., Williams, M. and Yi, Y.: An
5372 assessment of the carbon balance of Arctic tundra: Comparisons among observations,
5373 process models, and atmospheric inversions, *Biogeosciences*, doi:10.5194/bg-9-3185-
5374 2012, 2012.

5375 McGuire, K. J., McDonnell, J. J., Weiler, M., Kendall, C., McGlynn, B. L., Welker, J. M. and
5376 Seibert, J.: The role of topography on catchment-scale water residence time, *Water*
5377 *Resour. Res.*, doi:10.1029/2004WR003657, 2005.

5378 Messenger, M. L., Lehner, B., Grill, G., Nedeva, I. and Schmitt, O.: Estimating the volume and
5379 age of water stored in global lakes using a geo-statistical approach, *Nat. Commun.*,
5380 doi:10.1038/ncomms13603, 2016.

5381 Millot, R., Gaillardet, J., Dupré, B. and Allégre, C. J.: Northern latitude chemical weathering
5382 rates: Clues from the Mackenzie River Basin, Canada, *Geochim. Cosmochim. Acta*,
5383 doi:10.1016/S0016-7037(02)01207-3, 2003.

5384 Moosdorf, N., Hartmann, J., Lauerwald, R., Hagedorn, B. and Kempe, S.: Atmospheric CO₂
5385 consumption by chemical weathering in North America, *Geochim. Cosmochim. Acta*,
5386 doi:10.1016/j.gca.2011.10.007, 2011.

5387 Mudryk, L. R., Derksen, C., Kushner, P. J. and Brown, R.: Characterization of Northern
5388 Hemisphere snow water equivalent datasets, 1981-2010, *J. Clim.*, doi:10.1175/JCLI-D-
5389 15-0229.1, 2015.

5390 Mulholland, P. J.: Dissolved Organic Matter Concentration and Flux in Streams, *Journal*
5391 *North Am. Benthol. Soc.* 16, no. 1 (Mar., 1997) 131-141. *Journal North Am. Benthol. Soc.*,
5392 16(1), 131-141., doi:10.2307/1468246, 1997.

5393 Myers-Pigg, A. N., Louchouart, P., Amon, R. M. W., Prokushkin, A., Pierce, K. and Rubtsov,
5394 A.: Labile pyrogenic dissolved organic carbon in major Siberian Arctic rivers:
5395 Implications for wildfire-stream metabolic linkages, *Geophys. Res. Lett.*,
5396 doi:10.1002/2014GL062762, 2015.

5397 Nachtergaele, F. et al.: The harmonized world soil database, FAO, ISRIC, ISSCAS, JRC,
5398 doi:3123, 2010.

5399 Naipal, V., Ciais, P., Wang, Y., Lauerwald, R., Guenet, B. and Van Oost, K.: Global soil
5400 organic carbon removal by water erosion under climate change and land use change
5401 during AD-1850-2005, *Biogeosciences*, doi:10.5194/bg-15-4459-2018, 2018.

5402 Ngo-Duc, T., Laval, K., Ramillien, G., Polcher, J. and Cazenave, A.: Validation of the land
5403 water storage simulated by Organising Carbon and Hydrology in Dynamic Ecosystems
5404 (ORCHIDEE) with Gravity Recovery and Climate Experiment (GRACE) data, *Water*
5405 *Resour. Res.*, doi:10.1029/2006WR004941, 2007.

5406 Nicolsky, D. J., Romanovsky, V. E., Romanovskii, N. N., Kholodov, A. L., Shakhova, N. E. and
5407 Semiletov, I. P.: Modeling sub-sea permafrost in the East Siberian Arctic Shelf: The
5408 Laptev Sea region, *J. Geophys. Res. Earth Surf.*, doi:10.1029/2012JF002358, 2012.

5409 O'Donnell, J. A., Aiken, G. R., Swanson, D. K., Panda, S., Butler, K. D. and Baltensperger, A.
5410 P.: Dissolved organic matter composition of Arctic rivers: Linking permafrost and parent
5411 material to riverine carbon, *Global Biogeochem. Cycles*, doi:10.1002/2016GB005482,
5412 2016.

5413 Oki, T., Nishimura, T. and Dirmeyer, P. A.: Assessment of annual runoff from land surface
5414 models using Total Runoff Integrating Pathways (TRIP), *J. Meteorol. Soc. Japan*, 1999.

5415 Overduin, P. P., Liebner, S., Knoblauch, C., Günther, F., Wetterich, S., Schirrmeister, L.,
5416 Hubberten, H. W. and Grigoriev, M. N.: Methane oxidation following submarine
5417 permafrost degradation: Measurements from a central Laptev Sea shelf borehole, *J.*
5418 *Geophys. Res. Biogeosciences*, doi:10.1002/2014JG002862, 2015.

5419 Pekel, J.-F., Cottam, A., Gorelick, N. and Belward, A. S.: Global Surface Water - Data Users
5420 Guide (JRC) High-resolution mapping of global surface water and its long-term changes,
5421 Nature, doi:10.1038/nature20584, 2016.

5422 Peterson, B. J., Holmes, R. M., McClelland, J. W., Vörösmarty, C. J., Lammers, R. B.,
5423 Shiklomanov, A. I., Shiklomanov, I. A. and Rahmstorf, S.: Increasing river discharge to the
5424 Arctic Ocean, Science (80-.), doi:10.1126/science.1077445, 2002.

5425 Ponomarev, E. I., Kharuk, V. I. and Ranson, K. J.: Wildfires dynamics in Siberian larch
5426 forests, Forests, doi:10.3390/f7060125, 2016.

5427 Prigent, C., Papa, F., Aires, F., Rossow, W. B. and Matthews, E.: Global inundation
5428 dynamics inferred from multiple satellite observations, 1993-2000, J. Geophys. Res.
5429 Atmos., doi:10.1029/2006JD007847, 2007.

5430 Qiu, C., Zhu, D., Ciais, P., Guenet, B., Krinner, G., Peng, S., Aurela, M., Bernhofer, C.,
5431 Brümmer, C., Bret-Harte, S., Chu, H., Chen, J., Desai, A. R., Dušek, J., Euskirchen, E. S.,
5432 Fortuniak, K., Flanagan, L. B., Friborg, T., Grygoruk, M., Gogo, S., Grünwald, T., Hansen, B.
5433 U., Holl, D., Humphreys, E., Hurkuck, M., Kiely, G., Klatt, J., Kutzbach, L., Langeron, C.,
5434 Laggoun-Défarge, F., Lund, M., Lafleur, P. M., Li, X., Mammarella, I., Merbold, L., Nilsson,
5435 M. B., Olejnik, J., Ottosson-Löfvenius, M., Oechel, W., Parmentier, F. J. W., Peichl, M., Pirk,
5436 N., Peltola, O., Pawlak, W., Rasse, D., Rinne, J., Shaver, G., Peter Schmid, H., Sottocornola,
5437 M., Steinbrecher, R., Sachs, T., Urbaniak, M., Zona, D. and Ziemblinska, K.: ORCHIDEE-
5438 PEAT (revision 4596), a model for northern peatland CO₂, water, and energy fluxes on
5439 daily to annual scales, Geosci. Model Dev., doi:10.5194/gmd-11-497-2018, 2018.

5440 Raymond, P. A.: Temperature versus hydrologic controls of chemical weathering fluxes
5441 from United States forests, Chem. Geol., doi:10.1016/j.chemgeo.2017.02.025, 2017.

5442 Raymond, P. A. and Hamilton, S. K.: Anthropogenic influences on riverine fluxes of
5443 dissolved inorganic carbon to the oceans, Limnol. Oceanogr. Lett.,
5444 doi:10.1002/lol2.10069, 2018.

5445 Raymond, P. A., McClelland, J. W., Holmes, R. M., Zhulidov, A. V., Mull, K., Peterson, B. J.,
5446 Striegl, R. G., Aiken, G. R. and Gurtovaya, T. Y.: Flux and age of dissolved organic carbon
5447 exported to the Arctic Ocean: A carbon isotopic study of the five largest arctic rivers,
5448 Global Biogeochem. Cycles, doi:10.1029/2007GB002934, 2007.

5449 Raymond, P. A., Oh, N. H., Turner, R. E. and Broussard, W.: Anthropogenically enhanced
5450 fluxes of water and carbon from the Mississippi River, Nature,
5451 doi:10.1038/nature06505, 2008.

5452 Raymond, P. A., Hartmann, J., Lauerwald, R., Sobek, S., McDonald, C., Hoover, M., Butman,
5453 D., Striegl, R., Mayorga, E., Humborg, C., Kortelainen, P., Dürr, H., Meybeck, M., Ciais, P.
5454 and Guth, P.: Global carbon dioxide emissions from inland waters, Nature,
5455 doi:10.1038/nature12760, 2013.

5456 Regnier, P., Friedlingstein, P., Ciais, P., Mackenzie, F. T., Gruber, N., Janssens, I. A.,
5457 Laruelle, G. G., Lauerwald, R., Luyssaert, S., Andersson, A. J., Arndt, S., Arnosti, C., Borges,
5458 A. V., Dale, A. W., Gallego-Sala, A., Goddérís, Y., Goossens, N., Hartmann, J., Heinze, C.,
5459 Ilyina, T., Joos, F., Larowe, D. E., Leifeld, J., Meysman, F. J. R., Munhoven, G., Raymond, P.
5460 A., Spahni, R., Suntharalingam, P. and Thullner, M.: Anthropogenic perturbation of the
5461 carbon fluxes from land to ocean, Nat. Geosci., doi:10.1038/ngeo1830, 2013.

5462 Reynolds, C. A., Jackson, T. J. and Rawls, W. J.: Estimating soil water-holding capacities by
5463 linking the Food and Agriculture Organization soil map of the world with global pedon
5464 databases and continuous pedotransfer functions, Water Resour. Res.,
5465 doi:10.1029/2000WR900130, 2000.

5466 Rhein, M., Rintoul, S., Aoki, S., Campos, E., Chambers, D., Feely, R. A., Gulev, S., Johnson, G.,

5467 Josey, S., Kostianoy, A., Mauritzen, C., Roemmich, D., Talley, L., Wang, F. and IPCC:
5468 Observations: Ocean. In: Climate Change 2013: The Physical Science Basis. Contribution
5469 of Working Group I to the Fifth Assessment Report of the Intergovernmental Panel on
5470 Climate Change., 2013.

5471 Rosenqvist, L., Hansen, K., Vesterdal, L. and van der Salm, C.: Water balance in
5472 afforestation chronosequences of common oak and Norway spruce on former arable
5473 land in Denmark and southern Sweden, *Agric. For. Meteorol.*,
5474 doi:10.1016/j.agrformet.2009.10.004, 2010.

5475 Roser, C., Montagnani, L., Schulze, E.-D., Mollicone, D., Kolle, O., Meroni, M., Papale, D.,
5476 Marchesini, L. B., Federici, S. and Valentini, R.: Net CO₂ exchange rates in three different
5477 successional stages of the “Dark Taiga” of central Siberia, *Tellus B*, doi:10.1034/j.1600-
5478 0889.2002.01351.x, 2002.

5479 Sapart, C. J., Shakhova, N., Semiletov, I., Jansen, J., Szidat, S., Kosmach, D., Dudarev, O., Van
5480 Der Veen, C., Egger, M., Sergienko, V., Salyuk, A., Tumskey, V., Tison, J. L. and Röckmann,
5481 T.: The origin of methane in the East Siberian Arctic Shelf unraveled with triple isotope
5482 analysis, *Biogeosciences*, doi:10.5194/bg-14-2283-2017, 2017.

5483 Sawakuchi, H. O., Neu, V., Ward, N. D., Barros, M. de L. C., Valerio, A. M., Gagne-Maynard,
5484 W., Cunha, A. C., Less, D. F. S., Diniz, J. E. M., Brito, D. C., Krusche, A. V and Richey, J. E.:
5485 Carbon Dioxide Emissions along the Lower Amazon River, *Front. Mar. Sci.*,
5486 doi:10.3389/fmars.2017.00076, 2017.

5487 Sawamoto, T., Hatano, R., Yajima, T., Takahashi, K. and Isaev, A. P.: Soil respiration in
5488 siberian taiga ecosystems with different histories of forest fire, *Soil Sci. Plant Nutr.*,
5489 doi:10.1080/00380768.2000.10408759, 2000.

5490 Schädel, C., Schuur, E. A. G., Bracho, R., Elberling, B., Knoblauch, C., Lee, H., Luo, Y., Shaver,
5491 G. R. and Turetsky, M. R.: Circumpolar assessment of permafrost C quality and its
5492 vulnerability over time using long-term incubation data, *Glob. Chang. Biol.*,
5493 doi:10.1111/gcb.12417, 2014.

5494 Schlesinger, W. H. and Melack, J. M.: Transport of organic carbon in the world’s rivers,
5495 *Tellus*, doi:10.3402/tellusa.v33i2.10706, 1981.

5496 Schulze, E. D., Lloyd, J., Kelliher, F. M., Wirth, C., Rebmann, C., Luhker, B., Mund, M., Knohl,
5497 A., Milyukova, I. M., Schulze, W., Ziegler, W., Varlagin, A. B., Sogachev, A. F., Valentini, R.,
5498 Dore, S., Grigoriev, S., Kolle, O., Panfyorov, M. I., Tchebakova, N. and Vygodskaya, N. N.:
5499 Productivity of forests in the eurosiberian boreal region and their potential to act as a
5500 carbon sink - a synthesis, *Glob. Chang. Biol.*, doi:10.1046/j.1365-2486.1999.00266.x,
5501 1999.

5502 Schuur, E. A. G., Vogel, J. G., Crummer, K. G., Lee, H., Sickman, J. O. and Osterkamp, T. E.:
5503 The effect of permafrost thaw on old carbon release and net carbon exchange from
5504 tundra, *Nature*, doi:10.1038/nature08031, 2009.

5505 Schuur, E. A. G., McGuire, A. D., Schädel, C., Grosse, G., Harden, J. W., Hayes, D. J., Hugelius,
5506 G., Koven, C. D., Kuhry, P., Lawrence, D. M., Natali, S. M., Olefeldt, D., Romanovsky, V. E.,
5507 Schaefer, K., Turetsky, M. R., Treat, C. C. and Vonk, J. E.: Climate change and the
5508 permafrost carbon feedback, *Nature*, doi:10.1038/nature14338, 2015.

5509 Selvam, B. P., Lapierre, J. F., Guillemette, F., Voigt, C., Lamprecht, R. E., Biasi, C.,
5510 Christensen, T. R., Martikainen, P. J. and Berggren, M.: Degradation potentials of
5511 dissolved organic carbon (DOC) from thawed permafrost peat, *Sci. Rep.*,
5512 doi:10.1038/srep45811, 2017.

5513 Semiletov, I., Pipko, I., Gustafsson, Ö., Anderson, L. G., Sergienko, V., Pugach, S., Dudarev,
5514 O., Charkin, A., Gukov, A., Bröder, L., Andersson, A., Spivak, E. and Shakhova, N.:

5515 Acidification of East Siberian Arctic Shelf waters through addition of freshwater and
5516 terrestrial carbon, *Nat. Geosci.*, doi:10.3233/978-1-61499-868-6-158, 2016.

5517 Semiletov, I. P., Pipko, I. I., Repina, I. and Shakhova, N. E.: Carbonate chemistry dynamics
5518 and carbon dioxide fluxes across the atmosphere-ice-water interfaces in the Arctic
5519 Ocean: Pacific sector of the Arctic, *J. Mar. Syst.*, doi:10.1016/j.jmarsys.2006.05.012,
5520 2007.

5521 Semiletov, I. P., Pipko, I. I., Shakhova, N. E., Dudarev, O. V., Pugach, S. P., Charkin, A. N.,
5522 Mcroy, C. P., Kosmach, D. and Gustafsson, Ö.: Carbon transport by the Lena River from its
5523 headwaters to the Arctic Ocean, with emphasis on fluvial input of terrestrial particulate
5524 organic carbon vs. carbon transport by coastal erosion, *Biogeosciences*, doi:10.5194/bg-
5525 8-2407-2011, 2011.

5526 Semiletov, I. P., Shakhova, N. E., Sergienko, V. I., Pipko, I. I. and Dudarev, O. V.: On carbon
5527 transport and fate in the East Siberian Arctic land-shelf-atmosphere system, *Environ.*
5528 *Res. Lett.*, doi:10.1088/1748-9326/7/1/015201, 2012.

5529 Serreze, M. C. and Barry, R. G.: Processes and impacts of Arctic amplification: A research
5530 synthesis, *Glob. Planet. Change*, doi:10.1016/j.gloplacha.2011.03.004, 2011.

5531 Shakhova, N. and Semiletov, I.: Methane release and coastal environment in the East
5532 Siberian Arctic shelf, *J. Mar. Syst.*, doi:10.1016/j.jmarsys.2006.06.006, 2007.

5533 Shakhova, N., Semiletov, I., Salyuk, A., Yusupov, V., Kosmach, D. and Gustafsson, Ö.:
5534 Extensive methane venting to the atmosphere from sediments of the East Siberian Arctic
5535 Shelf, *Science (80-.)*, doi:10.1126/science.1182221, 2010.

5536 Shakhova, N., Semiletov, I., Leifer, I., Sergienko, V., Salyuk, A., Kosmach, D., Chernykh, D.,
5537 Stubbs, C., Nicolsky, D., Tumskoy, V. and Gustafsson, Ö.: Ebullition and storm-induced
5538 methane release from the East Siberian Arctic Shelf, *Nat. Geosci.*, doi:10.1038/ngeo2007,
5539 2014.

5540 Shakhova, N., Semiletov, I., Sergienko, V., Lobkovsky, L., Yusupov, V., Salyuk, A.,
5541 Salomatin, A., Chernykh, D., Kosmach, D., Panteleev, G., Nicolsky, D., Samarkin, V., Joye, S.,
5542 Charkin, A., Dudarev, O., Meluzov, A. and Gustafsson, O.: The East Siberian Arctic Shelf:
5543 Towards further assessment of permafrost-related methane fluxes and role of sea ice,
5544 *Philos. Trans. R. Soc. A Math. Phys. Eng. Sci.*, doi:10.1098/rsta.2014.0451, 2015.

5545 Shvartsev, S. L.: Geochemistry of fresh groundwater in the main landscape zones of the
5546 Earth, *Geochemistry Int.*, doi:10.1134/S0016702908130016, 2008.

5547 Shvidenko, A. and Nilsson, S.: A synthesis of the impact of Russian forests on the global
5548 carbon budget for 1961-1998, *Tellus, Ser. B Chem. Phys. Meteorol.*, doi:10.1034/j.1600-
5549 0889.2003.00046.x, 2003.

5550 Smith, L. C. and Pavelsky, T. M.: Estimation of river discharge, propagation speed, and
5551 hydraulic geometry from space: Lena River, Siberia, *Water Resour. Res.*,
5552 doi:10.1029/2007WR006133, 2008.

5553 Sommerkorn, M.: Micro-topographic patterns unravel controls of soil water and
5554 temperature on soil respiration in three Siberian tundra systems, *Soil Biol. Biochem.*,
5555 doi:10.1016/j.soilbio.2008.03.002, 2008.

5556 Sorokin, Y. I. and Sorokin, P. Y.: Plankton and primary production in the Lena River
5557 Estuary and in the south-eastern Laptev sea, *Estuar. Coast. Shelf Sci.*,
5558 doi:10.1006/ecss.1996.0078, 1996.

5559 Spencer, R. G. M., Mann, P. J., Dittmar, T., Eglinton, T. I., McIntyre, C., Holmes, R. M., Zimov,
5560 N. and Stubbins, A.: Detecting the signature of permafrost thaw in Arctic rivers, *Geophys.*
5561 *Res. Lett.*, doi:10.1002/2015GL063498, 2015.

5562 Starr, M., Lindroos, A. J., Ukonmaanaho, L., Tarvainen, T. and Tanskanen, H.: Weathering

5563 release of heavy metals from soil in comparison to deposition, litterfall and leaching
5564 fluxes in a remote, boreal coniferous forest, *Appl. Geochemistry*, doi:10.1016/S0883-
5565 2927(02)00157-9, 2003.

5566 Steele, M. and Ermold, W.: Loitering of the retreating sea ice edge in the Arctic Seas, *J.*
5567 *Geophys. Res. Ocean.*, doi:10.1002/2015JC011182, 2015.

5568 Stets, E. G., Butman, D., McDonald, C. P., Stackpoole, S. M., DeGrandpre, M. D. and Striegl,
5569 R. G.: Carbonate buffering and metabolic controls on carbon dioxide in rivers, *Global*
5570 *Biogeochem. Cycles*, doi:10.1002/2016GB005578, 2017.

5571 Striegl, R. G., Dornblaser, M. M., Aiken, G. R., Wickland, K. P. and Raymond, P. A.: Carbon
5572 export and cycling by the Yukon, Tanana, and Porcupine rivers, Alaska, 2001-2005,
5573 *Water Resour. Res.*, doi:10.1029/2006WR005201, 2007.

5574 Stroeve, J. C., Markus, T., Boisvert, L., Miller, J. and Barrett, A.: Changes in Arctic melt
5575 season and implications for sea ice loss, *Geophys. Res. Lett.*,
5576 doi:10.1002/2013GL058951, 2014.

5577 Stuart Chapin, F., Matson, P. A. and Vitousek, P. M.: *Principles of terrestrial ecosystem*
5578 *ecology.*, 2012.

5579 Stubbins, A., Mann, P. J., Powers, L., Bittar, T. B., Dittmar, T., McIntyre, C. P., Eglinton, T. I.,
5580 Zimov, N. and Spencer, R. G. M.: Low photolability of yedoma permafrost dissolved
5581 organic carbon, *J. Geophys. Res. Biogeosciences*, doi:10.1002/2016JG003688, 2017.

5582 Tank, S. E., Raymond, P. A., Striegl, R. G., McClelland, J. W., Holmes, R. M., Fiske, G. J. and
5583 Peterson, B. J.: A land-to-ocean perspective on the magnitude, source and implication of
5584 DIC flux from major Arctic rivers to the Arctic Ocean, *Global Biogeochem. Cycles*,
5585 doi:10.1029/2011GB004192, 2012a.

5586 Tank, S. E., Raymond, P. A., Striegl, R. G., McClelland, J. W., Holmes, R. M., Fiske, G. J. and
5587 Peterson, B. J.: A land-to-ocean perspective on the magnitude, source and implication of
5588 DIC flux from major Arctic rivers to the Arctic Ocean, *Global Biogeochem. Cycles*,
5589 doi:10.1029/2011GB004192, 2012b.

5590 Tank, S. E., Frey, K. E., Striegl, R. G., Raymond, P. A., Holmes, R. M., McClelland, J. W. and
5591 Peterson, B. J.: Landscape-level controls on dissolved carbon flux from diverse
5592 catchments of the circumboreal, *Global Biogeochem. Cycles*,
5593 doi:10.1029/2012GB004299, 2012c.

5594 Tank, S. E., Striegl, R. G., McClelland, J. W. and Kokelj, S. V.: Multi-decadal increases in
5595 dissolved organic carbon and alkalinity flux from the Mackenzie drainage basin to the
5596 Arctic Ocean, *Environ. Res. Lett.*, doi:10.1088/1748-9326/11/5/054015, 2016.

5597 Tank, S. E., Fellman, J. B., Hood, E. and Kritzberg, E. S.: Beyond respiration: Controls on
5598 lateral carbon fluxes across the terrestrial-aquatic interface, *Limnol. Oceanogr. Lett.*,
5599 doi:10.1002/lol2.10065, 2018.

5600 Tanski, G., Lantuit, H., Ruttor, S., Knoblauch, C., Radosavljevic, B., Strauss, J., Wolter, J.,
5601 Irrgang, A. M., Ramage, J. and Fritz, M.: Transformation of terrestrial organic matter
5602 along thermokarst-affected permafrost coasts in the Arctic, *Sci. Total Environ.*,
5603 doi:10.1016/j.scitotenv.2016.12.152, 2017.

5604 Tarnocai, C., Canadell, J. G., Schuur, E. A. G., Kuhry, P., Mazhitova, G. and Zimov, S.: Soil
5605 organic carbon pools in the northern circumpolar permafrost region, *Global Biogeochem.*
5606 *Cycles*, doi:10.1029/2008gb003327, 2009.

5607 Teodoru, C. R., Del Giorgio, P. A., Prairie, Y. T. and Camire, M.: Patterns in pCO₂ in boreal
5608 streams and rivers of northern Quebec, Canada, *Global Biogeochem. Cycles*,
5609 doi:10.1029/2008GB003404, 2009.

5610 Tesi, T., Semiletov, I., Hugelius, G., Dudarev, O., Kuhry, P. and Gustafsson, Ö.: Composition

5611 and fate of terrigenous organic matter along the Arctic land-ocean continuum in East
5612 Siberia: Insights from biomarkers and carbon isotopes, *Geochim. Cosmochim. Acta*,
5613 doi:10.1016/j.gca.2014.02.045, 2014.

5614 Tootchi, A., Jost, A. and Ducharme, A.: Multi-source global wetland maps combining
5615 surface water imagery and groundwater constraints, *Earth Syst. Sci. Data*,
5616 doi:10.5194/essd-11-189-2019, 2019.

5617 Tranvik, L. J., Downing, J. A., Cotner, J. B., Loiselle, S. A., Striegl, R. G., Ballatore, T. J., Dillon,
5618 P., Finlay, K., Fortino, K., Knoll, L. B., Kortelainen, P. L., Kutser, T., Larsen, S., Laurion, I.,
5619 Leech, D. M., Leigh McCallister, S., McKnight, D. M., Melack, J. M., Overholt, E., Porter, J. A.,
5620 Prairie, Y., Renwick, W. H., Roland, F., Sherman, B. S., Schindler, D. W., Sobek, S.,
5621 Tremblay, A., Vanni, M. J., Verschoor, A. M., Von Wachenfeldt, E. and Weyhenmeyer, G. A.:
5622 Lakes and reservoirs as regulators of carbon cycling and climate, *Limnol. Oceanogr.*,
5623 doi:10.4319/lo.2009.54.6_part_2.2298, 2009.

5624 Venkiteswaran, J. J., Schiff, S. L. and Wallin, M. B.: Large carbon dioxide fluxes from
5625 headwater boreal and sub-boreal streams, *PLoS One*,
5626 doi:10.1371/journal.pone.0101756, 2014.

5627 Vitousek, P. M. and Hobbie, S.: Heterotrophic nitrogen fixation in decomposing litter:
5628 Patterns and regulation, *Ecology*, doi:10.1890/0012-
5629 9658(2000)081[2366:HNFIDL]2.0.CO;2, 2000.

5630 Vitousek, P. M. and Sanford, R. L.: Nutrient Cycling in Moist Tropical Forest, *Ecology*,
5631 doi:0.1146/annurev.es.17.110186.001033, 1986.

5632 Van Vliet, M. T. H., Yearsley, J. R., Franssen, W. H. P., Ludwig, F., Haddeland, I.,
5633 Lettenmaier, D. P. and Kabat, P.: Coupled daily streamflow and water temperature
5634 modelling in large river basins, *Hydrol. Earth Syst. Sci.*, doi:10.5194/hess-16-4303-2012,
5635 2012.

5636 Van Vliet, M. T. H., Franssen, W. H. P., Yearsley, J. R., Ludwig, F., Haddeland, I.,
5637 Lettenmaier, D. P. and Kabat, P.: Global river discharge and water temperature under
5638 climate change, *Glob. Environ. Chang.*, doi:10.1016/j.gloenvcha.2012.11.002, 2013.

5639 Vonk, J. E. and Gustafsson, Ö.: Permafrost-carbon complexities, *Nat. Geosci.*,
5640 doi:10.1038/ngeo1937, 2013.

5641 Vonk, J. E., Sanchez-Garca, L., Van Dongen, B. E., Alling, V., Kosmach, D., Charkin, A.,
5642 Semiletov, I. P., Dudarev, O. V., Shakhova, N., Roos, P., Eglinton, T. I., Andersson, A. and
5643 Gustafsson, A.: Activation of old carbon by erosion of coastal and subsea permafrost in
5644 Arctic Siberia, *Nature*, doi:10.1038/nature11392, 2012.

5645 Vonk, J. E., Mann, P. J., Davydov, S., Davydova, A., Spencer, R. G. M., Schade, J., Sobczak, W.
5646 V., Zimov, N., Zimov, S., Bulygina, E., Eglinton, T. I. and Holmes, R. M.: High biolability of
5647 ancient permafrost carbon upon thaw, *Geophys. Res. Lett.*, doi:10.1002/grl.50348, 2013.

5648 Vonk, J. E., Tank, S. E., Mann, P. J., Spencer, R. G. M., Treat, C. C., Striegl, R. G., Abbott, B. W.
5649 and Wickland, K. P.: Biodegradability of dissolved organic carbon in permafrost soils and
5650 aquatic systems: A meta-analysis, *Biogeosciences*, doi:10.5194/bg-12-6915-2015,
5651 2015a.

5652 Vonk, J. E., Thienpont, J. R., Rühland, K. M., Pisaric, M. F. J., Kokelj, S. V., Kimpe, L. E., Blais,
5653 J. M., Smol, J. P., Spencer, R. G. M., Mann, P. J., Dittmar, T., Eglinton, T. I., McIntyre, C.,
5654 Holmes, R. M., Zimov, N., Stubbins, A., Rudy, A. C. a, Lamoureux, S. F., Treitz, P.,
5655 Collingwood, A., Rouse, W. R., Douglas, M. S. V., Hecky, R. E., Hershey, a. E., Kling, G. W.,
5656 Lesack, L., Marsh, P., McDonald, M., Nicholson, B. J., Roulet, N. T., Smol, J. P., Murton, J. B.,
5657 Lewkowicz, A. G., Harris, C., Lantz, T. C., Kokelj, S. V., Gergel, S. E., Henry, G. H. R.,
5658 Tunnicliffe, J., Lacelle, D., Lantz, T. C., Chin, K., Fraser, R., Jin, H., Yu, Q., Lu, L., Guo, D., He,

5659 R., Yu, S., Sun, G., Li, Y., Harris, C., Lewkowicz, A. G., Grom, J. D., Pollard, W. H., Balsler, A.
5660 W., Gooseff, M. N., Jones, J. B., Bowden, W. B., Anisimov, O. a. and Nelson, F. E.: Detecting
5661 the signature of permafrost thaw in Arctic rivers, *Glob. Planet. Change*,
5662 doi:10.1002/2015GL063498. Received, 2015b.

5663 Vonk, J. E., Tank, S. E., Bowden, W. B., Laurion, I., Vincent, W. F., Alekseychik, P., Amyot,
5664 M., Billet, M. F., Canário, J., Cory, R. M., Deshpande, B. N., Helbig, M., Jammet, M., Karlsson,
5665 J., Larouche, J., MacMillan, G., Rautio, M., Walter Anthony, K. M. and Wickland, K. P.:
5666 Reviews and Syntheses: Effects of permafrost thaw on arctic aquatic ecosystems,
5667 *Biogeosciences Discuss.*, doi:10.5194/bgd-12-10719-2015, 2015c.

5668 Vorosmarty, C. J., Fekete, B. M., Meybeck, M. and Lammers, R. B.: Global system of rivers:
5669 Its role in organizing continental land mass and defining land-To-Ocean linkages, *Global*
5670 *Biogeochem. Cycles*, doi:10.1029/1999GB900092, 2000.

5671 Walz, J., Knoblauch, C., Böhme, L. and Pfeiffer, E. M.: Regulation of soil organic matter
5672 decomposition in permafrost-affected Siberian tundra soils - Impact of oxygen
5673 availability, freezing and thawing, temperature, and labile organic matter, *Soil Biol.*
5674 *Biochem.*, doi:10.1016/j.soilbio.2017.03.001, 2017.

5675 Wang, T., Otlé, C., Boone, A., Ciais, P., Brun, E., Morin, S., Krinner, G., Piao, S. and Peng, S.:
5676 Evaluation of an improved intermediate complexity snow scheme in the ORCHIDEE land
5677 surface model, *J. Geophys. Res. Atmos.*, doi:10.1002/jgrd.50395, 2013.

5678 Wanninkhof, R. H.: Relationship between wind speed and gas exchange, *J. Geophys. Res.*,
5679 doi:10.1029/92JC00188, 1992.

5680 White, A. F. and Blum, A. E.: Effects of climate on chemical_ weathering in watersheds,
5681 *Geochim. Cosmochim. Acta*, doi:10.1016/0016-7037(95)00078-E, 1995.

5682 Whitefield, J., Winsor, P., McClelland, J. and Menemenlis, D.: A new river discharge and
5683 river temperature climatology data set for the pan-Arctic region, *Ocean Model.*,
5684 doi:10.1016/j.ocemod.2014.12.012, 2015.

5685 Wickland, K. P., Waldrop, M. P., Aiken, G. R., Koch, J. C., Jorgenson, M. T. and Striegl, R. G.:
5686 Dissolved organic carbon and nitrogen release from boreal Holocene permafrost and
5687 seasonally frozen soils of Alaska, *Environ. Res. Lett.*, doi:10.1088/1748-9326/aac4ad,
5688 2018.

5689 Wild, B., Schnecker, J., Alves, R. J. E., Barsukov, P., Bárta, J., Čapek, P., Gentsch, N., Gittel, A.,
5690 Guggenberger, G., Lashchinskiy, N., Mikutta, R., Rusalimova, O., Šantrůčková, H.,
5691 Shibistova, O., Urich, T., Watzka, M., Zrazhevskaya, G. and Richter, A.: Input of easily
5692 available organic C and N stimulates microbial decomposition of soil organic matter in
5693 arctic permafrost soil, *Soil Biol. Biochem.*, doi:10.1016/j.soilbio.2014.04.014, 2014.

5694 Wild, B., Gentsch, N., Capek, P., Diáková, K., Alves, R. J. E., Bárta, J., Gittel, A., Hugelius, G.,
5695 Knoltsch, A., Kuhry, P., Lashchinskiy, N., Mikutta, R., Palmtag, J., Schleper, C., Schnecker, J.,
5696 Shibistova, O., Takriti, M., Torsvik, V. L., Urich, T., Watzka, M., Šantrůčková, H.,
5697 Guggenberger, G. and Richter, A.: Plant-derived compounds stimulate the decomposition
5698 of organic matter in arctic permafrost soils, *Sci. Rep.*, doi:10.1038/srep25607, 2016.

5699 Woods, G. C., Simpson, M. J., Pautler, B. G., Lamoureux, S. F., Lafrenière, M. J. and Simpson,
5700 A. J.: Evidence for the enhanced lability of dissolved organic matter following permafrost
5701 slope disturbance in the Canadian High Arctic, *Geochim. Cosmochim. Acta*,
5702 doi:10.1016/j.gca.2011.08.013, 2011.

5703 Wu, Y., Clarke, N. and Mulder, J.: Dissolved organic carbon concentrations in throughfall
5704 and soil waters at level II monitoring plots in Norway: Short- and long-term variations,
5705 *Water. Air. Soil Pollut.*, doi:10.1007/s11270-009-0073-1, 2010.

5706 Xue, K.: Tundra soil carbon is vulnerable to rapid microbial decomposition under

5707 climatewarming, *Nat. Clim. Chang.*, doi:10.1038/NCLIMATE2940, 2017.

5708 Xue, K., Yuan, M. M., Shi, Z. J., Qin, Y., Deng, Y., Cheng, L., Wu, L., He, Z., Van Nostrand, J. D.,
5709 Bracho, R., Natali, S., Schuur, E. A. G., Luo, C., Konstantinidis, K. T., Wang, Q., Cole, J. R.,
5710 Tiedje, J. M., Luo, Y. and Zhou, J.: Tundra soil carbon is vulnerable to rapid microbial
5711 decomposition under climate warming, *Nat. Clim. Chang.*, doi:10.1038/nclimate2940,
5712 2016.

5713 Yang, H., Zhou, F., Piao, S., Huang, M., Chen, A., Ciais, P., Li, Y., Lian, X., Peng, S. and Zeng,
5714 Z.: Regional patterns of future runoff changes from Earth system models constrained by
5715 observation, *Geophys. Res. Lett.*, doi:10.1002/2017GL073454, 2017.

5716 Ye, B., Yang, D. and Kane, D. L.: Changes in Lena River streamflow hydrology: Human
5717 impacts versus natural variations, *Water Resour. Res.*, doi:10.1029/2003WR001991,
5718 2003.

5719 Ye, B., Yang, D., Zhang, Z. and Kane, D. L.: Variation of hydrological regime with
5720 permafrost coverage over Lena Basin in Siberia, *J. Geophys. Res. Atmos.*,
5721 doi:10.1029/2008JD010537, 2009.

5722 Yu, Z.: Holocene carbon flux histories of the world's peatlands: Global carbon-cycle
5723 implications, *Holocene*, doi:10.1177/0959683610386982, 2011.

5724 Yue, C., Ciais, P., Zhu, D., Wang, T., Peng, S. S. and Piao, S. L.: How have past fire
5725 disturbances contributed to the current carbon balance of boreal ecosystems?,
5726 *Biogeosciences*, doi:10.5194/bg-13-675-2016, 2016.

5727 Zakharova, E. A., Pokrovsky, O. S., Dupré, B., Gaillardet, J. and Efimova, L. E.: Chemical
5728 weathering of silicate rocks in Karelia region and Kola peninsula, NW Russia: Assessing
5729 the effect of rock composition, wetlands and vegetation, *Chem. Geol.*,
5730 doi:10.1016/j.chemgeo.2007.03.018, 2007.

5731 Zhang, K., Kimball, J. S., Mu, Q., Jones, L. A., Goetz, S. J. and Running, S. W.: Satellite based
5732 analysis of northern ET trends and associated changes in the regional water balance
5733 from 1983 to 2005, *J. Hydrol.*, doi:10.1016/j.jhydrol.2009.09.047, 2009.

5734 Zhang, X., Hutchings, J. A., Bianchi, T. S., Liu, Y., Arellano, A. R. and Schuur, E. A. G.:
5735 Importance of lateral flux and its percolation depth on organic carbon export in Arctic
5736 tundra soil: Implications from a soil leaching experiment, *J. Geophys. Res.*
5737 *Biogeosciences*, doi:10.1002/2016JG003754, 2017.

5738 Zhu, D., Peng, S., Ciais, P., Zech, R., Krinner, G., Zimov, S. and Grosse, G.: Simulating soil
5739 organic carbon in yedoma deposits during the Last Glacial Maximum in a land surface
5740 model, *Geophys. Res. Lett.*, doi:10.1002/2016GL068874, 2016.

5741 Zimov, S. A., Schuur, E. A. G. and Stuart Chapin, F.: Permafrost and the global carbon
5742 budget, *Science (80-.)*, doi:10.1126/science.1128908, 2006.

5743 Zolkos, S., Tank, S. E. and Kokelj, S. V.: Mineral Weathering and the Permafrost Carbon-
5744 Climate Feedback, *Geophys. Res. Lett.*, doi:10.1029/2018GL078748, 2018.

5745 Zona, D., Gioli, B., Commane, R., Lindaas, J., Wofsy, S. C. and Miller, C. E.: Cold season
5746 emissions dominate the Arctic tundra methane budget, *Proc. Natl. Acad. Sci.*,
5747 doi:10.1073/pnas.1516017113, 2015.

5748 Zubrzycki, S., Kutzbach, L., Grosse, G. and Desyatkin, A.: Organic carbon and total
5749 nitrogen stocks in soils of the Lena River Delta, *Biogeosciences*, doi:10.5194/bg-10-
5750 3507-2013, 2013.

5751